PULSED GMAW PARAMETER VARIATION TO MINIMIZE INTERFERENCE FROM TACK WELDS

by

GREGORY C. KOLODZIEJCZAK

B.S., Physics, United States Naval Academy
(1978)

S.M., O.E., Massachusetts Institute of Technology
(1985)

SUBMITTED IN PARTIAL FULFILLMENT
OF THE REQUIREMENTS FOR THE
DEGREE OF

DOCTOR OF PHILOSOPHY

at the

MASSACHUSETTS INSTITUTE OF TECHNOLOGY

May 1987

Signature of Author__

Department of Ocean Engineering
May 20, 1987

Certified by_____

Koichi Masubuchi
Thesis Supervisor

Accepted by_____

Douglas Carmichael
Chairman, Departmental Graduate Committee

PULSED GMAW PARAMETER VARIATION TO MINIMIZE INTERFERENCE FROM TACK WELDS

by

Gregory C. Kolodziejczak

Submitted to the Department of Ocean Engineering in partial fulfillment of the requirements for the degree of Doctor of Philosophy in Ocean Engineering.

ABSTRACT

Tack welds are used extensively in shipbuilding to secure metal pieces in preparation for final welding. This thesis is a comprehensive analysis of the effect of tack welds on shipbuilding and the possible means by which they can be dealt with more effectively. It is organized into three areas. The first is an overview of the shipbuilding process, with emphasis on modern shipbuilding techniques and their relation to flexible automation and automated welding. The problem of tack welds is discussed and shown to be significant.

The second area is a specific examination of the welding phenomena occurring at tack weld sites in steel butt joints. Experimentally, tack welds are shown to be a major source of defects. Lack of penetration, lack of fusion, and discontinuities at the beginnings and ends of tack welds are prevalent. Underbead temperature profiles are measured and compared to predictions using the Rosenthal solution. Agreement is good, and the differences are discussed in terms of the Rosenthal assumptions and the effects of transient heat flow at the tack weld sites.

The third area is an analysis of pulsed gas metal arc welding as a means of better handling tack welds by increasing penetration. Four mechanisms of penetration are discussed in detail: arc pressure, compound vortex, weld pool convection, and droplet momentum. The effect of current pulsing on each mechanism is analyzed, and five strategies are devised for increasing penetration: low frequency pulsing, high frequency pulsing, high duty cycle pulsing, high peak pulsing, and mid-peak drop transfer. All five strategies are tested experimentally, and all except high frequency pulsing are found to increase penetration. A discussion of the success of the other mechanisms and the failure of high frequency pulsing is presented. The use of pulsed GMAW in the development of a control strategy for dealing with tack welds is discussed, as are alternatives to current pulsing.

Thesis Committee:

Professor Koichi Masubuchi	Dept. of Ocean Engineering
Professor Tom Eagar	Dept. of Materials Science and Engineering
Professor Paul Sullivan	Dept. of Ocean Engineering
Dr. John Agapakis	Automatix, Inc.

ACKNOWLEDGEMENTS

It has been a great privelege to have Professor Koichi Masubuchi as my thesis adviser and committee chairman. He is truly a pleasure to work for, and I benefitted greatly from his expertise, support, and patience. I am deeply indebted to Professor Tom Eagar, both for the use of his laboratory facilities and for his excellent guidance, particularly during the final stages of this work. His rigorous approach to problem solving is demanding but enlightening. Thanks to Dr. John Agapakis of Automatix, Inc. for his expertise, help, and suggestions, and to Professor Paul Sullivan for his confidence, motivation, and support. I am also grateful to Professor Francis Ogilvie for his overall guidance throughout the past few years, to Professor Nick Patrikalakis for being on my Part II committee, and to Dr. Carl Sorensen for his many contributions.

The technical support of my colleagues is similarly acknowledged. Steve Eickhoff taught me more about laboratory equipment and procedures than I thought there was to know, Mansoor Khan was very helpful with computer plotting techniques, and John Spencer assisted me in the many hours of welding, cutting, and grinding. I am deeply indebted to Muriel Bernier, Mary Kreuz, and particularly Colleen DeCoste for their help with the final preparation of this work. I know that Colleen is as glad to be done with it as I am. Finally, I want to thank the US Navy for giving me the opportunity to pursue this work at MIT.

On the personal side, my deepest and warmest thanks go to Allison Koury for her unfailing support, encouragement, and love. More than she can realize, she taught me much about life and made life worth living. To her I dedicate this thesis. The friendship that Bill Luebke and I have developed over the past few years is proof that misery loves company. I hope that I can someday assist him as much as he has helped me. And thanks to my dear friend Debbi Karpowicz, who is a constant source of inspiration. Her unending energy, faith, and belief in the future are contagious. Finally, thank you to my family for always encouraging me to have the faith in myself to take risks and strive for the best. And most importantly, I thank the Lord for establishing the principles upon which I strive to live my life.

To Allison

TABLE OF CONTENTS

LIST OF FIGURES

LIST OF TABLES

CHAPTER 1

INTRODUCTION

"The main objective of industrial robot study in the USSR is the creation of a worker replacement which does not drink, is never absent, and works without any coffee breaks" (1). While this objective might accurately represent the conventional robotic wisdom in many countries, it is an objective doomed to economic failure. Robots were initially viewed by many in industry as direct replacements for labor, and this led to unrealistic expectations regarding the ability to quickly incorporate robots into the workplace. Properly viewed, a robot is just one component in a comprehensive strategy of flexible automation, as will be discussed in chapter 2. Despite its versatility, a robot requires a well organized and disciplined environment in which to function (2). When it is introduced into an undisciplined or poorly organized environment, its capabilities cannot be exploited, and its investment cost cannot be favorably recovered.

Although this has produced much initial disappointment, the long term effects will be extremely beneficial, since it is forcing industries to closely examine their work organization. As inefficient methods and operations are upgraded, the overall manufacturing process improves, and robots can be successfully introduced. Much of that reorganization has been accomplished, and robots are now being incorporated into industrial processes at a rapid pace. According to the Robotic Industries Association, there were 20,000 operational industrial robots in the U.S. by the end of 1985, compared to 6300 three years earlier (2). The

automobile industry has been the major user thus far, accounting for approximately half of the installed units (3). It is likely, however, that the automobile industry will begin to saturate in the next few years, and robots will have to establish themselves in new industries such as electronics, aerospace, and packaging.

One of the most difficult industries for robotic implementation is shipbuilding. Automation is best suited to industries that perform a large volume of identical or very similar tasks. As the volume and similarity of the tasks decrease, the automation must become more flexible in order to remain economically viable. Shipbuilding is characterized by the production of a small quantity of very large and unique final products. Until recently, it was also characterized by poor organization and outmoded processes, all of which strongly deter the introduction of robotics. However, beginning with the establishment of the National Shipbuilding Research Program in 1970, the industrial organization of shipbuilding has greatly improved, and automation is now being successfully implemented on a limited basis.

Arc welding has been identified as one of the prime targets for future automation, not only in shipbuilding, but in other industries as well. Reference (4) estimates an ultimate potential of over 200,000 arc welding robots nationwide. In addition to a well understood and well organized environment in which to operate, though, a robot requires a thorough understanding of the specific task it is to perform. Unfortunately, arc welding is an extremely complex process, and our current understanding of it will support automation on only a limited basis.

The overall objective of this thesis is to improve the ability to apply automated welding to shipbuilding. It will do so by specifically examining one of the major technical obstacles to automation -- tack welds. Chapter 2 will provide the broad background for this by taking a closer look at the shipbuilding process, flexible automation, automated welding, and the overall significance of tack welds. Chapter 3 reviews the fundamantal phenomena occurring in arc welding, analyzes the mechanisms of penetration in gas metal arc welding, and discusses pulsed gas metal arc welding as a method of improving our ability to deal with tack welds. Chapter 4 contains analytical and experimental descriptions of the transient phenomena occurring at tack weld sites. Chapter 5 describes the apparatus and procedures used in the experimental portion of the thesis. Chapter 6 presents and discusses the experimental results. Chapter 7 discusses issues involved in the application of these results to an actual welding control system. Summary and conclusions are given in chapter 8.

CHAPTER 2

SHIPBUILDING, AUTOMATION, AND WELDING

2.1 The Shipbuilding Process

2.1.1 The Productivity Problem

Shipbuilding is among the least competitive of this nation's international industries. It is a business plagued by low market share, high prices, schedule delays, and unsteady demand. This stands in vivid contrast to U.S. shipbuilding achievements in WWII. Between 1939 and 1945, a total of 5777 merchant ships were delivered in the U.S. Maritime Commission program (5). In monetary terms, these ships represented over $13 billion in contracts. Naval ships, while only one-fourth the number (6), represented an even greater financial investment, totalling over $18 billion, exclusive of ordnance costs. A detailed analysis of these accomplishments and the factors responsible for them is presented in reference (7).

Following WWII, however, the U.S. paid little attention to shipbuilding, and the industry quickly deteriorated. Japan, on the other hand, embarked on a vigorous program to rebuild its industrial base, with shipbuilding given much attention as the primary export-oriented heavy industry (8). Government policies encouraged research, development, and investment in shipbuilding, and the shipyards eagarly sought to learn new industrial and shipbuilding techniques from any available source. Ironically, it was an American company that taught the Japanese many of the fundamental principles that led to Japan's eventual dominance in shipbuilding. National Bulk Carriers arranged a ten year lease in 1951

with the Kure Naval Shipyard, which had a 150,000 deadweight ton capacity drydock with good cranes. NBC needed the large drydock to build very large iron-ore carriers for the U.S. - Venezuela trade, and such facilities were unavailable in the U.S. Elmer Hann, who had produced Liberty Ships for Henry Kaiser during WWII, provided the organizational and industrial expertise for the Kure operation, and he passed much of it on to the over 4000 Japanese engineers who visited the yard during the period of the lease.

> Elmer Hann taught the Japanese organization of work in accordance with the basic principles of group technology, emphasis on welding without distortion to control costs, the importance of college-educated middle managers trained in the entire shipbuilding system, etc. With such methods and only pre-WWII shipyards, Japanese yards were producing 40% of the world's total shipbuilding tonnage by 1964 (9).

The aggressive attitude of the Japanese contrasted sharply with that of U.S. shipbuilders, whose share of the world market had dropped to 4.9% by 1962 (10). To make matters worse, national industrial productivity was growing at only 3.1% annually by the mid-1960's, compared to 11% in Japan and 5 to 6% in Western Europe. By 1973, the U.S. ranked tenth in merchant ships under construction and on order, with only 2.6% of the world total. The approximate 1973 selling price of an 86,000 dwt tanker was $30 million for a U.S. built ship, compared to $18.5 million for a Japanese built ship and $20 million for one built in northern Europe (11). Although U.S. companies began to focus attention on improving their shipbuilding methods and facilities in the 1970's, these efforts took many years to yield measurable results. Consequently, U.S. shipbuilding competitiveness continued to decline through the rest of the 1970's, prompting John Arado, Vice-President of Chevron Shipping Company, to write

in 1983:

> In our latest survey of prices around the world, U.S. prices for tankers were 90% higher than in Europe and 2 to 3 times higher than in the Far East. The delivery situation in the U.S. seems, if anything, to be worsening. Unfortunately, long and delayed deliveries in U.S. yards appear to be a way of life (12).

Several studies were conducted around 1980 to pinpoint the cause of this price differential, and the unanimous conclusion was that foreign countries, particularly Japan, were simply able to build equivalent merchant ships with fewer direct labor hours, as well as lower material costs. The most detailed of these studies was done by the Levingston Shipbuilding Company in 1980. The study compared labor hours and material costs at IHI in Japan to those at Levingston for construction of a modified IHI designed bulk carrier. The results, shown in table 2.1, reveal that IHI was able to construct a similar ship with only 27% of the labor hours and 65% of the material costs of the U.S. yard.

Table 2.1 Ratio of IHI to Levingston labor hours and material costs. (11)

Item	Labor Hours	Material Costs
Preliminary and staff items	0.24	0.54
Hull steel items	0.22	0.78
Minor steel items	0.42	0.58
Machinery items	0.47	0.66
Outfitting items	0.35	0.56
ALL ITEMS	0.27	0.65

The fundamental difference that caused this wide disparity lies in

the basic organization and control of the shipbuilding work. Fortunately, the improvements that U.S. yards began to make in the 1970's are now paying off, and the differential between U.S. and Japanese shipbuilding productivity is probably smaller in 1987. Many of these improvements are the result of the National Shipbuilding Research Program. The NSRP began as a joint venture of industry, the U.S. Maritime Administration, and the U.S. Navy, although the U.S. Maritime Administration is ending its participation because of the absence of non-military shipbuilding in the U.S. Program costs are shared by industry and the government, and individual projects have had payback factors as high as 25 times the cost (14). These improvements are the subject of the next section.

2.1.2 Modern Shipbuilding Techniques

Ship design and construction is an extremely lengthly and complex process. A key issue, therefore, is deciding how to break it up into smaller, more manageable components. Traditionally, this division occurred by system. Performance requirements were specified by system, plans were issued by system, and the ships were built by system. Construction began with keel-laying, and when the hull was nearly complete, outfitting began with the installation of machinery, electrical, piping, and ventilation systems (15). In fact, outfit drawings generally weren't even issued until hull construction was well underway. Although this method has a certain logical appeal to it, it is a very inefficient way to build ships. The preferred method today is zone construction and outfitting. Zone construction is based on dividing the ship into geographical units rather than breaking it down functionally by system. Essentially, it is modular fabrication, and most shipyards already use the zone method for hull construction. The modular breakdown for the TAO oiler built at Avondale Shipyards is shown in figure 2.1, and that for the

FFG-7 is shown in figure 2.2.

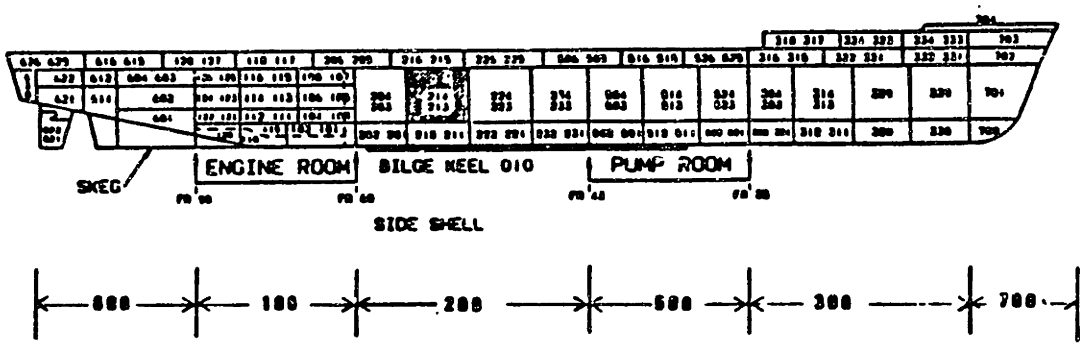

Figure 2.1 Hull block breakdown for TAO at Avondale Shipyards, Inc. (14)

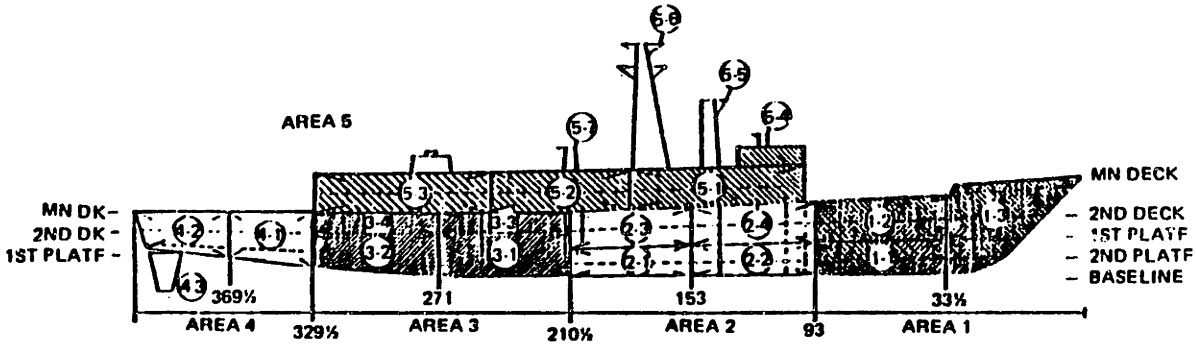

Figure 2.2 FFG-7 hull block breakdown.

Zone outfitting is more difficult to accomplish than zone hull construction, and shipyards are still in the process of trying to implement it. The goal is to make outfitting an integral part of the hull construction process by outfitting individual modules before putting them together. This allows components to be installed "at the times and under the conditions that produce the lowest overall costs" (13). The two primary factors which affect the ease with which components can be

installed are congestion and orientation. A module in its early stages of construction, with few workers in it and very few other components already installed, is much more conducive to easy installation of components than is a congested compartment on the ship during the final hectic weeks prior to a key event. Furthermore, an isolated module or part of a module can be physically oriented to provide optimum working conditions. For installing pipes, brackets, and other components in the overhead, for example, the module could be turned upside-down, thereby giving easier access to workers, reducing the need for rigging eqipment, and eliminating out-of-position welding.

In addition to dividing the ship into geographical zones, it is useful for discussion purposes to divide the shipbuilding process into chronological stages. Reference (19) defines four stages of hull construction:

(1) subassembly
(2) assembly
(3) block assembly
(4) erection

Subassembly work consists primarily of small components which are either completed items in themselves, such as foundations, or are intermediate components, such as stiffeners, which are then built into the next stage of construction. A large percentage of assembly work consists of flat and curved panel fabrication. The panels are then put together to form blocks during the block assembly stage. The maximum allowable block size is a function of the shipyard facilities, particularly crane capacity. Finally, the blocks are joined together to form the entire hull during the

erection stage.

Outfitting can take place at various stages of construction, but three distinct types of outfitting are commonly referred to in the literature:

(1) on-unit

(2) on-block

(3) on-board

On-unit outfitting is done on a pre-assembled machinery package, separate from any ship's structure. On-block outfitting is done in structural blocks prior to their erection on the ways. On-board outfitting occurs after erection. Although it is still organized by zone, it requires 30% more labor hours than on-block outfitting and 70% more than on-unit (20). On-board outfitting should therefore be limited to equipment whose size, weight, or susceptibility to damage precludes preliminary outfitting, and to certain distributed systems (such as electrical cables) that are not amenable to division at block boundaries.

The degree of pre-outfitting (outfitting prior to erection) has now become a progress standard at many yards, as is shown in figure 2.3 for Avondale Shipyards. Avondale uses the term "unit" to designate a hull block, and it can be seen that pre-outfitting has increased dramatically over recent contracts. The net result has been a substantial improvement in schedule and cost. Keel-laying to launch time has decreased over 20% and launch to delivery time has decreased over 30% on non-combat ship construction (13). Citing the adoption of these modern shipbuilding techniques as the reason, Avondale was able to underbid Lockhead by about

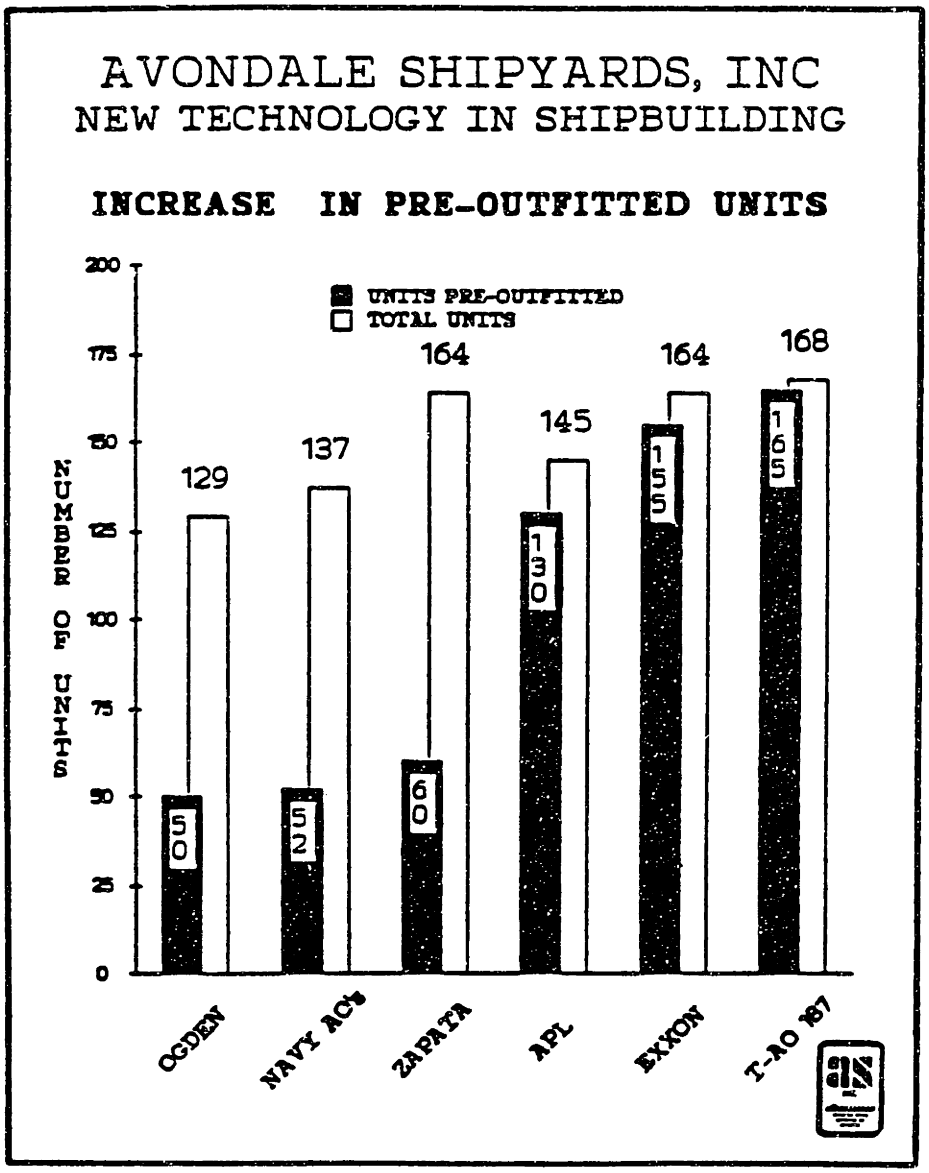

Figure 2.3 Pre-outfitting at Avondale. (16)

30% on the contract for construction of new LSD'S, even after Lockheed had already built the first three ships of the class.

The Soviet Union, too, has had excellent results from the use of modular construction methods. Reference (1) lists a number of specific benefits, including the following:

(1) A 50% to 70% reduction of construction time on the building ways.

(2) A 150% to 200% improvement in labor productivity.

(3) A 10% to 15% reduction in total construction costs resulting from more efficient material utilization.

Two other aspects of modern ship construction that are relevant to automation are process flow lanes and accuracy control. Process flow lanes are the heavy industry equivalent of assembly lines. Each process lane consists of a series of workstations and produces a given type of product. The product similarity within a lane allows repitition to be exploited to increase efficiency. Process flow lanes will undoubtedly enjoy increased utilization as shipbuilding continues to modernize, and they serve as a convenient basis for the adoption of automation, as will be discussed in section 2.3.2.

Accuracy control is the method of applying statistical rigor to the establishment of realistic accuracy goals and the development of procedures and controls to achieve those goals. The shift to modular construction techniques has made accuracy a much more critical issue, since pre-fabricated modules cannot be force-fit together in the same manner that single plates or beams can be. While accuracy control is well established in Japan, it is still relatively new in the U.S., but early indications are that it is yielding significant benefits. Research conducted by the University of Washington on the construction of navy ocean surveillance vessels at Tacoma Boatbuilding Company concluded that the short-term benefit of reduced rework alone outweighed the cost of implementing the accuracy control system (17). The long-term benefits

from further refinement of the system and from improved product design were not yet known, but were expected to be even more significant. Accuracy control is significant for automation in that it specifies what tolerance is expected from a given process (or series of processes), while the automation process has specific requirements on what tolerance is necessary for the successful completion of the ensuing process. Nowhere is this more true than with welding, where fit-up tolerances are a critical issue. The Japanese developed accuracy control based on the statistical control work of Dr. W. Edwards Deming, and it quickly grew to such prominence that the Japanese Society of Naval Architects reported in 1967 that statistical control "laid the foundation of modern ship construction methods and made it possible to extensively develop automated and specialized welding" (9).

2.1.3 The Shipbuilding Industry

"Shipbuilding" in the U.S. today is nearly synonymous with "naval shipbuilding." The inability of U.S. shipyards to compete in the world merchant shipbuilding market has led to the nearly total annihilation of that section of the industry. Even if U.S. yards continue to make productivity gains, it will be very difficult to recapture a significant market share from the Japanese and northern Europeans, and even more difficult to compete with Far Eastern countries such as Taiwan, South Korea, and mainland China. These countries are now entering the shipbuilding market with modern facilities, modern techniques, and extremely low wages, giving them a significant advantage over even the most efficient foreign firms.

Naval shipbuilding, on the other hand, will always be done in the U.S. for security and strategic reasons. In 1984 there were 17 privately

owned U.S. shipyards actively engaged in naval shipbuilding with a projected five year total value of $88.8 billion. These yards are listed in table 2.2. General Dynamic's Quincy facility has since closed down.

In addition to the $10.8 billion spent in fiscal year 1985 for new ship construction and conversion, $6.1 billion was budgeted for repair, overhaul, and modernization. The specific breakdown of these funds is shown in table 2.3. Cost analysis will be discussed further in section 2.1.5.

Table 2.2 Shipyards involved in naval shipbuilding in 1985. (6)

	Combatant			
	Nuclear ($34 billion)	Non-Nuclear ($30 billion)	Noncombatant ($24 billion)	Coastal ($0.8 billion)
GD - Electric Boat	*			
Newport News	*			
Bath Iron Works†		*		
Ingalls		*		
Todd†		*		
American			*	
Avondale†			*	
Beth-Sparrows Point			*	
GD-Quincy			*	
Lockheed†			*	
NASSCO†			*	
Penn Ship			*	
Tacoma			*	
Bell Halter				*
Derektor				*
Marinette				*
Peterson				*

† Currently employing Japanese consultants

Table 2.3 Shipbuilding cost analysis (18). GFE is Government Furnished Equipment, which is equipment the government buys and provides to the shipbuilder for installation. CFE is Contractor Furnished Equipment, which is equipment the shipbuilder buys and installs.

(A) New ship construction and conversion.

GFE:	5.4 billion
CFE:	2.7 billion
Labor:	2.7 billion
	10.8 billion

(B) Repair, overhaul, and modernization.

CFE:	1.8 billion
Labor:	4.0 billion
Non-SY:	0.3 billion
	6.1 billion

2.1.4 Naval Shipbuilding

Since naval ship construction and repair dominates the U.S. shipbuilding industry, it is worth commenting on the difference between naval and merchant vessels. Naval combatant ships have multiple missions, contain many complex systems, support large crews, and operate in the most adverse of environments. From a construction standpoint, this complexity manifests itself in a much larger amount of outfitting than is characteristic of merchant ships. Merchant ships tend to be mostly structure, since their primary function is to provide large open spaces in which cargo can be kept. Much of the naval ship outfitting is electrical, and electrical zone outfitting is limited by the current inability to

divide electrical cables into zones. Additionally, naval combatants stress performance above all else. Although producibility is now receiving increased attention, naval combatants will always contain performance features that make them more difficult to build. A higher percentage of curved structural panels, tighter quality assurance standards, and shock hardening requirements are just three examples. Further differences are discussed in reference (19).

2.1.5 Cost and Work Content Analysis

In assessing the impact that new shipbuilding methods could have on the total cost of a ship, it is important to have a clear understanding of where the total cost comes from. The shipyard construction of a naval ship represents less than half the total acquisition cost of that ship. The acquisition costs of a typical follow ship are listed in table 2.4.

Table 2.4 Naval ship acquisition costs. (7)

Item	Description	Percent
1	Plan costs	0.5
2	Basic construction	38.0
3	Change orders	2.0
4	Electronics	14.0
5	H, M, & E	2.0
6	Other costs	1.0
7	Ordnance	30.5
8	Escalation	7.0
9	P. M. growth	5.0

Although basic construction costs are the single largest line item, they represent much less than half the total acquisition cost of the ship. Ordnance and electronics are both GFE, and together they form the combat systems suite. Escalation accounts for the cost impact of inflation. It is primarily felt in basic construction, which typically spans several

years. Program manager growth accounts for the cost impact of modifications to the GFE package which occur during the contract period, while change orders do similarly for modifications to the basic construction package. Hull, mechanical, and electrical (H,M,&E) is non-combat systems GFE, such as the small boats, anchors, and certain navigational equipment. On a nuclear vessel it would also include the nuclear power plant and would be much larger. Other costs are used to fund NAVSEA expenses, such as design agents. Plan costs include the cost of producing the detailed design plans, developing test plans and procedures, and writing technical manuals. These costs are very significant for the lead ship of a class (about 9% of total), but are small for follow ships.

To put these costs in perspective, the GFE related items combine to make up 53.5% of the total cost. Thus, over half the cost of a ship is beyond the control of the industrial process of shipbuilding. The shipyard has direct control over only 38% of the total cost, and partial control over another 7% (escalation). In merchant shipbuilding, on the other hand, there are no GFE costs, so basic construction is by far the largest item. Even in non-combatant naval shipbuilding, the GFE costs are much lower, giving the shipyard more control over the total cost.

The next step is to divide basic construction costs into its three components: material, direct labor, and overhead. It should be mentioned here that accurate determination of costs is extremely difficult. Such data is proprietary and therefore not readily volunteered by shipbuilders. Furthermore, the shipbuilders themselves do not have the consistent accounting methods with which to provide accurate cost information:

> Standard definitions of words and phrases do not exist. One person's "cost" is another person's "price" and another person's "bid". There are many different types of labor. There is direct and indirect labor. There is also labor included in "materials". One shipyard's "cost" may include a different amount of overhead, profit, or burden compared with another shipyard. (18)

Costs also vary among ship types, but for an average surface combatant, reference (20) estimates that material accounts for approximately 50% of the basic construction cost, with direct labor accounting for 20% and overhead and profit accounting for 30%. The thrust of flexible automation is generally considered to be reduction of direct labor costs, which represent only 20% of the basic construction cost of a naval combatant, or 7.6% of the total acquisition cost. Other estimtes have come up with similar results. Ray Ramsey of the Naval Sea Systems Command estimated the actual manufacturing costs of a ship to be less than 8% of the total acquisition cost (11). A 50% reduction in direct labor would therefore result in less than a 4% savings for the navy. Flexible automation, then, should not be viewed as the final solution to high ship acquisition costs. Clearly, other major issues must be addressed if the cost of naval ships is to be significantly reduced.

Nevertheless, a few percent of a billion dollar ship is significnat, and flexible automation can also impact material and overhead costs as well. Excessive rework due to poor quality industrial processes can significantly increase material costs, as can inefficient utilization of raw materials due to poorly thought out cutting plans. Overhead costs increase when poorly planned work flow causes in process inventory to pile up. As the experience in Japan, the Soviet Union, and other countries demonstrates, modern shipbuilding methods can affect a wide range of factors and significantly bring down the total ship cost. In relative

terms, this will be more significant for merchant ships and non-combatants, but in absolute terms, it will be just as significant for naval combatants.

Despite the potential for reducing material and overhead costs, the remainder of this section will be devoted to direct labor costs. Analysis of direct labor costs is subject to as many difficulties as the analysis of basic construction costs. "Open job orders attract charges like a magnet, including questionable ones. Closed job orders attract charges which may require months to adjudicate" (18). Although direct labor charges might not accurately reflect direct labor utilization, they do provide the best data available, and table 2.5 summarizes the division of direct labor charges by craft for a typical naval surface combatant.

Table 2.5 Direct labor charges by craft. (7)

Craft	%
Burners/welders	16
Electricians	14
Pipefitters	14
Shipfitters	11
Sheetmetal	11
Laborers	5
Painters	4
Marine machinists	3
Other	22
Total	100

While welding (along with burning) is shown to be the number one cost driver, this provides no information on the nature of the welding, since welding is done to support a wide variety of work -- hull structure, foundations, piping, sheetmetal, etc. Further insight is gained by examining the cost breakdown by navy SWBS (Ship Work Breakdown Structure) group, as listed in table 2.6. These figures are in substantial agreement

with reference (15), which claims that 19% of shipyard direct labor is for hull structure, while 51% is for outfitting. It also claims that welding accounts for 15% of all direct labor in merchant shipbuilding, with the breakdown as listed in table 2.7. These figures are probably accurate for

Table 2.6 Cost division by navy SWBS group. (7)

SWBS Group		%
100	Hull structure	17
200	Propulsion plant	5
300	Electric plant	13
400	Command and surveillance	4
500	Auxiliary systems	18
600	Outfit and furnishings	15
700	Armament	2
800	Integration/engineering	8
900	Ship assembly and support services	18
	Total	100

Table 2.7 Shipyard welding utilization. (7)

Item	%
structural	55-65
pipe	18-23
burning	15-18
sheetmetal	3- 7

naval auxiliary ships, but for naval combatants, pipe welding would have a

higher percentage relative to structure.

To summarize, it is clear that while outfitting dominates naval combatant ship construction, welding is still the single most expensive trade. Most welding manhours are used for structural work, although burning and pipefitting are also significant. To get some idea of the extent and nature of structural welding in ship construction, reference (1) estimates a 12,000 dwt tanker to have 20,000 meters of welded seams. Reference (15) estimates that 20-25% of shipbuilding welds are butt welds, and 75-80% are fillet welds.

With this rudimentary understanding of the shipbuilding process, it is now appropriate to consider how it might be automated. Section 2.2 will overview flexible automation in general, and section 2.3 will attempt to apply it to shipbuilding.

2.2 Flexible Automation

2.2.1 Introduction

There can be little doubt that automation is and will continue to be an important trend affecting the fundamental nature of almost all fabrication industries. A firm's decision to automate is generally economically motivated by the desire to increase productivity. Machines can frequently do the work of many humans, they can work faster, lift heavier loads, and they have a higher working duty cycle (operator factor). A human welder, burner, grinder, or blaster spends only 25-30% of his time in actual productive work, whereas a machine can perform these tasks continuously (21). Automation can also increase productivity by improving quality and consistency, thereby decreasing rework. Machines have greater repeatability than do humans, and this translates into a

quality advantage when there are large numbers of repetitive tasks to accomplish. Machines don't get bored, tired, or careless, and they never quit, thereby necessitating rehiring and retraining.

Health and safety factors can also provide the motivation for automation. Many jobs expose human workers to such hazards as smoke, dust, toxic fumes, noise, glare, heat, and radiation. Social concern might prompt the decision to automate in such cases even if the economics of the move are not favorable.

Although the U.S. generally has an ample supply of skilled workers, this is not always the case abroad. Skilled labor shortages have sometimes provided the incentive to automate in the United Kingdom (22), and perhaps in other countries as well.

Finally, automation sometimes makes a process technically feasible that simply isn't possible by any other means. This could be due to the remote or hazardous location of the task, or to the exceptionally complex or delicate nature of the task.

For all its advantages, though, a machine must be "told" exactly what what to do, and it therefore lacks one overwhelmingly important characteristic -- flexibility. A human's flexibility comes from a combination of his sensing capabilities, reasoning capabilities, and manual dexterity. These are characteristics that originate in the most complex parts of the human mind and body, and machines will be hard-pressed to ever come close to duplicating them. The state-of-the-art in robot assembly was described in 1985 as follows:

> First thing you do is rub petroleum jelly on your glasses. Second thing you do is tie one hand behind your back. Then you put mittens on. And then you pick up chopsticks. Now you have arrived at the current state of robot assembly. (4)

While this may be an exaggeration, it does properly indicate that robots do have severe constraints. To top it off, this machine with limited sensory perception and limited coordination is extremely expensive. It is therefore important to understand the limitations of automation and not to view it as an easy solution to all productivity problems. The next two sections will examine two key concepts in automation -- flexibility and levels of integration. In striving to explain what automation is, what constitutes flexible automation, and how the industrial process being automated affects the final success or failure of the venture, this thesis will approach automation from the productivity standpoint. Health and safety do provide additional justification for automated welding, but it is doubtful that any company would automate welding tasks if the economic analysis didn't independently support it.

2.2.2 Flexibility

Automation is a broad term, encompassing a broad range of production strategies. These strategies can be thought of as forming an automation hierarchy, with flexibility increasing as one moves up. At the bottom, then, is fixed automation, with no flexibility. This is essentially the same thing as hard tooling or mechanisation, although some authors distinguish mechanisation from fixed automation. Reference (23) defines mechanisation as the "partial or complete replacement of manual work by a piece of equipment or machine," whereas it claims that automation includes both full mechanisation of the fabrication task and mechanisation of the loading and unloading of the part. This distinction seems intuitively

reasonable, although one could certainly imagine a manually loaded robotic workstation and still properly refer to it as automation.

What, then, is meant by the term "flexible"? Reference (24) defines the "flexibility" of automation as the "ability to process a variety of parts." Reference (25) defines flexible automation as "any automated or semi-automated process which is able to adapt or be rearranged to some degree to accomodate changing job configurations, sizes, times, or other important conditions." Clearly, variety and change are the keys to flexibility, and the extent of variety or the degree of accomodation determine the degree of flexibility. Numerical control is a simple example of flexibility. It permits the processing of different parts by utilizing different sets of pre-programmed instructions. Since it is entirely predetermined, though, it is a rather unsophisticated and limited form of flexibility.

It is important here to distinguish adaptability from flexibility. "Flexibility is the capability of a machine system to perform a variety of tasks; adaptability is the ability to cope with unpredictable conditions" (21). In the present discussion, though, adaptability will simply be considered a higher form of flexibility, so the term "flexibility" will include adaptability at the top of its hierarchy. Within adaptability there are several echelons of sophistication, ranging from feed-forward control, in which the process is open-loop adapted to workpiece variations based on sensor preview, to full feedback control, in which the process is closed-loop adapted based on comparisons between actual and desired outputs. Flexibility and adaptability will be discussed in more detail as they apply to welding in section 2.4.

As the flexibility of a machine increases, it is able to process a wider variety of parts, but this must be balanced against the increased cost that inevitably accompanies the increased sophistication. The optimum degree of flexibility is therefore inextricably linked to the product mix and quantity. Additionally, in order to effectively optimize the degree of automation, it is necessary to go beyond the specific machine and its tasks and study the entire fabrication process, as will be discussed in more detail in section 2.2.3.

Given this conceptual framework for flexible automation, where do robots fit in? Robots are nothing more than tools for implementing flexible automation. The official definition of industrial robots in the Federal Republic of Germany is as follows:

> An industrial robot is an automaton carrying out movements and of universal use, working in several axes and where the movements can be freely programmed and, if necessary, controlled by sensors. It may be equipped with holding devices, tools, or other means of fabrication and can carry out handling or construction work. (23)

The essential parts of a robot are the end-effector, which is the "hand" or tool that actually does the work, a power driven arm that positions and orients the end-effector, and a control system (including sensors) that plans and carries out the robot's actions. There are many ways of classifying robots, including the following:

* type of end-effector
* number of degrees of freedom of movement
* range of movement
* path control (point-to-point or continuous)

* type of coordinate axes (rectangular, cylindrical, spherical, anthropormorphic, or some combination of these) (26)

* drive (electric, hydraulic, or pneumatic)

* control system sophistication

* sensor capabilities

All of these (and others) are important when specifying a robot for a particular application, but it is the control system sophistication and sensor capabilities which primarily determine the degree of flexibility.

2.2.3 Levels of Integration

Besides the specifications of the robot itself, it is critical to carefully consider the environment in which the robot will be operating. The fabrication environment will be a function of the level at which the flexible automation is implemented. There are (somewhat arbitrarily) four possible levels, generally referred to as "levels of integration" (27):

Level 1 -- standalone
Level 2 -- cells
Level 3 -- linked islands
Level 4 -- full integration

Level 1, standalone, describes a robot or other single piece of machinery in isolation. There is no change in overall production strategy, and the robot simply replaces a worker, group of workers, or older piece of equipment, with a resultant increase in productivity. The cost and the risk are confined to that one area. It is difficult to economically justify a standalone robot, and they have frequently been installed to satisfy a company's urge to have the latest technology.

Unless the entire production process has been analyzed and modified to provide a suitable environment for the robotic workstation, the robot will not be able to reach its full potential, and a favorable return on investment will never be realized. The robot must depend on the upstream and downstream workstations and on material handling and transport in order to do its job to the fullest extent. If these surrounding processes can't keep up and are thereby incapable of supporting the robot, then the addition of the robot will just create bottlenecks. It will sit idle most of the time, and overall productivity will not improve. An example of effective use of standalone automation would be to automate a process that had previously been the source of bottlenecks or had caused persistent quality problems. Even here, though, the cost of the robot should be compared to the cost of hiring additional workers to relieve the bottleneck or of additional training to relieve the quality problems.

Level 2, cells, consists of several pieces of equipment clustered together to perform an organized function. A typical robotic workcell, or "island of automation," includes one or more robot manipulators, a workcell controller, part positioners, fixturing, and interchangeable end-effectors (28). A cell produces parts that have similar manufacturing attributes, thereby allowing their fabrication with a minimum of set-up time. The cell is physically arranged to minimize transport and handling. A process flow lane is a linearly arranged cell or group of cells. The design of a workcell is a tradeoff between flexibility and efficiency, and the optimum balance between the two depends on the quantity, similarity, and complexity of parts being manufactured by the shop. A highly flexible cell has a somewhat lower efficiency per part, but that flexibility is essential if the shop manufactures relatively few identical or similar parts. Generally the parts a shop makes can be divided into a number of

groups, and a cell designed for each of the larger groups. The tradeoff between the number of groups and individual group size is critical to overall productivity. If not enough divisions are made, each group is too diverse, and the cells must contain excessive flexibility and therefore inefficiency. Conversely, if too many divisions are made, each group is too small, and equipment cannot be kept busy. Thus, a typical shop productivity curve as a function of the number of workcells might look like that shown in figure 2.4. The exact shape of the curve will vary

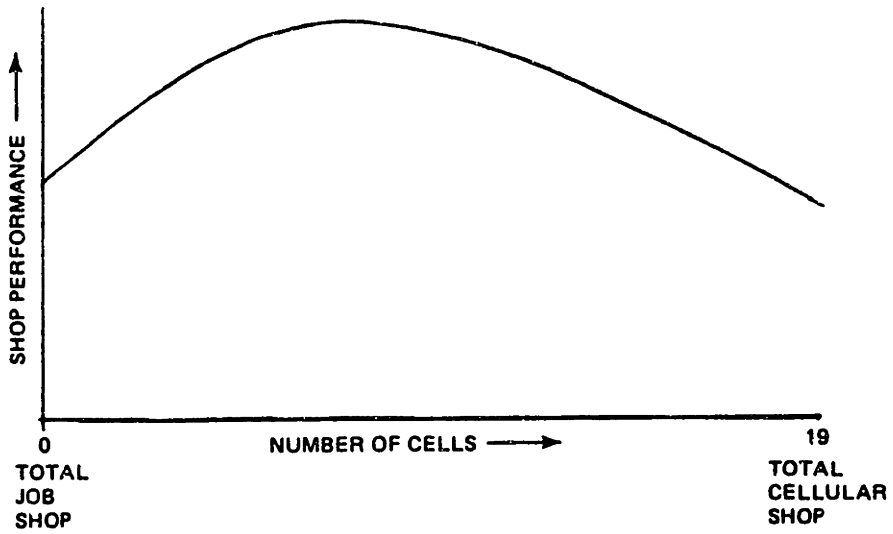

Figure 2.4 Productivity vs. number of workcells. (29)

with product group breakdown, output volume, and cell design. For shops producing a low volume of dissimilar products, the group sizes might be too small to justify any robotic workcells. Even for large volume shops, certain groups will remain outside the product range covered by workcells. Group Technology, as described in references (30-36), can be used to aid in identifying similar manufacturing attributes and in forming product groups. The robotic workcell is the most common type of installation in

industry today.

Level 3, linked islands, is a more coordinated version of level 2. The cells are linked together with other parts of the design and manufacturing process through complex informational networks. CAD/CAM and automated storage and retrieval systems are properly classified as level 3.

Level 4, full integration, is even more extensive in that the level 3 systems are linked together with all the other company functions -- storage, transport, cost accounting, top management, design, marketing, etc. Computer Integrated Manufacturing (CIM) is a term frequently used to describe this level of integration, and this is the level of implementation in the popularized "factory of the future".

While robots were first introduced to industry in level 1, the trend is strongly toward higher levels of integration.

> More and more we are seeing robots designed as integral components in automated manufacturing cells; we are seeing those cells grow from isolated "islands of automation" to more extensive automated production lines and, ultimately, "factories of the future". (37)

To conclude, then, it is critical to view a robot or any other piece of automation equipment as just one part of a comprehensive strategy. To properly define that strategy requires a thorough understanding of the entire fabrication process. As will be discussed in the next section, that level of understanding is just beginning to be achieved in the shipbuilding industry.

2.3 Automation in Shipbuilding

2.3.1 The Challenge

The shipbuilding industry presents some rather formidable barriers to automation. The nature of the process, the nature of the product, and the present nature of the industry all mitigate against successful automation. Specifically, four factors will be discussed:

(1) Complexity of the process

(2) Product design

(3) Product quantity

(4) Unstable economic outlook

(1) Complexity of the process

Section 2.2.3 closed by pointing out that it is critical to thoroughly understand the process being automated, and the immense complexity of the shipbuilding process makes this difficult. Unlike a small appliance that has a handful of parts and takes just a few minutes to assemble, a ship has tens or even hundreds of thousands of parts and can take several years to construct. Even the word we chose to describe the process -- "construction" -- implies a job that is orders of magnitude more complex than the common jobs we describe with "manufacture" or "assembly". And the overall process contains many individual tasks, such as welding, machining, brazing, inspecting, and painting, that are each technically complex in and of themselves, let alone in combination. Consequently, the thought of analyzing the entire shipbuilding process in the hopes of managing and automating it is a rather ominous concept. Traditionally, shipbuilders have divided the process up by system in order to manage it, as discussed in section 2.1.2, but this type of division makes automation virtually impossible. Now that the divisions are being

made by geographic zone, the process is finally starting to be understood in a manner that is amenable to automation. There is still a long way to go, though, and there is also much that is still not understood regarding the individual tasks. Reference (25) concluded:

> In U.S. shipyards, most activities are based on experience. Scheduling, outfit planning, bend and distortion allowances, to cite a few examples, are established manually. Although the experience base is strong, the scientific knowledge behind it is weak or missing, and this gap is not recognized.

To be technically feasible, automation requires accurate process models of the tasks being accomplished. But for many of the shipbuilding processes, such models do not exist. Welding is a prime example of this. Not only do we lack accurate, robust models to predict the weld bead geometry, but we also have considerable difficulty in predicting and controlling the final shape of the welded pieces due to distortion. This creates a tolerance nightmare. Automation flourishes in an environment of tight tolerances. Shipbuilding is characterized by large and unpredictable tolerances. Not only do welding and other processes distort pieces in unique ways, but even the weather can have a significant impact due to thermal expansion from the sun. Accuracy control, as previously described, is an attempt to better understand and control shipbuilding tolerances, and it has proven itself to be very effective. Nevertheless, because of the physical size of the components and the nature of welding, shipbuilding will always be characterized by tolerances that are fairly large relative to other industries. This and the other complexities of the process will inherently make automation more difficult.

(2) Product design

Physical size was already mentioned as contributing to the complexity

of the process. Additionally, physical size makes material handling and transport more difficult and places excessive requirements on the automation equipment's range of motion. Ship blocks cannot be easily moved from workstation to workstation as a car body can. Once a large component is in a workstation, it cannot be easily oriented, and the equipment end-effector may be required to move over large distances and into remote areas to complete its work. This places shipbuilding beyond the capability of most automation equipment. Furthermore, the extensive distributed systems in ships -- primarily piping, ventilation, and electrical -- are not amenable to automation.

Zone construction and outfitting are helping to facilitate automation, but more extensive product design changes must occur to support this. As ships are built increasingly in a modular fashion, the modules and subassemblies must be designed for ease of construction. Detail designers must place more emphasis on standardization relative to optimization. The navy's new emphasis on producibility should help this, although naval ships will always be designed with some degree of optimization.

(3) Product quantity

Shipbuilding epitomizes a process that is unfavorable for automation. Automation prefers a large number of small, simple, similar products. Ships are large, complex, unique, and produced in very small quantity. One of the factors that contributed to the success of the WWII shipbuilding program was the shear number of orders for identical ships. Reference (7) estimated that quantity production improved efficiency by 100% and made it possible to use extensive mechanisation. Shipbuilding in 1987 is not so fortunate. Small batch size is the order of the day. At best a shipyard can hope to build on the order of 30 ships of a class, but

there will likely be design variations even within that small number. The key, then, is to identify similar jobs within each ship. There are probably hundreds of subassemblies on each ship that are or could be similar enough to be made by the same automated process, given a reasonable degree of flexibility.

> The challenge to flexible automation is to make jobs similar enough so that they can be accomplished economically by a piece of flexible automation... If too few jobs are similar enough, the machine cannot be kept busy. If the jobs are not similar enough, the machine, in order to accomodate them, will be so complex and expensive that it will be slow, uneconomical, and unreliable. (25)

As shipyards gain experience with modular design and construction and continue to focus attention on producibility and subassembly similarity, significant progress will undoubtedly be made. Much of it will come directly from the corporate knowledge and experience of the designers and production engineers. Additional progress can come from the use of Group Technology (GT) to identify similar design and manufacturing attributes. There is a natural tendency in shipbuilding, as in any other industry, to continually design new parts and assemblies for use in new products. Existing parts, perhaps with minor modifications, might do the job, but the designer isn't always aware of all the existing parts and might not have an incentive to use them. "Design engineers are creative and talented people. Being creative does not lend itself to the adoption and use of mundane standards" (32). However, the use of GT to identify existing parts or subassemblies that meet a design need has been shown to reduce new part designs by an average of 5-10%, and in some cases as much as 40% (63). This reduction in the number of different parts translates into an increase in batch size and an advantage for automation.

(4) Stability of economic outlook

Flexible automation equipment is expensive, and a firm's decision to automate will create a shift from labor to capital cost. This investment in capital will require a payback period, and the firm's economic outlook must be predictable through the payback period in order to justify the investment. Shipbuilding, unfortunately, is subject to rather large and sometimes unpredictable fluctuations. Merchant shipbuilding is almost nonexistent in the US, and naval shipbuilding is subject to the whims of politics and the federal budget process. To further worsen the situation, it is doubtful that naval shipbuilding alone can sustain the current number of U.S. shipyards, so an industry shakeout is likely. Companies therefore face a difficult dilemma. A yard that doesn't automate is sure to lose the competitive battle and be forced out of the industry, while a yard that does automate is taking a tremendous risk. Even if it substantially improves productivity, there just might not be the orders for new ships in a few years to keep it in business. Ship repair represents a much more stable workload than ship construction, so automation of ship repair tasks presents an inviting opportunity. However, repair jobs tend to be much more unique and difficult to automate than construction tasks, so it is questionable how much of the four billion dollars spent annually for direct and indirect labor in public and private shipyards for repair, overhaul, and modernization could be switched over to automation.

To summarize, shipbuilding is exceptionally difficult to automate. Reference (25) concluded: "There is little work that is truly repetitive, there is not enough process knowledge and economic data, and most items have not been designed for automation and are technically infeasible as

designed." Current trends in the industry will help considerably, but the fundamental nature of ships and shipbuilding will always keep it more difficult than the vast majority of other industries. Opportunities do exist, though, and the next section will overview some of them.

2.3.2 The Opportunities

Automation in shipbuilding has been the subject of considerable academic, economic, and political interest during the past few years. Several studies have been conducted on the topic, and they have identified a number of promising areas of application, as well as a number of obstacles. The SRI study entitled "Advanced Automation for Shipbuilding" (21), although seven years old, was the most specific in its recommendations and identified the following processes as being the best candidates for automation: cutting, welding, blasting, and grinding. This section will take a brief look at possible methods of automating each of these processes, followed by an analysis of where and when these might be applied during ship construction and repair. Finally, the major remaining technical obstacles will be discussed.

Cutting is an attractive prospect because a mechanized system can use a plasma-arc cutting (PAC) head, whereas manual cutting is constrained to oxyfuel flame torches. The tenfold increase in cutting speed available with PAC coupled with the threefold increase in operator factor (duty cycle) gives a system output equivalent to that of thirty men. Virtually all construction shipyards now employ mechanized plasma-arc cutting to a large degree, although the actual use of robots is still fairly low. Most of the systems are numerically controlled, and some of them interface with the shipyard's CAD/CAM system. A conceptual single station fixed base cutting robot is shown in figure 2.5. SRI estimates a 232% return on a

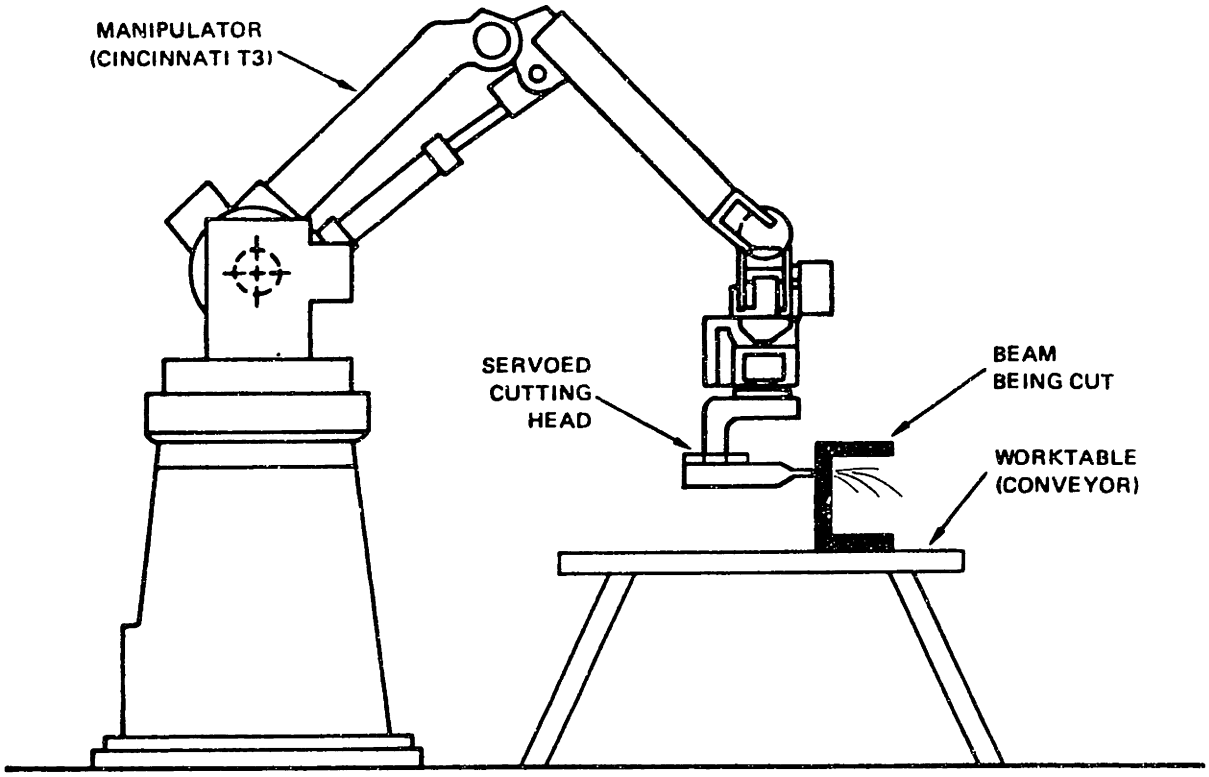

Figure 2.5 Conceptual single station fixed base cutting robot. (21)

$111,000 investment from this system, although this is optimistic since it both ignores robot software and factory reorganization costs and assumes an ideal flow of workpieces to the robot (the robot never sits idle).

Arc welding is the second prospective candidate, and it was identified by the SRI study as being the most essential process to automate. The study describes a gantry-mounted two-armed electrically driven robot. A tack-welded workpiece is brought under the gantry, and the robot begins welding at a predetermined position. Its path and welding parameters are direct numerical control (DNC), but a vision system provides the ability to adapt to actual groove locations that differ from the pre-programmed path. This system has an initial cost of $195,000 and

a ROI of 40%. A somewhat similar system with only one arm and no vision system would cost $122,500 and return 34% on the investment. This system though, requires on-line programming, as the operator must position the weld head at the beginning and end points of straight welds in order to teach the robot its path, which is then limited to straight line segments. Although the ROI of both welding robot concepts was much lower than the cutting ROI, shipyards spend six times more manhours on welding than on cutting. Hence, welding offers the greatest potential for absolute savings.

The automated blasting concept consists of a heavy-duty blasting head mounted on a robot arm in an enclosed cell. Parts are brought in on a conveyor, and the use of a robot allows utilization of a larger blast head and heavier blast material, both of which increase productivity. The system would be equivalent to 20 - 30 manual sandblasters and would offer a return of 78% on an investment of $223,000.

The advantage in grinding similarly comes from the ability of a robot to handle a more powerful tool than a man, and to do so continuously and with more force. The resulting higher removal rate and higher operator cycle would give a substantial productivity increase and a return of 214% on a $115,000 investment. The system would require an operator to program the robot by teaching it the location of the edges and surfaces to be ground. ASEA currently makes a grinding robot.

Given these basic processes that can be automated, either through the conceptual designs described above or through any number of other designs, the next issue to consider is the specific shipbuilding tasks in which these could be applied. Four items will be discussed: ship

repair, propeller manufacture, small batch fabrication and panel process flow lanes.

Previously it was mentioned that ship repair provides extensive opportunities for automation, both because the labor content is high and the workload is stable. On the other hand, the work environment is much less structured than ship construction, making automation more difficult. Nevertheless, reference (39) describes several potential applications in ship maintenance and repair. Underwater hull and propeller cleaning and the cleaning and preservation of tanks, voids and bilges are all amenable to at least partial automation with existing technology. These and other applications are being studied by NAVSEA 070A for possible implementation in naval shipyards.

Propeller manufacture is a tedious operation involving welding, machining, grinding and measuring. Figure 2.6 shows the automated workstation for the measuring process. The resulting surface description of the blades is used to generate control programs for cladding, machining and grinding the surface as necessary to achieve the desired contour. Philadelphia Naval Shipyard will be the first facility to receive this installation.

Section 2.3.1 mentioned the possibility of identifying subassemblies with similar manufacturing attributes, and references (8, 21, 25, 39) all identify small scale subassembly fabrication as a promising area for robotic application. The fabrication of subassemblies from plate and profile stock is a significant part of ship construction. Welding, blasting, painting, certain assembly tasks and possibly inspection are all candidates for robots. Small foundations and pipe spools are two examples

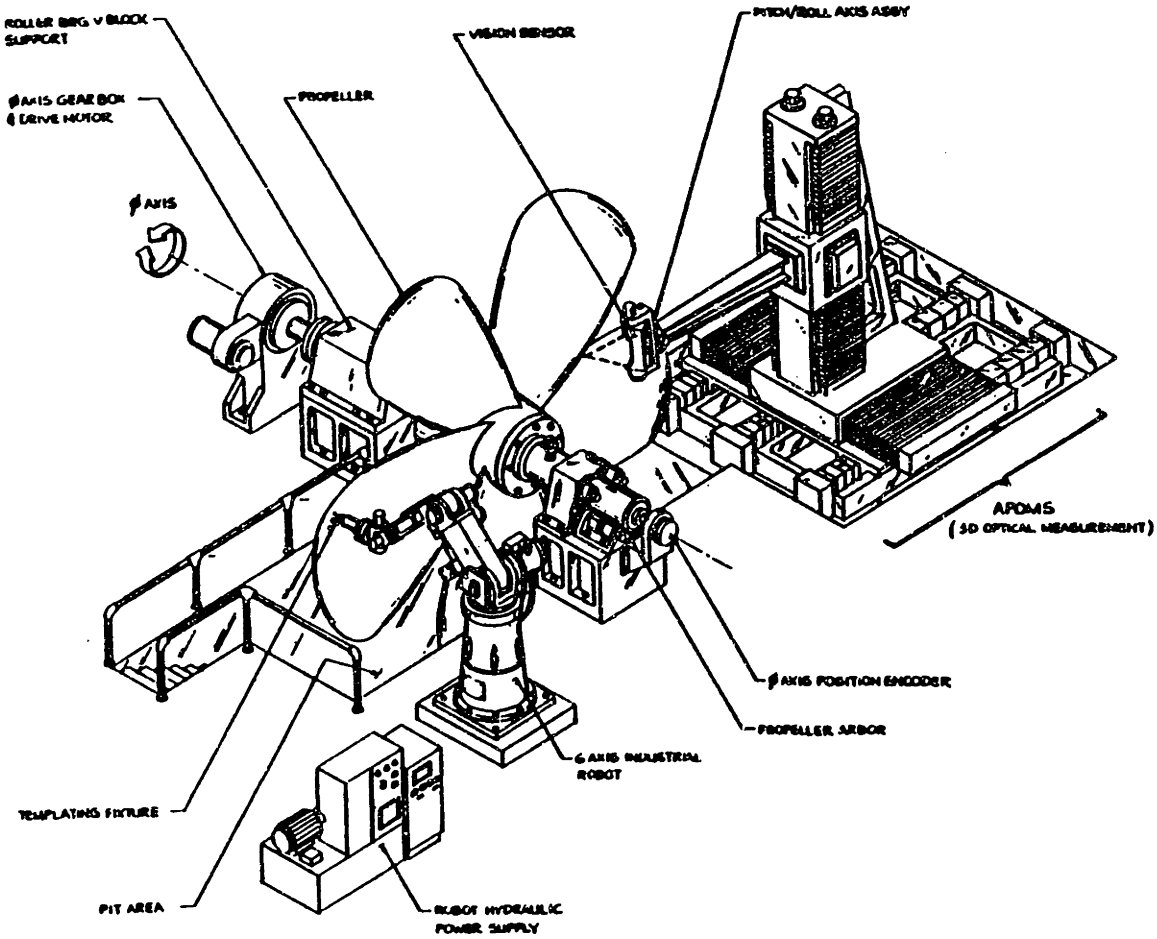

Figure 2.6 Conceptual automated propeller manufacturing station. (39)

of pieces that could be made by such systems. Avondale Shipyards already uses automated welding for both flange and branch welds in its automated pipe facility (25). Todd Pacific Shipyards has a prototype arc welding work station utilizing a Cincinnati-Malacron T3 industrial robot which it has used successfully in welding small parts (8). These types of applications should see expansion in the future.

On a larger scale, the production of flat panel assemblies (and perhaps curved panels in the future) appears to be promising. This process consists primarily of welding longitudinal and transverse

stiffeners to plate. The large distances involved require a robot with a large range of motion, which could be achieved by either a gantry mounted robot or a mobile robot. The conceptual design described earlier in this section is a suitable example of the former, and various designs have been proposed for crawling robots and mechanized welding tractors. A crawling GTAW machine was developed by NKK in Japan for use in welding corrugated LNG tanks. It is very successful and will be discussed further in section 2.4.2. Another example is the Doodle Bug made by M.K. Products, Inc. of Irvine, California. This mobile dual head stiffener welder, shown in figure 2.7, simultaneously produces fillet welds on both sides of a stiffener. Bath Iron Works uses it extensively in welding stiffeners to flat plate. Both the NKK machine and the Doodle Bug use tactile sensing.

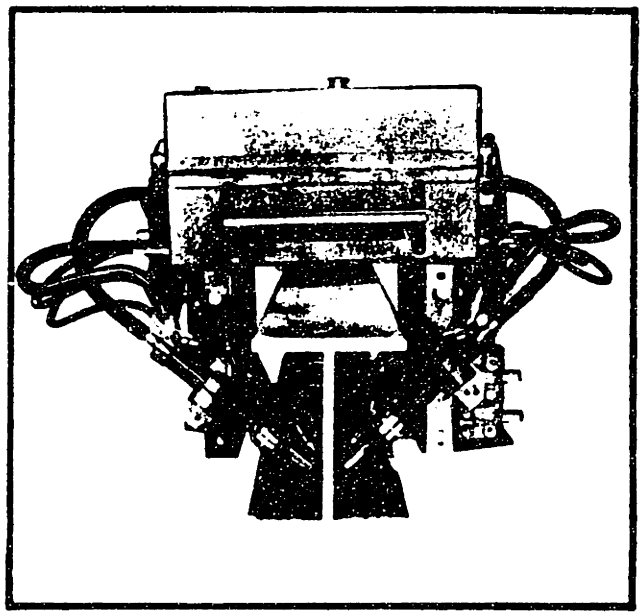

Figure 2.7 Doodle Bug mobile welding machine. (40)

These, then, are just a few examples of rather simplistic automation already in existence, and of shipbuilding processes and tasks in which more sophisticated automation could be exploited.

While it was clear that flexible automation can play a significant role in ship construction, it is also clear that there are a number of obstacles standing in the way. Some of these, as already discussed, derive from the basic nature of shipbuilding and place inherent limitations on the extent to which shipbuilding will ever be automated. We are highly unlikely to see ships produced in the same manner as cars. Other obstacles derive from the poorly organized manner in which we have built ships for so many years. The current revolution in shipbuilding methods should alleviate these and open the way for substantial implementation of automation technology. Still other obstacles derive from the limitations on that technology itself.

The remainder of this thesis will deal with welding. Welding has already been shown to be the single largest cost driver in ship construction, and it is used extensively in shipbuilding tasks, such as panel construction, which are amenable to automation. The successful implementation of welding automation would therefore provide substantial economic benefits, as well as health and safety improvements. What, then, are the technical obstacles preventing such implementation? The major technical obstacle is adaptability, or lack thereof.

> The greatest impediment to cost-effective use by the Navy is the inability of commercially available robotic welding systems to adapt to variations or changes in joint geometry brought on by thermal expansion, poor initial fit up or other variables associated with the welding process. (39)

Section 2.4 will take a detailed look at automated welding including adaptability.

2.4 Automated Welding

2.4.1 Introduction

When a human performs a process, he or she uses experience and intuition to relate the process inputs, which he controls, to the process outputs, which he desires. Automation turns this control function over to a machine, which understands only mathematical descriptions and algorithms. Automation therefore requires an accurate process model which mathematically relates the outputs to the inputs. Any attempt to automate welding must begin with the development of such a process model.

The open loop welding process is shown in a black box representation in figure 2.8.

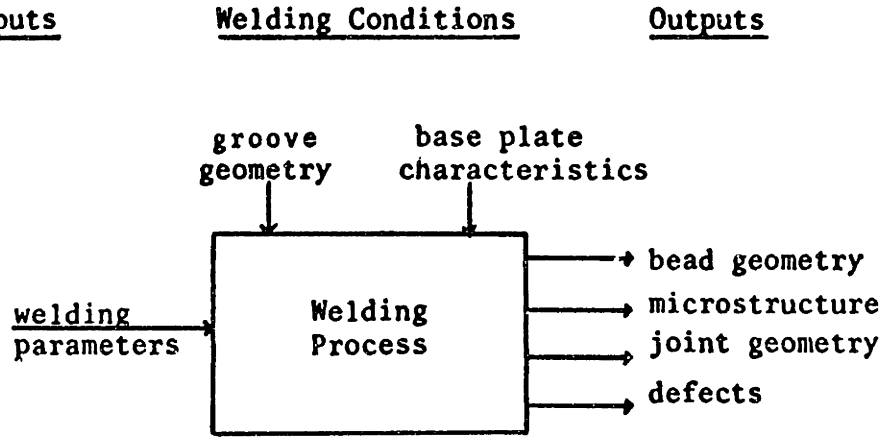

Figure 2.8 The open loop welding process.

While our objective is to control the inputs in order to achieve the desired outputs, we as yet are unable to quantitatively describe the relationship between the inputs and outputs. The major outputs of interest are the weld bead geometry (penetration, width, reinforcement area, dilution factor, toe angle, etc. as shown in figure 2.9) and the

microstructure of the weld and the heat affected zone. Additionally, we want to prevent defects and minimize distortion and residual stresses.

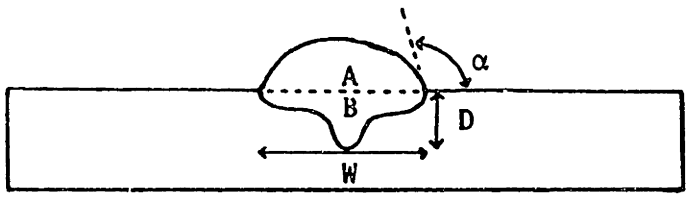

A = Reinforcement area
B = Fusion area
B/(A+B) = Dilution factor
W = Width
D = Penetration
α = Toe angle

Figure 2.9 Weld bead geometry for a bead-on-plate weld.

Two of the factors that affect the outputs, groove geometry and base plate characteristics (composition and surface condition), are not included as inputs since they are not within the control of the person or machine performing the welding. They are listed collectively in the diagram as welding conditions. The items that are controllable are known collectively as the welding parameters, and these can be categorized as pre-set or variable. The pre-set parameters are controllable only during the welding set-up period. These include wire diameter and composition, shielding gas composition, and power supply characteristics (including polarity, slope and open circuit voltage). Once the set-up is complete and the welding begins, these parameters are not normally controllable. The variable welding parameters are available for continuous control during welding. These include current, voltage, wire feed speed, torch position (height, lateral position, work angle and travel angle) and travel speed. Of the first four of these, only three are independent.

For example, if voltage, WFS and torch height are specified, then current is determined by the process and the power supply characteristics, and it cannot be independently controlled. One of the major research efforts in welding today is aimed at acquiring a quantitative description relating the variable inputs to the outputs.

The traditional control strategy for a system with poorly defined open loop characteristics is to use feedback. However, feedback in welding is very difficult, since some of the most important outputs (penetration, fusion area, microstructure and certain defects) can be determined only after the weld is completed and then destructively examined. Other outputs, such as distortion, residual stresses and certain defects, develop over a finite time period after completion of welding. Development of sensing systems to measure these output variables in real time is another area of current research, but the practical use of such sensing systems appears still to be a long way off.

The rest of section 2.4 will overview automated welding, building on the generic description of flexible automation given in section 2.2. The intent is to describe the various conceivable levels of automation and the sensing and control capabilities required for each level. Examples of current industrial applications are given where possible.

2.4.2 Levels of Automation

Fundamentally, a robot attempts to simulate the actions of a human being (although this is frequently not the most efficient method of operation). It is therefore instructive to begin with an analysis of the actions of a welder. A welder performs three functions: physical functions, programming functions, and control functions (41). Physical

functions are those actions which require muscular exertion, such as moving the torch. Programming functions are associated with establishing the proper values of the welding variables, such as voltage, wire feed speed, etc. Control functions are the means by which the welder supervises the results of his programming and physical actions and makes changes as necessary to accommodate abnormal conditions. Programming and control are jointly referred to as intelligent functions.

Automation can be described by these same three functions. There are several distinct levels of automation, depending on which of the functions are carried out by the machine and to what degree. These levels are shown in figure 2.10.

Automation Level	Machine Function
Manual	None
Mechanization	Physical
Numerical Control	Programming
Seam Tracking	Control
Adaptive Process Control	Control

Figure 2.10 Levels of welding automation. "Manual" is included only as a baseline.

(1) Mechanization

Mechanization is the lowest level of automation and frequently is not even included in the term "automation". Mechanization occurs when the physical functions are done by the machine, with man still doing the intelligent functions. It can also be referred to as hard tooling, and it is extremely cost effective for a repetitive workload. Mechanization,

however, is inflexible, making it economical only for high volume production, and it is unable to compensate for part to part variations which might arise from normal engineering tolerances. "Mechanized welding is generally performed with fixed welding parameters, which may cause uneven quality owing to variations in groove position and geometry" (42). This problem is particularly severe in the shipbuilding industry, where the small lot size generally makes mechanization uneconomical, and the huge size of the subassemblies makes tolerances so large that mechanization is unable to cope with the part to part variations. An exception to this was in WWII, when the massive quantities of identical ships being built made mechanized welding very efficient (7).

(2) Numerical Control

Some degree of flexibility is achieved by adding programming functions to the machine. This is typically done through numerical control (NC). The machine can be programmed to weld a variety of different patterns with a variety of different welding parameters. The machine still doesn't think for itself -- it blindly carries out the pre-programmed instructions of an overall supervisor -- but at least one machine is able to weld a variety of different parts. Since it doesn't actually set the parameters itself, as it would if it fully performed the programming functions in an expert system type of application, NC might be classified more properly as flexible mechanization. The development of computers provided the technology to enable NC to become a reality. Rather than being controlled by a mechanical track of some sort, the welding apparatus is controlled by a microcomputer, carrying out steps stored in memory.

It was through NC that robots achieved their first widespread use in

welding. The auto industry was perhaps the first to take advantage of NC welding, and it did so with resistance spot welds, which are much easier to program than continuous arc welds. By 1981, the average Chrysler built car, for example, contained 700 to 800 robot-made welds. John Deere Harvester Works utilizes a Unimation robot to gas metal arc weld a complex 3-1/2 foot weldment on the cutting head of a soybean combine. The system, which costs $250,000, makes 20,000 weldments annually, and the cutting head frames it produces average 20% stronger than manually welded frames (43). The Unimation system demonstrates a slight variation on normal NC programming. The program is developed not by a programmer at a computer terminal typing in commands, but rather by manually leading the robot along the weld groove in a "teach" mode. Each step is recorded in the computer memory, along with weld parameter instructions, so that future identical pieces can be welded just by recalling the memory.

The Axle Division of Hayes-Dana began using NC robots in mid 1979 to fabricate six different families of axle housings. The company has 18 Advanced Robotics Corporation Cyro robots arranged in seven work stations in an assembly line fashion. Programming is similar to John Deere's Unimate system. The path is taught by manually walking the robot through a teach mode, while welding parameters are programmed using standard NC commands. The company's total investment in robots, computer hardware and software, mechanical handling equipment, and start-up costs was $2 million. Annual production is around 100,000 units, with individual production runs between 500 and 1500 units (44).

A robot which is popular in sheet metal fabrication is the IRb-6 robot made by ASEA. The Mayville Metal Products Company of Lomira, Wisconson, uses the IRb-6 to weld cabinets and frames for electronic

equipment (45). The robot itself has 5 degrees of freedom with an accuracy of .2mm. It is taught using a hand held programmer which moves the robot from point to point with manual control. "Traverse" points (for path following) can be located several feet apart, but "weld" points (for parameter programming) are spaced at one inch intervals for optimum accuracy (46). The system can store 5 different programs in its memory.

The mobile Radio Department of General Electric also uses the IRb-6 robot in its Lynchburg, Virginia, plant to weld radio cabinets and other sheetmetal components. It takes the robot 40 seconds to weld the cabinet doors, compared to 4 minutes by hand. Westinghouse has similarly had good results using the IRb-6 to arc weld circuit breaker components in its Beaver, Pennsylvania, plant. The robot work cell, shown in figure 2.11, cost $125,000 but is saving the company over $30,000 per year (47). As with many robot applications, the system includes a positioning table that moves in conjunction with the robot to maintain the part in the optimum welding orientation.

Another division of Westinghouse, the Nuclear Components Division in Pensacola, Florida, is using an NC robot designed by the Westinghouse Industry Automation Division to weld spent nuclear fuel storage cells. The system cut welding time on each cell down from 60 minutes to 20 minutes (48).

Although pre-programmed NC welding has enjoyed widespread successful application, it has one major drawback that severely limits its ultimate potential, that being that the robot only has the capability to blindly repeat the previously taught program and is unable to adapt to changing

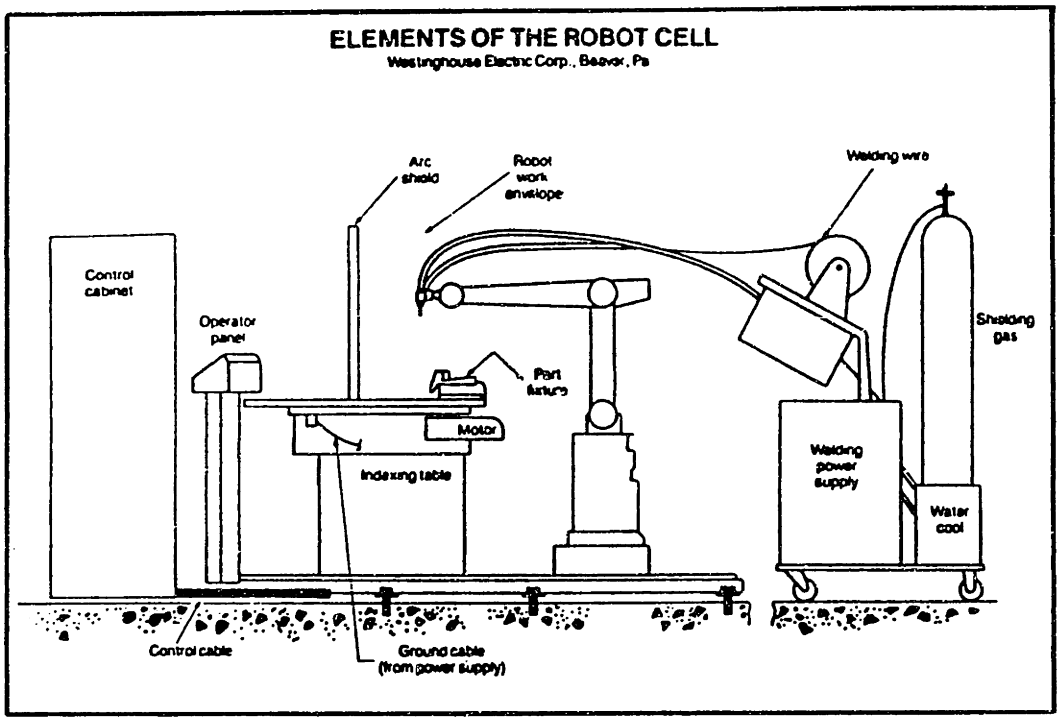

Figure 2.11 IRb-6 work cell at Westinghouse. (47)

conditions. It treats all parts of a given design exactly the same, ignoring part to part variations and fitup variations due to normal engineering tolerances. This requires that the parts presented to the robot must have extremely tight tolerances of plus or minus half the electrode diameter (49). Unfortunately, this is generally not possible, as "the average welding environment is currently insufficiently structured to accept the present generation of robots. The long reliance upon manual labor has created a manufacturing environment where precision, organization, and uniformity of components are not yet ready for the world of automation" (50). While a manual welder can see and compensate for bad preparations, poor fitups, tack welds, spatter, and gross variations in joint volume, and NC robot cannot (51).

There are two sources of error that are of concern: joint location

variations and joint shape/volume variations. Relative misalignment between the robot and the joint location has four sources: robot repeatability, weld positioner repeatability, fixture repeatability and piece part repeatability. The first two contribute very little to misalignment (about .008" each), but the last two can be very significant (52). Joint shape and volume variations are also functions of piece part repeatability and fixturing, but are additionally influenced by the presence of sudden disturbances such as tack welds and spatter. The term "piece part repeatability" as used here includes everything from plate thickness and edge preparation to distortion caused by prior welding on the part.

Shipbuilding presents unique challenges to automated welding and vividly demonstrates the limitations of NC robots. The low volume production of complex and relatively unique units makes robotics application difficult to begin with and makes flexibility essential. Furthermore, the workpieces are massive in comparison to cars, axle housings, circuit breakers, electronics cabinets, or any of the other products that have experienced successful fabrication automation. This makes handling and orientation difficult and creates enormous dimensional uncertainties as tolerances stack up and distortion becomes significant. Additionally, large metal structures are highly subject to thermal expansion and contraction. In outdoor assembly, large structural components can grow several inches from the sun's heat (53). The resulting large variations in weld groove size, shape, and location are incompatible with NC robots.

Even the industries that have successfully applied NC robotic welding have found tolerances to be a problem. They all had to improve

their part tolerances to enable the robots to weld successfully. Of the $250,000 that John Deere spent on its system, $70,000 went for the robot itself while $80,000 went for improved fixturing. Other users report spending half again the cost of the basic robot on improved fixturing (47). Whatever the exact figure, it is very significant, and in some industries it is prohibitively expensive.

(3) Seam Tracking

The alternative to minimizing tolerances is to provide the robot with sensors and the capability to adjust to varying conditions. Sensors fall into one of two categories. The first are sensors that provide data on the groove location and are used to appropriately position the welding torch (seam-tracking). The second are sensors that provide data that is used to control the welding parameters (adaptive process control).

Seam-tracking sensors have been the subject of considerable research recently, and there has been significant success in their development. There are three basic types of seam-tracking systems: tactile, through-arc and vision. Tactile sensors are the simplest and were the first to be developed. A tactile sensor is just a mechanical probe that rides in the groove a short distance ahead of the torch. It can use a variety of methods to transmit location data to the torch, such as direct mechanical linkage, LVDT with electrical link, etc. Because tactile sensors are inexpensive and rugged, they are the most commonly used of the three seam-tracking technologies, with over 2000 units in field operation in the US (49). Most of these, however, are in "hard automation" systems rather than flexible automation systems. An excellent example of an operational tactile sensing system is the one developed by Japanese steelmaker and shipbuilder NKK for use in the

fabrication of LNG tanks. The interior of the tanks are currugated, giving a waffle appearance as shown in figure 2.12. NKK developed an automatic GTAW machine with a tactile sensor that can weld continuously

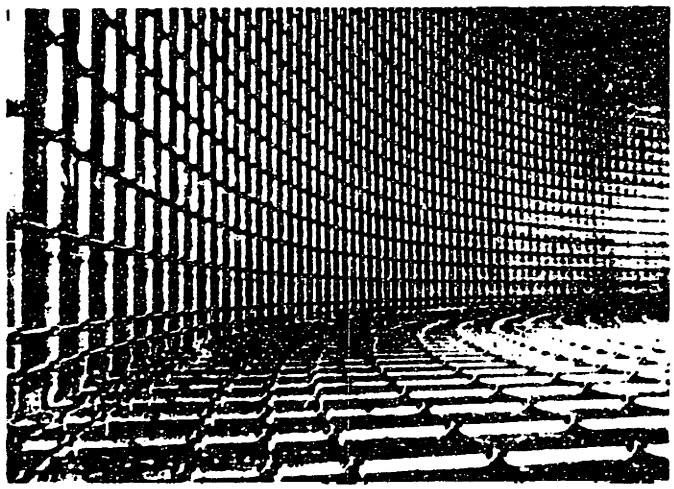

Figure 2.12 Interior of LNG tank built by NKK. (54)

over flat and corrugated sections. The sensor is shown in figure 2.13. It guides the unit along the parallel stiffeners and detects the perpendicular stiffeners, causing the machine to adjust the torch position and change a number of welding parameters (travel speed, peak current, average current, and pulse frequency). Over 90% of the 20,000 meters of weld in the tank were done with this automated method, the other 10% being done manually. All welds passed dye penetrant testing, and during ammonia leak testing, the only leak detected was in a manual weld (54).

The second type of sensor is the through-arc sensor. This sensor gathers data on the weld groove based on measured variations in the arc characteristics. The torch must weave from side to side within the weld

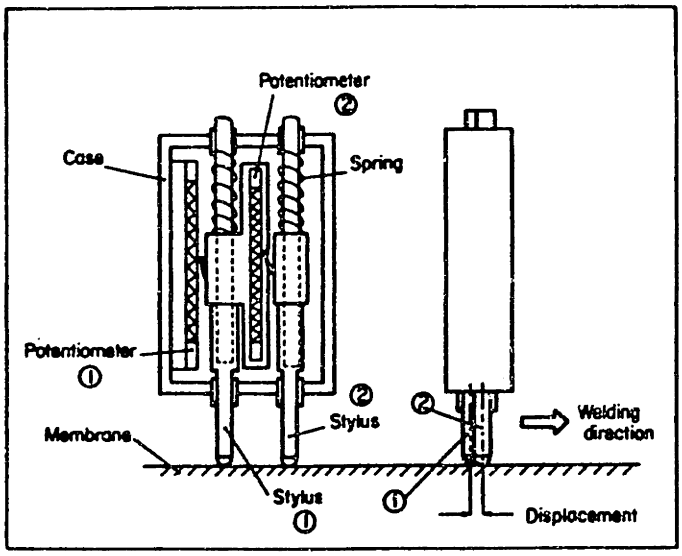

Figure 2.13 Tactile sensor on NKK welding machine. (54)

groove in order to gain information on the groove profile. It is, effectively, bouncing off the groove sidewalls. As the torch approaches the groove sidewall, the arc length shortens, thereby increasing the current. The controller uses this data to signal the torch to switch directions, until the opposite sidewall in encountered. Thus, through-arc sensors can identify not only the groove location (generally defined as halfway between the two sidewalls) but also groove width. Through-arc sensing has the advantage that no additional sensing hardware (such as a mechanical probe) is required, but it cannot be used on thin metals with negligible sidewalls, and linear welding speed is limited to about 40 ipm by the requirement to weave. Electric Boat uses through-arc sensing in the fabrication of submarine hulls at its Quonset Point facility. Nationwide, over 1000 through-arc sensing units are operational, many on robots.

Optical seam-tracking using a vision system is the newest and most promising technology. A typical vision system illuminates the weld groove

with a laser, then gathers the reflected light with an optical sensor. The resulting signals are then processed to provide information on the groove location and profile. The specific details of the illumination, optical sensor, and signal processing vary considerably among different systems, but a typical system sensor configuration is shown in figure 2.14. Vision systems are very versatile and can gather considerable information on the

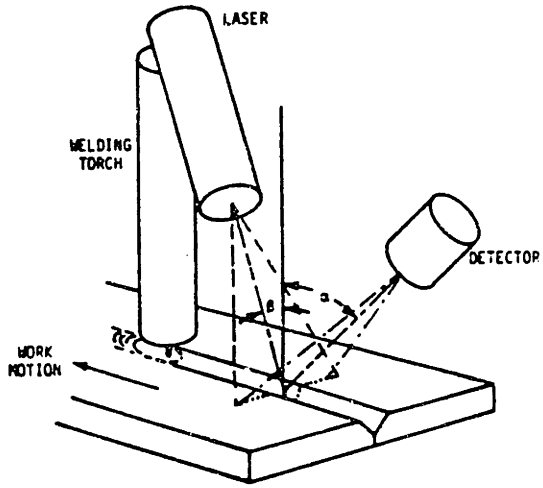

Figure 2.14 Typical optical sensor configuration. (55)

groove size and shape. Furthermore, there is no direct contact with the weldment, and the system operates independently of the arc. Travel speed is therefore unaffected, and existing optical trackers operate at up to 100 ipm. On the other hand, vision systems are complex and require delicate equipment to operate in close proximity to the fumes, sparks and spatter of the welding arc. The intense light of the arc is also a problem for vision systems and necessitates careful choice of illumination wavelength and considerable filtering. "It is estimated that there are currently fewer than 50 installed optics-based welding joint trackers" (49). One such system is GE's MIG Trak Welding Seam Tracker System, used by the Copeland Corporation of Sydney, Ohio, to manufacture compressors.

Table 2.8 lists a number of other existing vision systems, but ongoing research is expanding the list and their capabilities.

The implication of the preceeding discussion was that the seam-tracker

Table 2.8 Existing vision systems. (55)

System Name/Developer	Major Characteristics	Type of Sensor	Overall Operating Performance
Autovision II by Automatix [1]	vision system observes the weld seam ≈ 4 cm ahead of the arc	A fiber optic bundle carries the image to a solid state square matrix camera; a line or stripe pattern is projected by laser light through a fiber optic bundle to illuminate the work	high weld travel speeds of 100 cm/min are achieved on various seam configuration in a single pass (during welding)
Unika 80A by Kawasaki and Unimation; Univision II by Unimation [6]	a vision pass makes individual part comparisons to a standard pretaught path prior to welding pass	fiber optics have replaced lenses between a solid state square matrix camera and the work; an incandescent lamp and lens project a stripe pattern onto the work	high vision and weld pass travel speeds once the initial joint geometry is preprogrammed
Mitsubishi Electric Corporation Vision System [7]	a compact visual sensor unit provides joint preview data	a lens and 2-D position sensitive lateral effect diode observe a line pattern of dots projected onto the work; a lens, rotating mirror and infrared LED project the linear dot pattern coded at 10,000 Hz.	extensive joint information (width, depth, etc.) is produced while traveling at high speeds
General Electric Weldvision [8]	GTA weldpool and joint observed with system through the welding torch, image aligned with the electrode	fiber optic bundle in torch carries image to solid state TV camera; arc light and parallel laser stripe pattern projected onto joint provide illumination	1" diameter field of view around torch; puddle is viewed and weld geometry analyzed for use in adaptive control
Mitsui Engineering and Shipbuilding [10]	TV camera mounted in robot hand for single pass tracking in fillet welding during welding	50 × 50 element CCD camera detects projected circular image on fillet; illumination is by xenon lamps	transmittance filters minimize the effect of the arc, end of seam (fillet) can be detected; spatter and fume effect minimized
Komatsu, Ltd. [12]	in process, tandem GMA weld tracking and weld parameter feedback using digital TV camera	weld pool geometry and position of wire electrode (filler) determined by thresholding image and line scan analysis of TV image of weld pool and joint ahead of torch; illumination from arc light	torch/TV camera separation about 800 mm; system operates at welding speeds of up to 500 mm/min.
University of California, Berkeley	weld seam trajectory and joint geometry characterization based on scanning laser light pattern for torch control during GMA welding	lateral effect 2-D photo diode with lens and interference filter; oscillating mirror mechanism scans a He-Ne laser beam across the joint to illuminate joint features	location of centerline of U and V joints determined during GMA welding to ± .020 inch; joint geometry data (depth and width) available; preliminary evaluation

operated during the actual welding process. This is always the case for through-arc sensing, but not always for tactile or vision systems. These can also operate in a teach mode, similar to the manual teach mode, used for NC programming. The Unika-80A, designed in a joint venture between Unimation Inc. and Kawasaki Heavy Industries, uses a teach mode with a visual sensor. The initial teaching is done manually by the operator, and the taught path is stored in memory. The robot then executes a "repeat" mode in which the vision system compares the actual weld groove path to the taught path and stores the corrected taught path in memory. Finally, the robot repeats the corrected taught path and makes the actual weld. Separate robot and effectors can be used for the "repeat" pass and the welding pass (56, 57). Although this system allows the robot to adjust to part to part variations in the weld groove, it is unable to compensate for distortion during welding, and it is time consuming. Although the initial teaching need only be done once, the separate repeat and welding passes must be done for every workpiece.

While teach modes are very popular, they all suffer from the shortcomings that an additional pass must be made for each workpiece, the end effector must generally be changed to make the welding pass, and they are unable to adapt to distortion which occurs during the welding pass.

Oxford University performed an interesting study which economically compared improved fixturing to adding seam-tracking capability to the robot via a vision system. The study was done for robotic arc welding of the front suspension crossmember assembly of a motorcar manufactured by BL Ltd. To successfully gas metal arc weld the assembly by conventional robots without sensors would have necessitated reducing tolerances from

3mm to .5mm at a cost of 240,000 pounds initial capital outlays and 34,000 pounds recurrent annual operating costs. To add a vision system and appropriate controls to the robot that would give successful welds with the existing 3mm tolerance would have cost 22,300 pounds initial capital outlays and 5,000 pounds recurrent annual costs (58). For this particular application, therefore, it is much more economical to add sensing capability to the robot.

(4) Adaptive Process Control

Assuming that the robot is now able to follow the weld groove accurately, we can turn our attention to welding process control. Virtually all automated welding applications incorporate a process control strategy of some form or another. The process we are attempting to control was shown previously in figure 2.8, and the controllable inputs were discussed in section 2.4.1. The process disturbances are variations in the welding conditions: groove size and shape, base plate composition, the presence of tack welds, etc. The overall process output is the weld quality. While weld quality is determined by a number of factors, this thesis will restrict itself to bead geometry and the absence of defects. Microstructure is a function of cooling rate, and it can be controlled by maintaining heat input within specified boundaries, or by the addition of a second (trailing) torch as is being studied by Hardt (66). Final joint geometry and strength due to distortion and residual stresses is another important measure of quality, and it is particularly critical in shipbuilding. Control of distortion and residual stresses is the subject of research described in references (59, 60).

The simplest and most common control strategy is known as stabilization control, in which the welding variables are continuously

monitored and necessary action is taken to keep them constant in the face of changing welding conditions. The underlying assumption is that constant welding variables will result in constant weld quality, which, of course, is not true. A block diagram of stabilization control is shown in figure 2.15. Since the welding conditions enter the diagram after the feedback loop, they act as uncontrolled disturbances which are not compensated for. This is what drives the requirement for very tight tolerances in stabilization controlled systems. Tighter tolerances mean smaller disturbances and less variation in weld quality.

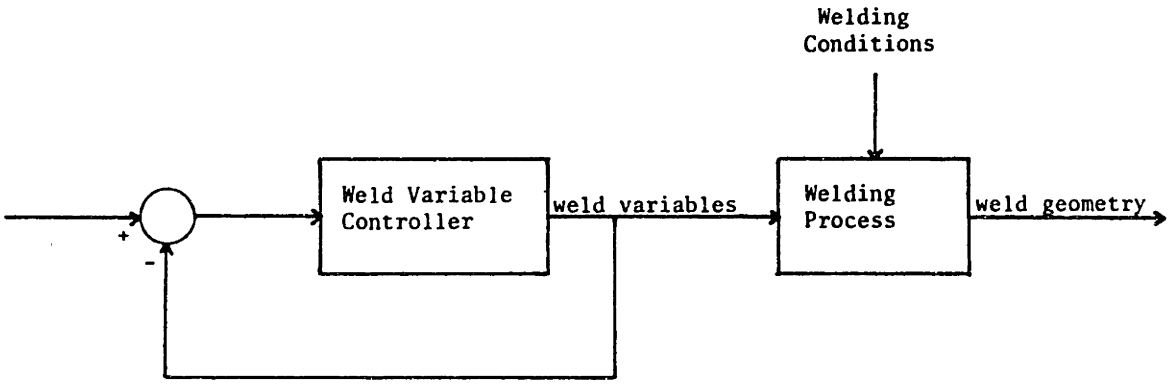

Figure 2.15 Stabilization control.

Stabilization control is not adaptive control. The essence of adaptive control is to change the welding variables to suit the varying welding conditions, thereby giving consistent weld bead geometry. One way to get some level of adaptive control is to use a feed forward loop (61). Vision systems are capable of measuring variations of weld groove size and shape, making it possible to predict the primary process disturbances. We can then adjust the welding variables based on that prior knowledge, as shown in Figure 2.16. This method does not close the

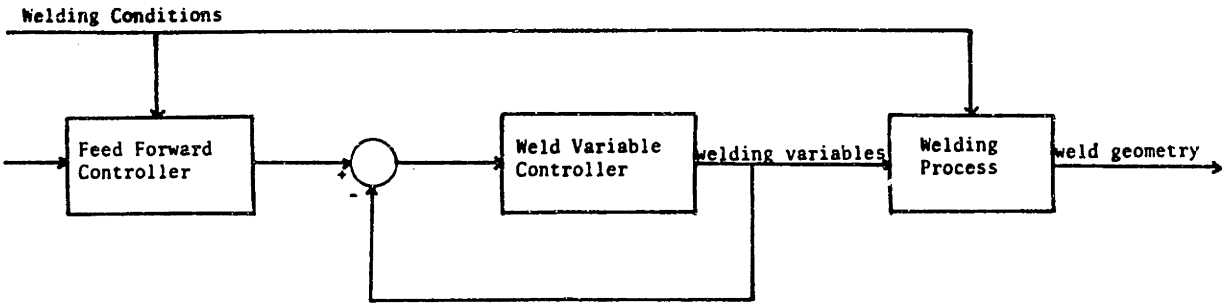

Figure 2.16 Feed forward adaptive control.

loop on the weld bead geometry, but it does attempt to adapt to changing welding conditions. "Knowing the geometric characteristics of a weld seam and using the proper preset weld parameters result in acceptable welds a high percentage of the time" (62). The trick, of course, is to accurately determine the "proper" preset weld parameters. These can either be determined by mathematical algorithms or by a look-up table. The accuracy of the algorithms or table over a wide range of conditions and variables is the key to the success of this method. Development of algorithms/tables is an ongoing research area in the overall effort to model the welding process. Unfortunately, the welding process is so complex that success thus far has been limited. Analytical models tend not to be very accurate, and empirical models are so specific that they are not generally applicable.

We could help to alleviate this problem by adding an adaptive feedback loop to figure 2.16, as shown in figure 2.17. This is full adaptive control, but it is nearly impossible to implement because some of the output variables (such as penetration) are not presently measurable in real time. It is possible, though, to measure one or more

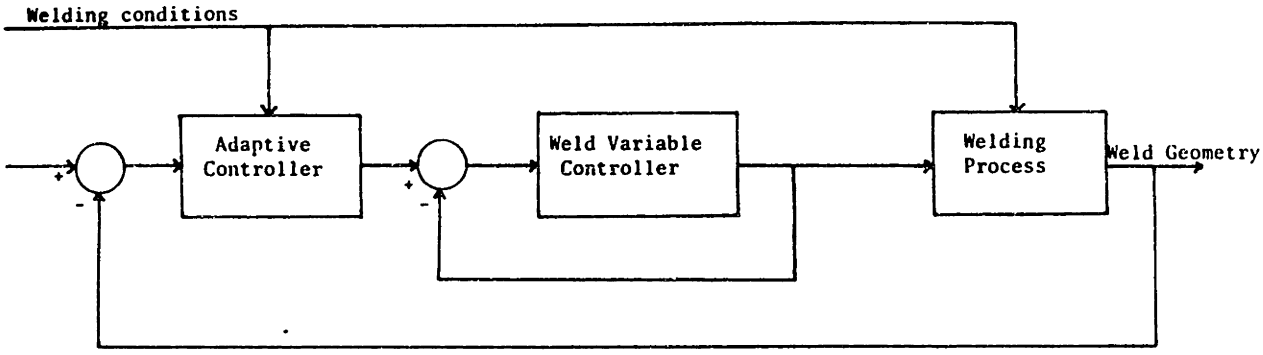

Figure 2.17 Full adaptive feedback control.

of the weld bead dimensions and then make assumptions regarding the other dimensions based on these measurements. The easiest dimension to measure in real time is the width of the weld pool. Work in this area has been ongoing for a decade, and very limited progress was achieved using a proportional plus integral controller with travel speed as the only controlled input (63). More advanced systems could control multiple inputs based on multiple output feedback. In full penetration welds, the backbead width can be measured by either thermal or optical sensors located behind the workpiece (64) or by vibration analysis of the weld pool. Ultrasound is also being investigated as a means of measuring the weld pool depth, thereby making real time feedback of penetration depth possible (65). Industrial implementation of ultrasound or backbead measurement is difficult, though, due to access limitations. The interpretation of the ultrasound readings is also not yet fully developed.

In summary, seam tracking progress has been substantial in recent years, and robot adaptation to variations in joint location is now a reality. Vision technology has made detection of variations in groove

geometry a reality. How to respond to those variations, though, is still an area in need of considerable progress. This thesis will focus on the sudden variation in groove geometry caused by the presence of a tack weld. Section 2.5 will overview the significance of the tack weld problem in the shipbuilding industry.

2.5 Tack Welds

2.5.1 Introduction

Tack welds are used extensively in heavy industries to hold metal pieces in place in preparation for final welding. In shipbuilding, they are used in both butt and fillet welds, they are generally at least an inch long, an they are spaced at an average of 12 to 16". Sometimes spacing is wider, but it is never over 4'. Spacing is determined by both pre-existing and expected distortion. If there is considerable pre-existing distortion, then the pieces must be forced together, and large, closely-spaced tack welds are required to hold them in place. Similarly, if significant unrestrained distortion would be expected during the ensuing production weld, the tack welds must be large and closely-spaced to prevent them from yielding. Given that the new class of naval cruisers has 70,000' of double fillet welds, as well as large amounts of single fillet welds and tens of thousands of feet of butt welds, tack welds are a significant item in shipbuilding.

Tack welds are generally made by shipfitters rather than welders. Shipyards consider it wasteful to devote skilled welders to the tedious task of making tack welds. It is much easier for shipfitter to make the tacks themselves as they align the metal pieces. Shipfitters, though, are not skillful at welding, and the tacks they make tend to be poor in quality and large in size. The large size results from the fear of making them to small and having them break. Hence, they make them large, "just to be sure". Bath Iron Works recently conducted a study of weld size that included over 300 tack welds and 3000 feet of completed fillet welds (67). BIW found that tack welds made under typical conditions averaged 40% oversize. BIW is implementing a training program to correct the problem, and the tacks made as part of this program were not at all oversized. If

tack welds are to be successfully dealt with, it is critical that their size be brought under control first. Efforts such as that at BIW should be assiduously pursued.

Exactly what sort of problems do tack welds cause, and what is the proper procedure for handling them? The answer to the latter question is not known. Ideally, the tack weld should be melted and incorporated into the final weld, but achieving this is very difficult. Experience at BIW (68) has shown that fillet tack welds of 5/32" leg length or less are consumed into the final weld fairly well and can be ignored, but larger tacks are not consumed. A 5/32" leg length corresponds to a cross-sectional area of approximately $8mm^2$, which is extremely small. To be made with a .045" wire at 10 ipm travel speed, the maximum wire feed speed would be 80 ipm, which is unreasonably low. The resulting low current ensures a tack weld with poor fusion and penetration characteristics. Very few real tack welds are this small, especially since they are generally made with stick welding rather than GMAW.

In manual welding, the welder is able to adjust his welding parameters as he sees fit when he encounters a tack weld. There are two general strategies that are used. One is to slow down while going over the tack, thereby increasing the heat input in the hopes of remelting it. The other is to speed up while going over the tack, thereby decreasing the metal deposition rate in the hopes of leaving a smooth surface contour. The first strategy gives up on the surface contour, while the second gives up on remelting the tack. Welders do not, however, like to leave an uneven surface contour, since such welds are frequently rejected by visual inspectors. In order to minimize the hump at the tack weld site, welders frequently make the entire weld larger. What we are left with, therefore,

is a great deal of uncertainty regarding final weld quality, which brings back the question regarding the problems that tack welds cause.

2.5.2 Problems Caused by Tack Welds

There are five types of problems that are caused by tack welds and the present inability to effectively deal with them. They are:

(1) weld defects

(2) excessive weld size

(3) prevention of one-sided welding

(4) excessive fixturing

(5) impedement of automation

(1) Weld Defects

Weld defects will occur when a defective tack weld is not remelted during the final weld. Defects could also occur at the transitions at the beginning and end of each tack. An alternate strategy for handling tack welds is to make them of final production quality and size, and then just do production welding between the tacks. This unfortunately creates a high propensity for defects at the start and stop points. Making high quality tacks of slightly smaller size, and then just speeding up over the tacks to maintain a smooth surface contour, would seem to be a viable strategy. Unfortunately, shipyards have been notoriously unsuccessful in their attempts to achieve quality tack welds, and it might be unrealistic to expect such achievement in the future. It is well known that starting and stopping points are common sources of defects, and that's essentially all a tack weld is -- a start and a stop. This might, therefore, be an inherent limitation of tack welds, even when made by skilled welders.

It is impossible at this time to quantify the number of weld defects attributable to tack welds. The BIW study attributed "excessive" weld defects to poor quality tack welds, but this was only from surface contour inspections. It is also likely that there are many backside defects (lack of penetration) which are never discovered in non-controlled fillet welds. Since these are in non-critical applications, it is doubtful that any catastrophic failures ever result, but they could be an eventual source of fatigue cracking.

(2) Excessive Weld Size

The BIW study concluded that final weld size was frequently excessively large in order to cover up the tacks and provide a smooth surface contour. 53% of the linear footage of final weld was oversized by at least 1/16" leg length on the welds made under normal conditions. This excessive size is costly in four ways: weight, time, money and distortion. The additional weight came to .07 lbs/ft due to the excess metal. This equates to 140 lbs per 1000 feet of double fillet weld. Given the 70,000 feet of such weld on the new cruiser class, this is nearly 10,000 lbs per hull, which is quite significant. Time is wasted since it takes longer to make a larger weld. Money is wasted in paying for both the extra time and the extra materials. The higher metal deposition rate and accompanying higher heat input cause additional distortion.

Buckling distortion is particularly sensitive to overwelding since there is a critical heat input below which buckling is negligible and above which it is significant. The critical heat input depends on the plate dimensions and can be generalized by incorporating plate thickness

and plate span along with heat input into a critical buckling parameter: Qb/t^3. Figure 2.18 shows the central defection versus this parameter. Below about 4 cal/cm^3, there is little danger of buckling, but above that,

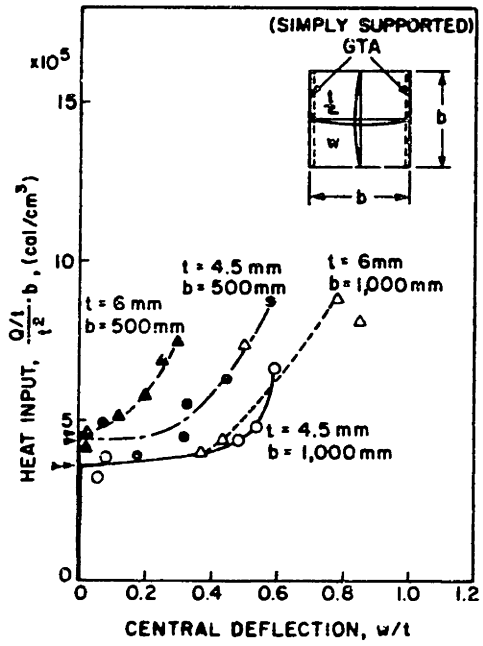

Figure 2.18 Buckling distortion as a function of the critical buckling parameter. (88)

buckling increases precipitously. The heat input, Q, is proportional to the cross-sectional area of the deposited weld metal, which is proportional to the leg length squared for a fillet weld.

As an example, consider a 3/16" fillet weld on 1/4" plate with a 30 inch span. The fillet weld cross-sectional area is approximately .018 in^2. Assume that the weld is made with a .045" wire, which has a cross-sectional area of .00159 in^2. The ratio of wire feed speed to travel speed must therefore be 11.3. If we assume an electrode extension of 1/2" and a 200 A current (just above transition to spray), then Lesnewich's curves (69) give a wire feed speed of 225 ipm. The travel

speed must therefore be 19.9 ipm, or .842 cm/s. Assume an arc voltage of 26 and a 70% arc efficiency. The conditions are summarized as follows:

$$I = 200A$$

$$V = 26\ V$$

$$\eta = .70$$

$$TS = .842\ cm/s$$

$$t = .635\ cm$$

$$b = 76.2\ cm$$

The heat input and critical buckling parameter are calculated as follows:

$$Q = (.70)\ (200A)\ (26V)\ \left(\frac{1\ s}{.842\ cm}\right)\ \left(\frac{cal}{4.184\ J}\right)$$

$$Q\ b/t^3 = 3.1 \times 10^5\ cal/cm^3$$

This is below the critical buckling level, so there would be only bending distortion. A small increase to a 1/4" fillet weld size, however, would increase the cross-section area to .032 in^2, which could be achieved by slowing the TS to .474 cm/s. The resulting heat input would be 1835 cal/cm, and the buckling parameter would be 5.5×10^5 cal/cm^3. This exceeds the threshold level and would cause a significant increase in distortion. Thus even a slightly oversized weld can have severe distortion consequences.

(3) Prevention of One-Sided Welding

Shipbuilding involves considerable butt welding of 3/8" and 1/2" steel plate. When the plates are tack welded together, the inability to effectively weld through the tacks prevents the shipyard from performing one-sided GMA welding with ceramic backing strips. When conditions permit

the use of submerged arc welding, it can be done successfully through tack welds, since the high heat input melts through them. When GMAW is required, though, the top side must be welded, which generally takes five passes, then the backside must be gouged out and rewelded, generally with three passes. The back gouging must be done in order to eliminate the defects at the tack weld sites. If the tack welds could be welded through, then the back gouging and three additional weld passes wouldn't be necessary, and there would be a significant savings in time, material and cumulative heat input. BIW has tried to find a way to do one-sided welding through tacks, but has had no success with it.

(4) Excessive Fixturing

In order to avoid the problems of tack welds, some yards use extensive fixturing instead of tack welds to hold the metal pieces in place. BIW has had considerable success with one-sided welding of fixtured plates. The fixturing for butt welds consists of studs welded onto both plates approximately every foot, with clips attached to the studs to align and hold the plates in place. Afterwards, the clips and studs are removed and the plate surface is ground smooth. Each stud/clip combination is relatively simple to install, but the vast number of them does represent a fairly large investment in time and material.

(5) Impedement of Automation

Unlike the manual welder described in the introduction, automated welding equipment cannot use intuition in deciding on a strategy to handle tack welds. The strategy must be programmed into the control algorithms. Automation state-of-the-art allows the detection of tack welds and the determination of the dimensions. There is, however, considerable uncertainty regarding what to do with that information, and defective welds

result. In cases in which that is unacceptable, extensive and expensive fixturing is used to avoid the tack welds. In other cases, the automation cannot be applied and the welds must be done manually. The scenarios that the SRI study identified for the fixed base welding robot, the gantry mounted welding robots and the robotic subassembly fabrication workstation all had the workpieces tack welded together before being brought to the robot workstation. These conceptual designs assume that the robots have the adaptive process control capability to effectively deal with the tack welds, but that capability is not yet a reality.

2.5.3 Tack Weld Strategy

What is the proper way to handle a tack weld? The ultimate goal is to remelt the tack weld while maintaining a smooth surface contour. However, remelting tack welds requires a higher heat input, while maintaining a smooth surface contour requires a lower metal deposition rate. Such a strategy is shown in figure 2.19. Since heat input and deposition rate are coupled in GMAW, this is not possible. Limited decoupling is

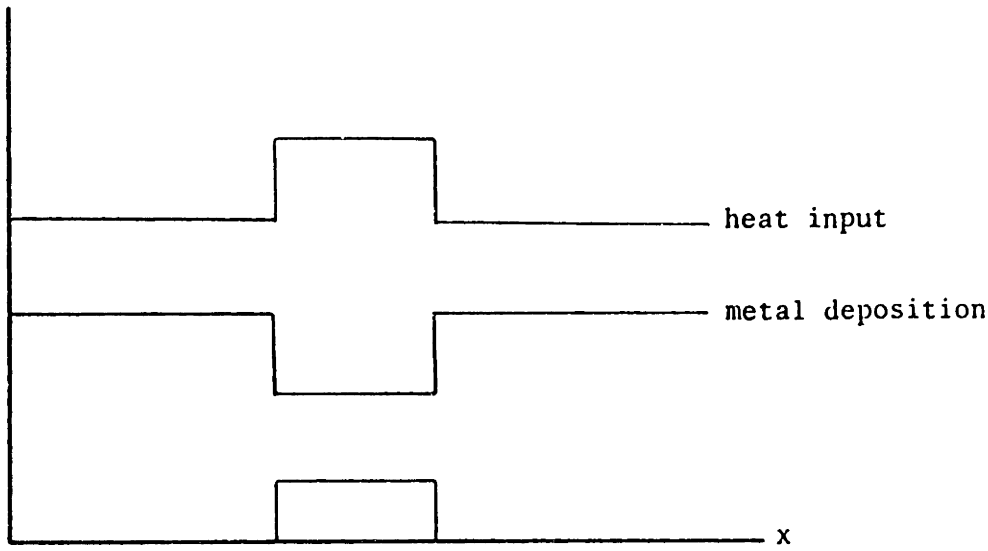

Figure 2.19 Strategy for handling tack welds.

possible by changing the electrode extension, but not to the extent necessary for this.

The amount of additional heat required to remelt the tack weld can be easily calculated using an enthalpy analysis. The heat required to bring the tack weld to the melting temperature and melt it is given by:

$$H_m = m \int C_p dt + mh_t + mh_f$$

where

m = mass of the tack weld
C_p = heat capacity
h_t = heat of transformation
h_f = heat of fusion

If we replace the temperature dependent heat capacity by an average heat capacity, we can write:

$$H_m = A\rho \ (C_p \Delta T + h_t + h_f)$$

where

A = tack weld cross-sectional area
C_p = .7 $Jg^{-1}\ K^{-1}$
ρ = 7.8 gcm^{-3}
h_t = 39.8 Jg^{-1}
h_f = 272 Jg^{-1}
$\Delta T = T_m - T_o$ = 1500 K

Inserting these values gives:

$$H_m = A_w \frac{WFS}{TS} \ (10{,}622\ Jcm^{-3})$$

where A_w is the wire cross-sectional area. For a .045" wire with a wire feed speed of 250 ipm and a travel speed of 10 ipm, the heat required is 2725 J/cm. The welding heat is given by:

$$Q = \eta\ VI/TS$$

For a 25V, 250A arc with a 10 ipm travel speed and a 75% arc efficiency, Q = 11.1 KJ/cm. Melting of the tack weld could therefore be accomplished with a 25% increase in the effective heat input, requiring a 33% increase in arc energy. Although this would be fairly easy to achieve, there are practical limitations. First, it assumes that the arc efficiency remains at 75% and that all of the additional heat input goes into melting the tack weld. If the arc energy increase were achieved by an increase in current to 333A, efficiency would drop due to higher radiation losses. Weld pool surface vaporization would decrease the heat available to melt the tack weld. The accompanying increase in the metal deposition rate would create an uneven surface contour, and the enlarged weld pool would adversely affect penetration. Increasing the voltage to 33V would increase the arc length and adversely affect penetration. Decreasing the travel speed to 7.5 ipm would increase the linear metal deposition rate, again causing an uneven surface contour and an enlarged weld pool. In all cases, the higher heat input will increase distortion and residual stresses, perhaps precipitating buckling distortion.

As an alternative to overwhelming the tack welds with increased heat input, this thesis will examine the use of current pulsing to penetrate the tack welds. This alone will not eliminate all tack weld defects, but it could eliminate the most serious ones. If it is possible to fully penetrate the tack welds, that would take care of the backside defects. Since these are surface defects, they are much more serious than any subsurface defects which could only be eliminated by full remelting of the tack welds. Even if full penetration cannot be achieved, the increased

penetration will do a better job at the beginning and end points of the tack welds. The defects in tack welds will be discussed in more detail in section 4.3. The intention is to increase penetration without increasing heat input or metal deposition rate. Chapter 3 will be devoted to a thorough analysis of penetration and the ways in which current pulsing could be used to increase it.

CHAPTER 3

MECHANISMS OF PENETRATION IN GMAW

3.1 Introduction

Ultimately, the weld bead shape is determined by heat flow. The bottom surface of the weld pool is the melting isotherm of the base plate, and it is the delivery of heat to the workpiece as well as conduction and convection within the weld pool that determine that isotherm. The key to controlling the weld bead geometry, therefore, is to control the delivery of the heat to the workpiece and the fluid flow pattern within the weld pool. In a purely conductive weld pool formed by an arc striking the top of it, the isotherms would look something like those shown in figure 3.1. The isotherms decrease in temperature from T_o at the pool center surface to T_m at the pool perimeter. Natural

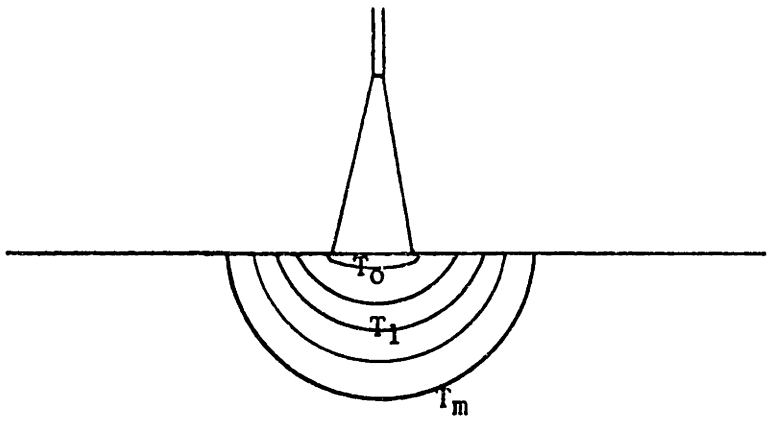

Figure 3.1 Isotherm patterns in a purely conductive weld pool. $T_o > T_1 > T_m$

convection would not significantly alter this pattern, since the hotter, less dense fluid is already at the surface.

The problem of heat flow within the workpiece has been studied extensively by a number of investigators. Rosenthal (70) began by studying pure conduction from a point heat source. Rykalin (71, 72, 73) modeled the arc as a gaussian heat source. Other investigators have included convection and surface depression in their models. For GMAW, there is also heat transfer and fluid flow resulting from the metal transfer. Each of these items makes the model considerably more complex than Rosenthal's, and accurate solutions to the complete model are not yet available.

There are three factors which distinguish a real GMA weld from the idealized situation shown in figure 3.1:

(1) surface depression
(2) pool convection
(3) metal transfer

Surface depression allows the delivery of heat at a level below the undistorted surface of the weld pool. This pushes the melting isotherm down and gives deeper penetration. Surface depression can result from the arc pressure, which will be discussed in section 3.3, from the formation of a compound vortex, which will be discussed in section 3.4, or from the impact of the metal droplets hitting the pool surface, as will be discussed in section 3.6.

Pool convection redistributes the very hot molten metal formed directly under the arc. Depending on the flow pattern, this will give either a wide shallow weld or a narrow deep weld, as will be discussed in section 3.5. The impact of the metal drops hitting the weld pool both depresses the surface and carries hot metal below the surface, as will be

discussed in section 3.6.

For a given heat input, then, there are four mechanisms which determine the depth of penetration: arc pressure, compound vortex, pool convection and droplet momentum. Conduction is obviously a penetration mechanism too, but it will not be discussed in detail. The intent of this thesis is to examine methods of controlling penetration independently of metal transfer rate, and conduction does not offer any significant potential for such control. Penetration via conduction is primarily a function of the magnitude of the heat input. It is also a function of the distribution of the heat input, but within the actual range of feasible arc shapes, the penetration differences due to conduction will be overwhelmed by those due to the other mechanisms. When there is significant weld pool convection, conduction is only a factor at the melting interface and in the solid base plate. At these distances from the heat source, the heat input distribution has been averaged by convection and is no longer a factor. Controlling penetration by varying the magnitude of the heat input is certainly possible, since penetration is generally reported to be proportional to current, but we are interested in controlling penetration independently of heat input. Hence, conduction will not be discussed further, and sections 3.3 through 3.6 will be devoted to the other four penetration mechanisms. First, though, section 3.2 will discuss pulsed GMAW. Current pulsing is a potential means of controlling penetration independently of heat input via the four penetration mechanisms.

3.2 Pulsed GMAW

3.2.1 Description

Pulsed GMAW uses a DC power source with current as the independent

output variable. Rather than being constant, however, the current pulses as shown in figure 3.2. The waveform is completely described by four parameters: base current (I_b), base period (T_b), peak current (I_p) and

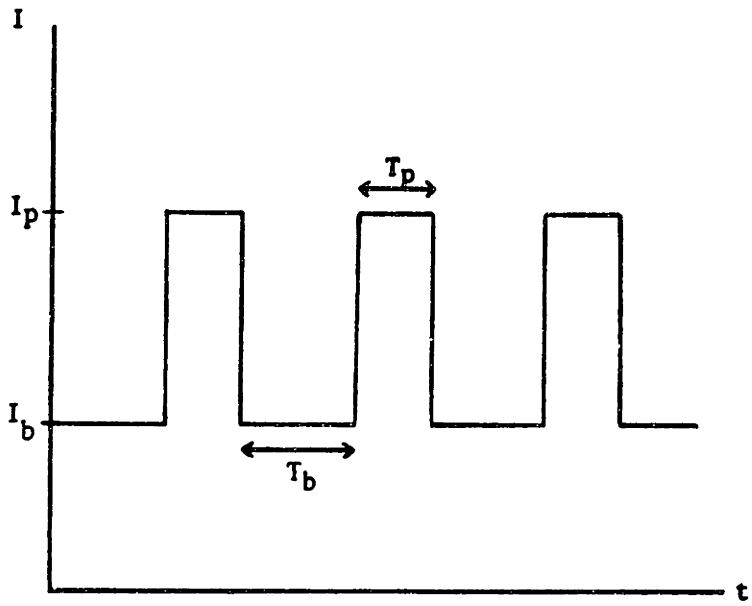

Figure 3.2 Current waveform in pulsed welding.

peak period (T_p). Other parameters that are frequently used to describe the waveform are:

$$\text{frequency} = f = \frac{1}{T_b + T_p} \tag{3.1}$$

$$\text{current excess} = I_e = I_p - I_b \tag{3.2}$$

$$\text{average current} = I_{ave} = \frac{I_p T_p + T_b T_b}{T_p + T_b} \tag{3.3}$$

The purpose of pulsing is to allow spray transfer at a lower average current. The background phase maintains the arc and preheats the wire, then the pulse forms a droplet and propels it to the workpiece. Pulsed GMAW is generally operated in the one drop per pulse mode, meaning that

one drop is formed and detached during each cycle. Drop frequency therefore equals pulse frequency. The size of the drops and the timing of the detachment depend on the pulse parameters, the wire feed speed, and the electrode stickout distance.

Successful GMAW, whether pulsed, constant current or constant voltage, requires both that the wire feed rate is balanced by the melting rate and that there is stable transfer of metal from the wire to the weld pool (74). The wire melting rate in pulsed GMAW is similar to that in traditional GMAW, except that it must be averaged over the entire waveform:

$$\dot{m}_b = aI_b + b\ L\ I_b^2 \tag{3.4}$$

$$\dot{m}_p = a\ I_p + b\ L\ I_p^2 \tag{3.5}$$

$$\dot{m} = \frac{m_b T_b + m_p T_p}{T_b + T_p}$$

$$\dot{m} = aI_{ave} + bLI_{eff} \tag{3.6}$$

where

$$I_{eff} = \frac{I_b T_b^2 + I_p T_p^2}{T_b + T_p} \tag{3.7}$$

Because the effective current in equation 3.6 is larger than the average current, the melting rate in pulsed GMAW is larger than in traditional GMAW with an equivalent average current. This is due to the extensive ohmic heating which occurs during the peak current excursions.

Pulsed GMAW has become a subject of considerable interest in recent years, and much has been written regarding the selection of pulse parameters. The only absolute requirements on the pulse parameters are

that the background current be high enough to maintain the arc (about 30 amps), the pulse current be greater than the spray transition current (about 190 amps), and the resultant burnoff rate be equal to the wire feed rate. Beyond these minimum requirements, there is considerable latitude in selecting the parameters, and the parameters that are selected can have an immense impact on the weld characteristics. But just what that impact will be is not yet fully understood. Before attempting to improve that understanding, section 3.2.2 will discuss the advantages of pulsed welding, and section 3.2.3 will discuss the procedures currently used to select parameters.

3.2.2 Advantages of Pulsed Welding

Pulsed GMAW was originally developed to allow spray transfer at a low mean current. This is particularly significant for out-of-position and thin plate welding. The high current required for spray transfer causes a large weld pool that runs when welding out of position and causes burnthrough when welding thin plate. The background period of pulsed welding can be thought of as allowing the weld pool to partially solidify, thereby reducing its size and making all position welding possible. Prior to pulsed welding, short circuit transfer had to be used for out of position welds, but short circuit welding is a low integrity process, plagued by poor fusion and excessive spatter.

Pulsed welding was first developed in the 1960's as an alternative to short circuit welding, but power supply technology has only recently advanced to the point of being able to fully support the process. With modern power supplies, pulsed GMAW can produce excellent quality welds. In one study (75), the average yield strength of three synergic pulsed welds was 24% higher than short circuit welds. Tensile strength was also 24% higher, and the absorbed energy in a Charpy test at -30°C was 48%

higher. Other researchers have reported improvements in grain size, porosity, and hot and cold cracking susceptibility (76). Pulsed GTAW has also been investigated extensively, with essentially the same set of advantages being found (except that weld puddle size is not such a problem in GTAW). Additionally, the pulsing has been found to "markedly reduce sensitivity to component and material variations, resulting in a more uniform weld bead and less distortion" (77).

3.2.3 Parameter Selection

Current thinking on parameter selection revolves around achieving stable metal transfer, and it is commonly felt that the optimum metal transfer is achieved in the one drop per pulse mode described earlier. In this mode, the background current maintains the arc and preheats the wire. The peak current then melts enough wire to form a drop and causes the drop to detach. The peak current and duration are the critical parameters, with the background current and duration having little or no effect on the metal transfer (78). The peak parameters are closely interrelated as shown in figure 3.3. The peak duration must be long enough to allow the drop to form and detach, but not so long that multiple drops detach. Experiments show that I_p and T_p are related mathematically by:

$$I_p^2 \, T_p = D = \text{constant} \qquad (3.8)$$

where D, the detachment parameter, depends on wire composition, wire diameter, and shielding gas composition. The key factor here is drop detachment time, T_D, which is defined as the time between pulse initiation and drop detachment. T_D decreases with increasing I_p, as shown in figure 3.4. The squared dependence of I_p in equation 3.8 is due to the fact that the electromagnetic pinch force, which is responsible for high

current drop detachment, is proportional to the square of the current.

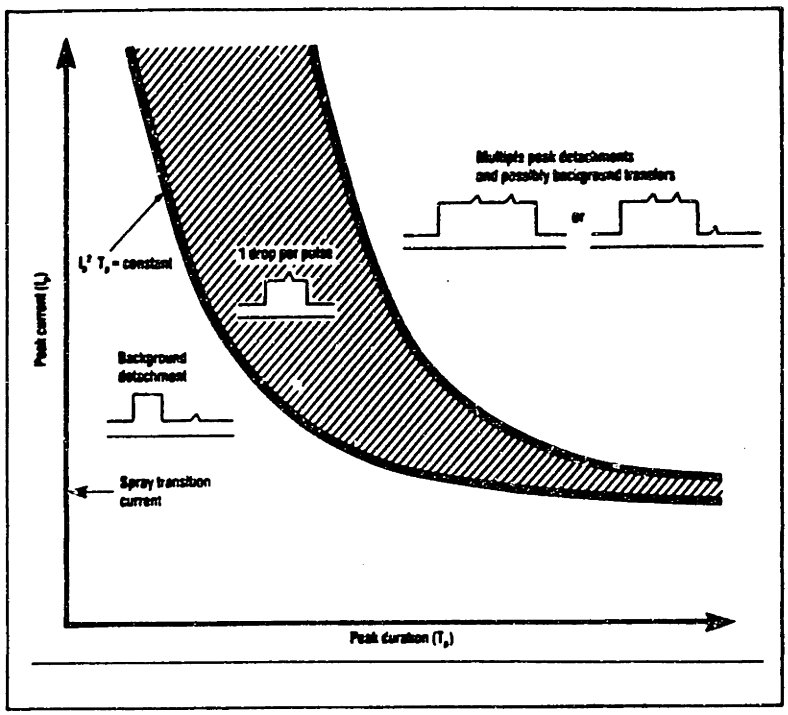

Figure 3.3 Influence of peak parameters on metal transfer. (79)

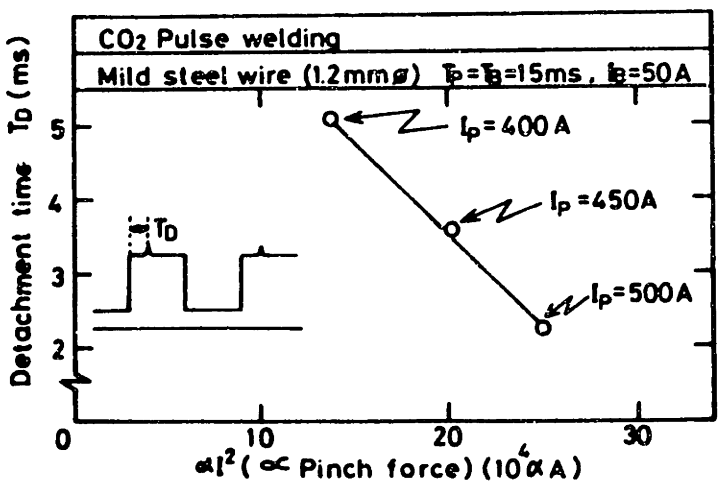

Figure 3.4 Detachment time at various peak currents. $T_p = T_b$, I_b = 50 amps, CO_2 shielding. (80)

Higher peak currents therefore result in not only quicker detachment but

also faster drop velocity (81).

If we stay within the bounds of figure 3.3 that result in one drop per pulse transfer, then we can derive some simple rules of thumb to aid in choosing the specific parameters. Begin with equation (3.6) and neglect the minute amount of burnoff that occurs during the background phase:

$$\dot{m} = aI_{ave} + bLI_p^2T_p/(T_b + T_p) \tag{3.9}$$

Substitute equations 3.1 and 3.8:

$$\dot{m} = aI_{ave} + bLDf \tag{3.10}$$

If $\dot{m}$ is the burnoff rate in units of mass per unit time, then it is related to the wire feed speed, W, the wire cross sectional area, A, and the wire density, ρ, by:

$$\dot{m} = WA\rho \tag{3.11}$$

Equation (3.10) can then be rewritten as:

$$W = \alpha I_{ave} + \beta LDf \tag{3.12}$$

where $\alpha = a/A\rho$ and $\beta = b/A\rho$. Typical values of α and β for a 1.2 mm mild steel wire are: (82)

$$\alpha = .27 \text{ mm } A^{-1} S^{-1}$$
$$\beta = 6 \times 10^{-5} A^{-2} S^{-1}$$

When one drop is transferring per pulse, the drop frequency equals f, and the burnoff rate is given by:

$$W = \phi f/_A \tag{3.13}$$

where ϕ is the drop volume. Combining (3.12) and (3.13) gives:

$$\phi f = \alpha A I_{ave} + \beta A L D f \tag{3.14}$$

$$\phi = \alpha A (I_{ave}/_f) + \beta A L D \tag{3.15}$$

For a given wire composition, diameter, and stickout, then, the drop size is purely a function of I_{ave}/f. Equation (3.14) can be rearranged to give:

$$f/_{I_{ave}} = \frac{\alpha A}{\phi - \beta A L D} \tag{3.16}$$

Ostensibly, this is the inverse of the previous statement. For a given wire, stickout, and drop volume, the ratio of frequency to mean current is predetermined. The predominant ratio used in the literature is 50Hz/100A for a 1.2 mm wire. For 1.0 and 1.6 mm wires, the ratios are 60Hz/100A and 40Hz/100A, respectively. Although equation 3.16 would seem to indicate larger ratios for larger wires, variations in α and β make the opposite true. For the 1.2 mm wire, this ratio gives a drop volume of 1.1 mm^3 for a stickout of 15 mm and a detachment parameter of 480, which would be representative of Ar/5%CO_2 shielding gas. The drop diameter is therefore 1.28 mm, essentially equal to the wire diameter.

This frequency-to-mean current ratio forms the basis of the following

commonly used pulse parameter selection process (82):

(1) Choose an appropriate mean current based on desired heat input.

(2) Choose an appropriate wire size based on mean current, equipment considerations, etc. Larger wires are appropriate for larger mean currents as follows:

1.0 mm	60-170A
1.2 mm	85-250A
1.6 mm	140-305A

(3) Choose peak current and duration based on equation 3.8. There is some leeway in the value of D, the detachment parameter, as indicated by the range of appropriate values shown in figure 3.3. Figure 3.5 shows specific values for three wire sizes.

(4) Choose frequency based on the f/I_{ave} ratio.

(5) Calculate T_b from f and T_p.

(6) Calculate I_b from I_p, T_p, T_b and I_{ave}.

(7) Choose a stickout distance based on torch height and desired arc length, and calculate wire feed speed from equation 3.12. Conversely, choose wire feed speed based on desired deposition rate, and calculate the stickout distance.

The primary flexibility in this process comes from step 3. The choices made in steps 1, 2 and 7 are probably dictated by the situation, but there is a wide range of acceptable choices in step 3 with resultant changes in finished weld bead characteristics. These changes, as well a the initial choice of one drop per pulse, will be investigated further in section 5.2.2 and chapter 6.

This process of parameter selection is rather lengthy and cumbersome for a welder to go through as he is welding. The desire for a system in which the parameters could be easily yet systematically changed to accommodate varying welding conditions has led to the development of

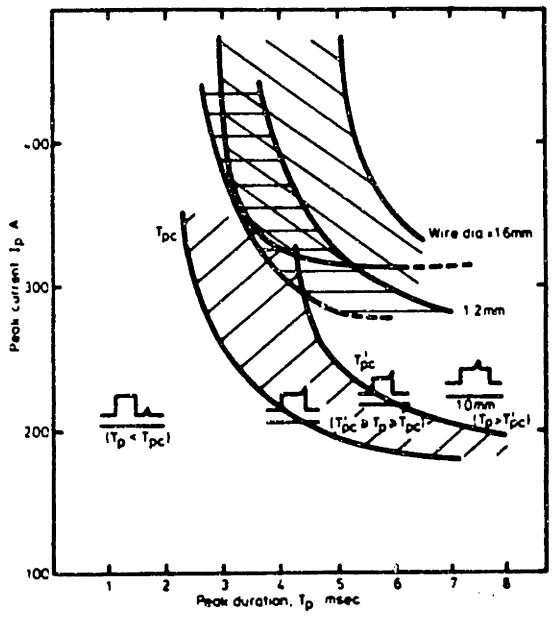

Figure 3.5 Influence of peak parameters on metal transfer for mild steel wire in Ar/5%CO_2. (78)

"synergic" welding. Synergic, or "one-knob" control, has been defined as "a control system for MIG welding whereby the output of the welding power source adapts automatically to the wire feed speed or the arc voltage, so maintaining a steady state welding arc" (83). Synergic welding leaves the operator with the need to control only one variable -- wire feed speed -- and the control system determines all other variables based on its logic structure. This leaves the operator with the ability to adapt to changes in groove size, while still being simple enough to accomplish in real time.

There are several logic structures available in the synergic welding marketplace. They begin with the simplifying assumption that mean current is the single determinant of burnoff rate. Mean current is therefore set at a level which will balance the wire feed speed, as measured by a tachometer. Each system is different in its method of selecting the appropriate parameter combination to give the desired burnoff rate. One

method is to keep the peak duration and current excess constant while varying background current and pulse frequency in proportion to the wire feed speed. Another method is to keep the frequency and current excess constant while varying the background current and the peak duration. The waveforms for these two strategies are shown in figure 3.6. The Clean Mag power supply from Mitsubishi varies nothing but the background duration. The Synergic M500 power supply from AWP varies the background current,

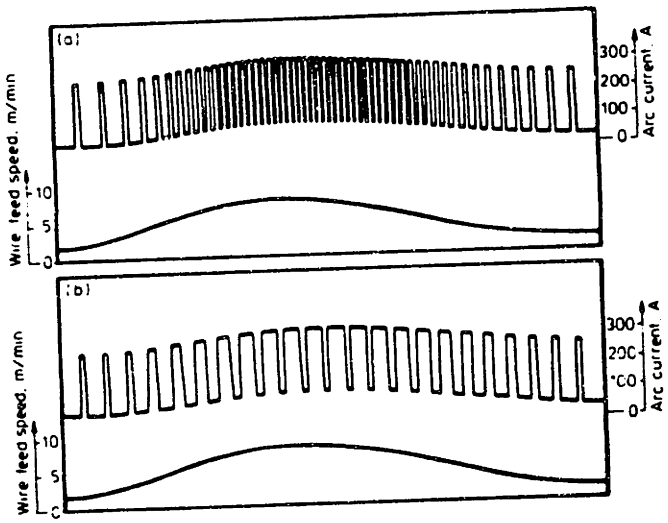

Figure 3.6 Synergic pulse response to changes in wire feed speed: a) variable frequency, b) variable peak duration. (84)

background duration, and peak current, keeping only the peak duration and current excess constant. (78)

One other method of control is based on voltage rather than wire feed speed. It is similar to the self-regulation of constant potential welding, except that the current changes are controlled by the logic structure rather than by the sloping characteristics of the power supply. The actual voltage is compared to a reference voltage, and the difference is used as a basis for adjusting the pulse parameters. If the measured

voltage were too high, for example, then the arc length is too long, and the burnoff rate needs to be reduced. This would be achieved by lowering the mean current, perhaps by increasing the background duration. As with wire feed speed control strategies, various logic structures are available.

Each logic structure has its strengths and weaknesses, but they all suffer from one limitation -- they are locked into a pre-determined set of process instructions. With wire feed based control, for example, it is the wire feed speed and not the groove geometry that determines the pulse parameters. A given mean current will always correspond to a particular set of parameters, and this could prove to be quite restrictive. Different welding conditions could require the same wire feed speed and mean current, but much different pulse parameters. Two of the reasons for the acceptance of this limitation are that it provides ease of operation and that the effect of varying pulse parameters at a given mean current is not yet well understood. This thesis will provide additional understanding in this area.

3.3 Arc Pressure

3.3.1 Theory

Arc pressure increases penetration by depressing the surface of the weld pool, thereby delivering the arc heat at a level that is below the surface of the undepressed weld pool and is therefore closer to the solid metal lying beneath the pool. Arc pressure is the result of the plasma jet flowing from the electrode to the workpiece. The stagnation pressure of the plasma jet being arrested at the workpiece is the theoretical arc pressure, and it can be integrated over the impinged area to give the arc force.

There are several ways of studying arc pressure. The first is by direct measurement through an orifice in a water cooled copper block. The second is by direct measurement of plasma jet velocities. The third is by any of a number of theoretical tools. Reference (85) uses both analytical and numerical means to solve the governing Maxwell and Navier-Stokes equations. Other investigators have used simplifying assumptions of varying degree. This section will review the theory of arc pressure and how it affects penetration. Section 3.3.2 will analyze the effect of current pulsing on arc pressure and therefore penetration.

The plasma jet originates from the interaction of a moving charge with a magnetic field:

$$\underline{F}_b = q\ \underline{v} \times \underline{B} \tag{3.17}$$

$\underline{F}_b$	= force on the charge	(Newtons)
q	= electric charge	(coulombs)
$\underline{v}$	= velocity of charge	(m/s)
$\underline{B}$	= magnetic field	(Weber/m^2)

The charge is also subject to an electrostatic force:

$$\underline{F}_e = q\underline{E} \tag{3.18}$$

where E is the electric field strength (V/m). The sum of F_b and F_e is the Lorentz force, but since $F_b \gg F_e$ in welding, we approximate the Lorentz force as being equal to F_b. When, instead of a single charge, there is a flow of charges of density ρ_e moving at velocity $\underline{v}$, then the Lorentz force per unit volume is given by the familiar equation:

$$\underline{F}_L = \underline{J} \times \underline{B} \tag{3.19}$$

where J is the current density in amps/m^2.

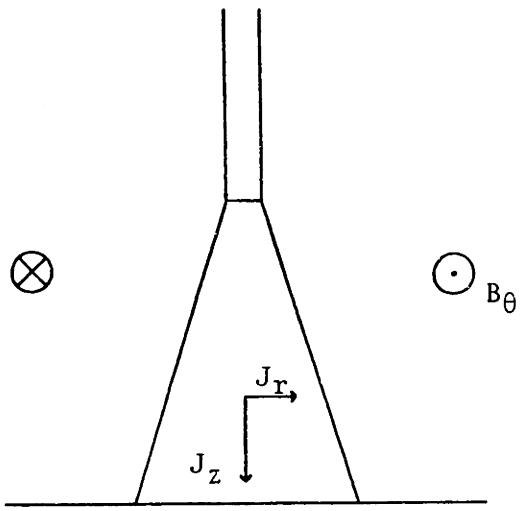

Figure 3.7 A divergent welding arc and its magnetic field.

Figure 3.7 shows a welding arc and its magnetic field. The current density vector has both an axial and a radial component.

$$\underline{J} = J_z\hat{u}_z + J_r\,\hat{u}_r \tag{3.20}$$

$$\underline{B} = B_\theta\hat{u}_\theta \tag{3.21}$$

The Lorentz force is therefore given by:

$$\begin{aligned}\underline{F}_L &= (J_z\,\hat{u}_z + J_r\,\hat{u}_r)\times(B_\theta\hat{u}_\theta)\\ &= J_z\,B_\theta\,(\hat{u}_z\times\hat{u}_\theta) + J_r\,B_\theta(\hat{u}_r\times\hat{u}_\theta)\\ &= -J_zB_\theta\hat{u}_r + J_rB_\theta\hat{u}_z\end{aligned} \tag{3.22}$$

For an arc of radius R with current I and uniform current density:

$$J_z = \frac{I}{\pi R^2} \tag{3.23}$$

$$B_\theta(r) = \frac{\mu I}{\pi R^2}\left(\frac{r}{2}\right) \tag{3.24}$$

where μ is the permeability constant. The radial current density is derived in reference (86) to be:

$$J_r(r) = \frac{I}{\pi R^3}\left(\frac{dR}{dz}\right)r \tag{3.25}$$

Substituting 3.23, 3.24 and 3.25 into 3.22 yields:

$$\underline{F}_L = -\frac{\mu}{2}\left(\frac{I}{\pi R^2}\right)^2 r\hat{u}_r + \frac{\mu}{2}\left(\frac{I}{\pi R^2}\right)^2\frac{r^2}{R}\left(\frac{dR}{dz}\right)\hat{u}_z \tag{3.26}$$

The Lorentz force has both a radially inward component that tends to

compress the plasma and an axially downward component that accelerates the plasma toward the workpiece. This has been derived here for a divergent arc, which is of practical interest. For a convergent arc, though, the math is exactly the same and the same equation holds. dR/dz is negative in such a case, and the axial force is directed upwards.

Both components of the Lorentz force contribute to the arc pressure. The radially inward force is balanced by a pressure gradient which increases toward the arc's center. If p(r) is the pressure, then equilibrium requires that:

$$\underline{F}_L \cdot \hat{u}_r = \frac{dp(r)}{dr} \tag{3.27}$$

Substituting equation 3.26 for $\underline{F}_L$ gives

$$\frac{dp(r)}{dr} = - \frac{\mu}{2} \left(\frac{I}{\pi R^2}\right)^2 r \tag{3.28}$$

We are interested in finding the pressure at the radius r, so we integrate from r to R. From R on out to infinity, the pressure is the ambient pressure, designated p_o.

$$\int_r^R dp(r) = \int_r^R - \frac{\mu}{2} \left(\frac{I}{\pi R^2}\right)^2 rdr$$

$$p(R) - p(r) = - \frac{\mu}{2} \left(\frac{I}{\pi R^2}\right)^2 \frac{1}{2} (R^2 - r^2)$$

$$p(r) - p_o = \frac{\mu I^2}{4\pi^2 R^2} \left(1 - \frac{r^2}{R^2}\right) \tag{3.29}$$

This higher pressure in the arc column exerts a force on the weld pool. The magnitude of that force is found by integrating the pressure above ambient over the area on which it is acting:

$$F_p = \int_0^R \frac{\mu I^2}{4\pi^2 R^2} \left(1 - \frac{r^2}{R^2}\right) 2\pi r dr$$

$$F_p = \frac{\mu}{8\pi} I^2 \tag{3.30}$$

The axially downward component of the Lorentz force can also be integrated to give the actual force acting on the weld pool. Imagine a section of the arc extending from z_1 to z_2, with respective radii of R_1 and R_2. The total downward force will be:

$$F_d = \int_{z_1}^{z_2} dz \int_0^R F_z 2\pi r dr \tag{3.31}$$

where F_z designates the axial component of the Lorentz force. The integration is carried out as follows:

$$F_d = \int_{z_1}^{z_2} dz \int_0^R \frac{\mu I^2 r^3}{\pi R^5} \left(\frac{dR}{dz}\right) dr$$

$$= \int_{z_1}^{z_2} dz \frac{\mu I^2}{4\pi R} \left(\frac{dR}{dz}\right)$$

When the variable of integration changes from z to R, the limits of integration change from z_1 and z_2 to R_1 and R_2:

$$F_d = \int_{R_1}^{R_2} \frac{\mu I^2}{4\pi} \left(\frac{dR}{r}\right)$$

$$= \frac{\mu I^2}{4\pi} \ln \left(\frac{R_2}{R_1}\right) \qquad (3.32)$$

The total force on the weld pool is found by adding 3.30 and 3.32:

$$F = \frac{\mu I^2}{8\pi} \left(1 + 2 \ln \frac{R_2}{R_1}\right) \qquad (3.33)$$

This derivation makes several simplifying assumptions. First, beginning with equation (3.23), it assumes that the current density distribution is uniform across the arc's cross-section. The differences this makes in the final answer is certainly quantitative rather than qualitative. Reference (87), for example, shows that in a non-uniform distribution, F_p is still independent of radius and depends only on the square of the current. Second, viscous drag has been ignored. Viscosity will both counteract the body force to some extent and cause surrounding air to be entrained in the plasma jet, thereby slowing it down. Third, thermal expansion has been ignored. Gases are rapidly expanded by the arc heat at the electrode, and this contributes to the plasma jet. Reference (85) noted that allowance for such compressible flow effects would bring theoretical plasma velocity predictions closer to measured values.

Now that the total arc force has been derived, it is necessary to consider the distribution of the force. If it were uniformly distributed over the entire surface of the weld pool, there would be no surface distortion. That would simply increase the pressure to some level above

ambient, but it is only when the pressure is concentrated in one area that surface depression results. Experiments indicate that the actual pressure distribution is more or less Gaussian, as shown in figure 3.8. Such a distribution can be described by:

$$p(r) = p_m \, e^{-(3r^2/R_p^2)} \tag{3.34}$$

p_m = maximum pressure, at arc centerline

R_p = effective radius of the pressure distribution

R_p is the radius at which p(r) has dropped to 5% of p_m. The total arc force is the integrated arc pressure, given by:

$$\begin{aligned} F &= \int_0^{R_p} p(r)\, 2\pi r dr \\ &= 2\pi p_m \int_0^{R_p} r e^{-(3r^2/R_p^2)} \, dr \\ &= \frac{\pi}{3} p_m R_p^2 \, (1 - e^{-3}) \\ &\approx \frac{\pi}{3} p_m R_p^2 \end{aligned}$$

We can equate this with the total arc force given by equation (3.33):

$$\frac{\pi}{3} p_m R_p^2 = \frac{\mu I^2}{8\pi} \left(1 + 2 \ln \frac{R_2}{R_1}\right) \tag{3.36}$$

$$p_m = \left(\frac{3\mu}{8\pi^2}\right) \left(\frac{I^2}{R_p^2}\right) \left(1 + 2 \ln \frac{R_2}{R_1}\right) \tag{3.37}$$

R_1 in this case is the radius of the very top to the arc, which is simply the electrode radius. In the theoretical development that led to equation 3.33, R_2 was taken to be the radius at the bottom of the current

expansion, which would be the arc radius at the workpiece. However, in

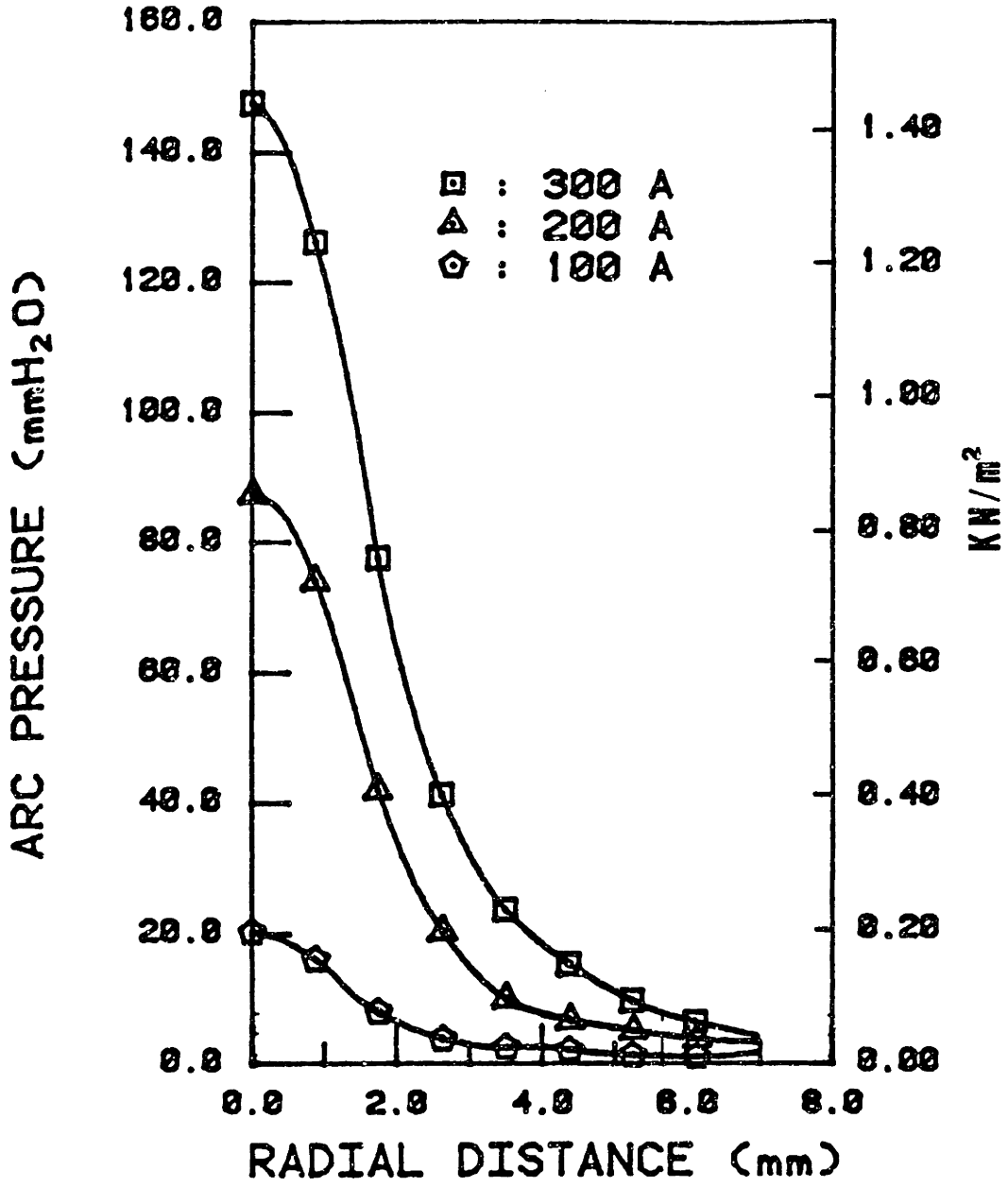

Figure 3.8 Arc pressure distribution taken from reference (89). Straight polarity, 4 mm Th-W (90°) electrode, 5 mm arc length, argon shielding gas.

reality, the plasma accelerates over a short range and reaches its maximum velocity just below the arc. From that point on, it spreads out and slows

down due to viscosity. The exact location of that point will vary considerably with current, electrode diameter, electrode tip angle (for GTAW), shielding gas composition, and possibly other parameters as well. For qualitative purposes, we will somewhat ambiguously designate this radius as the arc radius, R_a. R_p, on the other hand, is unambiguously measured at the workpiece.

Next consider how the pressure varies with current. First rewrite 3.37 with the new variables:

$$P_m = \left(\frac{3\mu}{8\pi^2}\right)\left(\frac{I^2}{Rp^2}\right)\left(1 + 2 \ln \frac{R_a}{R_o}\right) \tag{3.38}$$

R_a = arc radius

R_o = wire radius

Assume for the sake of qualitative discussion that the arc radius squared is proportional to current:

$$R_a^2 = c_1 I \tag{3.39}$$

This is in agreement with Mills (90), who claims that current density remains constant as current increases. Hamloy (91) also suggests that arc radius increases less than proportionately to current. Equating R_a and R_p would be reasonable although not exact. A larger arc radius will give a larger pressure radius, but it is more accurate to estimate them as being proportional:

$$R_p^2 = c_2 I \tag{3.40}$$

Substituting 3.39 and 3.40 into 3.38 yields:

$$p_m = \left(\frac{3\mu}{8\pi^2}\right)\left(\frac{I^2}{c_2 I}\right)\left(1 + 2 \ln \frac{\sqrt{c_1 I}}{R_o}\right)$$

$$p_m = \left(\frac{3\mu}{8\pi^2 c_2}\right) I \left(1 - 2 \ln R_o + \ln c_1 + \ln I\right)$$

For a .045" (1.143 mm) diameter wire:

$$p_m = \left(\frac{3\mu}{8\pi^2 c_2}\right) I \left(2.12 + \ln c_1 + \ln I\right) \qquad (3.41)$$

c_1 has units of mm^2/A, since R_o was taken as .5715 mm. c_2 must have units of m^2/A if the μ is taken to be the standard 4×10^{-7} henries/m. For a 300 A arc with an arc radius of 2 mm and a pressure radius of 4 mm, this gives a centerline pressure of 943 N/m^2, which is the same order of magnitude as that shown in figure 3.8. Exact agreement is not expected, since these radii are just estimates and figure 3.8 is for a 4 mm diameter tungsten electrode. The important point is the dependence on current, not the precise numerical result. This analysis has shown arc pressure to increase faster than I, but much slower than I^2. Other investigators have found results between I and I^2. Selyanenkov et al (92) claim that arc pressure scales parabolically with current. Data from Lin (89) and Yamauchi and Taka (93) is shown in figure 3.9. Lin's data for 30^o and 60^o tip angles is very close to linear, while the rest appears to be closer to parabolic. There is obviously uncertainty regarding the true nature of the scaling, but equation 3.41 would seem to be a viable theoretical estimate.

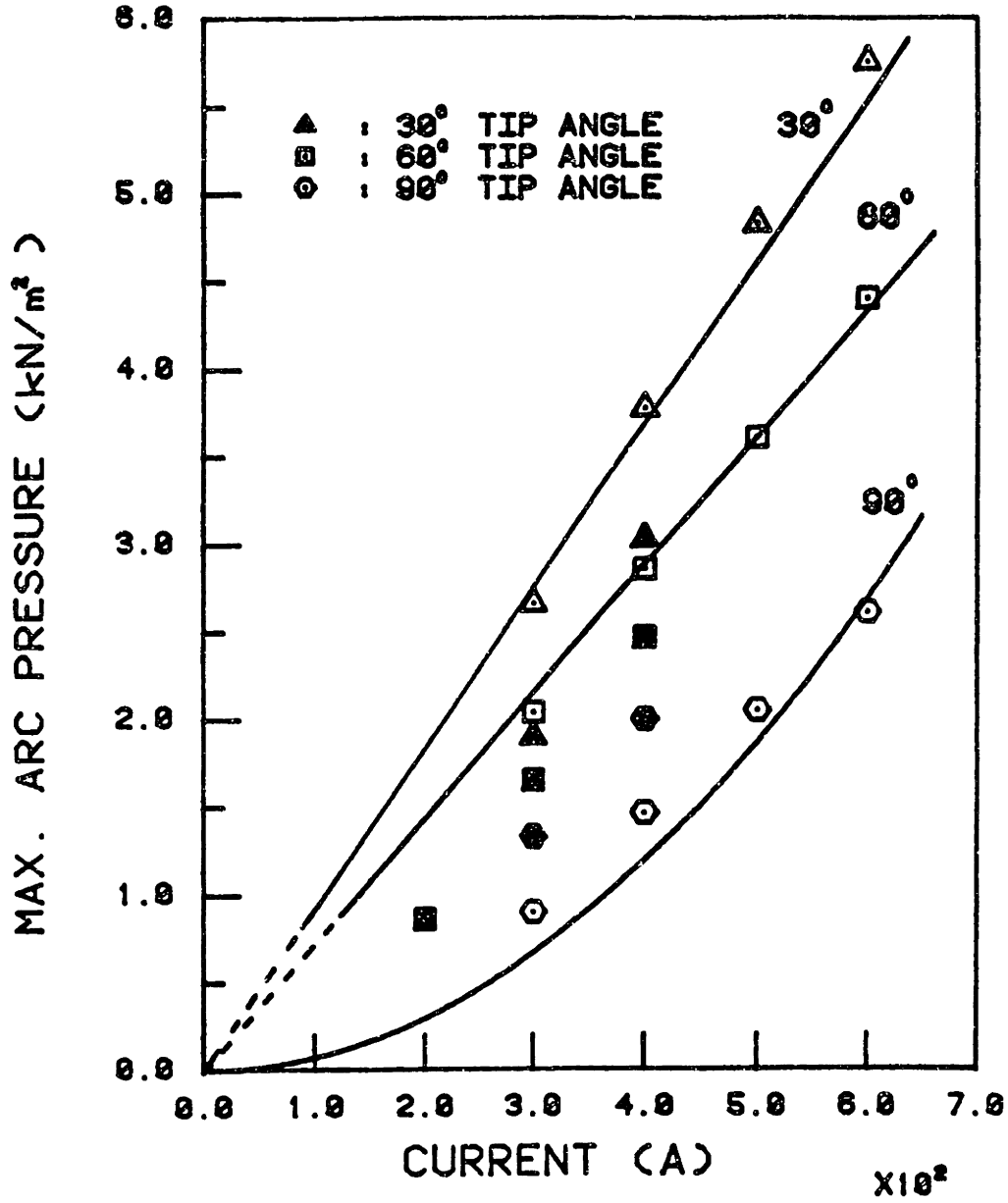

Figure 3.9 Maximum arc pressure vs. current at different electrode tip angles (89). Solid symbols represent data from reference (93) and hollow symbols represent data from reference (89).

Another way of analyzing arc pressure is to look at plasma jet velocity and treat arc pressure as the stagnation pressure of the jet being stopped by the weld pool surface. According to Bernoulli's equation for steady rotational flow along a streamline in an inviscid fluid:

$$p + 1/2\rho v^2 + \rho gy = \text{constant} \tag{3.42}$$

The ρgy term is negligible here, so we can write:

$$p_1 + 1/2\rho v_1^2 = p_2 + 1/2\rho v_2^2 \tag{3.43}$$

If subscript 1 represents a point a short distance above the weld pool and subscript 2 represents the surface of the weld pool, then:

$$p_2 - p_1 = (1/2)\rho v_2^2 \tag{3.44}$$

As expected, the pressure increase at the pool surface on the arc centerline is proportional to the plasma jet velocity squared. The plasma jet velocities calculated numerically in reference (85) are shown in figures 3.10 and 3.11.

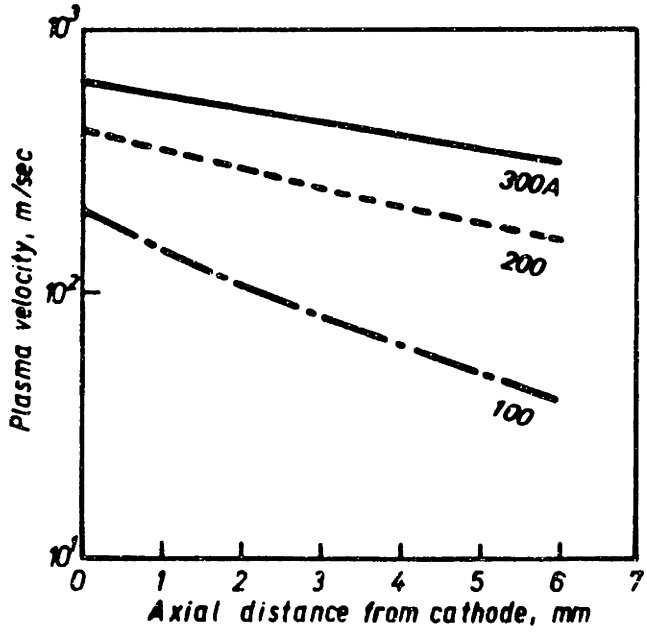

Figure 3.10 Plasma velocity along arc axis for straight polarity arcs in argon. (85)

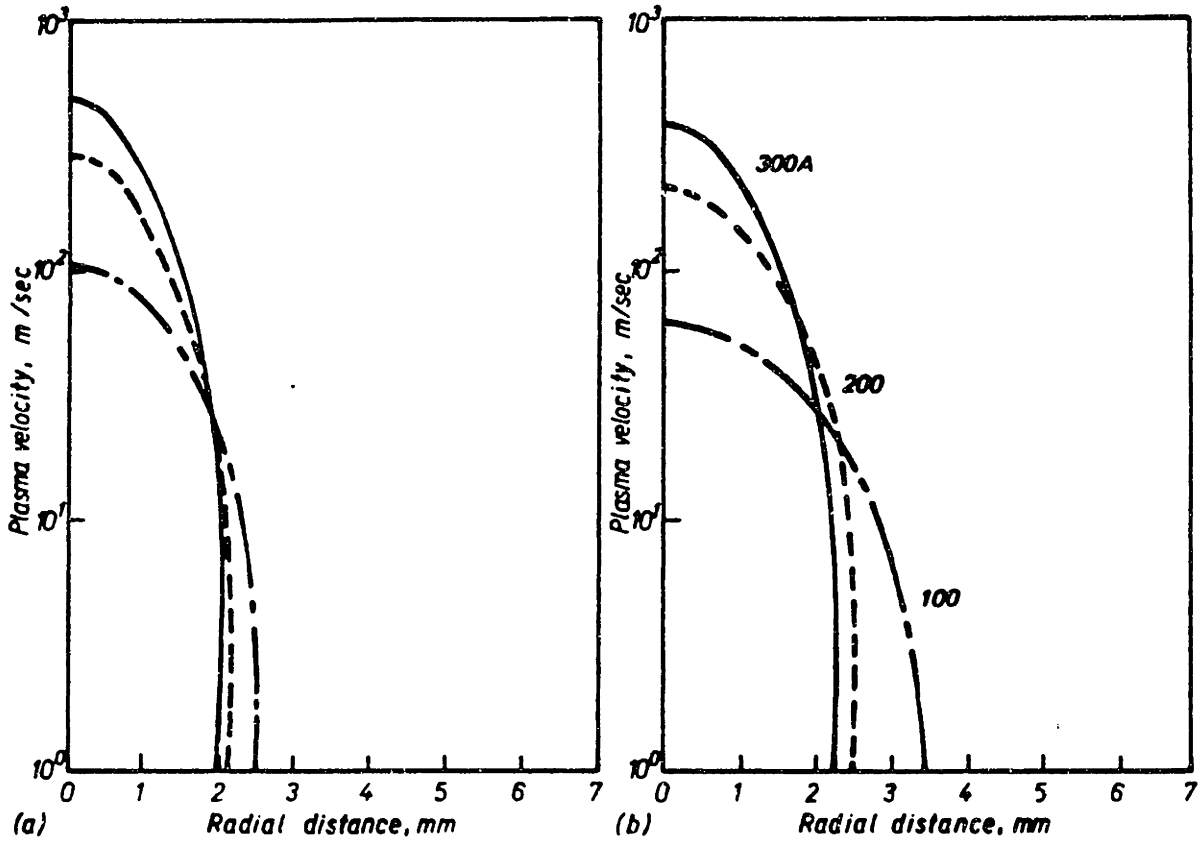

Figure 3.11 Plasma velocity radial profiles for straight polarity arcs in argon (a) 2 mm and (b) 4 mm from cathode. (85)

As shown in figure 3.10, the centerline velocity for a 300 A arc 5 mm below the cathode is approximately 370 m/s. Using a plasma density of 1.8×10^{-2} kg/m^3 (as listed in reference 85) the resultant pressure excess is 1230 N/m^2. The static pressure at the point just above the weld pool surface (p_1 in equation 3.44) must now be added to this, and it can be calculated from equation 3.29. The static pressure (above atmospheric) at the arc centerline is

$$p\ (r=0) = \frac{\mu I^2}{4\pi^2 R^2} \qquad (3.45)$$

Using the permeability of free space ($\mu = 4 \times 10^{-7}$ henries/meter) and a

radius of 3 mm at that point gives a pressure of 320 N/m^2. Thus:

$$p_2 = p_1 + (1/2)\rho v_1^2 = 320 + 1230 = 1550 \ N/m^2$$

This is slightly above but very close to the value of 1480 N/m^2 shown in figure 3.8. However, the stagnation pressure assumes that the fluid comes to a complete stop at the weld pool surface. In reality it does that only for the infinitesimally small point at which the streamlines separate. At all other points, the gas simply changes direction and moves radially outward, slowing down in the process. The streamlines for a 200A Argon arc were determined by computer simulation in reference (94) and are shown in figure 3.12.

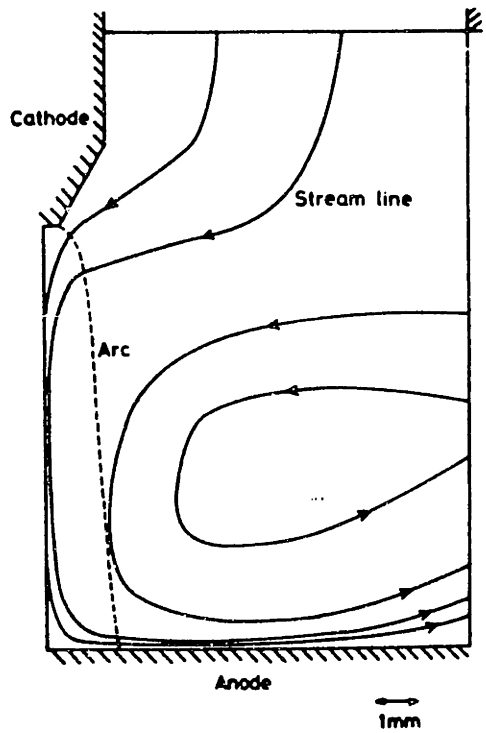

Figure 3.12 Computed flow pattern for a 10 mm straight polarity 200 A argon arc. (94)

If the gas velocity were to slow from 370 m/s to 150 m/s, the calculated pressure excess would be 1030 N/m^2 rather than 1230 N/m^2, and the total

pressure would be 1350 N/m^2. However, much of the velocity decrease is due to viscosity, and the decrease does not manifest itself in a higher static pressure. Making allowance for this would reduce the calculated pressure even further. Consequently, when this method is based on theoretical plasma velocities it would appear to somewhat underestimate the arc pressure. It would be wise, therefore, to compare the theoretical plasma velocities with those that have been determined experimentally.

The numerical and analytical calculations of reference (85) are compared to measured values in figure 3.13. The calculated velocities are slower than the measured velocities, especially for shorter arcs. This is

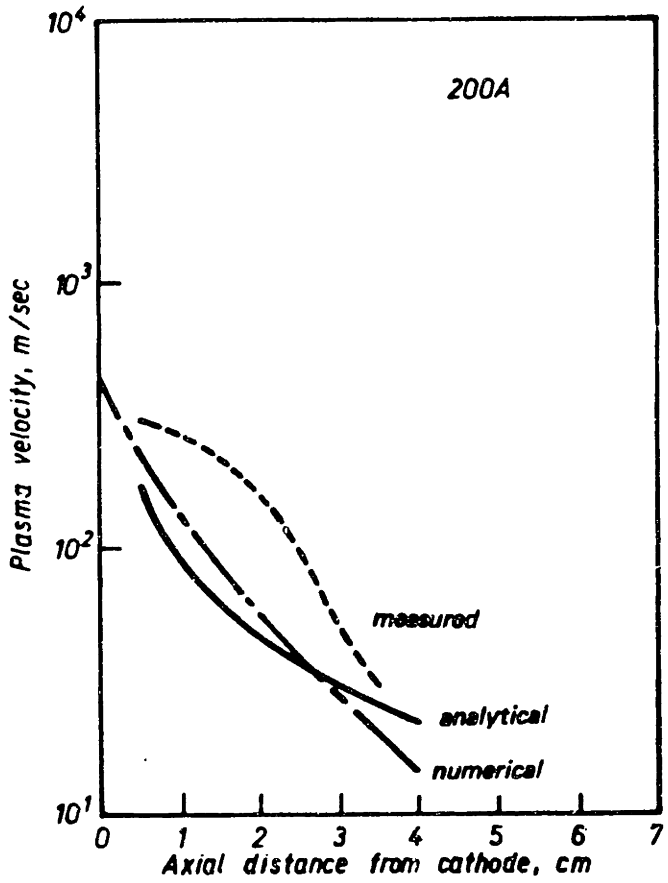

Figure 3.13 Comparison of calculated plasma velocities with measured velocities for a 200 A arc. (85)

believed to be due to the omission of thermal effects in the calculations. Inclusion of these effects would bring the calculated velocities closer to the measured velocities, and would increase the calculated stagnation pressure. Stagnation pressure is therefore a reasonable method of estimating the maximum arc pressure. From an accuracy standpoint, though, there is considerable uncertainty regarding thermal expansion, viscous losses, and the gas flow pattern on the workpiece surface, especially when applied to the irregular surface contour encountered in actual welds.

Additionally, the preceding analysis has been based on a straight polarity (electrode negative) GTA weld. When applied to a reverse polarity GMA weld, there are four major differences. First, there are metal droplets in the plasma. These will interface with the fluid flow and are likely to slow it down slightly as some plasma momentum is transferred to the droplets. Second, the GMA weld pool is much larger than in the GTA case, thereby changing the surface contour and flow pattern on the workpiece. It is difficult to predict how this will affect the arc pressure, especially since the surface contour is highly variable and largely unknown. Third, the electrode in GMAW is the anode rather than the cathode. Although most of the same analysis applies, the anode has a higher temperature than the cathode, giving rise to greater thermal expansion and higher plasma velocities. On the other hand, anode and cathode spot phenomena differ considerably. Cathode spots are much smaller, thereby causing a much larger current density with the resulting larger radial Lorentz force, and a larger radial current density with the resulting larger axial Lorentz force. Anode and cathode phenomena are so poorly understood, though, that it is difficult to assess the quantitative impact of this. Fourth, the electrode tip geometry in GMAW is much different from that in GTAW. Tip geometry has been shown to strongly

affect plasma velocity, as indicated in figure 3.14. The results in the figure are based on identical arc profiles for all three tips, meaning that tip geometry strongly affects plasma velocity independently of its effect on the arc profile.

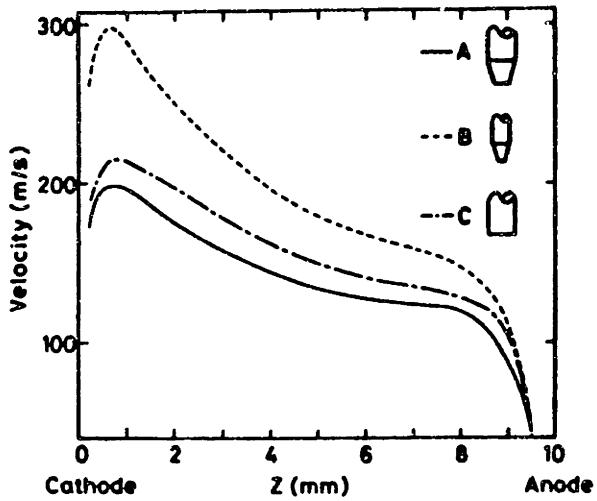

Figure 3.14 Plasma velocities along the arc centerline for various tip geometries. The arc shape was assumed to be identical in all three cases. (94)

Experimental pressure measurements have also shown a strong dependence on tip geometry. Lin (89) found that the maximum arc pressure increased with sharper tip angles, as shown in figure 3.15.

In GMAW, there is no such thing as tip geometry. The tip is molten, and its shape continuously changes in irregular and unpredictable ways. It is safe to assume that the plasma velocity and pressure are therefore lower than they would be from a sharp, well-defined tungsten electrode tip, but it is difficult to predict beyond that. The surface tension of the molten metal will always keep the surface somewhat spherical, which

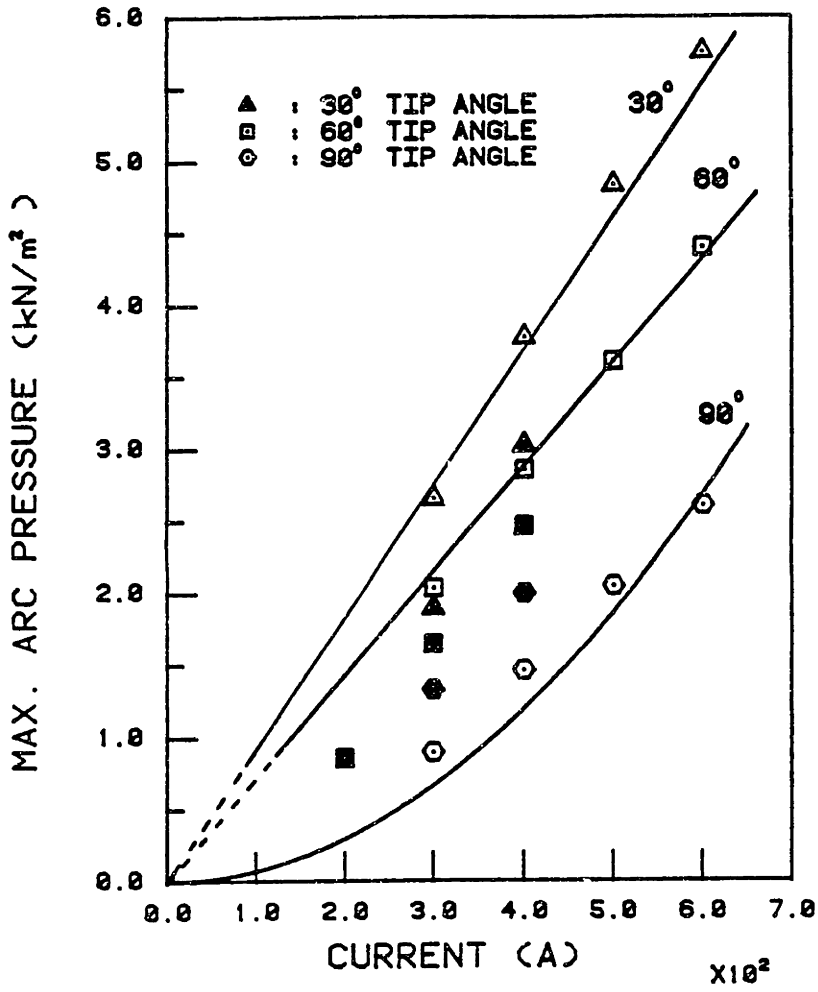

Figure 3.15 Arc centerline pressure versus current for various electrode tip geometries. (89)

would seem to be most closely approximated by tip A in figure 3.13. Figure 3.16 shows several GMAW tip geometries for a 250 A constant current weld in $Ar/2\%O_2$. Since a 250 m/s jet traverses a 10 mm arc in 40 μs, plasma velocity changes should easily keep up with tip geometry changes, which have characteristic times on the order of 1 ms. A quantitative description of those changes would require extensive numerical simulation.

To summarize the differences between GTAW and GMAW arc pressure, the GMAW plasma velocity will be theoretically lower due to tip geometry,

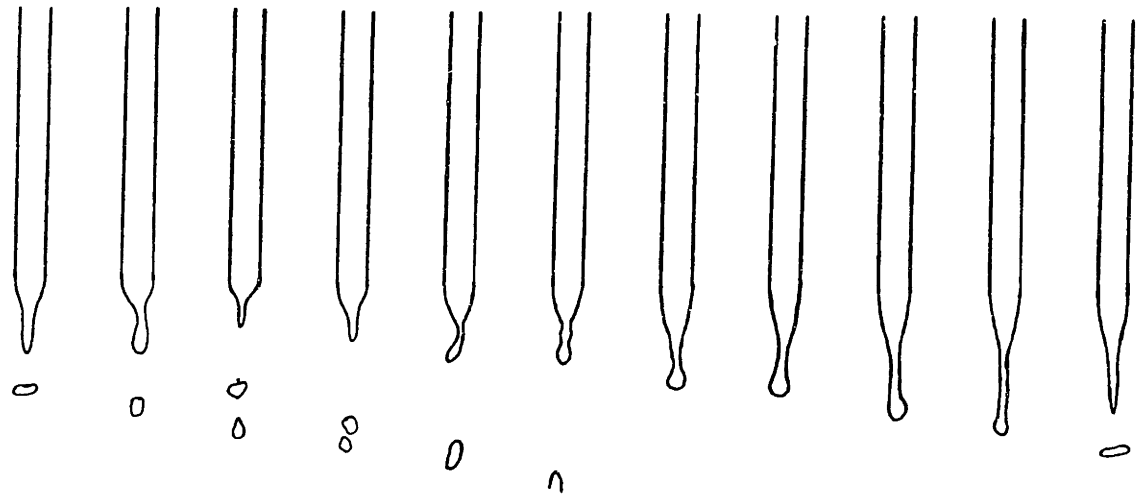

Figure 3.16 Tip geometries in 250A GMA weld in Ar/2%O_2 with .045" wire. Sketches are .25 ms apart.

lower anode current density, and flow pattern interference from the metal droplets. Conversely, there is greater thermal expansion due to the higher anode temperature. For a very short arc, this could conceivably make the arc pressure higher in GMAW, but for a long arc it is probably much lower. Unfortunately, the accumulation of metal on the workpiece prevents the gas metal arc pressure from being measured experimentally.

Given the preceding background on arc pressure, the next critical issue to address is the effect of arc pressure on weld pool surface depression and penetration. Figure 3.17 shows a hypothetical arc and the resulting surface depression. The diagram represents a condition of equilibrium among the forces of gravity, surface tension and arc pressure. There is also the impact of the metal droplets to consider in GMAW, but discussion of this will be reserved for section 3.6. Several investigators have studied the effect of arc pressure on surface depression. Lin (89) used calculus of variations to balance the work performed by the arc pressure with the changes in surface and

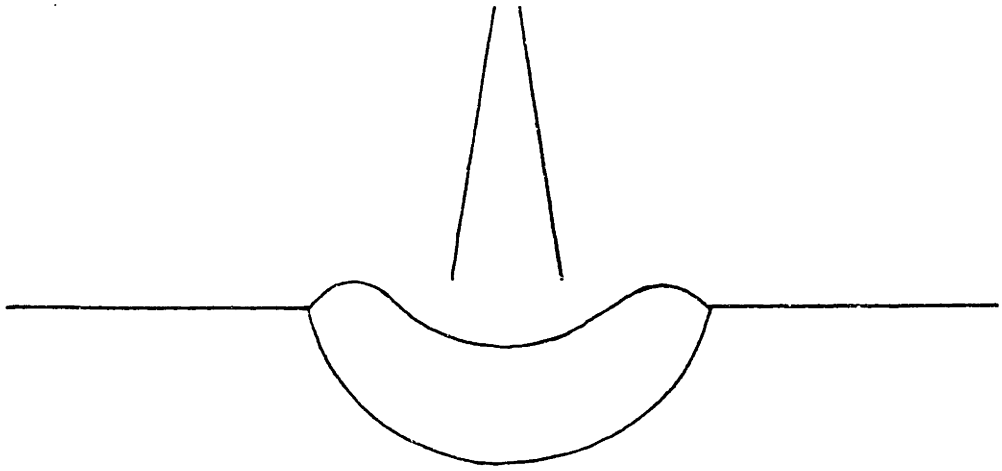

Figure 3.17 Weld pool surface depression from arc pressure.

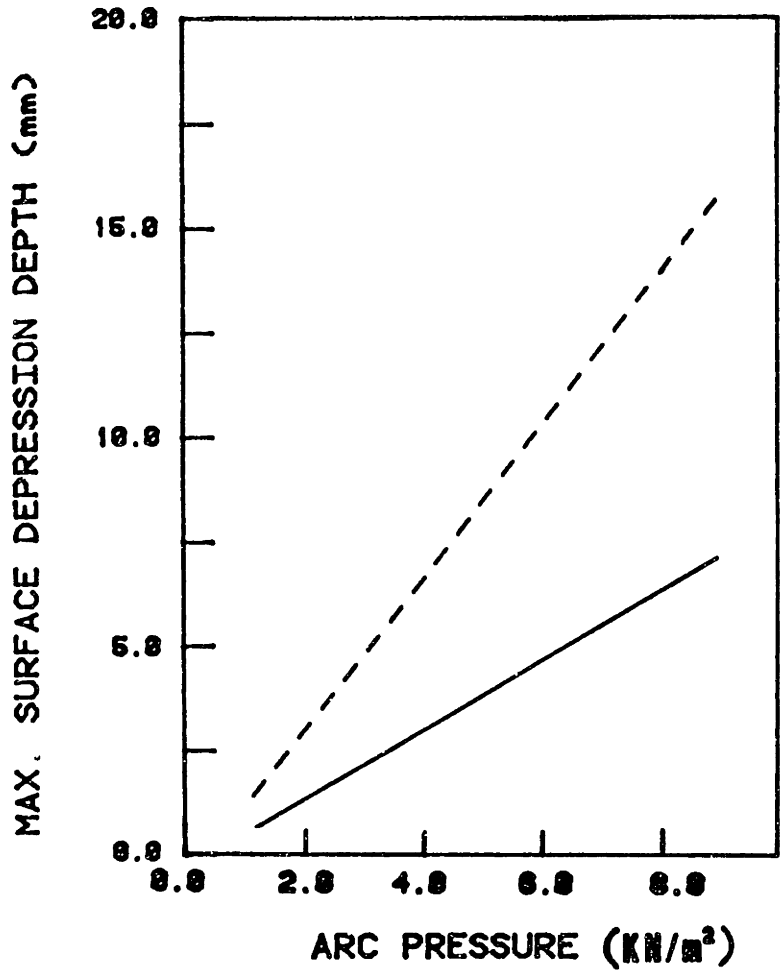

Figure 3.18 Maximum surface depression versus centerline arc pressure for steel (——) and aluminum (- - -). (89)

metallostatic potential energy that result from surface distortion. Using the arc pressure distribution for 300 amps shown in figure 3.8 and scaling up the magnitude, Lin determined the surface depression as a function of the pressure. Figure 3.18 shows the maximum surface depression versus centerline arc pressure.

What we are more interested in, though, is surface depression as a function of current. Using the measured arc pressure vs. current shown in figure 3.9 for a 30° tip angle, Lin (89) calculated the resulting surface depression profiles. The half profiles for a 10 mm diameter steel weld pool are shown in figure 3.19. Maximum depression can be seen to increase

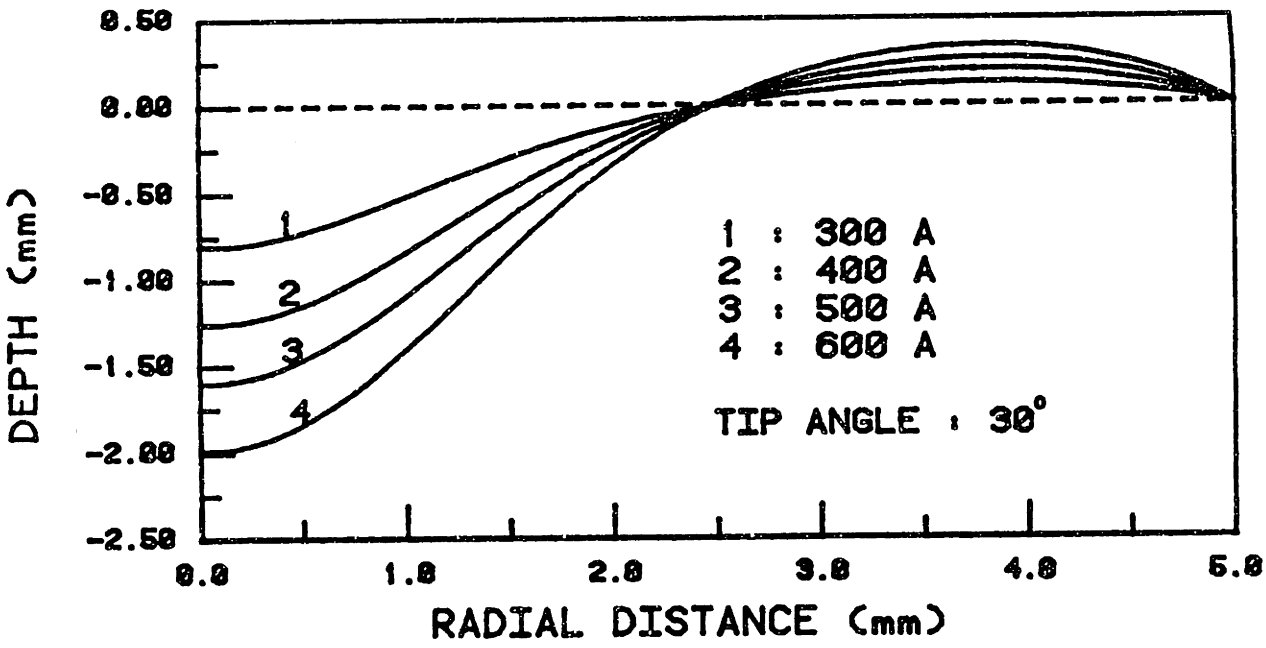

Figure 3.19 Surface depression half profiles calculated by Lin (89) assuming that the work performed by the arc pressure is reversible.

slightly faster than linearly with current. The increase in depression is

most closely approximated by $I^{1.35}$, which is somewhat faster than I ln I. Experimental measurements of surface depression versus current have yielded somewhat different results, but these will be reserved for section 3.4.

If current has a slightly higher than linear theoretical impact on surface depression, what impact does it have on penetration? Although a depressed surface would seem to allow delivery of heat closer to the pool bottom, for a gaussian heat distribution most of the heat goes into the pool sides and doesn't directly reach the bottom. This phenomenon is illustrated in figure 3.20. Lin (89) found that the penetration in a

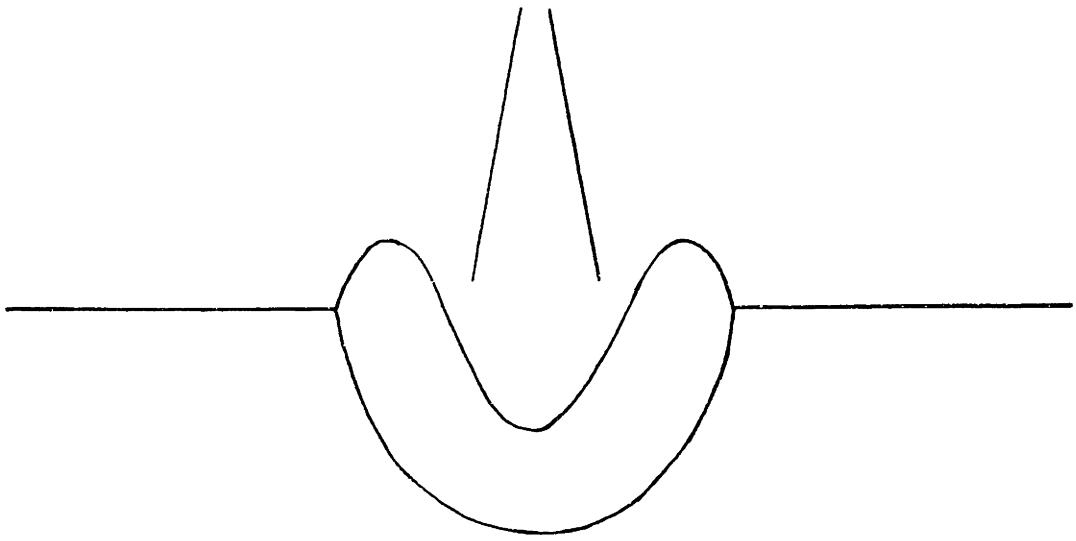

Figure 3.20 Delivery of heat to pool sides in a depressed weld pool.

285A GTA spot weld did not increase as the welding time increased from 3 to 24 seconds, indicating that the current was primarily entering the weld pool through the sides of the depression. Width continued to increase almost linearly with time. As a result, penetration is somewhat self limiting.

Three factors, however, differentiate an actual GMA weld from a stationary GTA weld. First, as will be discussed in section 3.6, the hot metal droplets are going to the bottom of the depression, so more heat is being delivered closer to the bottom of the weld pool. Second, due to metal transfer, the average surface of the weld pool is elevated, although this doesn't change the basic nature of the problem. Neither does the lower heat evolution at the workpiece of a reverse polarity weld. Third, the axisymmetric weld pool shown in figure 3.20 is not representative of a weld made with a moving arc. Such a weld is affected by the so-called scouring action, in which the arc force impinges on the front of the weld pool and pushes the liquid metal back. As illustrated in figure 3.21, the result is that the arc impinges on bare or nearly bare metal.

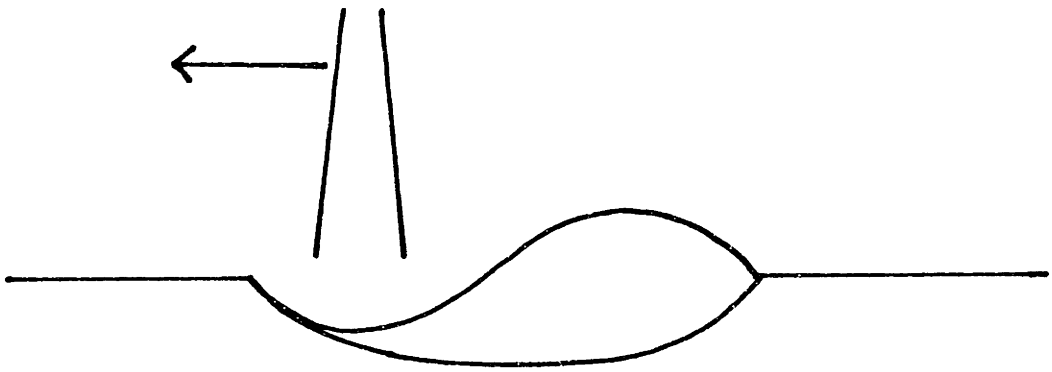

Figure 3.21 Scouring action in a travelling weld.

Ishizaki (95) describes two modes of penetration -- primary and secondary. Primary penetration results from the scouring action, whereby the arc directly "digs" into the bare base plate. Secondary penetration results from heat flow through the weld pool by a combination of conduction and convection. The amount of primary versus secondary penetration depends on the arc force, the travel speed, and the metal transfer rate. The end result is that penetration is not as self-limiting

as previously indicated, and penetration can be somewhat decoupled from deposition rate by proper manipulation of wire feed speed and travel speed. This technique will be discussed in section 7.4.

3.3.2 Effect of Current Pulsing

Current pulsing provides the capability to manipulate the effect of arc pressure on penetration through two phenomena: arc constriction and weld pool resonance.

Arc Constriction

The current flowing between the electrode and the workpiece must traverse a length of plasma which is characterized by its electrical conductivity σ. The resulting current density can be derived from fundamental electromagnetics:

$$\nabla \cdot \underline{J} + \frac{\partial \rho_e}{\partial t} = 0 \qquad (3.46)$$

This simply states that the rate of change of current density equals the rate of loss of charge per unit volume. For a neutral plasma, $\rho_e = 0$, leaving:

$$\nabla \cdot \underline{J} = 0 \qquad (3.47)$$

In a stationary conductor, the solution is given by the familiar equation:

$$\underline{J} = \sigma \underline{E} \qquad (3.48)$$

The electrical conductivity is a function of ionization, which in turn

is a function of temperature. Figure 3.22 shows the electrical conductivity of argon, helium, and air as a function of temperature. In a transient situation, it takes a finite time for the gas to heat up and

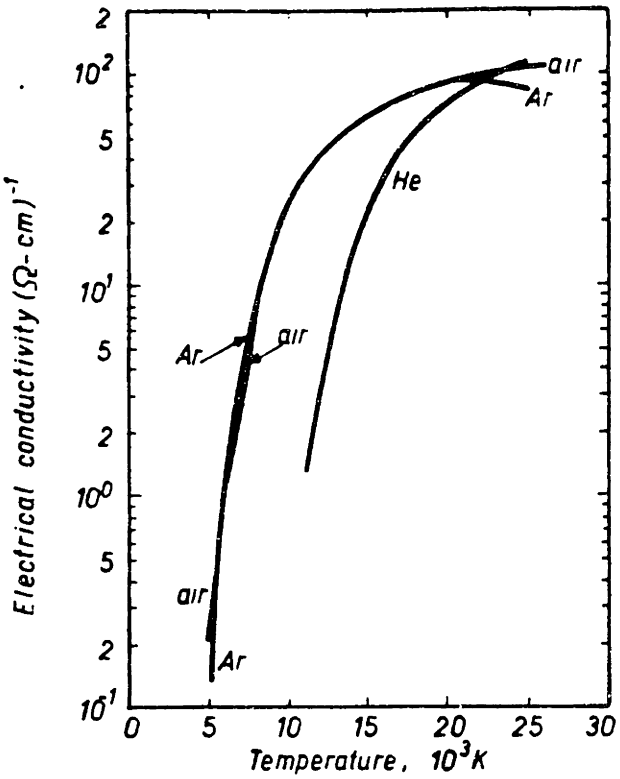

Figure 3.22 Electrical conductivities of argon, helium, and air as functions of temperature. (96)

ionize. Converti (87) studied the propagation velocity of luminosity (corresponding to temperature) when the current was pulsed in an argon arc. When pulsing from 70 to 128 amps with a 46.8° tungsten electrode, the velocity was 46 m/s. In general, the propagation velocity was independent of pulse amplitude but correlated strongly with average current:

$$\text{Propagation velocity (m/s)} \approx (1/2)\ I_{ave}\ \text{(amps)} \qquad (3.49)$$

For a 250A average current, this gives a propagation velocity of 125 m/s, which will traverse a 1 cm arc in 80 μsec. This equals the pulse duration of a 6.25 kHz square wave, meaning that above 6.25 kHz, the current channel has insufficient time to fully re-establish itself during the pulse. However, the photo-diode traces taken by Converti show that the increase in luminosity is a gradual rather than a step occurrence. Therefore, there is no threshold frequency below which the current channel fully develops and above which it does not. Rather, the current channel fully develops at low frequencies, but at higher frequencies it begins to fall behind and develop only partially. The current channel also maintains itself for a finite time after the end of the pulse. At very high frequencies, the size of the current channel ends up being an average of the background and pulse current steady state channels. Saedi (97) studied current channels with photo diode arrays. The results for an average current of 150 A are shown in figure 3.23. As the frequency

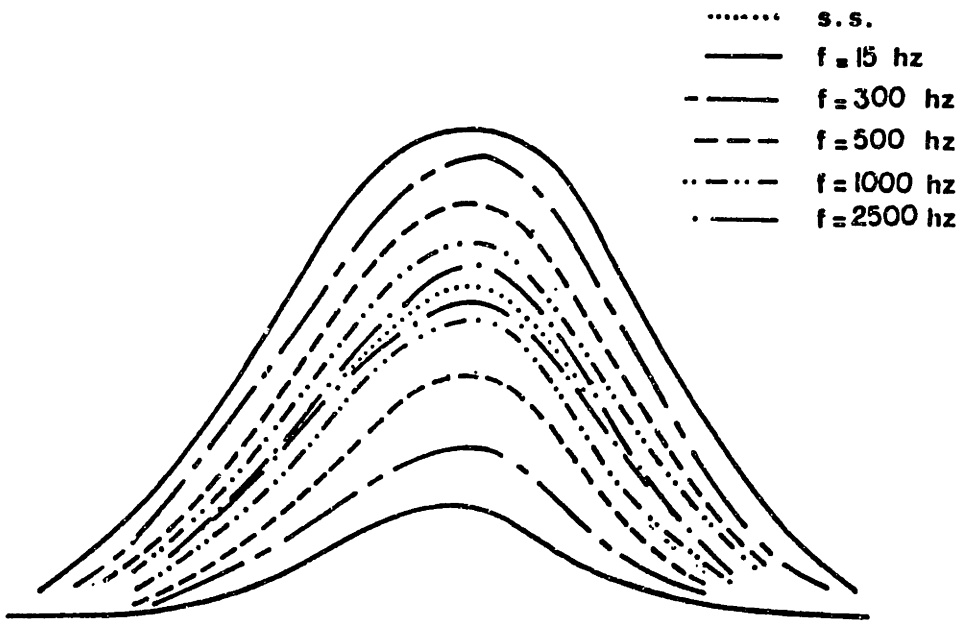

Figure 3.23 Photo diode array traces as a function of pulsing frequency. (97)

increases, the current channel approaches that of the steady state average current.

For example, consider a square wave current of 100/400 amps. At low frequencies, the current channel is that of a 100 A steady state arc during the background phase, and that of a 400 A steady state arc during the peak phase. At very high frequencies, the current channel will be that of a 250 A steady state arc. Since a 250 A current channel is narrower than a 400 A channel, the end result is a concentration of the arc. The peak current will deliver its force over a smaller area, resulting in a higher arc pressure and a deeper penetration. Yamaoto et al (98) measured arc pressure as a function of frequency for a 5/150 A pulsed arc with a 50 A mean current. Results are shown in figure 3.24.

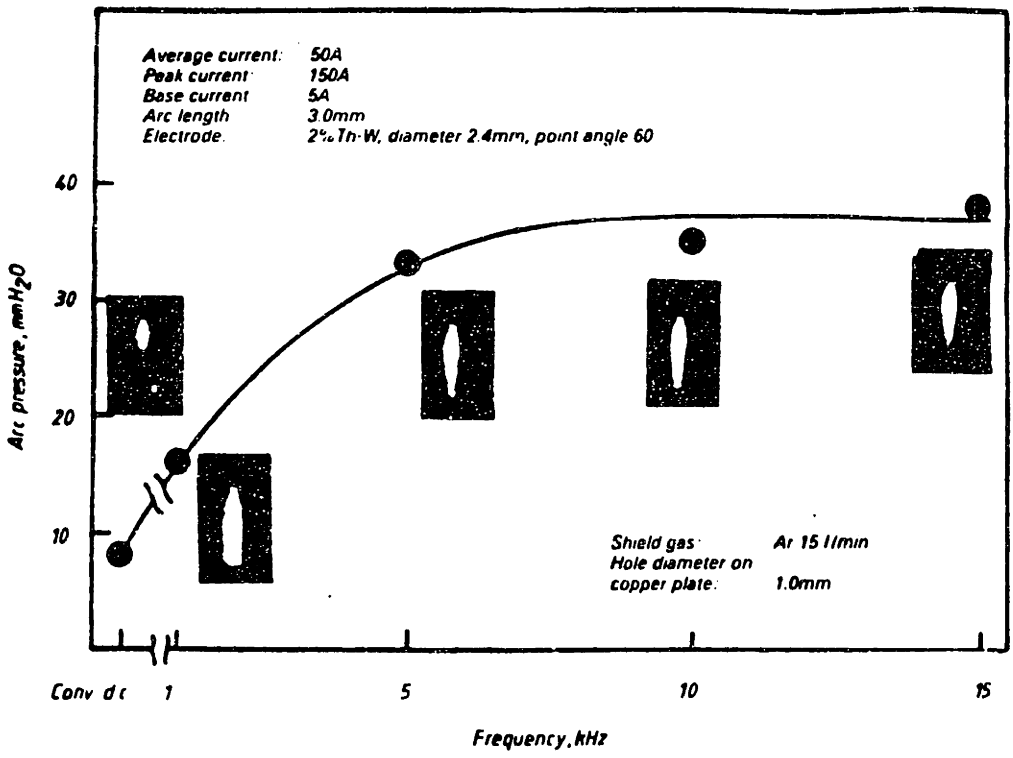

Figure 3.24 Arc pressure as a function of pulsing frequency. (98)

Pressure increases sharply up to 5 kHz, then remains constant after 8 kHz.

This increase in arc pressure should have an effect on penetration, and Saedi (97) has found that to be the case, as shown in figure 3.25. When pulsing with a 150 A mean current, he found almost a 25% increase in

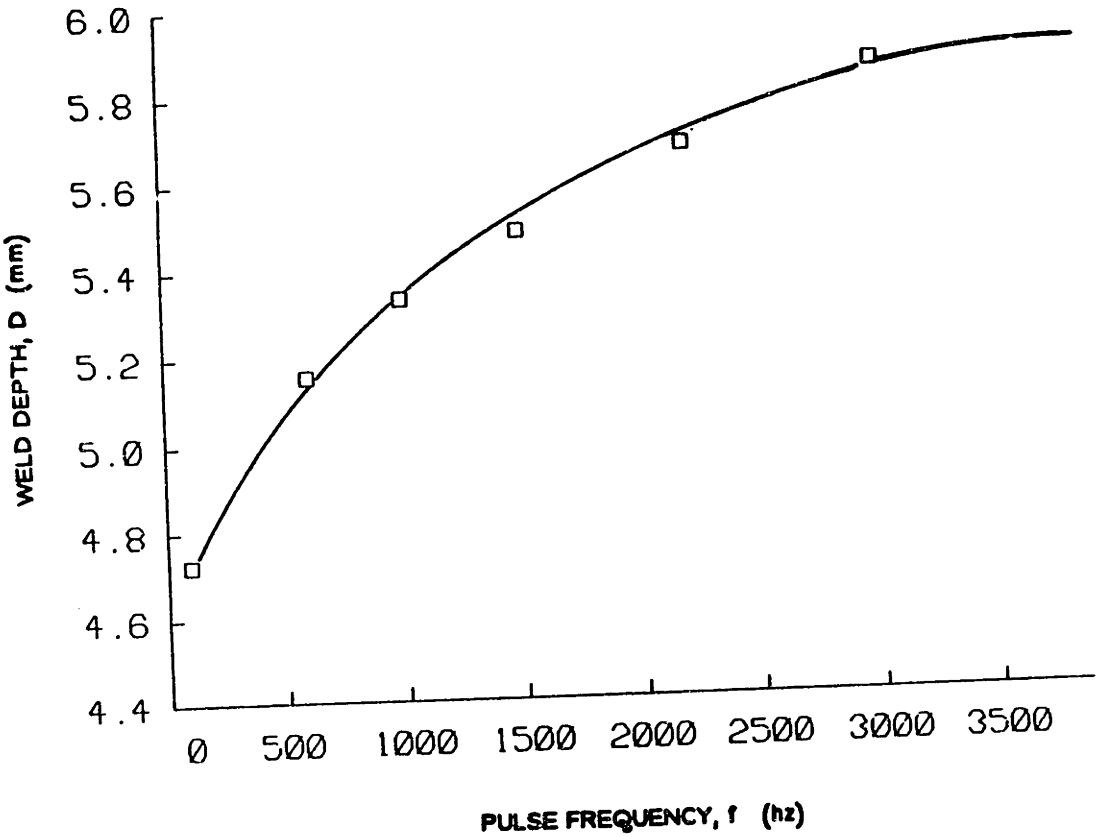

Figure 3.25 GTAW penetration as a function of pulsing frequency.

penetration when going from steady state to 3000 Hz, and it would appear to continue to increase moderately above that. It is clear, therefore, that at least under some circumstances, pulsing can increase the arc pressure and penetration of a GTA weld.

Other investigators have studied the effect of pulsing on the arc

without looking specifically at frequency. Converti (87) studied arc stiffness by analyzing and measuring the momentum of the plasma jet. Equation 3.33 showed that the arc force increases with the square of the current, and Converti concluded that the plasma jet momentum is proportional to the time integral of the square of the current. Since $\langle I^2 \rangle > \langle I \rangle^2$, pulsing gives a larger momentum than a steady state arc of equivalent mean current. Bachelis (99) similarly concluded that a pulsed tungsten arc deflects less than a steady current arc when an external magnetic field is applied, indicating that it has greater momentum. Kang (100) found that penetration increases as $\langle I^2 \rangle$ increases at a given heat input (i.e. fixed mean current).

It is impossible, though, to separate these effects from frequency, since they have their fundamental basis in the difference in time constants between various arc phenomena. Arc constriction results from the time constant of the adjustment of the current channel being slower than the pulse duration. It is therefore important to consider how the arc time constant is affected by the use of a consumable metal electrode. A consumable electrode adds metal vapor to the plasma, and this has a significant effect on conductance. Schellhase and Weinschenk (101) studied the transient characteristics of a consumable metal arc during the short time period immediately following a sudden arc cutoff. They identified two distinguishable processes characterized by two separate time constants. The first is the rapid collapse of the luminous arc column, characterized by τ_c, the thermal time constant of the arc column. The second is a slower variation in the shape of the arc due to persisting streams of metal vapor. This phase is characterized by τ_e, the thermal time constant of vaporization of arc attachment points. τ_c is approximately 6 msec, whereas τ_e is in the range of 50 to 100 msec,

meaning that metal vapors continue to boil off of the electrode surface and linger in the arc long after the plasma temperature (and therefore luminosity) has dropped substantially. Since metal vapors have a very low ionization potential, they maintain limited arc conductance long after it would have disappeared in a gas tungsten arc. Consequently, the arc current channel should be able to establish itself much more quickly in GMAW than in GTAW, and there might not be the same arc constriction that appears in pulsed GTAW. This will be experimentally checked in chapter six.

Weld Pool Resonance

Current pulsing results in pressure pulses impinging on the weld pool surface. If these pulses can be timed to arrive at the natural frequency of the weld pool, then there will be a resonant condition, the puddle motion will be amplified, and the penetration might increase substantially. The key factor is to determine the natural frequency of the weld pool, and various attempts have been made to do this, both analytically and experimentally. Converti (87) used a very generic approach to estimate the natural frequency as:

$$f_n \approx \frac{1}{2\pi}\sqrt{g/L} \tag{3.50}$$

where L is a characteristic pool dimension. A weld pool width of 1 cm gives a natural frequency on the order of 5 Hz.

Sorensen (102) did a more extensive analysis by developing both a lumped parameter and a distributed parameter model of the weld pool. Both models assume an axisymmetric weld pool with the center moving up and down in opposition to the outer region. The lumped parameter model treats the

weld pool as two capacitance elements connected by a resistance and an inertance, and the bond graph method was used to derive the following natural frequency:

$$\omega_n^2 = \frac{g}{D} \cdot \frac{1}{b^2(1-b^2)} + \frac{12\gamma}{\pi\rho D W^2} \cdot \frac{b^4 + 2(1-b^2)^2}{b^4(1-b^2)^2} \qquad (3.51)$$

g = acceleration due to gravity

D = weld pool depth

W = total weld pool width

W_1 = width of inner section of weld pool (which is moving in opposition to the outer section)

$b = W_1/W$

ρ = liquid metal density

γ = surface tension

The distributed parameter model assumes a cylindrical geometry for the weld pool and solves the governing partial differential equation subject to the applicable boundary conditions. The natural frequency was found to be:

$$\omega_n^2 = \left(\frac{7.66g}{W} + \frac{449\gamma}{W^2\rho}\right) \tanh\ (7.66D/W) \qquad (3.52)$$

Sorensen checked the accuracy of these solutions experimentally by exciting the weld pool of stationary welds with a current pulse and using Fourier transform techniques to analyze the resulting voltage spectrum and extract the natural frequency. The distributed parameter model predicts frequencies which much more closely match the experimental results. Although a depth term is included in the distributed parameter solution, that term is negligible. For realistic D/W ratios, tanh (7.66 D/W) is

very close to unity and can be neglected. The remaining solution contains a gravity term and a surface tension term, as did the lumped parameter solution, but the only remaining dimensional term is the weld pool width. Figure 3.26 is a graph of natural frequency versus width for a steel weld

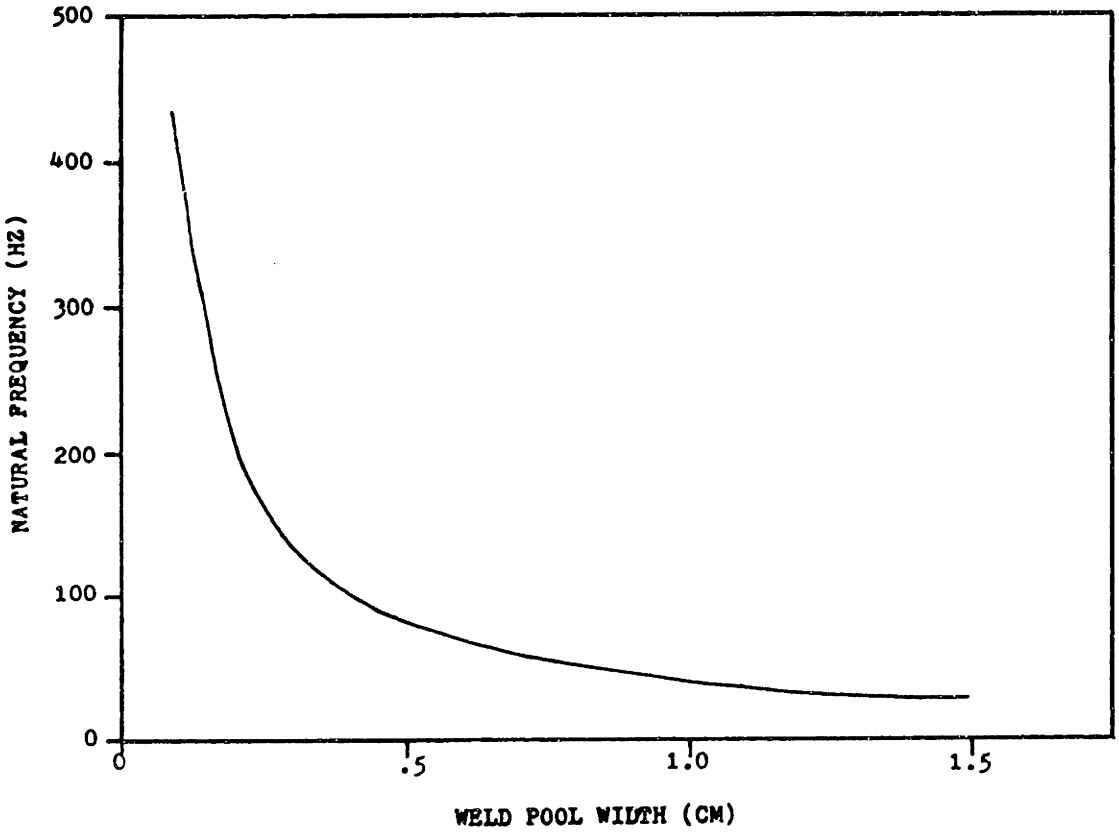

Figure 3.26 Weld pool natural frequency as a function of pool width based on equation 3.52 for steel, neglecting the finite depth correction.

pool. For typically sized weld pools (W = 1.2 cm) and γ = 1000 dynes/cm, equation 3.52 predicts natural frequencies in the vicinity of 34 Hz. There is, however, an important distinction between Sorensen's analysis and real welds, and that is that a real weld loses axisymmetry due to travel speed. A non-stationary weld pool is closer to an ellipse than a circle, and the arc force strikes the pool at one end rather than in the

center. Tam (103) modeled full penetration welds as thin membranes which must satisfy the wave equation:

$$\nabla^2 f = \frac{1}{c^2} \frac{\partial^2 f}{\partial t^2} \tag{3.53}$$

f = membrane displacement perpendicular to membrane plane

$c^2 = T/\rho$

T = membrane surface tension (1000 dynes/cm)

ρ = membrane surface density

This can be solved using separation of variables, yielding an infinite sum of Bessel functions and trigonometric terms. Each Bessel function order defines a distinct mode of vibration. The first mode is a gross up and down motion of the membrane, and its natural frequency is given by:

$$f_o = \frac{156}{W} \text{ Hz} \tag{3.54}$$

where W is the pool width in mm. In the second mode, one side of the membrane moves in opposition to the other, and the natural frequency is given by:

$$f_1 = \frac{249}{W} \text{ Hz} \tag{3.55}$$

For 12 mm wide weld pools, these give natural frequencies of 13 Hz and 21 Hz. These are noticeably lower than Sorensen's predictions, and this requires some explanation. Intuition would suggest a higher modal frequency for thin membrane, since mass plays a more significant role in a three dimensional distributed parameter model than it does in a thin membrane model, and larger masses give lower natural frequencies. Conversely, surface tension plays a much larger role in a thin membrane,

since it acts through the entire cross section of the mass. In Sorensen's model, surface tension acts only on the top surface of the pool. Since surface tension is equivalent to a spring constant in a dynamic system, greater surface tension involvement would be expected to give a higher resonant frequency. The lower frequencies found by the membrane model are attributable to two factors. First, the 13 Hz and 21 Hz modes are not what Sorensen modelled. He modelled the center moving in opposition to the outer ring, which is equivalent to the third or fourth membrane mode. The n^{th} modal frequency is defined by the zero of the n^{th} order Bessel function:

$$J_n \left(\frac{\omega_n a}{c}\right) = 0 \qquad (3.56)$$

where "a " is the pool radius and "c" was defined with equation 3.53. The third and fourth zeroes are at 5.135 and 6.379, giving model frequencies of 28 Hz and 35 Hz, respectively. The second factor is the value of surface density used by Tam. He defined surface density as volume density times thickness and used a 3.1 mm thickness, giving a surface density of 2.42 gm/cm^2. The 3.1 mm thickness is really beyond the limitations of the thin membrane model, so using it in that way gives an extremely high surface density and a lower natural frequency. The natural frequency varies as the inverse square root of surface density, so applying the thin membrane model to a membrane that really is thin would give a higher natural frequency, as expected.

Tam extended his analysis to moving weld pools by considering an elliptical membrane. The shape of the ellipse is characterized by the eccentricity, ϵ:

$$\epsilon = (1 - a^2/b^2)^{1/2} \tag{3.56}$$

a = minor radius

b = major radius

For a weld pool in which b = 1.5a, ϵ = .75 and the natural frequencies of the first two modes are given by:

$$f_o = \frac{136}{W} \text{ Hz} \tag{3.57}$$

$$f_1 = \frac{191}{W} \text{ Hz} \tag{3.58}$$

W now corresponds to 2a, the transverse width of the weld pool. A 12 mm width gives 11 Hz and 16 Hz for the first and second modes, respectively. These are slightly lower than for the circular membrane, and as the pool becomes more elongated and the eccentricity increases, the natural frequencies will continue to decrease. The effect is much more pronounced for the second mode, in which the two halves of the ellipse (separated by the minor axis) are moving in opposition to one another. This mode should accurately represent the action of the weld pool surface in a moving weld with current pulsing.

Tam's and Sorensen's models give reasonably close frequency predictions when applied to identical modes. Two conclusions can be drawn. First, the modal frequencies of an ellipse are lower than those of a circle. This is partly because the width of the ellipse is taken as the minor diameter, so the ellipse has a larger mass than a circle with the same width. The ellipse has a higher natural frequency than a circle whose diameter equals the major diameter of the ellipse, since the circle

has a larger area and mass in that case. However, for the oscillatory modes that could be expected in an actual weld, it is more realistic to compare the smaller circle with the ellipse. These expected modes are the additional reason that ellipse frequencies are lower. A circle excited at its center would oscillate with the entire membrane moving up and down in phase. While this mode is feasible for a full penetration weld in thin sheet, it is not possible for a partial penetration weld. Nor is it possible for a full penetration weld in which penetration occurs through a narrow root gap. For these welds, the surface center area will move in opposition to the surface outer area, which is a higher mode with a correspondingly higher frequency. An elliptically shaped weld pool, on the other hand, is excited at on end, and the resulting sloshing motion is a lower mode with a correspondingly lower frequency. Hence, a moving weld should have a lower natural frequency than a stationary weld.

The second conclusion is that frequencies on the order of 20 Hz or less should be expected for elliptical welds oscillating in the second mode (sloshing). It is difficult to predict the frequency of actual welds, since the geometries involved will be irregular and complex, and other modes could be excited. Nevertheless, there should be some oscillatory motion corresponding to the sloshing mode, and it should occur at a frequency in the general vicinity of 10 to 20 Hz.

Richardson and Renwick (104) studied stationary GTA weld pool oscillations experimentally in a manner similar to Sorensen. They excited mild steel weld pools with 3.5 ms current pulses superimposed on base currents of 50 to 100 A. Oscillations were determined by changes in arc voltage. For weld pools ranging from 3.73 to 7.21 mm in width and 1.27 to 4.93 mm in depth, the measured frequencies ranged from 130 to 393 Hz,

with maximum vibration amplitudes of approximately .4 mm. Their best curve fit to weld pool geometry came from the frequency being proportional to the inverse of the square root of width times depth. Thus, depth played a major role, compared to the negligible effect it had in Sorensen's analysis. Assuming a surface tension of 1000 dynes/cm, Sorensen's analysis predicts 55 Hz and 130 Hz for the 7.21 mm and 3.73 mm welds, respectively, which are considerably lower than what was observed. Assuming a higher value for surface tension, which is certainly possible, would increase Sorensen's predications, but they would still be fairly low. Sorensen's own observed frequencies were higher than his predicted frequencies in the range above 100 Hz up to 200 Hz, so modelling error might play a role too. Additionally, Richardson and Renwick could not identify the mode of oscillation from their high speed films. Although it seems reasonable to assume the mode would have been the same as in Sorensen's, they used helium shielding whereas Sorensen used argon. Helium's lower density and higher thermal conductivity could change the arc force enough to affect the modal shapes and therefore the modal frequencies.

This same reasoning could lead to different frequencies in actual GMA welds. The metal transfer will elevate the surface of a GMA bead on plate weld, thereby changing the modal shape as shown in figure 3.27 for the axisymmetric mode and in figure 3.28 for the sloshing mode. The elevated surface will increase the angle through which the surface tension force works at the pool edge during half the cycle, and it will decrease it during the other half. Since the vertical component of that force depends on the sine of that angle, the largest rate of change of the force with respect to the angle occurs at small angles, and the half cycle angular decrease will have a larger effect than the half cycle angular increase.

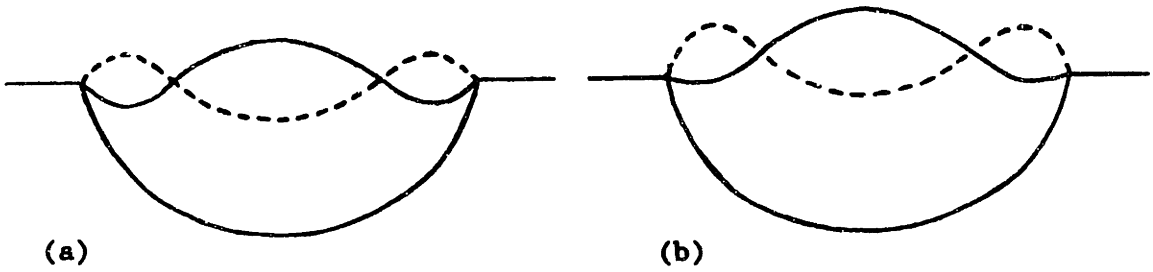

Figure 3.27 Weld pool surface oscillatory modal shapes for axisymmetric stationary welds: a) GTA, b) GMA.

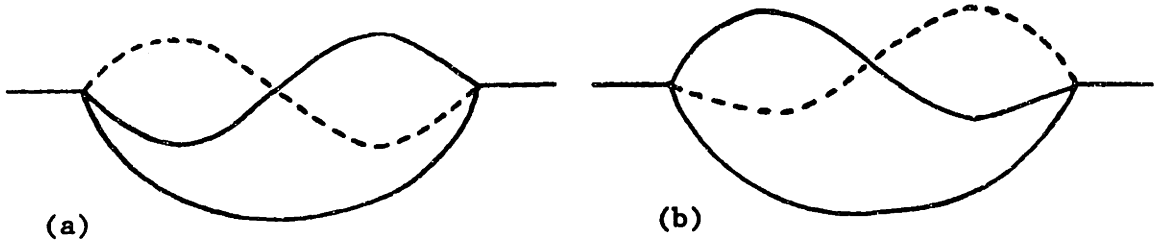

Figure 3.28 Weld pool surface oscillatory modal shapes for sloshing mode in moving welds: a) GTA, b) GMA.

The net result is a lower effective spring constant and a lower frequency. In a V-groove, the metal transfer elevates the surface but does not change the angle at the pool's edge. When welding over a tack weld, the geometry could become extremely complex, and it is very difficult to predict the effect on modal shapes and frequencies. If the tack weld were small relative to the groove and relative to the metal transfer rate, the edge angles would not change. If the tack weld were relatively large, though, it would be similar to the bead on plate situation. Industrial welds are further complicated by the irregularity of the shape of the tack welds and the metal transfer in GMAW. This metal transfer adds another force to the weld pool surface, and gives GMAW the ability to excite more modes than GTAW.

3.4 Compound Vortex

3.4.1 Theory

If arc pressure alone were responsible for surface depression and penetration, then these would increase in a very smooth manner with current. However, researchers have found otherwise. Chihoski (105) found that penetration in GTA welds increases sharply from 200 to 300A and moderately above 450A, but that there is very little increase in penetration from 100 to 200A and almost no increase from 300 to 450A. These results are shown in figure 3.29. Chihoski explains these results

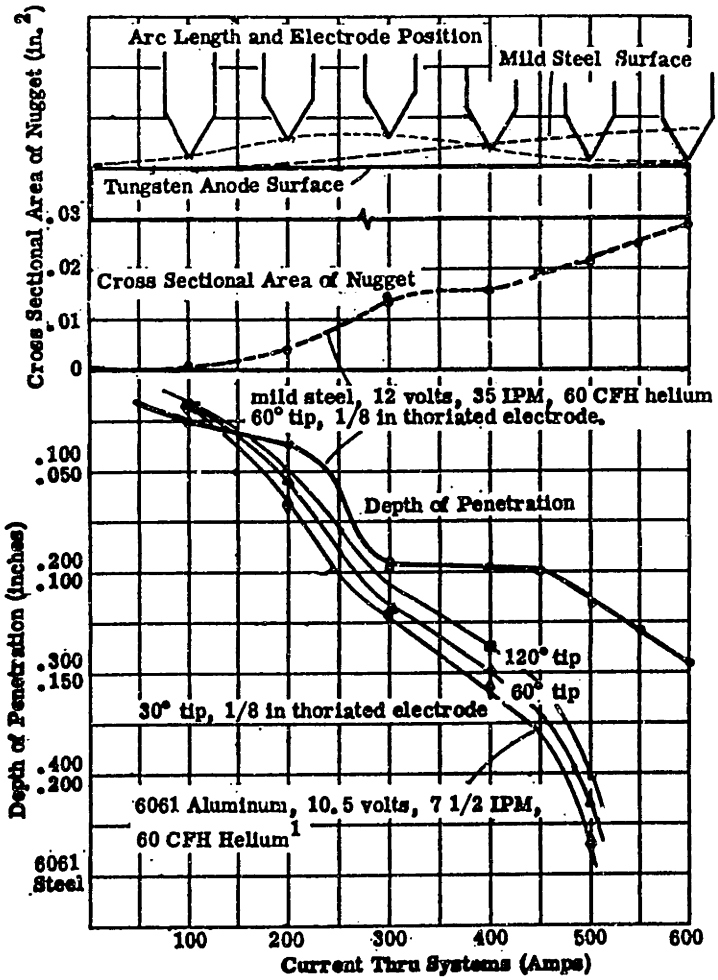

Figure 3.29 GTAW penetration and cross sectional area as a function of current. Mild steel, 12V, 35 ipm travel speed, 60 cfh He, 1/8" thoriated tungsten electrode with 60° tip. (105)

as a consequence of the reapportionment of heat distribution that occurs as the current varies.

Lin and Eagar (107) measured surface depression as a function of current, with the results shown in figure 3.30.

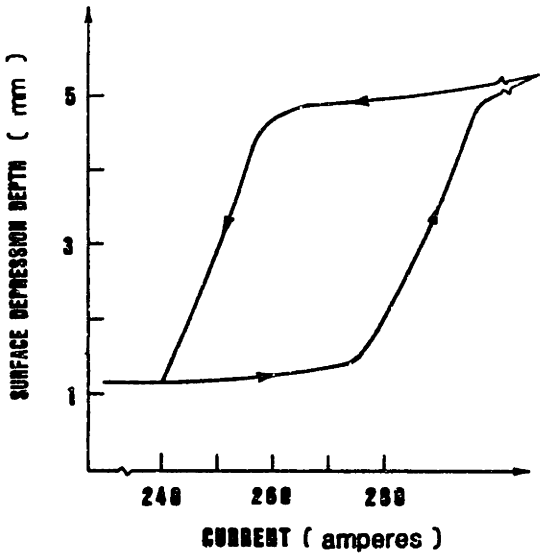

Figure 3.30 GTAW surface depression as a function of current. (106)

Similarly to Chihoski, they found a steep increase around 260A, but they attribute it to the formation of a compound vortex. The remainder of this section will discuss the vortex, then compare it to Chihoski's explanation of the sudden penetration increase phenomenon.

The implications of current flowing through a liquid metal conductor have been studied by various researchers (107, 108, 109), and magnetohydrodynamic theory predicts a toroidal fluid flow pattern for an axisymmetric geometry and current. There will be an accompanying circumferential flow, but it will be very slight for the purely symmetric

case. The asymmetry involved in a real weld, however, increases the circumferential flow to the point where a sink effect develops above a certain current level. Lin and Eagar model this effect as a compound vortex, shown in figure 3.31. The compound vortex is an inner forced

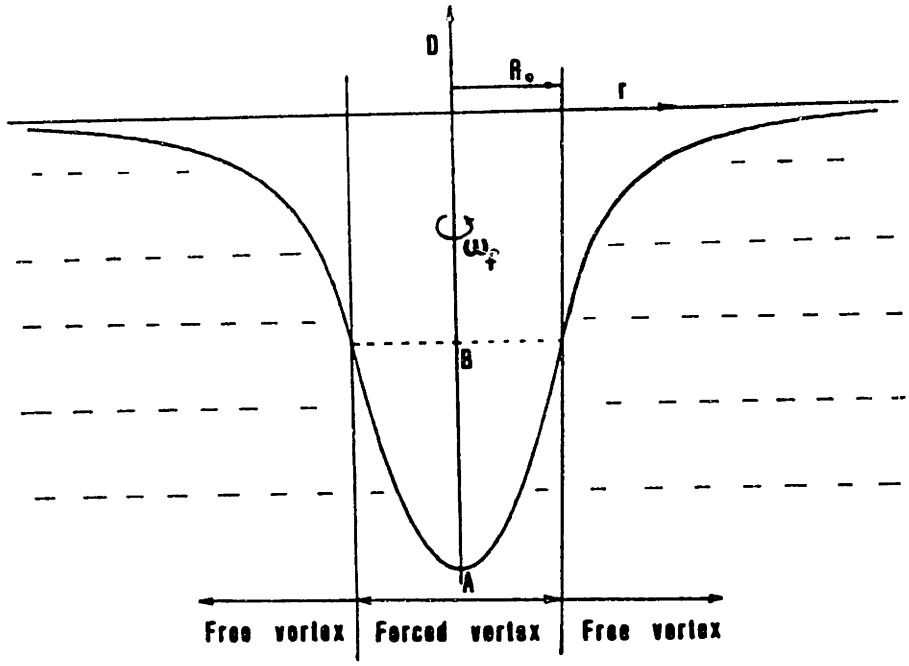

Figure 3.31 Compound vortex model. (106)

vortex with constant angular velocity surrounded by an outer free vortex with constant angular momentum.

Forced vortex velocities of 20 to 30 revolutions per second (with a 1.5 mm forced vortex radius) produce surface depressions of 4 to 8 mm, which could explain the sudden deep surface depression observed experimentally. Heiple et al (110) used high speed cinematography to observe the motion of aluminum oxide particles on the surface of weld pools. The average velocity of 17 particles was 94 cm/sec, which is even larger than the surface velocity arising from a compound vortex. However, this measured velocity was radially inward due to an imposed

surface tension gradient, as will be discussed in section 3.5. It was not a circumferential velocity, so even though it demonstrates that large surface velocities do occur in welds, it does not directly support the compound vortex theory. Compound vortex theory is supported, however, by magnetohydrodynamic theory, by other high speed movies which have shown circumferential flow, and by surface depression observations. Although radial flow will significantly affect penetration, it will have only a minor effect on surface depression. The compound vortex, therefore, appears to offer a reasonable explanation of the observed changes in surface depression with current. It also fits well with the hysteresis phenomenon shown in figure 3.30, since, intuitively, it would take a larger current to form a vortex than to keep one going.

The compound vortex also agrees with Chihoski's observations. Chihoski used a 12V constant potential system which maintained voltage by adjusting arc length. At very low currents, the arc is relatively cool, so the ionization is low and the arc resistance is high. 12V is therefore maintained with a very short arc length. As current increased to 200A, the arc temperature increased, the arc resistance decreased, and the arc length had to increase to maintain 12V. That increase in arc length explains the relatively flat penetration from 100A to 200A. Understandably, weld width increased 330% from 100A to 200A, which demonstrates that the longer arc was simply spreading out. Penetration more than doubled in going from 200A to 300A, while arc length remained essentially constant. Any decrease in arc resistance was evidently offset by an increase in the voltage drop in the electrode. Since Chihoski had no data points between 200A and 300A, it is very possible that the increase in penetration was precipitous, as would be predicted by compound vortex theory. From 300A to 450A, arc length shortened due to increasing

voltage drop in the electrode, yet the penetration remained constant. This region provides a strong argument for the vortex. Arc pressure is increasing substantially in this region, due to both the increasing current and the decreasing arc length. Penetration remains constant, though, because the vortex has already depressed the weld pool surface far beyond what arc pressure would be capable of, and the current is now being conducted into the sides of the depression. Hence, there is not sufficient heat delivery to the bottom of the depression to cause further melting, and the vortex has "bottomed-out" on solid metal. Above 450A, the increasing current together with the continued decrease in arc length results in a higher arc pressure that eventually dominates the vortex. The higher plasma jet velocities deliver sufficient heat to the depression base to cause further melting, and penetration increases.

Thus, Chihoski's results are entirely consistent with the compound vortex theory. One point that warrants mention, though, is that Chihoski used a travel speed of 35 ipm (14.8 mm/s). This does cast some doubt as to whether a vortex was able to form, since the scouring action at that travel speed is rather severe. A strong vortex requires some asymmetry, but it also requires molten metal on all sides of the arc. If all penetration is of the primary mode described by Ishizaki (95) then the arc is impinging on bare metal and a vortex cannot form. The short arc lengths used by Chihoski should have resulted in very rapid weld pool and vortex formation, so 35 ipm might still have been within the travel speed limits for vortex formation.

The metal transfer in GMAW will have three effects on the compound vortex. First, the larger weld pool will allow vortex formation at higher travel speeds. Second, the metal droplets will deliver heat to the bottom

of the vortex, thereby continuing to increase penetration in the 300A to 450A range. Third, the impinging droplets will cause some disruption of the circumferential flow pattern. At 20 to 30 revolutions per second, though, the vortex should be stable enough to withstand a reasonable amount of disruption.

3.4.2 Effect of Pulsing

In order to excite the vortex with current pulsing, the peak current must obviously be above the vortex formation threshold level, and the peak duration must be long enough to allow the vortex to form. No known direct study of vortex formation time has been done, but Lin (89) did study frequency effects on penetration in pulsed GTAW. His results, shown in figure 3.32, reveal a substantial peak at 10Hz. He attributes this peak

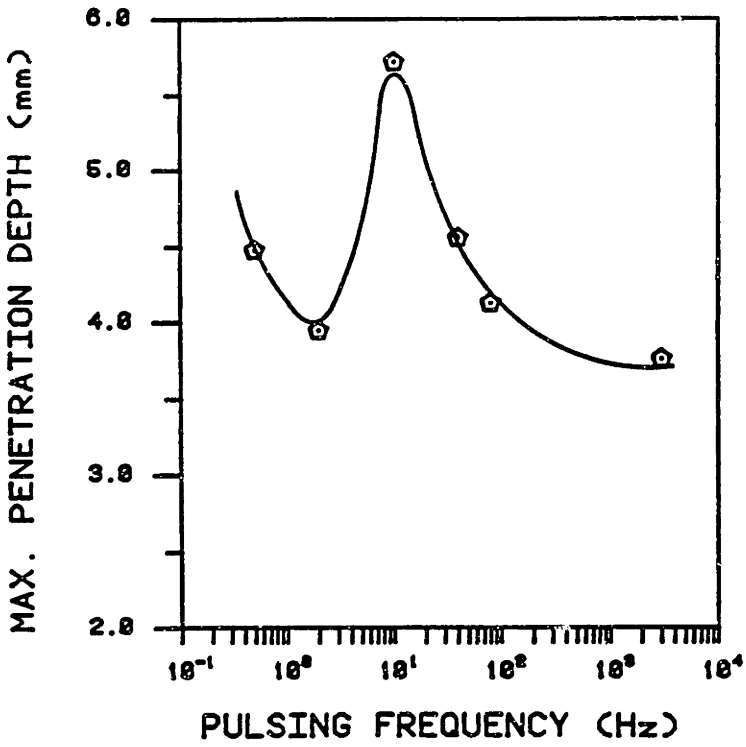

Figure 3.32 Frequency effects on GTAW penetration. (89) I_b=100A, I_p=300A, 80% duty cycle (80% at 300A, 20% at 100A), 1.2 mm/s travel speed.

to oscillatory sloshing of the weld pool, which high speed cinematography revealed. The 20 msec base period was insufficient to allow the cavity under the arc to fill in, and there was substantial heat delivery to the bottom of the pool. He attributes the slight increase at .5Hz to the formation of a vortex. The peak period at 5Hz (80% duty cycle) is 1.6 seconds. If it takes that long to form a vortex at 300A, then there is no way a vortex could have formed in Chihoski's work, since his torch traveled 23.7 mm during that time period. It is possible that the vortex can form much faster than Lin found, but that the sloshing motion prevented it.

Lin also tried a 20% duty cycle and found that the weld pool wouldn't respond at frequencies above 80Hz. Thus, a 2.5ms pulse would appear to be too short to permit excitation of any pool motion.

Intuitively, the vortex should form more rapidly at higher currents. Millere et al (109) characterize the electrovortex flow with a parameter that is proportional to current squared, and they characterize the speed of rotation with a parameter that is proportional to current. It is not clear how formation time should be characterized, but it is reasonable to assume that it decreases at least proportionately to the inverse of current, and possibly to the inverse squared. Regardless, vortex formation will evidently not occur at high frequencies, and it might even be restricted to low frequency pulsing.

3.5 Pool Convection

3.5.1 Theory

Convection plays a significant role in determining the heat flow and temperature distribution within the weld pool. It therefore strongly

affects the isotherm locations and the weld pool geometry. Pool convection has three sources: electromagnetic forces, buoyancy forces, and surface tension forces.

The electromagnetic force is identical to that described in section 3.3.1, except that the conducting medium is the molten metal rather than the hot plasma. The Lorentz forces cause an inward and downward motion of the molten metal, producing the convection pattern shown in figure 3.33.

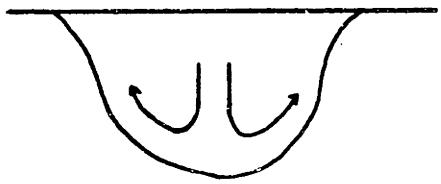

Figure 3.33 Convection pattern resulting from electromagnetic forces.

The hot metal directly under the arc center is drawn down to the pool bottom, and penetration increases.

Buoyancy forces are the result of density changes that occur along temperature gradients. Since the top of the pool is hotter, it is also less dense, and the buoyancy force acts upward, particularly near the centerline axis where the temperature gradient is steepest. Buoyancy will tend to produce a flow pattern opposite to that shown in figure 3.33.

Surface tension forces occur when surface tension varies with temperature. The surface of the weld pool is much hotter at the center than around the edges. If the surface tension increases with temperature, then the higher surface tension in the center will pull the liquid metal radially inward along the surface. If the surface tension decreases with

temperature, then the higher surface tension along the pool edge will pull the surface liquid metal radially outward. A positive surface tension gradient will therefore give the convection pattern shown in figure 3.34a, while a negative surface tension gradient will give the pattern shown in figure 3.34b.

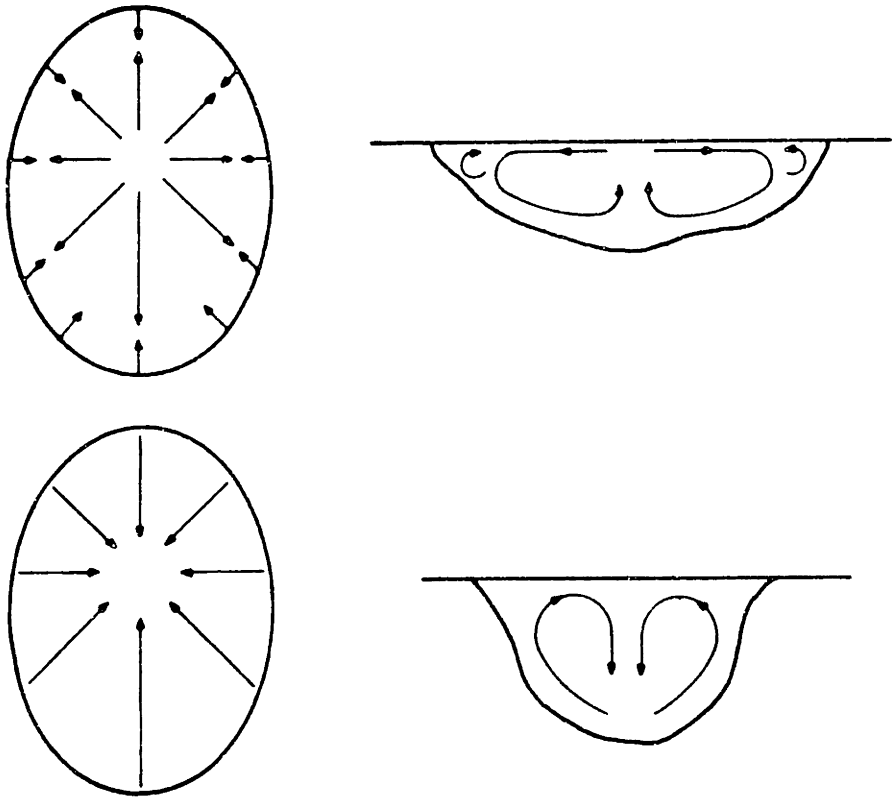

Figure 3.34 Convection patterns due to surface tension
a) positive gradient, b) negative gradient. (111)

Pure iron has a negative surface tension gradient, but the addition of impurities can create a positive gradient. Sulfur has generally been found to have the strongest effect of the common minor elements. Phosphorous and silicon also create positive gradients. Interestingly, these elements in combination have less effect than they do individually (111). Since a positive gradient causes deeper penetration, high quality steels with very low levels of impurities frequently exhibit poor penetration characteristics. The halides are also known to significantly

increase penetration. For example, zircaloy-2 produced by the vacuum melt method has lower levels of chlorine and hydrogen than that produced by the inert gas method, and the penetration in the latter is two to three times higher than in the former (112). It is not known, however, if this is due to changes in surface tension or changes in the arc. Halide fluxes can increase penetration by a factor of four, and the addition of gaseous halide compounds to the shielding gas substantially increases penetration (113). Arc voltage increased and the arc constricted in these cases, so the exact mechanism of the increased penetration is not yet clear.

Minor elements can thus affect the welding process in a number of ways that manifest themselves as changes in the bead geometry. Besides affecting surface tension and arc voltage, they can affect anode spot size, anode fall voltage, arc configuration, arc stability, anode and cathode work functions and weld pool fluidity, all of which can affect penetration. Glickstein and Yeniscavich (112) present a good review of these effects, but there is still much that is not understood. Unfortunately, even the minor chemical variations that occur within a given material specification can significantly affect the bead geometry through one or more of these mechanisms, making penetration difficult to predict and control.

Regarding convection, though, minor elements have their strongest effect on surface tension gradients, and surface tension is generally the dominant force in forming convection patterns. Whereas earlier analysis tended to look at the electromagnetic forces as dominant (114), more recent numerical solutions (115, 116, 117) have shown that surface tension is capable of producing fluid velocities on the order of 100 to

1000 mm/s, while electromagnetic forces produce velocities of 10 to 100 mm/s, and buoyancy is limited to 10 mm/s or less for typical welding conditions. The small size of the weld pool is thought to keep the flow primarily laminar, even for the higher velocities. Oreper et al (115) mapped the calculated fluid velocities for a variety of currents, current distributions and surface tension gradients. Surface tension was found to dominate the flow pattern, but electromagnetic forces had a significant effect too. The highest velocities occurred with a positive surface tension gradient, in which case the surface tension forces and electromagnetic forces work together. When the surface tension gradient is negative and the electromagnetic forces are strong, such as would be the case for a large current or a sharply focused arc, the double circulation pattern shown in figure 3.35 is formed.

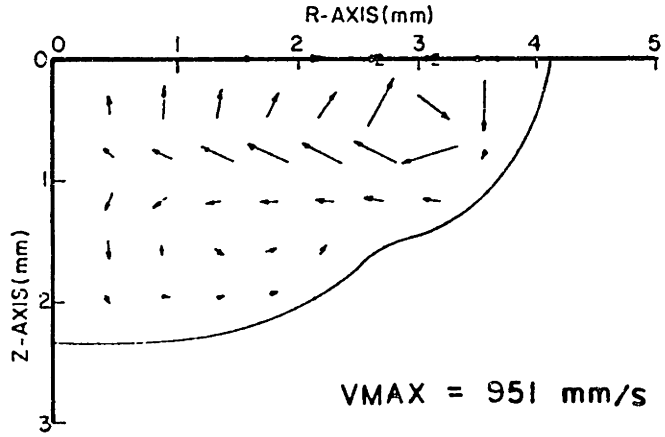

Figure 3.35 Double circulation pattern formed by a negative surface tension coefficient ($d\gamma/dT = -.49$ dyn $\cdot cm^{-1} \cdot K^{-1}$) and a sharply focused 190A arc. (115)

Oreper (115) also found that the high surface velocities were effective in dissipating the surface heat input from the arc, thereby lowering the surface temperature and reducing vaporization.

3.5.2 Effect of Pulsing

There is obviously nothing that can be done about the surface tension gradient through the control of the welding variables. The possibility of imposing a positive gradient by surface contamination or of affecting arc characteristics by halide additions to the shielding gas should be investigated, although the effects of such contamination on weld soundness and metallurgical characteristics would need to be watched closely. In the present study, though, attention will be focused on the welding variables, and these will exert their influence on convection through the electromagnetic forces.

As shown in section 3.3.1, the electromagnetic forces are proportional to the square of the current. The computations of references (115, 116, 117) are based on moderate current levels, but at very high currents, the electromagnetic forces will eventually dominate the convection pattern. Even at 190A, figure 3.35 shows the electromagnetic forces taking control of the lower central region of the weld pool, which is the critical region for penetration. Reasonably high currents, therefore, should be able to produce good penetration even in opposition to unfavorable surface tension gradients. In favorable (positive) surface tension gradients, high currents should produce very deep penetration.

Current pulsing, as previously mentioned in other contexts, is a way to obtain the benefits of high currents while maintaining a moderate average current. In this context, the current pulse could establish the desired circulation pattern and penetration, while the background phase would limit wire burnoff and heat input. A critical consideration is the time period over which the circulation pattern is established and then

dissipated. Intuitively, this time period will depend on distance, density, and viscosity. Dimensional analysis would then require that

$$\tau = \frac{L^2 \rho}{\mu}$$

as expressed by Szekely (117) for the establishment and inertial decay of convection. For a molten steel weld pool with a characteristic length of 1 cm, density of 6.6 gm/cm^3 and viscosity of 4 x 10^4 gm cm^{-1} s^{-1}, τ = .17 msec. This is very rapid and will allow the convection pattern to follow changes in current for frequencies below several kilohertz. Szekely showed melting and solidification phenomena to occur more slowly than this, with formation of the weld pool requiring on the order of seconds and solidification requiring tenths of a second. Thus, for all frequencies above about 10 Hz, the weld pool dimensions will not follow the current waveform, and the convection pattern will change within a stable weld pool shape that is determined by average heat flow characteristics.

Pulsing has been shown by some other investigators to produce more consistent penetration in spite of minor variations in base plate composition. This would be expected, since pulsing increases the relative significance of the controllable electromagnetic forces and decreases the relative significance of the uncontrollable surface tension forces, particularly in the lower central region of the pool. Pulsing produces larger electromagnetic convection than does an equivalent mean current due to the current squared dependence of the forces. The average of the square is greater than the square of the average, so the average convection pattern and resultant heat flow will be greater for pulsing than for a steady current.

3.6 Droplet Momentum

3.6.1 Theory

While the first three mechanisms apply to both GMAW and GTAW, this one obviously applies to GMAW exclusively. The metal drops transfer both heat and momentum to the weld pool. The drops contain heat that originated in the heat evolution at the electrode, and they account for approximately 25% of the total heat transfer to the workpiece (118). Essers and Walter (117, 118) report that the drops are strongly overheated, and they cite the work of Ando et al (120) and Jelmorini et al (121) as support. Jelmorini measured drop temperatures from 2100°C to 2170°C as current varied from 125A to 235A. Although their work dealt with plasma-MIG welding, other investigators have found similar results with MIG welding. Reference (122) states that calorimeter measurements have indicated average drop temperatures between 2000°C and 2700°C. Pyrometric measurements indicate that the electrode tip surface is at the boiling point for currents above 200A. Essers and Walter's calculations show that below 250A, the overheated droplets contain all the heat necessary to melt the metal contained in the final weld bead. Above 250A, the weld bead is so large that some additional heat from the arc is required. Their analysis neglects all heat losses, but it does show that the transferring drops are a significant factor in heat flow and in determining the weld bead geometry.

In addition to their heat content, the droplets carry momentum to the weld pool. This momentum depresses the weld pool surface and delivers the droplet heat content below the surface. Essers and Walter noted from high speed films of the weld pool that each drop forms a pit in the weld pool when it strikes. At slow drop frequencies, the pit fills in between

drops, but at higher frequencies, there is not sufficient time for it to fill in. The drops therefore enter the weld pool at the base of the depression, and their heat is delivered very effectively to the bottom of the pool. For a 1.2 mm steel wire with a 40 mm extension, the surface depression no longer fills in between drops for currents above 170A, corresponding to a droplet frequency of approximately 136 per second. This frequency is much higher than other frequencies reported in the literature for 170A, and it is due to the long electrode extension. A long extension lowers the spray transition current and produces higher drop frequencies at lower currents.

Essers and Walter claim that drop momentum is the primary factor controlling penetration in GMA welding. To support this they filmed a number of welds made under varying conditions. Specifically, they used 1.2 mm wire with both straight and reverse polarity and 1.6 mm wire with straight polarity. They determined droplet frequency, mass, and velocity from high speed films, then calculated the product of drop frequency and average drop momentum. Penetration was found to be a smooth monotonic function of this "total impact per second," as shown in figure 3.36. Penetration therefore appears to be a function of drop transfer characteristics, irrespective of other welding variables. While this doesn't prove a causal relationship, it certainly does indicate a strong correlation. Essers and Walter also used an external magnetic field to direct the drops off center. The field was timed to switch direction at the drop frequency, so that half the drops hit on one side and the other half on the other side. The penetration profile, shown in figure 3.37, clearly shows two separate finger penetrations at the points of impact. It could be argued that the magnetic field also affected arc configuration through direct arc deflection and through modification of the molten tip

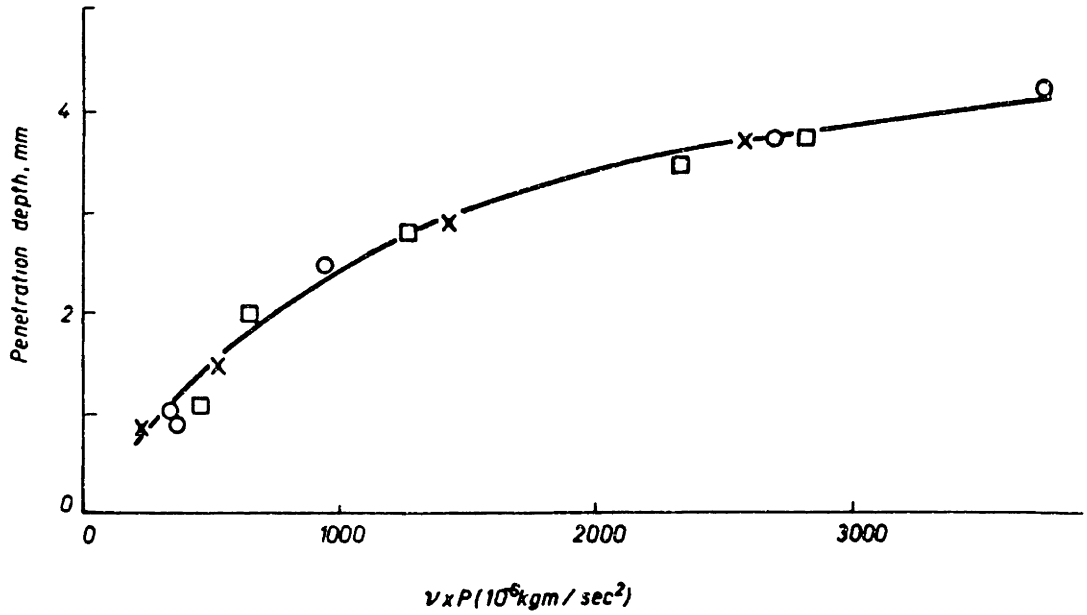

Figure 3.36 Penetration as a function of drop frequency times average drop momentum. X - 1.2 mm wire, straight polarity; □ - 1.2 mm wire, reverse polarity; 0 - 1.6 mm wire, straight polarity. (119)

Figure 3.37 Penetration produced when drops are electromagnetically controlled to strike off center. (119)

geometry. While these factors would reduce central penetration, they could not produce the type of side penetration shown in figure 3.37. Drop momentum, therefore, would appear to be an important mechanism of penetration in GMAW.

Before discussing the effect of pulsing on drop momentum, it will be

worthwhile to theoretically examine surface depression due to droplet impact. Reference (123) does this to a limited extent by modelling the weld pool depression as a cylindrical cavity with a radius of twice the drop radius. While this gives a reasonable phenomenological description of the process, it overestimates the work performed in forming the cavity since it maintains that large radius all the way down to the bottom. There are also several errors in the derivations (either typographical or otherwise), and the resulting equations do not support the conclusions when used with the data provided by the same reference.

Here the cavity will be modeled as a parabaloid, the cross section of

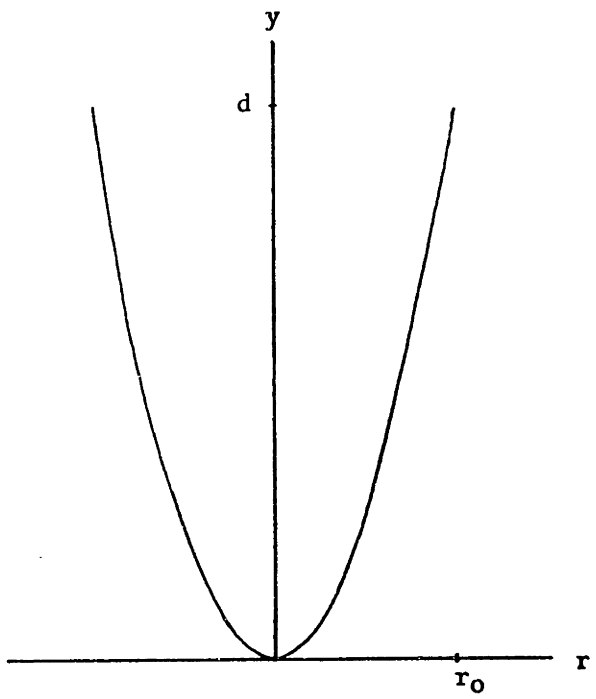

Figure 3.38 Cross section of paraboloid model of weld pool surface cavity.

which is shown in figure 3.38. The cross section is described by:

$$y = d \frac{r^2}{r_o^2} \tag{3.60}$$

where d is the maximum depth of the cavity and r_o is the radius at the weld pool surface. In forming this cavity, work is expended against both hydrostatic forces and surface tension forces. The work done against hydrostatic forces is:

$$W_h = \int pdV = \int_0^d \rho g(d-y)\ \pi r^2 dy \tag{3.61}$$

Substituting $r^2 = r_o^2\ y/d$ gives:

$$W_h = \int_0^d (\rho g \pi r_o^2/d)\ (d-y)\ y dy$$

$$W_h = \frac{\pi}{6} \rho g r_o^2 d^2 \tag{3.62}$$

This model will assume a constant value of surface tension. The work performed against surface tension is therefore the increase in area times the surface tension. The area of the parabaloid is given by:

$$S.A. = \int 2\pi r ds \tag{3.63}$$

where

$$ds = [1 + (\frac{dy}{dr})^2]^{1/2} dr \tag{3.64}$$

Thus:

$$S.A. = \int_0^{r_o} 2\pi r\ [1 + \frac{4d^2}{r_o^4} r^2]^{1/2}\ dr \tag{3.65}$$

To simplify the integration, let $x = 2dr/r_o^2$, and integrate over x:

$$S.A. = 2\pi\int_0^{2d/r_o} \frac{r_o^2}{2d}\, x\, (1 + x^2)^{1/2}\, \frac{r_o^2}{2d} dx$$

$$S.A. = \frac{\pi r_o^4}{2d^2} \left|_0^{2d/r_o} \right. \frac{1}{3} (1 + x^2)^{3/2}$$

$$S.A. = \frac{\pi r_o^4}{6d^2} \left[\left(1 + \frac{4d^2}{r_o^2}\right)^{3/2} - 1 \right] \qquad (3.66)$$

Applying L'Hospital's Rule twice shows that this correctly approaches πr_o^2 as d approaches zero.

The surface tension work, though, depends on the difference between the area given by equation 3.66 and that of a circle (since it depends on the increase in area). For temperature independent surface tension, this work is given by:

$$W_s = \gamma \left(\frac{\pi r_o^4}{6d^2} \left[\left(1+ \frac{4d^2}{r_o^2}\right)^{3/2} - 1\right] - \pi r_o^2\right) \qquad (3.67)$$

The total work is given by the sum of equations 3.62 and 3.67:

$$W = \frac{\pi}{6}\rho g r_o^2 d^2 + \pi r_o^2 \gamma \left(\frac{r_o^2}{6d^2} \left[\left(1 + \frac{4d^2}{r_o^2}\right)^{3/2} - 1\right] - 1\right) \qquad (3.68)$$

This work can be equated to the kinetic energy of the droplet as it strikes the pool surface. This will actually give an upper bound on the

size of the cavity, since it assumes that all of the droplet kinetic energy goes into forming the cavity. In reality, much of that energy is lost to the creation of extraneous fluid motion, both on and below the weld pool surface. Nevertheless, to find the upper bound, we have:

$$\frac{1}{2}mv^2 = \frac{\pi}{6}\rho g r_o^2 d^2 + \pi r_o^2 \gamma \left(\frac{r_o^2}{6d^2}\left[\left(1 + \frac{4d^2}{r_o^2}\right)^{3/2} - 1\right] - 1\right) \qquad (3.69)$$

Assume that the surface radius of the cavity equals twice the drop radius and that the densities of the pool and drops are essentially the same. Then:

$$\frac{1}{2}mv^2 = \frac{1}{2}\left(\frac{4}{3}\pi\frac{r_o^3}{8}\rho\right)v^2 = \frac{\pi}{12}\rho r_o^3 v^2 \qquad (3.70)$$

Combining 3.69 and 3.70 and cancelling terms gives:

$$\frac{\rho r_o v^2}{12} = \frac{\rho g d^2}{6} + \gamma\left(\frac{r_o^2}{6d^2}\left[\left(1 + \frac{4d^2}{r_o^2}\right)^{3/2} - 1\right] - 1\right) \qquad (3.71)$$

Unfortunately, this expression cannot be solved analytically for d. However, an iterative solution gives the results listed in table 3.1 when used with droplet data from Essers and Walter for a reverse polarity weld with a 1.2 mm wire (119):

Table 3.1 Cavity depth due to droplet impact.

current	drop radius ($r_o/2$)	drop velocity (v)	cavity depth (d)
150 A	1.19 mm	76 cm/s	2.0 mm
170	1.02	108	2.5
200	.62	158	1.8

These results are somewhat surprising in that the depth declines at 200A, whereas depth steadily increases in the analysis of reference (123). The decline at 200A is due to the decreased droplet kinetic energy. Each 200A droplet has 7.5×10^{-6} J of kinetic energy, compared to 12.2×10^{-6} J at 150A and 15.6×10^{-6} J at 170A. Since kinetic energy is proportional to the cube of the drop radius and the square of the drop velocity, the large decrease in radius at 200A outweighs the velocity increase. The actual cavity depth, however, will also be affected by drop frequency, and that will be considered shortly. The depths listed in reference (123) are in error in that the calculations are off by a factor of two for the 150A and 200A values. The proper depths using the cylindrical model should be 1.3 and 1.5 mm, respectively. As expected, the parabaloid model produces deeper depths due to the smaller cavity radius below the surface. The vast majority of energy is expended against surface tension. Of the 7.5×10^{-6} J in the 200A drop, for example, 7.3×10^{-6} J goes into forming the .06 cm^2 of new surface area, while only $.2 \times 10^{-6}$ J goes into forcing the fluid down against hydrostatic pressure. One of the weaknesses of this model is that it assumes reversible work is done against the hydrostatic pressure, but given the small percentage of the total work that this represents, it will make very little difference overall whether it is reversible or irreversible.

Another weakness of the model, as previously mentioned, is that it assumes that all of the droplet kinetic energy is converted into the cavity potential energy. The shape of the cavity and the radius of the cavity at the surface are also assumptions, so the calculated depths in table 3.1 are valid in a qualitative sense only.

These calculations apply to a theoretical cavity formed by a single drop. The cavity in an actual weld will also depend on the drop frequency. We therefore need an estimate of the time it will take for the cavity to fill back in. This will be done by forming the Lagragian and applying Hamilton's Principle. In order to keep the math at a reasonable level relative to the sophistication of the model, a cylindrical geometry will be assumed for the cavity. Let d be the maximum cavity depth and y the instantaneous cavity depth. Assume that the cavity maintains its radius and fills in from the bottom. The instantaneous potential energy of the cavity is then:

$$V = \frac{1}{2}\pi\rho g r_o^2 y^2 + 2\pi r_o y\gamma \qquad (3.72)$$

where the first term is hydrostatic potential energy and the second term is surface potential energy. The kinetic coenergy will be $1/2mv^2$, where v can be accurately represented by $\dot{y}$, the speed at which the cavity bottom rises. The actual mass moving at that velocity can be approximated by $\rho\pi r_o^2(d-y)$, but there will be additional fluid moving at a slower velocity in the surrounding region. Theoretically, all the fluid in the weld pool will move to some degree as the cavity fills in. This is analogous to the concept of added-mass in hydrodynamics. The added-mass is a weighted integration of the acceleration of all fluid particles as a result of the acceleration of a body moving through the fluid. For a cylindrical disk of fluid, the weighted integral of surrounding fluid motion will approximately equal the mass of the disk itself. We are interested in the case in which the cavity only partially fills in, but when we include the added-mass effect, it is reasonable to use $\rho\pi r_o^2 d$ as the fluid mass. The kinetic coenergy is therefore given by:

$$T^* = \frac{1}{2}\pi\rho r_o^2 d\dot{y}^2 \tag{3.73}$$

and the Lagrangian is given by:

$$L = T^* - V = \frac{\pi}{2}\rho r_o^2 d\dot{y}^2 - \frac{\pi}{2}\rho g r_o^2 y^2 - 2\pi r_o \gamma y \tag{3.74}$$

Next apply Hamilton's Principle in the form of Lagrange's equation with no generalized (non-conservative) forces:

$$\frac{d}{dt}\left(\frac{\delta L}{\delta \dot{y}}\right) - \frac{\delta L}{\delta y} = 0 \tag{3.75}$$

$$\pi\rho r_o^2 d\ddot{y} + \pi\rho g r_o^2 y + 2\pi r_o \gamma = 0 \tag{3.76}$$

$$\ddot{y} + \frac{g}{d}y + \frac{2\gamma}{\rho r_o d} = 0 \tag{3.77}$$

This is satisfied by a solution of the form:

$$y = c_1 \cos\left(\frac{g}{d}\right)^{1/2} t + c_2 \sin\left(\frac{g}{d}\right)^{1/2} t - \frac{2\gamma}{\rho g r_o} \tag{3.78}$$

The initial conditions are that:

$$y(0) = d$$

$$\dot{y}(0) = 0$$

These require the arbitrary constants to have the following values:

$$c_1 = d + \frac{2\gamma}{\rho g r_o}$$

$$c_2 = 0$$

Thus we are left with:

$$y = (d + \frac{2\gamma}{\rho g r_o}) \cos (\frac{g}{d})^{1/2} t - \frac{2\gamma}{\rho g r_o} \qquad (3.79)$$

Using the droplet frequencies from Essers and Walter (119), the cavity depths just prior to the next drop are calculated from equation 3.79 and listed in table 3.2.

Table 3.2 Cavity depth just prior to the impact of the second drop.

Current	drop frequency	r_o	max depth(d)	final depth
150 A	74 s^{-1}	2.38 mm	2.0 mm	0 mm
170	136	2.04	2.5	.14
200	320	1.24	1.8	.88

At low currents and low drop frequencies, each drop will strike a flat surface and will not efficiently deliver its heat to the bottom of the weld pool. At higher currents and frequencies, each drop will strike an already formed cavity, so it will both deliver its heat at a lower level and extend the cavity depth even deeper.

The penetrations measured or interpolated by Essers and Walter for 150, 170 and 200A were 2.45 mm, 2.92 mm and 3.65 mm, respectively. At these low currents there is very little surface depression due to arc pressure, and there is no compound vortex. All the penetration should therefore be from drop momentum, convection, and conduction. A possible area of further research would be to compare GMAW bead geometries with those of GTA welds made under the exact same welding conditions and using a hemispherically shaped electrode tip. There would still be some

inevitable differences in arc configuration, but these would nevertheless give some additional indication of the amount of penetration attributable to droplet momentum.

Two conclusions can be drawn from the preceding analysis. First, droplet momentum is a significant factor in weld pool surface depression. The cavity depth at 200A is greater than the surface depression resulting from the arc pressure of 300A in a 10 mm diameter weld pool, as calculated by Lin (89). When coupled with other mechanisms of surface depression, the effect of droplet momentum should be additive in nature (i.e., superposition should apply). Second, the model accurately predicted the approximate drop frequency at which the cavity would no longer fill in between drops (136 s^{-1} at 170A). This coorelates to the onset of finger penetration, which is due to a combination of cavity formation, the central downward convection induced by the impacting drops, and the increased plasma jet velocity that accompanies spray transfer. At higher currents, the compound vortex might play a significant role too.

3.6.2 Effect of Pulsing

Current pulsing gives greater control over metal transfer characteristics, thereby allowing exploitation of droplet momentum as a means of controlling penetration. Appropriate selection of pulse parameters can control droplet size, frequency, and velocity. In one drop per pulse transfer, the timing of the drop detachment and the magnitude of the current pulse are the key factors. If the drop detaches at the trailing edge of the pulse, then it will transfer during the background phase. Plasma velocity and the resultant drop acceleration is much lower during the background phase, so drop momentum should be small and penetration should be shallow. As the peak period increases, drop

detachment will occur before the trailing edge, and at least part of the transfer will occur under peak conditions. Increased drop velocity and penetration should result. Reference 122 shows the acceleration of a drop due to drag from the plasma jet to be:

$$a = \frac{9\pi}{32} \frac{v\rho_g}{R_d^2 \rho_m} (8\nu + 3R_d v) \qquad (3.80)$$

v = plasma velocity

R_d = drop radius

ρ_g = gas density

ρ_m = drop density

ν = gas viscosity

As the current increases, the plasma velocity increases and the drop radius decreases, both of which increase the acceleration. For downhand welding, the acceleration due to gravity must be added to the drag acceleration. Figure 3.39 shows this total acceleration versus current, along with experimental values measured by Pintard (124). At 200A, the acceleration is 56.4 m/s^2. Analysis of high speed films has shown that the drops accelerate quickly and reach their terminal velocity within a very short distance below the electrode tip. If the acceleration occurs over a distance of 4 mm, it will take 12 ms, resulting in a velocity of 67 cm/s. This is substantially lower than the 128 cm/s measured by Essers and Walter (118) at 200A, but reference (122) used a drop radius that is 71% larger than in reference (118). Regardless, the bottom line is that drop acceleration can be strongly affected by pulse duration and amplitude. Although pulsing is normally done in the one drop per pulse mode, this is not necessary, and other modes can provide different

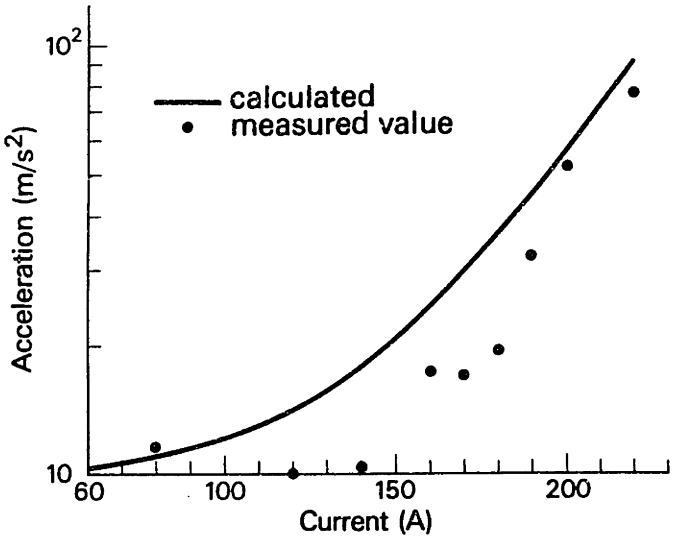

Figure 3.39 Acceleration of drops due to drag and gravity. (122)

penetration characteristics. Multiple drop detachment during the peak period, for example would permit the additional drops to fall into the cavity formed by the first drop, and this should increase the penetration. Alternative pulsing strategies will be discussed further in section 5.2.2.

PULSED GMAW PARAMETER VARIATION TO MINIMIZE INTERFERENCE FROM TACK WELDS

by

GREGORY C. KOLODZIEJCZAK

B.S., Physics, United States Naval Academy
(1978)

S.M., O.E., Massachusetts Institute of Technology
(1985)

SUBMITTED IN PARTIAL FULFILLMENT
OF THE REQUIREMENTS FOR THE
DEGREE OF

DOCTOR OF PHILOSOPHY
at the

MASSACHUSETTS INSTITUTE OF TECHNOLOGY
May 1987

Signature of Author Gregory C Kolodziejczak
Department of Ocean Engineering
May 20, 1987

Certified by Koichi Masubuchi
Koichi Masubuchi
Thesis Supervisor

Accepted by A Douglas Carmichael
A ~~Douglas~~ Carmichael
Chairman, Departmental Graduate Committee

Vol. 2

CHAPTER 4

LOCAL ANALYSIS OF TACK WELDS AS TRANSIENT DISTURBANCES

4.1 Introduction

Section 2.5 described the overall effect of tack welds on the shipbuilding process. This chapter will take a more detailed look at local phenomena occurring at the tack weld sites. Although this is a subject of considerable industrial interest, there is essentially no published research on it. References (125) and (126) apply finite element analysis to tack welded butt joints, but the research was directed toward distortion and residual stresses. Reference (60) similarly examines the thermal stresses produced in butt welds, with implications for required tack weld size and spacing. Reference (59) examines possible methods of reducing the stress and distortion produced during butt welding, thereby allowing fewer and smaller tack welds. However, none of the research deals with the weld quality at the tack weld sites, and this is of critical importance. This chapter studies the weld quality experimentally, as described in sections 4.2 and 4.3. Section 4.4 discusses the results and compares the experimental temperature data with theoretical predictions.

4.2 Experimental Description

Experiments were conducted on nine tack welded V-groove butt joints. The base plate was 3/8" mild steel with a 30 degree bevel, for a total groove angle of 60 degrees. Each joint was approximately one foot long and contained three or four tack welds. The joint configuration is shown in figure 4.1. The tack welds were made in the Department of Ocean

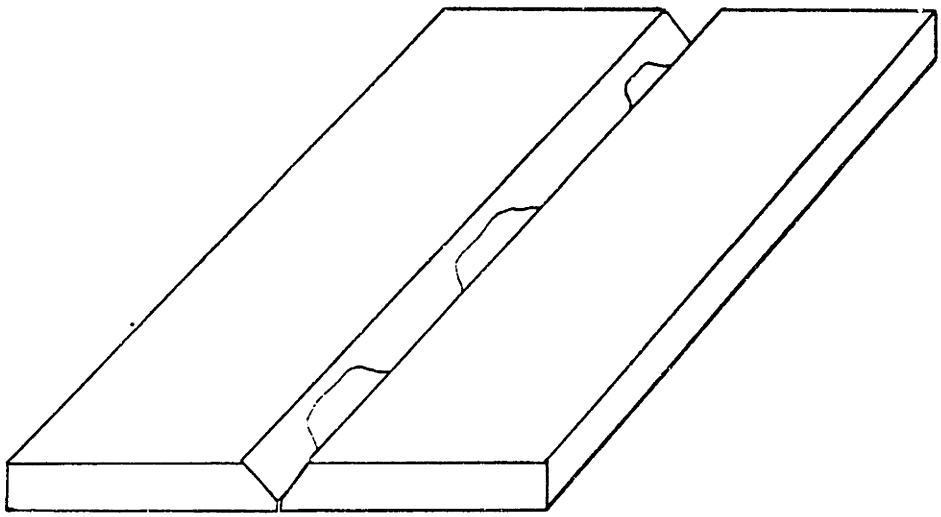

Figure 4.1 Tack welded butt joint used in experiments.

Engineering welding laboratory at MIT using a Miller Deltaweld 650 constant potential power supply, Argon/2% Oxygen shielding gas at 35 scfh, and .045" mild steel wire. The welding conditions used for each tack weld are listed in table 4.1. No special procedures were used in making the tack welds. The procedures and welding parameters were intended to produce tack welds that accurately represent those encountered in industry.

The prepared butt joints were welded at Idaho National Engineering Laboratory (INEL), using a Linde SVI-300 constant potential power supply, Argon/2% Oxygen shielding gas at 35 scfh, and .035" mild steel wire. Ceramic backing strips were placed beneath the groove on all plates except 4 and 5. A total of 35 type K (chromel - alumel) thermocouples were inserted in and around the tack welds. Insertion was made by drilling .067" diameter holes in the bottom side of the tack welds, then individually fusing a chromel and an alumel wire into the bottom of each

Table 4.1 Tack welding parameters. Wire feed speed in ipm, voltage in volts, travel speed in ipm, torch height in inches above the top surface of the base plates, tack weld cross-sectional area in mm^2, length in cm, and root gap in mm. #28 was made by several welds, each with no travel speed.

Plate	Tack Weld	WFS	V	TS	TH	Area	Length	Root Gap
1	1	275	24	10	.5	28.2	6.2	.5
	2	275	24	10	.5	28.2	2.3	.4
	3	275	24	10	.5	28.2	3.5	.4
2	4	275	24	10	.5	28.2	2.5	1.1
	5	275	24	10	.5	28.2	2.0	.8
	6	275	24	10	.5	28.2	3.4	.2
3	7	275	24	10	.5	28.2	2.4	1.8
	8	275	24	15	.5	18.8	3.9	1.6
	9	275	24	10	.5	28.2	4.8	1.4
4	10	250	26	15	.25	17.1	2.9	.4
	11	250	22	15	.25	17.1	1.4	.1
	12	250	23	15	.25	17.1	1.0	0
	13	250	25	15	.25	17.1	2.8	0
5	14	300	24	15	.5	20.5	3.4	1.1
	15	300	24	15	.5	20.5	2.3	.8
	16	300	24	15	.5	20.5	5.1	.5
6	17	300	24	15	.25	20.5	3.7	0
	18	300	24	15	.25	20.5	3.8	.2
	19	300	24	15	.25	20.5	2.4	.5
7	20	250	27	10	.5	25.7	2.5	2.2
	21	250	25	8	.5	32.1	2.3	2.0
	22	250	25	5	.5	51.3	2.9	1.8
8	23	125	22	5	.5	25.7	2.7	.5
	24	100	22	5	.5	20.5	1.8	.8
	25	125	22	5	.5	25.7	1.6	1.1
	26	250	25	10	.5	25.7	2.4	1.4
9	27	250	25	8	.5	32.1	2.5	1.6
	28	250	25	-	.5	-	2.3	2.0
	29	250	27	10	.5	25.7	2.0	2.4

hole with a current pulse. Good thermal contact was therefore ensured. Voltage readings were recorded on Hewlett-Packard strip chart recorders, then later converted to temperature. The precise thermocouple locations and temperature profiles will be given in section 4.3.2.

During the welding process, the weld pool was video-taped using an electro-optical system developed at INEL. The system illuminates the weld site with a pulsed nitrogen gas laser at 337.1 nm wavelength. The weld site image is transmitted to the video camera via an image intensifier tube, an optical bandpass filter, and a lens system. The image intensifier is electronically gated to operate only during the duration of each laser pulse (about 20 ns). This feature, along with the bandpass filter, eliminates virtually all of the arc light from the image and permits a clear presentation of the weld site. Information obtained from the weld pool videos is presented in section 4.3.3.

The completed welds were cut, polished, and etched with a 12% solution of nitric acid in alcohol. Most of the welds were cut longitudinally. The results are discussed in section 4.3.1.

The welding parameters for each plate are listed in table 4.2. The power supply was set at an open circuit voltage of 32V. The resulting arc voltage and current were measured every .93 seconds and recorded by a data acquisition system. Arc voltage held fairly steady, and scatter was bounded by $\pm$ .25 V from the average values listed in table 4.2. There was more scatter in the current readings, so the actual current traces are shown in figures 4.2 through 4.10. The data in these figures has been converted from time to longitudinal position along the groove. The longitudinal position of each tack weld is indicated at the base of each

Table 4.2 Welding parameters for tack welded butt joints. Contact tip to workpiece distance is inches above the base plate top surface.

Plate	WFS (ipm)	TS (ipm)	CTWP (in)	V	I
1	472	10	.75	25.7	205
2	472	10	.75	25.5	212
3	402	7.5	.50	25.2	221
4	307	7.5	.75	26.8	168
5	402	10	.50	25.2	221
6	402	10	.50	24.8	232
7	402	10	.50	25.1	224
8	708	15	.75	24.9	235
9	708	15	.50	23.8	268

plot. The height of each tack weld marker is proportional to the cross-sectional area of the tack weld (1 mm = 4 mm^2). Current fluctuations resulting from the arc encountering tack welds will be discussed in section 4.4.

4.3 Experimental Results

4.3.1 Penetration Profiles

There are two issues that must be addressed in this section. The first is the extent to which tack welds are penetrated by conventional welding. The second is the type and frequency of defects produced by welding over tack welds. Figure 4.11 shows sketches of selected weld transverse and longitudinal sections. The sketches are twice the actual size in order to more clearly show the profiles and the defects.

The major conclusion that can be made regarding penetration is that the tack welds are not fully penetrated by conventional welding techniques. This is not surprising, since full penetration of a typical

tack weld would require penetration of 5 to 9 mm. It is conceivable that a small tack weld could be fully consumed by a high heat input weld, as is the case in submerged arc welding, but for conventional GMAW with reasonable deposition rates, it would appear to be unrealistic to expect full penetration.

Figure 4.11 reveals four major types of defects associated with tack welds: lack of fusion (LOF), lack of penetration (LOP), porosity (P), and discontinuities at the beginning and end of the tack welds. Surface irregularities can be seen in the profiles of welds 10, 13, and 16, but they are primarily the result of the final weld not fully filling the groove. Surface contour will be discussed further in section 4.3.4.

The LOF defects were on the tack-weld/base-plate interface and therefore were formed during the tack welding. GMAW is susceptible to LOF defects to begin with, and the moderate wire feed speeds (and therefore moderate currents) used in making the tack welds aggravated the tendency. Several of the tack welds had very poor fusion along the entire sidewalls of the groove, as is particularly evident in tack welds 10, 22, and 23. LOF restricted to the root area is also common, as seen in tack welds 15 and 16. This is largely due to the poor quality of preparation of the root area surface on these plates. Tack weld LOP is evident in 6 and 23, both of which had very small root gaps (.2 mm and .5 mm, respectively). The tack welds did fully penetrate all root gaps larger than .5 mm, and .5 mm when the WFS was 300 ipm, which was the fastest WFS used. When the tack weld fails to fully penetrate or fuse the root area, either the final weld must correct for it or the root area must be back gouged and re-welded.

The discontinuities at the tack weld beginnings and ends show up quite clearly in the longitudinal sections of tack welds 8, 9, 20, 27, and 29. There is a gap between the bottom edge of the tack weld and the bottom edge of the production weld, almost as if an air pocket had been trapped there. It is worse when the tack weld "rolls over", thereby requiring the production weld metal to flow under the end of the tack weld. With a flat ceramic backing strip, this could be impossible, since there would be trapped gas in that location. The backing strips most widely in use, however, have a concave groove that prevents such entrapment. Tack welds 9 and 21 contained gross defects that were surprisingly unaffected by the final weld. They each had a large cavity, and although the final weld penetrated to the cavity, it did not fill the cavity to any noticeable extent. Figure 4.12 is a before and after photograph of the backside of tack weld 21, with the cavity showing up clearly in both.

Porosity was not as severe a problem, but it did occur more frequently in the tack weld vicinities than in the open groove areas. It is probably due to increased turbulence in the weld pool as it encounters the tack weld. Cracks were also found on an infrequent basis. Samples 10 and 22 contain cracks in the tack welds at the fusion boundary with the base plate. Sample 9 contains two cracks in the final weld at the fusion boundary with the tack weld.

Clearly then, tack welds are the source of a significant number of defects, and production welds are unable to correct these defects by consuming the tack welds. Short of fully consuming the tack welds, it would be desirable to fully penetrate them, thereby at least removing the defects in the critical root area. This, however, does not appear to be possible with conventional GMAW. Increased penetration would also provide

a better transition at the ends of the tack welds, since the mechanism responsible for the increased penetration should help to force the fluid metal into the gap that frequently occurs at the tack weld ends.

4.3.2 Thermocouple Profiles

A total of 35 thermocouples were installed in tack welds 1, 5, 8, 10, 11, 12, 13, 14, 17, 18, 19, 20, 21, 22, 27, 28, and 29. Figure 4.13 shows the relative locations of the thermocouples in each of these tack welds. In addition to the single thermocouple in tack weld 14, there were two thermocouples beside tack weld 14 and two thermocouples beside the bare groove between tack welds 14 and 15. Voltage traces were recorded for the thermocouples in tack welds 1 through 19. For tack welds 20 through 29, only the maximum voltage reading was recorded. The approximate depth of each thermocouple below the tack weld surface was estimated by measuring the depth of the thermocouple hole and the depth of the tack weld surface below the base plate surface, then subtracting the sum of these from the plate thickness. The samples were later cut, polished, and etched at some of the thermocouple locations, and the distance of the thermocouple below the fusion boundary was measured. Table 4.3 lists approximate thermocouple depth below the tack weld surface, the measured thermocouple depth below the fusion boundary, the applicable heat input, and the maximum temperature recorded by the thermocouple.

The maximum temperatures recorded by the thermocouples correlate fairly well with the initial depth of the thermocouple below the tack weld surface. Figure 4.14 is a plot of the maximum temperature as a function of the thermocouple depth. Given the degree of uncertainty in estimating the depth (on the order of a millimeter or more), the correlation is quite good. Figure 4.14 does not take into account differences in heat input,

Table 4.3 Thermocouple data. d_1 is the estimated thermocouple depth below the tack weld surface, and d_2 is the measured thermocouple depth below the fusion boundary.

Tack Weld	q(J/s)	Thermocouple	d_1(mm)	d_2(mm)	T_{max} (°C)
1	3994	1	1.1	-	melted
		2	8.0	-	692
		3	6.7	-	704
		4	5.9	3.0	716
		5	2.2	-	1232+ (off scale)
		6	3.8	1.2	855
5	4074	1	4.2	2.2	1183
		2	4.3	-	bad connection
		3	3.3	-	862
8	4134	1	2.9	-	1161
		2	2.2	.3	1383
		3	3.7	-	947
10	3377	1	7.6	-	728
		2	6.0	3.1	728
11	3377	1	4.0	1.8	858
12	3464	1	3.9	1.7	862
13	3464	1	4.3	2.0	803
14	4269	1	3.5	-	975
		2	6.1	-	752
		3	6.2	-	506
		4	5.8	-	996
		5	6.0	-	518
17	4333	1	5.2	1.5	815
18	4334	1	4.9	1.1	837
19	4314	1	3.2	.2	1300

20	4236	1	4.7	1.0	937
		2	3.3	-	bad connection
		3	1.5	.1	1420
21	4196	1	5.4	1.6	862
22	4273	1	7.2	2.0	801
27	4799	1	4.8	-	723
		2	4.4	2.7	757
		3	1.8	.3	1399
28	4750	1	3.2	.3	1306
29	4799	1	3.3	-	1183

although inclusion of a correction factor for this does not improve the correlation. Figure 4.15 is a plot of the maximum temperature as a function of thermocouple depth below the fusion boundary. The temperature remains surprisingly flat beyond 1 mm, dropping only 200°C over the next 2 mm compared to a 500°C drop over the first millimeter. The actual thermocouple profiles are shown in figures 4.16 through 4.21. There was not an accurate reference point on the recordings marking the time at which the arc was directly above the thermocouple. Hence, the relative longitudinal spacing of the profiles is not accurate. Further discussion and comparison with theory will be given in section 4.4.

4.3.3 Weld Pool Description

The videotapes of the weld pool taken by INEL'S vision system were interesting but unremarkable. Generally the weld pool seemed to encounter the tack welds fairly smoothly. The weld pool widened while going over the tack welds, due to the change in groove geometry. Weld pool width

versus location is shown in figure 4.22 for plate #1. This was the only plate for which the maximum weld pool width could be determined from the videotape. One or both sides of the weld pool was off screen on the other plates, but they appeared to follow a pattern similar to that in figure 4.22. Such information conceivably could be used in a control system to estimate the resonant frequency of the weld pool and adjust the pulsing frequency accordingly. However, the weld pool shape is somewhat irregular when going over the tack welds, and minor variations in shape can significantly alter the resonant frequency. Considerably more research would be required before weld pool width could be used as a feedback variable to control pulse parameters.

The advance of the weld pool front was also studied from the videotapes. Predictably, the front is held up momentarily when it encounters the tack weld, and it rushes forward at the end of the tack weld. Figures 4.23 through 4.26 show the weld pool advance relative to the torch advance for the weld pool encounters with tack welds 5, 6, 7 and 9, respectively. Although it doesn't show up in these graphs, the pool front was occasionally held up long enough for discontinuous melting to occur. In other words, the arc began melting a short distance into the tack weld, while the weld pool was still hung up at the beginning of the tack weld, and there was sometimes unmelted metal in between.

4.3.4 Surface Contour

Maintaining a smooth surface contour is one of the primary factors a welder considers when adjusting his welding parameters to deal with a tack weld. There are two objectives. One is to avoid surface defects such as undercutting and bad toe angles. The other is to avoid a large hump in the contour at the tack weld location. The joints in this experiment were

made with no adjustments to the welding parameters while going over the tack welds. Figure 4.27 shows post-welding photographs of tack welds 24, 25, 27, 28 and 29, and both pre- and post-welding photographs of tack welds 7, 8, 21, 22 and 26. These are representative of all the welds, and they reveal a wide range of surface irregularities. They are the types of welds that would result if an automated welding system did not adjust for tack welds. Most butt welds, however, are multiple pass welds. The surface contour of the root pass would therefore have subsequent passes during which to be smoothed out.

4.4 Analysis and Discussion

Discussion of defects, the weld pool, and surface contour was done in the applicable sections. This section will be devoted to a more thorough analysis of heat flow in the tack welds and the resultant temperature profiles and penetration depths. Rosenthal (70) developed the first major solution to the problem of heat flow through a weldment. For a point heat source applied to a semi-infinite slab, he derived the following expression for the temperature rise at a given point:

$$T - T_o = \frac{q}{2\pi\kappa} \frac{1}{R} e^{-\frac{v}{2\alpha}(R + x)} \qquad (4.1)$$

T_o = initial plate temperature

q = heat input

λ = thermal conductivity

α = thermal diffusivity

v = travel speed

x = distance along the line of travel from the torch to the point

R = absolute distance from the heat source to the point

Thus, for a point heat source moving at velocity v along the x-axis, T is the temperature at a point that is x ahead of and R away from the source. Equation 4.1 is based on conduction only. It ignores weld pool convection, heat of fusion, the temperature dependence of κ and α, heat loss from the plate surface, and it assumes that the welding has been proceeding for a sufficient time to reach a quasi-stationary state. Relative to a point moving with the heat source, the temperature distribution will appear constant.

Christensen et al (127) non-dimensionalized Rosenthal's solution as follows:

$$\frac{\theta}{n} = \frac{1}{\rho} e^{-(\rho + \lambda)} \qquad (4.2)$$

where

θ = dimensionless temperature = $\frac{T - T_o}{T_c - T_o}$

n = operating parameter = $\frac{qv}{4\pi\alpha^2 (H_c - H_o)}$

ρ = dimensionless radius = $vR/2\alpha$

λ = dimensionless x = $vx/2\alpha$

T_c = reference temperature (^oC)

H = heat content per unit volume (J/cm^3)

= $C_p \delta T$ (C_p = specific heat, δ = specific gravity)

In the proceeding calculations, α will generally be taken to be .05 cm^2/s, and the melting point of mild steel will be taken as 1520^oC. Graphs of α and $H_c - H_o$ as functions of temperature are provided in

appendix B. Equation 4.2 will be used to predict the temperature profiles for the welding parameters used in these experiments, and the predicted results will be compared to the experimental results. Christensen (128) also derived the time dependence of temperature by utilizing the quasi-stationery nature of the temperature profile. The time profile of temperature equals the longitudinal position profile of temperature scaled by the travel speed. These predicted time-temperature profiles will be compared to the profiles measured by the thermocouples.

Before calculating the theoretical profiles, the theoretical maximum temperatures will be calculated. The objective is to calculate the maximum temperature at the thermocouple location, such as 5 mm below the tack weld surface. However, since the estimate of the thermocouple depth below the tack weld surface is not extremely accurate, the tack weld surface does not provide a good reference position. Instead, the fusion boundary will be used as the reference position. This provides the additional benefit of correcting Rosenthal's solution for those factors affecting the weld pool shape, such as convection. The procedure will be explained with reference to figure 4.28.

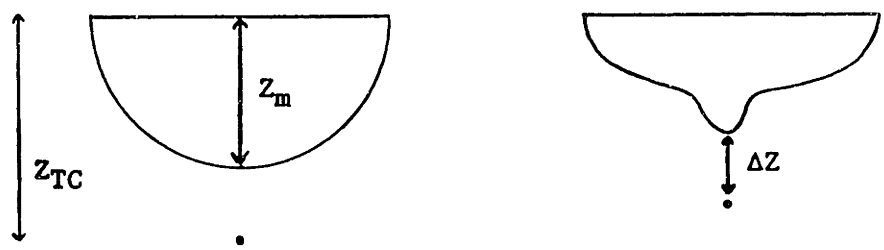

Figure 4.28 Theoretical and actual weld pool cross-sections. TC is thermocouple location.

Z_m is the theoretical weld pool depth based on equation 4.2. ΔZ is the measured depth of the thermocouple below the actual weld pool fusion boundary. Define Z_{TC} as the theoretical depth of the thermocouple below the plate surface:

$$Z_{TC} = Z_m + \Delta Z \tag{4.3}$$

The procedure will be to calculate Z_m from equation 4.2, with $T_c = 1520^oC$ and $\theta = 1$. Then calculate Z_{TC} from equation 4.3 using the values of ΔZ in table 4.3 (where they are listed as d_2). Finally, use equation 4.2 to calculate the theoretical temperature at Z_{TC}, and compare this with the measured temperatures listed in table 4.3. This can only be done for those thermocouples at which cuts were made (the same ones for which a d_2 value is listed in table 4.3). Calculation will not be made for tack weld 5, though, since the longitudinal cut was off center and an accurate determination of ΔZ is not possible.

The calculations are made more complicated by the fact that λ is not known a priori. The maximum penetration does not occur directly under the heat source in a conduction model. Since it takes a finite amount of time for the heat to diffuse through and melt the plate, the maximum penetration (Z_m) will occur at some distance (X_m) behind the heat source. Similarly, the maximum temperature at the thermocouple will be reached at some time and distance (X_{TC}) behind the heat source. Christensen's time-temperature profiles (appendix C) were used to estimate the time and distance lag. For the distance lag to maximum penetration, the operating parameter corresponding to 1520^oC (n_m) was calculated, and the time at which $\Theta = 1$ was determined from the graph. Knowing the travel speed, this time is easily converted to X_m and its associated non-dimensional

variable, λ_m. For the distance lag to the maximum temperature at the thermocouple, the operating parameter corresponding to the measured thermocouple temperature (n_{TC}) was used. Again, the time at which $\theta = 1$ was determined from the graph and converted into X_{TC} and λ_{TC}. Once the theoretical thermocouple temperature is calculated, the latter part of the procedure could be iterated by recalculating n_{TC} based on the calculated thermocouple temperature, and so on. However, unless the calculated and measured thermocouple temperatures are grossly different, the precision of such a procedure would exceed the precision with which ΔZ could be measured. Hence, no iterations will be made.

Given λ_m and λ_{TC}, the theoretical thermocouple temperature can be determined by the procedure outlined below. All terms have been previously defined except ξ, the non-dimensional Z coordinate. $\xi = vZ/2\alpha$. The subscript m refers to the melting isotherm, and the subscript TC refers to the thermocouple.

(1) Calculate ρ_m from: $$\frac{1}{n_m} = \frac{1}{\rho_m} e^{-(\rho_m + \lambda_m)}$$

(2) Calculate Z_m from: $$\xi_m^2 = \rho_m^2 - \lambda_m^2$$

and: $$Z_m = 2\alpha\xi_m/v$$

(3) Calculate Z_{TC} from: $$Z_{TC} = Z_m + \Delta Z$$

(4) Calculate ξ_{TC} from: $$\xi_{TC} = vZ_{TC}/2\alpha$$

(5) Calculate ρ_{TC} from: $$\rho_{TC}^2 = \xi_{TC}^2 + \lambda_{TC}^2$$

(6) Calculate θ from: $\frac{\theta}{n_m} = \frac{1}{\rho_{TC}} e^{-(\rho_{TC} + \lambda_{TC})}$

(7) Calculate T_{TC} from: $T_{TC} = (1500)\ \theta + 20$

The results of these calculations are summarized in table 4.4. Generally the calculated and measured temperatures are quite close, as

Table 4.4 Calculated thermocouple temperatures. The negative sign convention for χ_m and χ_{TC} indicates locations behind the heat source.

TW/TC	Z_m	χ_m	Z_{TC}	X_{TC}	T_{TC}	$T_{measured}$	ΔT
1/4	4.4mm	-4.5mm	7.4mm	-14.2mm	602°C	716°C	114°C
1/6	4.4	-4.5	5.6	-10.2	959	855	-104
8/2	5.0	-4.2	5.3	-6.8	1377	1383	6
10/2	4.5	-3.6	7.6	-11.0	624	728	104
11	4.5	-3.6	6.3	-9.8	837	858	21
12	4.5	-3.7	6.2	-9.9	863	862	-1
13	4.5	-3.7	6.5	-9.9	809	803	-6
17	4.6	-5.0	6.1	-12.3	883	815	-68
18	4.6	-5.0	5.7	-12.3	961	837	-124
19	4.6	-5.0	4.8	-7.6	1366	1300	-66
20/1	4.5	-5.0	5.5	-10.0	1038	937	-101
20/3	4.5	-5.0	4.6	-6.3	1453	1420	-33
21	4.5	-4.9	6.1	-11.8	862	862	0
22	4.6	-5.0	6.6	-12.3	787	801	14
27/2	4.1	-5.5	4.4	-15.6	601	757	156
27/3	4.1	-5.5	6.8	-8.1	1318	1399	81
28	4.1	-5.5	4.4	-8.5	1304	1306	2

shown in figure 4.31. There is no consistent pattern of either over or underestimation of the temperature, so it is believed that the primary source of error is the uncertainty in measuring ΔZ. The thermocouple holes were not perfect cylinders. They had conical bottoms from the drill bit, so the true hole depths weren't shown on the cross sections unless a particular cut was made exactly at the hole center. Estimated corrections were made for this when the measurements were taken, but some inaccuracy inevitably resulted. Other potential sources of error are the assumptions that the Rosenthal model is based on. Constant thermal properties, point heat source, no convection, no surface heat loss, no heat of fusion, infinite plate thickness, and quasi-stationary state will each be discussed in order.

Thermal properties entered into the calculations in the definition of the operating parameter, which has $\alpha^2(H_c - H_o)$ in the denominator, and in the non-dimensionalization of all the distance variables, which depend on $v/2\alpha$. $(H_c - H_o)$ is based on the curve in appendix B, which takes into account the changes in thermal properties. α varies significantly with temperature, as shown in appendix B, but it is relatively constant above 700°C. Since that is the temperature range of interest here, the error from assuming constant α should be small. Between 800°C and 1400°C, the average value of α is slightly higher that .05 cm^2/s, meaning that the heat would diffuse slightly faster than predicted. The result is that a given point will reach is maximum temperature sooner than with the lower value of α, but the maximum temperature will be lower. If α = .06 cm^2/s had been used in the calculations for the tack weld 13, for example, the calculated penetration depth would have been reduced from 4.52 mm to 4.34 mm, but it would have occurred only 2.81 mm behind the heat source, rather

than 3.71 mm. The maximum temperature at the thermocouple depth of 6.52 mm would have dropped from 809°C to 780°C, and it distance behind the heat source would have dropped from 9.91 mm to 8.04 mm. The minor variations in thermal properties in the temperature range of interest will therefore have an affect, but not a significant one.

The point heat source is responsible for the semi-circular cross section of the theoretical weld. A distributed heat source with a pure conduction model would give a wider, shallower weld. The thermocouple depth has been corrected for weld bead depth in these calculations, but the heat flow eminating from the fusion boundary will still be different from reality. A very flat penetration profile will produce a stronger heat flow below it than a semi-circular profile, but a finger type profile will produce a weaker heat flow. However, the effect on the temperature at Z_{TC} is an artificial result of the manner in which Z_{TC} has been defined. At a given point below the surface on the travel axis, the point heat source will produce a higher temperature then a distributed heat source, assuming no surface losses from radiation or vaporization.

The assumption of no convection affects both the weld pool shape and the temperature distribution within the weld pool. The effect on shape depends on the flow pattern, as discussed in section 3.5. The temperature distribution will be made more uniform by the convection, but there will be no net effect on the heat flow outside the weld pool (other than that caused by the charge in the weld pool shape). The flow pattern will contain a boundary layer along the fusion boundary, the thickness of which was derived by Blasius for a flat plate:

$$\delta = 4.9\sqrt{\nu x/U} \qquad (4.4)$$

ν = kinematic viscosity

x = distance along the plate

U = free stream velocity

The kinematic viscosity of liquid iron is approximately 6.5×10^{-7} m^2/s. For a characteristic distance along the weld pool boundary of 4 mm and a convection velocity of 500 mm/s, the boundary layer is on the order of .1 mm. Although a weld pool boundary is not a flat plate, the approximation is reasonable as long as the radius of curvature is much greater than the boundary layer thickness. The effect of the boundary layer on the temperature profile depends on the Prandtl number (ν/α), which is very low for liquid metals. Heat diffuses much faster than momentum, so the temperature profile will be largely unaffected by a momentum boundary layer. The Reynolds number of weld pool flow is small enough to indicate laminar flow, but if there is any turbulence along the boundary, it will effect the temperature profile. Such an analysis is beyond the scope of this thesis, but we can conclude that the local variations in temperature will be such that the temperature gradiant at the fusion boundary and the heat flow through the fusion boundary will be unaffected. Once steady state is reached, the heat flow out of the fusion boundary will equal the heat flow into the weld pool, regardless of the temperature profile within the weld pool.

The exception to this is heat loss from the surface. Convection lowers the surface temperature, thereby reducing heat loss from radiation and vaporization and increasing the heat flow into the workpiece. Rosenthal's solution neglects surface heat loss, and it therefore overestimates the heat flow into the workpiece. This can easily be compensated for by

decreasing the arc efficiency.

Although heat of fusion is included in the definition of the operating parameter (in the H_c - H_o term), it is not included in the dynamics of the weld pool formation and solidification. Figure 4.29 is a longitudinal diagram of the weld pool formed under a moving heat source. The solid line is based on pure conduction with no heat of fusion.

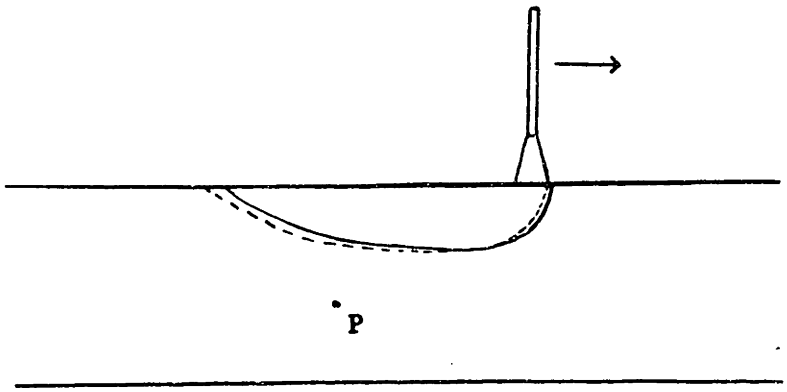

Figure 4.29 Weld formation.

The heat of fusion, though, acts a heat depository, delaying melting while it absorbs heat and delaying solidification while it gives up heat. The actual weld pool shape would then be shown by the dashed line. Since the maximum temperature at point P will be reached well after the heat source has passed, it will be more strongly influenced by the additional heat provided by solidification of the trailing end of the weld pool then by the heat absorbed during melting of the leading edge of the weld pool. Hence, neglecting latent heat effects would tend to underestimate the measured

temperatures below the penetration depth.

The infinite thickness assumption has a significant effect on heat flow, but it is likely to have little effect on the maximum temperatures other than near the plate bottom. The bottom edge of a finite plate is a poor heat dissipater, particularly when it is bounded by an insulating ceramic backing strip. Heat collects in the plate, and higher temperatures result. At significant distances away from the plate bottom, however, the maximum temperature will have already passed by the time the temperature gradient and the heat flow are affected. The distance that heat moves through a medium during time t is given by:

$$x = c\sqrt{\alpha t} \tag{4.5}$$

where c is a constant of proportionality varying from .5 to 2, depending on geometry, and taken as 1 for a point heat source dissipating in 3 dimensions through a slab. For a plate thickness of 9.5 mm, it will take on the order of 18 seconds for the heat to reach the plate bottom. Weld pool convection will speed this up to some degree, and the time for the heat to travel the approximately 5 mm below the fusion boundary will be on the order of 5 seconds. For all of the thermocouples in this study, the maximum temperature was reached within 2.5 seconds after maximum penetration was achieved. This time would be $|x_{TC} - x_m|/v$ from table 4.4. Therefore, the peak temperatures recorded by the thermocouples were unaffected by the finite thickness. A thermocouple located near the plate bottom would have been affected, and the cooling rates are significantly affected, as will be discussed shortly.

The quasi steady-state assumption is violated by the transient nature

of tack welds. The mathematics of transient heat flow require numerical simulation, but we can achieve a qualitative understanding by considering figure 4.30.

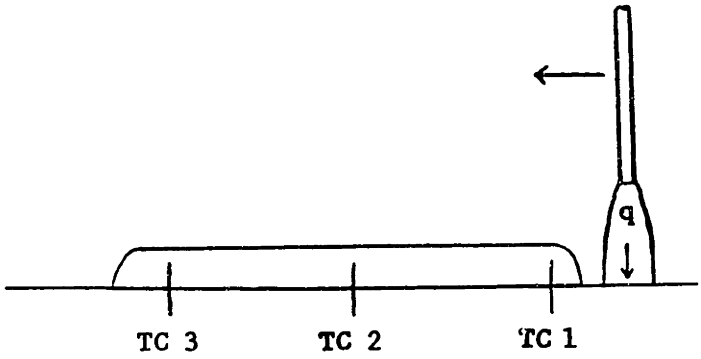

Figure 4.30 Heat input into a tack weld.

A tack weld receives heat input both along its top and at its ends. A long tack weld might reach the quasi steady-state at some point, but the ends will always be subject to transient phenomena. A point near an end, such as the locations of thermocouples 1 and 3 in figure 4.30, will receive substantial heat flow from both the top and the end of the tack weld. The heat sources will actually be distributed around the tack weld corners, but for qualitative analysis they will be assumed to be lumped into top and end sources. The temperature profile at a point will depend on the relative timing of the arrival of the heat flows. If the heat from both sources arrives simultaneously, the temperature will rise very sharply to a high peak. If one arrives shortly after the other, the rise will not be as sharp and the peak will not be as high, but it will be wider since the cooling will be slowed by the arrival of the second heat source. If one arrives considerably after the other, there could actually

be two peaks, but the second heat wave would have dissipated considerably during its relatively long transit. The second "peak" might therefore be nothing more than a slow down in the cooling rate.

As an example, consider thermocouple 6 in tack weld 1. Its position relative to the torch travel direction is the same as thermocouple 3 in figure 4.30. It is located 2.7 mm from the end and 3.8 mm below the surface of the tack weld. The travel speed is 4.23 mm/s; hence, the heat source will be directly above the thermocouple .6 s after passing the tack weld end. Using equation 4.5 with $\alpha = .06$ cm^2/s and $c = 1$, the heat from the end will take 1.2 s to reach the thermocouple, and the heat from the top will take 2.4 s plus the .6 s time delay, or a total of 3 s to reach the thermocouple. The actual heat flow will be gradual both because the heat sources are distributed, and because the heat arrives as a "wave" rather than a "wall". Nevertheless, the double peak effect is evident in the temperature profile of thermocouple 6, shown in figure 4.33.

The preceding assumptions have been summarized in table 4.5, along with the effect that the actual welding conditions will have relative to the assumed conditions.

Table 4.5 Summary of assumptions in the Rosenthal heat flow model and the effect of actual conditions relative to the assumed conditions.

Assumption	Effect
Constant thermal properties	Larger thermal diffusity will cause a point to reach its peak temperature sooner, but the peak temperature will be slightly lower.

Point heat source	Distributed heat source will result in slightly lower temperatures directly below the torch travel axis. Weld pool will be wider and shallower.
No convection	Convection will change the weld pool shape in a manner that depends on the flow pattern. The effect on temperature will depend on the change in weld pool shape.
No surface loss	Surface loss will lower the effective heat input and lower the resulting temperatures.
No heat of fusion	The measured temperatures below the penetration depth will be slightly higher than predicted.
Infinite thickness	Maximum temperatures at locations not close to the plate bottom will be unaffected, but the cooling rate will be slower. Close to the plate bottom, the maximum temperatures will be higher.
Quasi steady-state	Transient heat flow can significantly affect the temperature profile, depending on the size and shape of the tack weld and the location within the tack weld.

Besides the maximum temperatures, the thermocouples in tack welds 1, 5, 8, 10, 11, 12, 13, 17, 18 and 19 provided time-temperature profiles. Christensen's non-dimensional time temperature profiles shown in appendix C can be used for comparison. The comparison can be made in one of two

ways. First, the temperature profile for the predicted temperature listed in table 4.4 could be calculated from appendix C and compared with the actual profile. Second, the temperature profile for the measured temperature could be calculated and compared with the actual profile. Since the primary error in the predicted peak temperatures came from ΔZ and was random in nature, the second method was chosen for consistency. The procedure, therefore, was to calculate the operating parameter based on the welding conditions and the maximum thermocouple temperature, determine the non-dimensional profile from appendix C, and convert it to dimensional form. The predicted profiles are plotted with the measured profiles in figures 4.32 through 4.42. Since a time reference point was not included in the measured data, the longitudinal positions of the measured and predicted profiles were adjusted to coincide at the peak temperature.

Discussion is merited on two aspects of these plots - the peak shapes and the cooling rates. The peak shapes could be strongly affected by the transient heat flow phenomena described earlier. Table 4.6 lists the transient heat flow characteristics for each thermocouple and describes the peak shape. The transient heat flow is characterized by the leading edge time, trailing edge time, and surface time. These are the times, calculated with equation 4.5 with $\alpha = 6$ mm^2/s and $c = 1$, that it would take the arc heat to reach the thermocouple from the leading edge, the trailing edge, and the surface directly above the thermocouple, respectively. The times are referenced to the time at which the arc passes the leading edge. For example, the 6.5 s surface time for tack weld 13 includes 3.4 s for the arc to reach the position directly above the thermocouple and 3.1 s for the heat to reach the thermocouple from the surface. The surface times are based on the thermocouple depths below the

tack weld surfaces (d_1 in table 4.3).

Table 4.6 Transient heat flow characteristic times and peak shape characteristics.

TW/TC	L.E. time	T.E. time	S.time	Peak Characteristics
1/4	72	301	11	gradual rise, smooth peak
1/6	1.2	605	3.0	sharp rise, double peak
5	51	5.5	7.0	sharp rise and fall, double peak
8	60	75	5.3	Sharp rise and fall, double peak
10	29	51	9.1	gradual rise, smooth peak
11	7.5	12	4.3	smooth rise, smooth peak small glitch during cooling
12	3.5	7.6	3.6	smooth rise, smooth peak
13	34	38	6.5	gradual rise, smooth peak
17	33	92	7.8	gradual rise, smooth peak
18	47	82	8.0	sharp rise, double peak
19	6.6	58	3.2	sharp rise, glitch during cooling

With a few exceptions, the peak characteristics can be explained reasonably well with the qualitative description of transient heat flow presented earlier. The thermocouples that have large edge times and surface times greater than 6 s have gradual rises and smooth peaks, as expected. Large edge times (above 25-30 s) are extraneous and can be

neglected, since their effects will be small and will occur at or beyond the time limit of these plots. Larger surface times allow the heat wave to "smooth out" and the resulting temperature rise is more gradual. This would describe tack welds 1 (TC 4), 10, 13 and 17. Tack weld 18 should be in this category, and it is difficult to explain why it is not. This thermocouple had a temperature error of 124°C (from table 4.6), the highest of all the thermocouples listed in table 4.6. The transverse cut only showed the penetration at one location. A longitudinal cut might have revealed some anomilies that could help to explain the temperature results.

The sharp rises and double peaks in tack welds 1 (TC 6) and 5 can be explained by the close arrival of two of the thermal fronts. The temperature in tack weld 1 begins rising again 1.5 s after the first peak, which corresponds well with the transient times listed in table 4.6. It is possible that part of the shape of the tack weld 5 peak is due to the dual thermal fronts, but there also appears to electrical problems with the thermocouple. If there had not been such problems, it is not clear whether or not there would have been two peaks. The same is true of tack weld 8. The 833°C cooling rate immediately following the peak cannot be real, and if the sharp drop is faired in, there might not be a second peak. A dual peak is not indicated by the data in table 4.6. The thermocouple in 8 was extremely close to the weld pool, and the measured temperature of 1383°C exceeded the type K thermocouple temperature limit.

The temperature profiles in tack welds 11 and 19 do not have double peaks, but they do have glitches, or temporary slow downs, in the cooling rates. This occurs 5 s after the peak in number 11 and 2 s after the peak in number 19. These could be due to the transient characteristics, since

both have leading edge times approximately 3 s greater than the surface times. The only other temperature profile is for tack weld 13, and it is very unremarkable. All three transient times are short enough to affect the temperature profile, yet the profile is quite smooth. It does have a more rapid rise than the profiles in 1 (TC4), 10, 13 and 17, which could be due to both the shorter surface time and the relatively small edge times. A stronger effect would have been expected, though.

The preceding discussion was based on a very rudimentary transient analysis. The actual problem is complicated considerably by the geometry of an irregular tack weld in a V-groove, but at least this provides an intuitive understanding of some of the transient phenomena. The second significant aspect of the temperature profiles is the cooling rates. The cooling rates were determined for both the actual and predicted profiles by measuring the slopes of tangent lines drawn at several representative temperatures. These were compared to theoretical cooling rates taken from reference (130). Reference (130) estimates the cooling rate of the thick plate to be:

$$CR = \frac{2\pi\kappa}{H} (T_c - T_o)^2 \qquad (4.6)$$

and that for a thin plate to be:

$$CR = 2\pi\kappa\rho c \left(\frac{t}{H}\right)^2 (T_c - T_o)^3 \qquad (4.7)$$

where

CR = cooling rate ($^oC\ s^{-1}$) at temperature T_c (^oC)
κ = thermal conductivity = .028 $Wmm^{-1}\ ^oC^{-1}$
H = arc heat input to the workpiece ($J\ mm^{-1}$)
ρc = .0044 $Jmm^{-3}\ ^oC^{-1}$
t = plate thickness (mm)

T_o = ambient plate temperature (^oC)
T_c = temperature at which the cooling rate is being determined (^oC)

The distinction between thick and thin plate can be made by defining a relative plate thickness, τ:

$$\tau = t \frac{\rho c(T_c - T_o)}{H} \qquad (4.8)$$

For $\tau > .9$, the thick plate equation applies. For $\tau < .6$, the thin plate equation applies. For $.6 < \tau < .9$, the cooling rates are intermediate. Table 4.7 lists the measured and predicted cooling rates (from figures 4.32 through 4.42), the calculated thick plate cooling rate (from equation 4.60), the calculated thin plate cooling rate (from equation 4.7), and the calculated τ value. Calculations are based on a plate thickness of 9 mm. Other than the extreme cooling rates at the peaks of number 8 and number 19, the measured rates are all slower than the predicted rates. This is expected, since the predicted rates are based on a semi-infinite slab. The τ values indicate that the thin plate cooling rate equation applies, and the measured rates agree well with the thin plate rates. Generally the measured rates are slightly higher, and this too is expected since the actual plate does lose some heat from the top and bottom surfaces. The 833 $^oC/s$ cooling rate at 1200^oC in number 8 must be an electrical anomaly, as it is not possible to have that high a rate in the unforced cooling of steel. The $200^oC/s$ rate at 1200^oC in number 19 is prcbably exaggerated too. The τ value of .64 indicates that it is slightly above the thin plate regime, but well below the thick plate regime. The measured cooling rate is below the thick plate cooling rate, so it is not unrealistic, but it is much higher than expected.

Table 4.7 Measured, predicted, and calculated cooling rates ($^{o}C/s$).

TW/TC	Temp	Measured CR	Predicted CR	Thick CR	Thin CR	τ
1/4	700	15	46	86	22	.51
	550	7	34	52	10	.45
1/6	800	30	56	113	33	.54
	600	13	39	63	14	.47
5/1	800	34	92	111	32	.54
	500	11	37	42	7	.42
8/2	1200	833	135	188	61	.57
	900	33	80	105	25	.49
	650	14	48	54	9	.42
10/2	700	19	34	77	17	.48
	450	7	20	31	4	.38
11	800	45	63	101	26	.51
	550	12	34	47	8	.42
12	800	35	58	98	25	.51
	500	11	30	37	6	.40
13	750	28	43	86	21	.49
	500	11	30	37	6	.40
17	750	32	47	92	23	.50
	500	9	34	40	7	.41
18	800	36	49	104	28	.52
	500	11	32	48	9	.43
19	1200	200	115	240	99	.64
	600	12	51	58	12	.45

One last item that will be discussed briefly is the current data presented in figures 4.2 through 4.10. When welding over a tack weld

with a constant potential system, the arc length remains constant, so the stickout decreases and the current increases. There is some evidence of this in most of the plates, but most of the current increases are lost in noise. The only plate for which this is not the case is plate number 5. Plate 5 did not have a ceramic backing strip, and the root gap was large enough to allow the molten metal to drop through it. Therefore, the level of the weld pool in the bare v-groove was very low, and there was a noticeable difference in weld pool height at the tack weld locations. This is evident in the photographs of tack welds 14, 15 and 16 shown in figure 4.43. The photograph of tack weld 14 shows that the weld pool did not drop through the arc gap at the very beginning of the weld. This explains the higher current at the beginning of figure 4.6.

On average, the current increased 12 A while going over the tack welds, from approximately 215 A to approximately 227 A. Since the constant potential power supply maintains an essentially constant arc length, this change in current is due to a change in electrode stickout. Equation A.15 in appendix A is Lesnewich's empirical formula for melting rate, converted to mks units. Plate 5 was welded with a .035" wire at 472 ipm. The calculated stickout distance is 9.57 mm at 215 A and 8.15 m at 227 A. The stickout decreases by 1.4 mm to maintain the same arc length. The actual weld metal is about 4 mm higher on the tack welds than in the bare groove, but because the arc impinges to varying degrees at all levels of the v-groove, the increase in bottom level only partially affects it. Therefore, the self-adjustment in stickout that occurs in constant potential welding while going over a tack weld does not substantially increase the current.

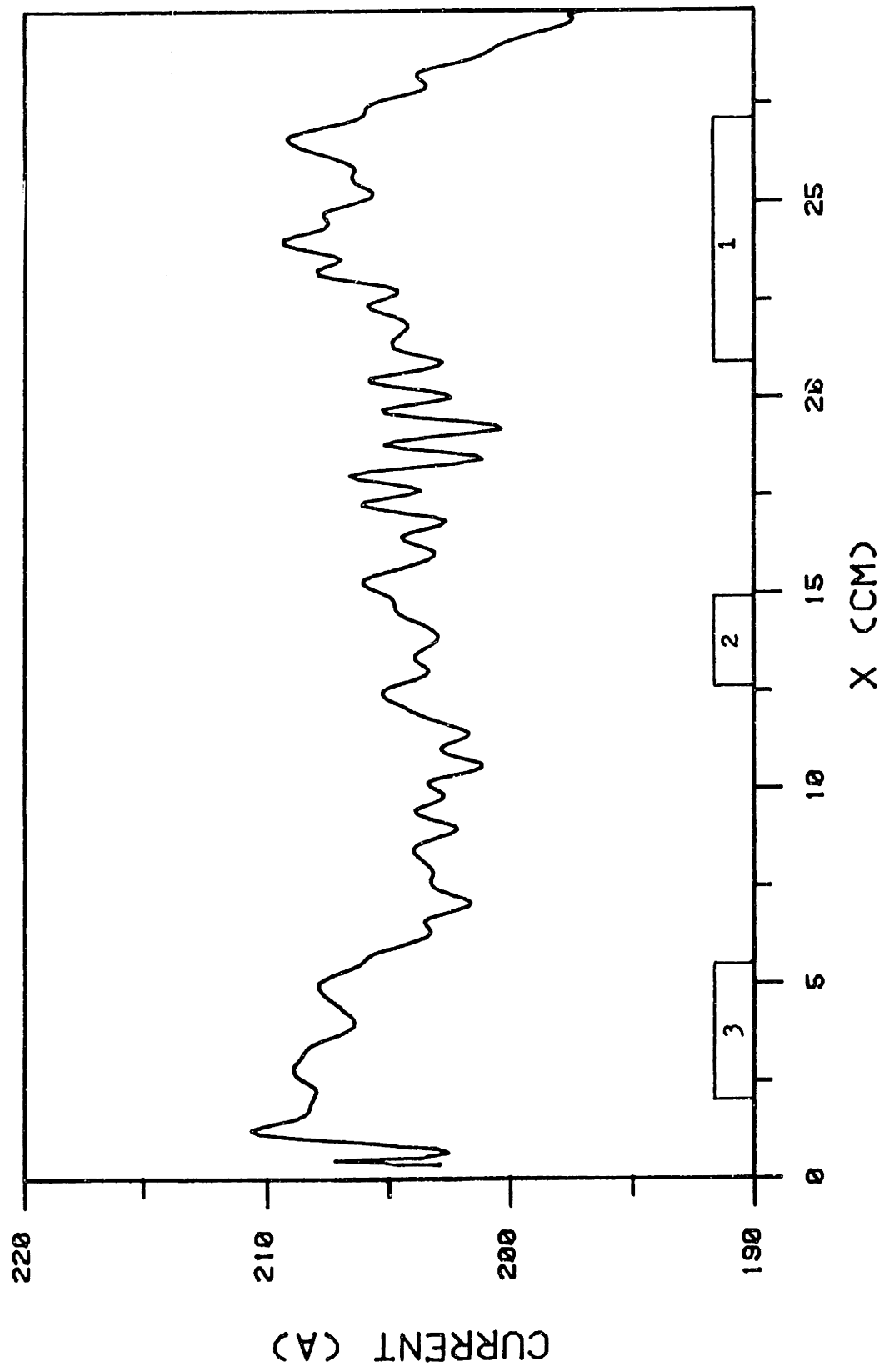

Figure 4.2 Welding current for plate 1.

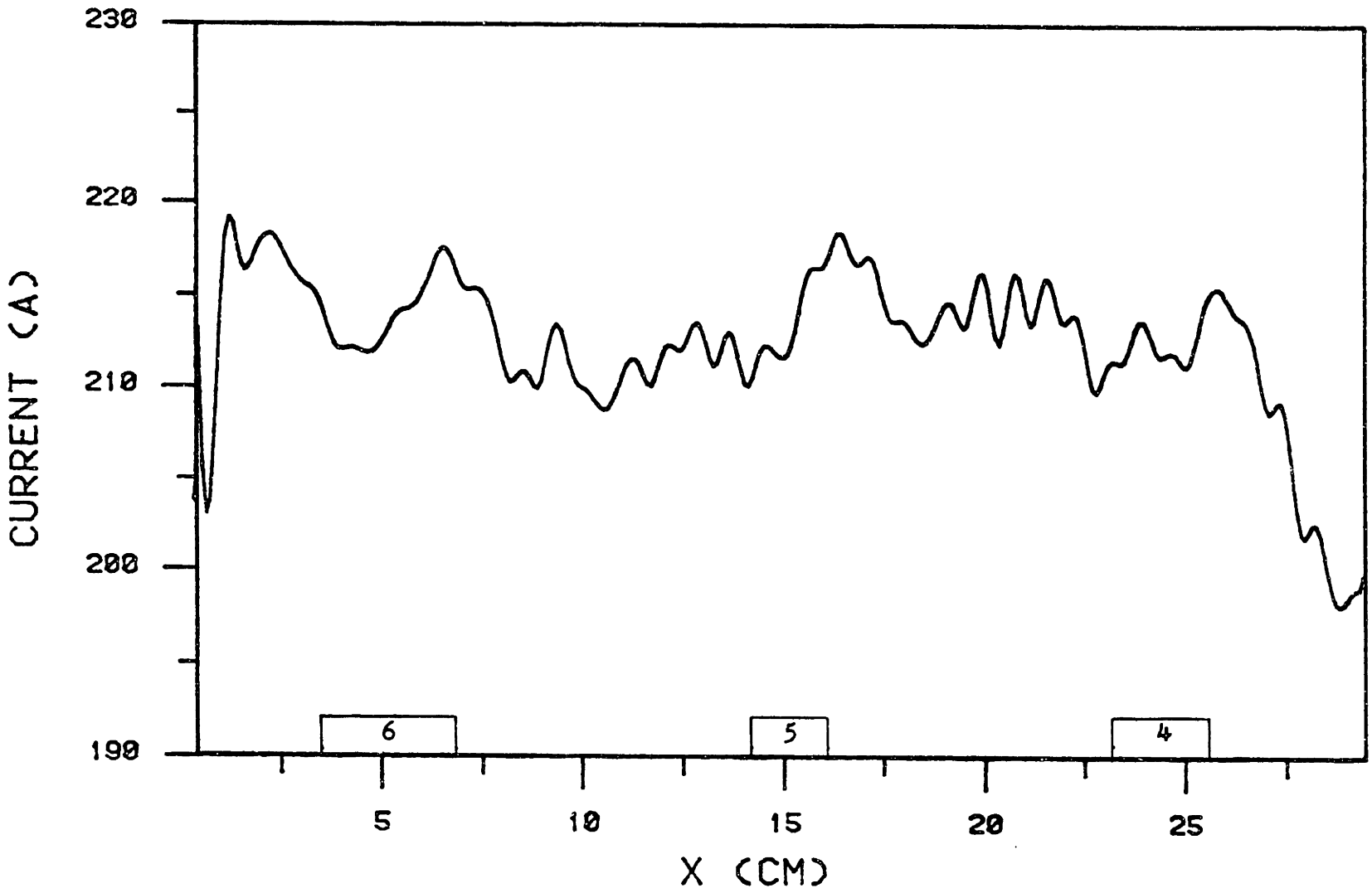

Figure 4.3 Welding current for plate 2.

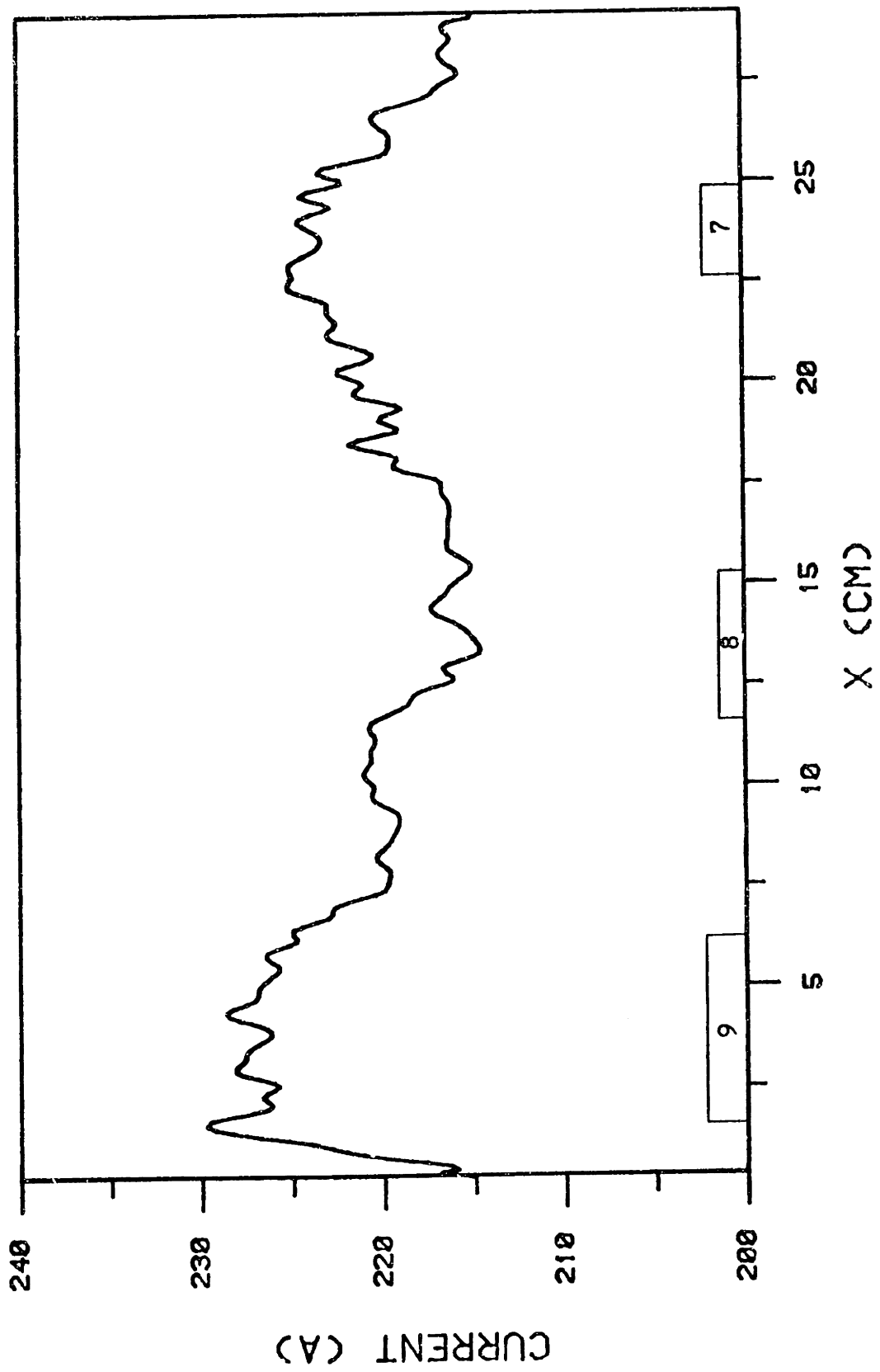

Figure 4.4 Welding current for plate 3.

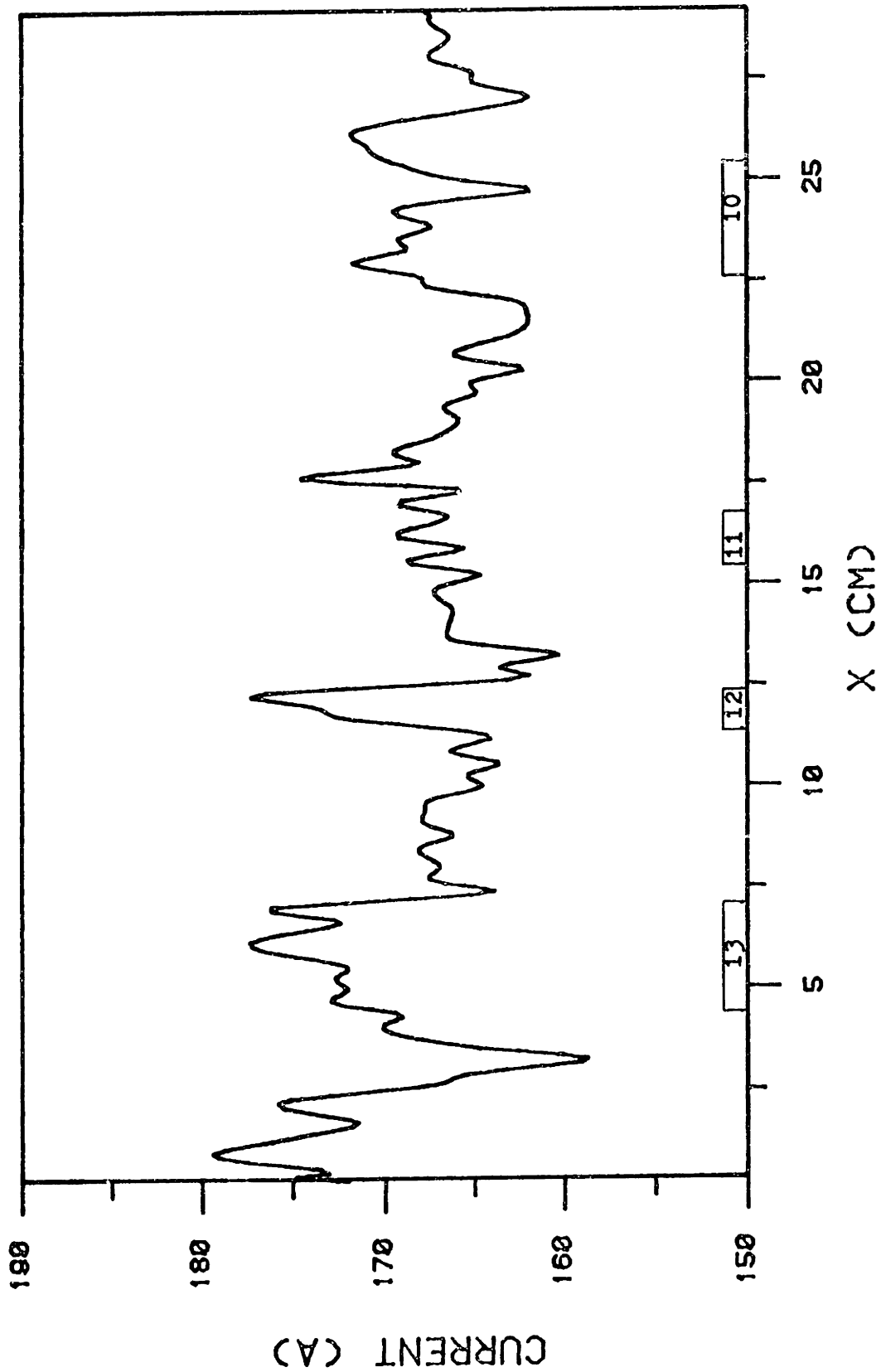

Figure 4.5 Welding current for plate 4.

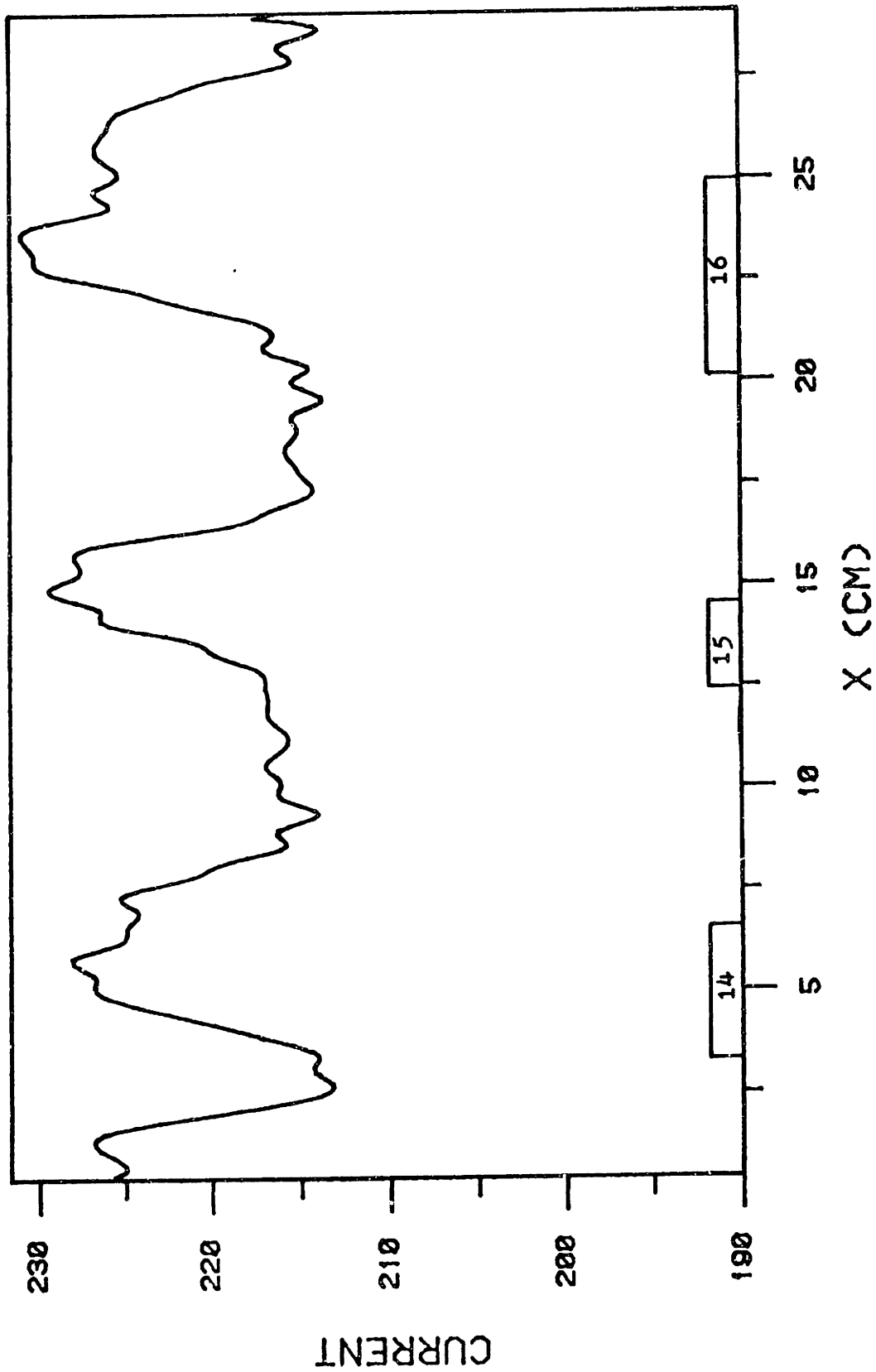

Figure 4.6 Welding current for plate 5.

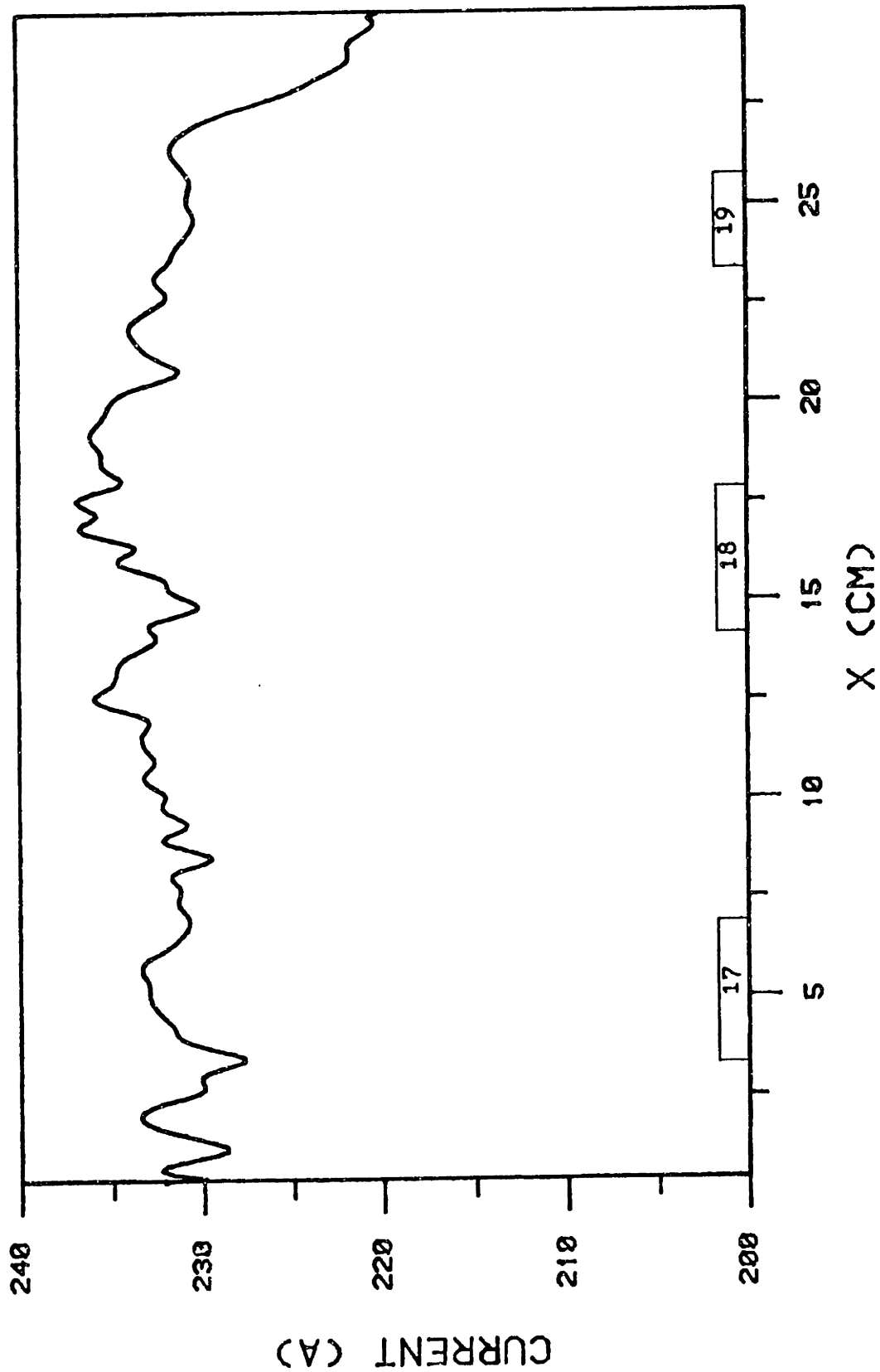

Figure 4.7 Welding current for plate 6.

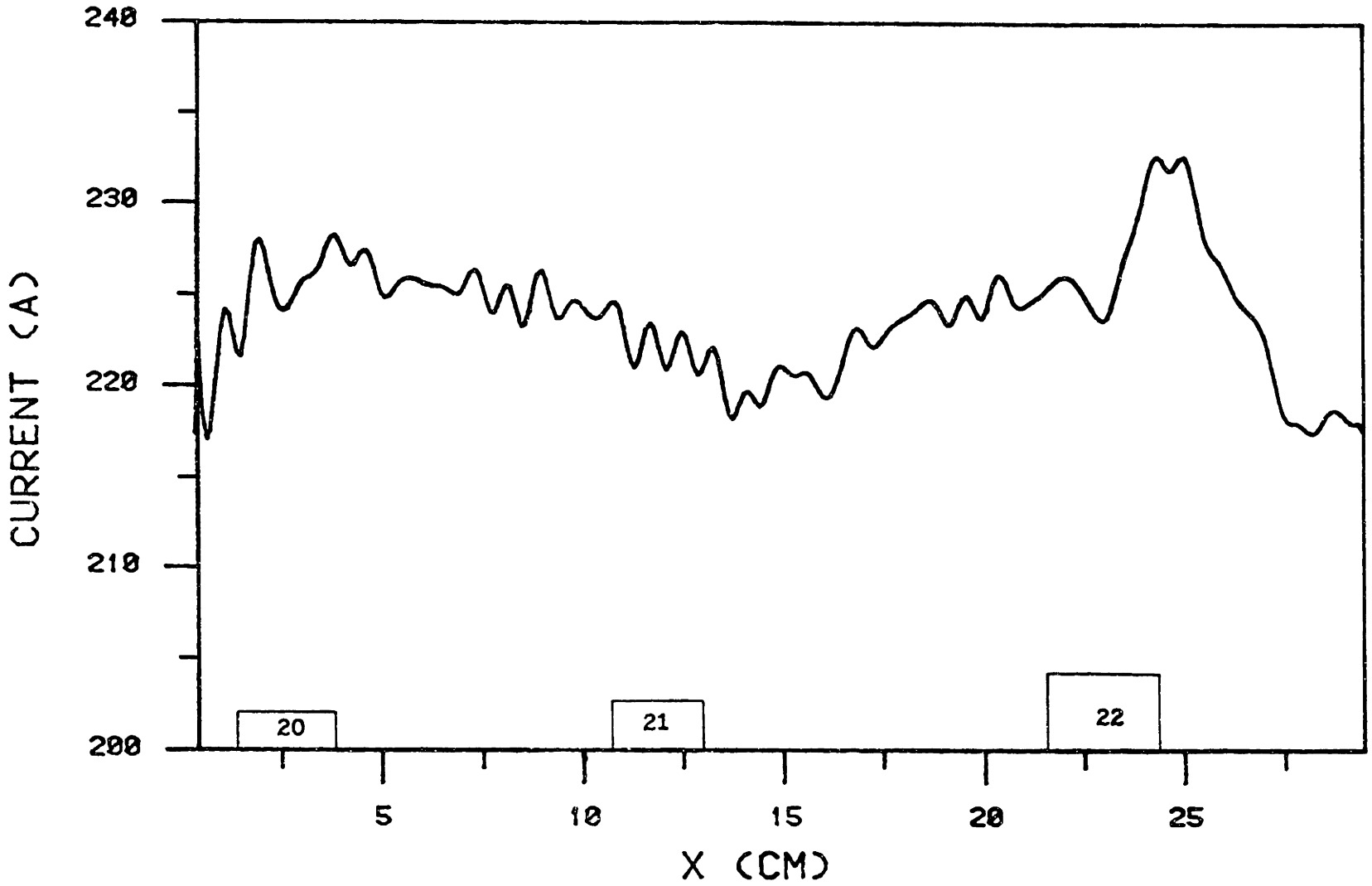

Figure 4.8 Welding current for plate 7.

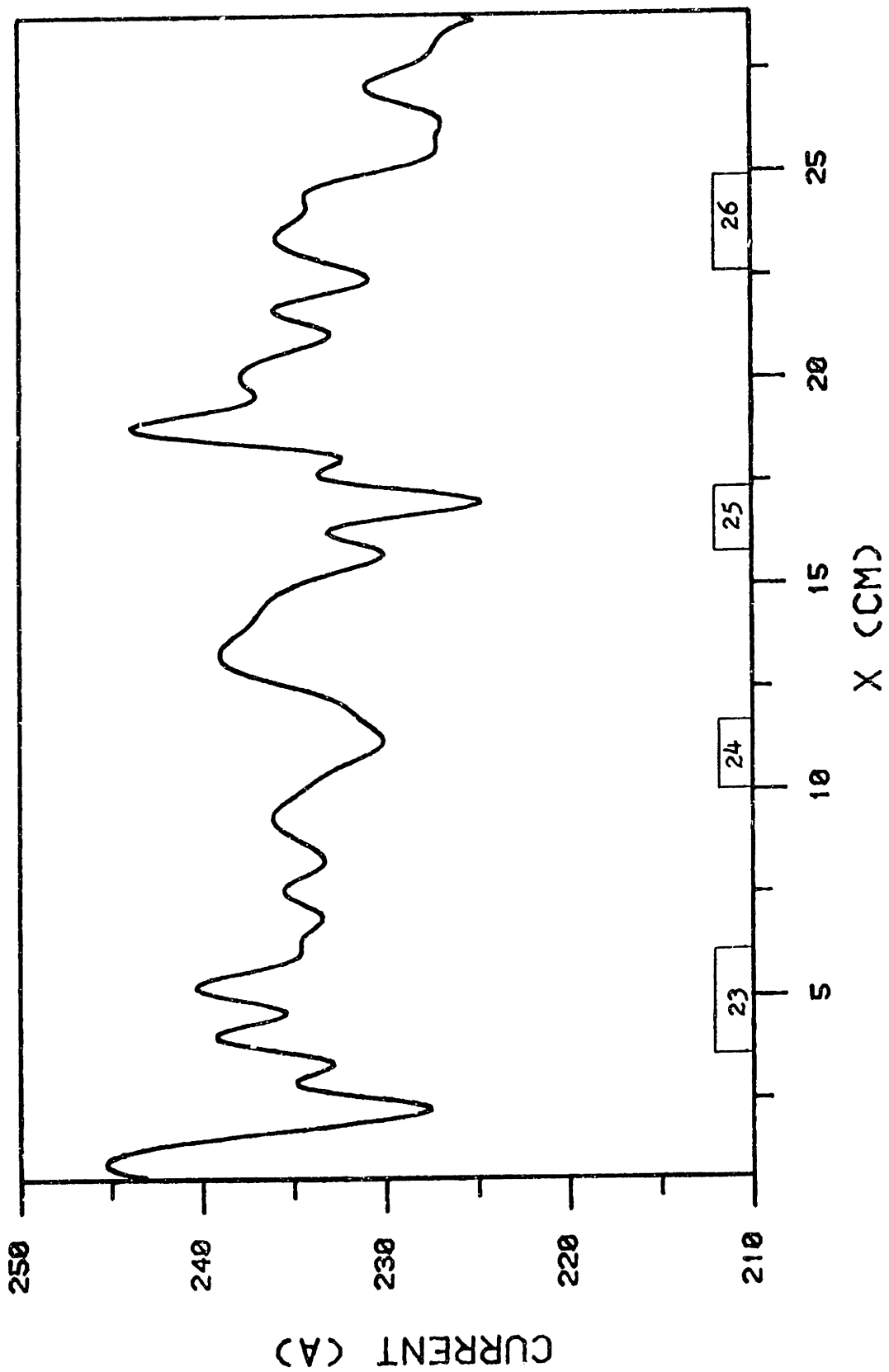

Figure 4.9 Welding current for plate 8.

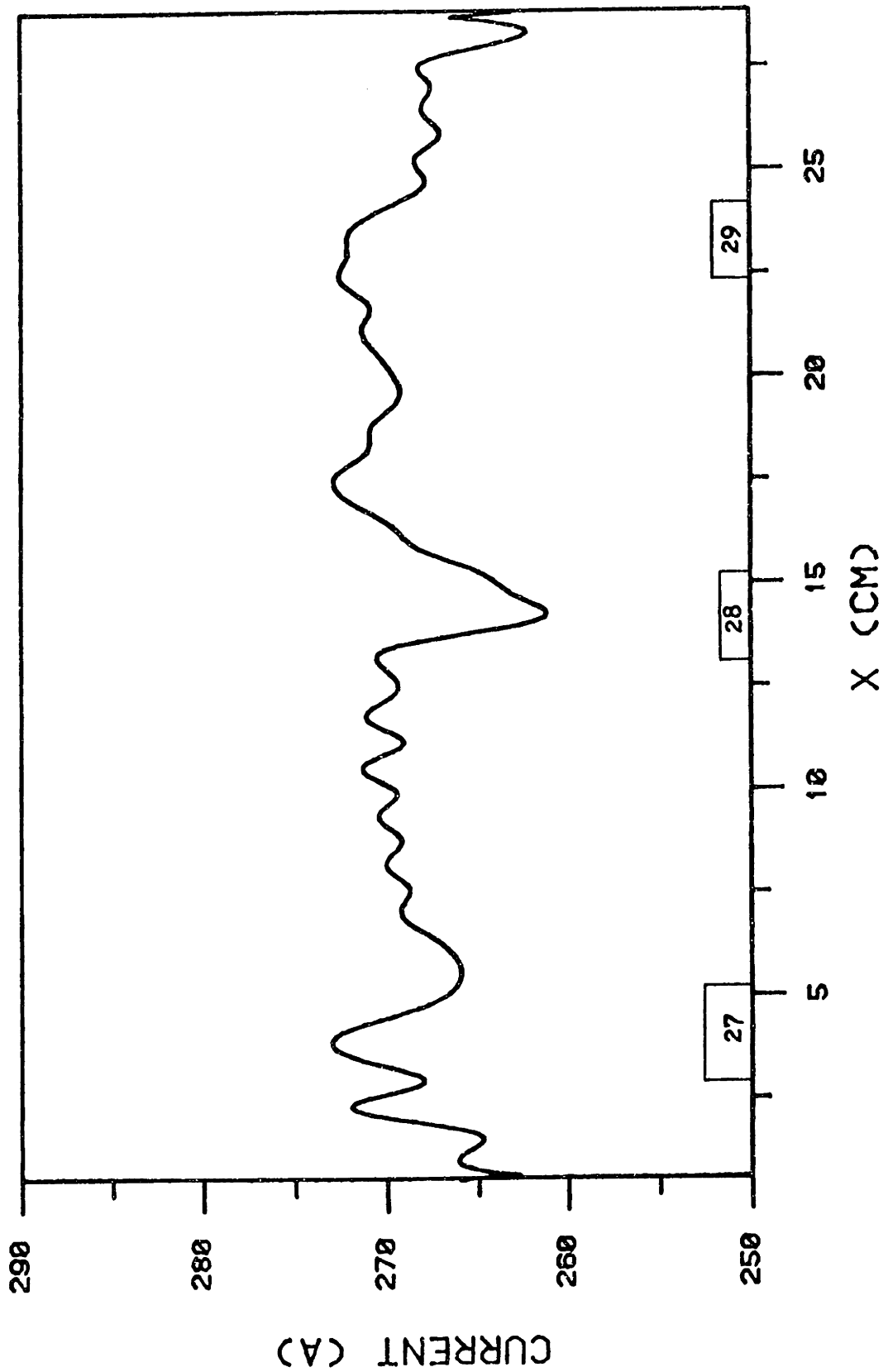

Figure 4.10 Welding current for plate 9.

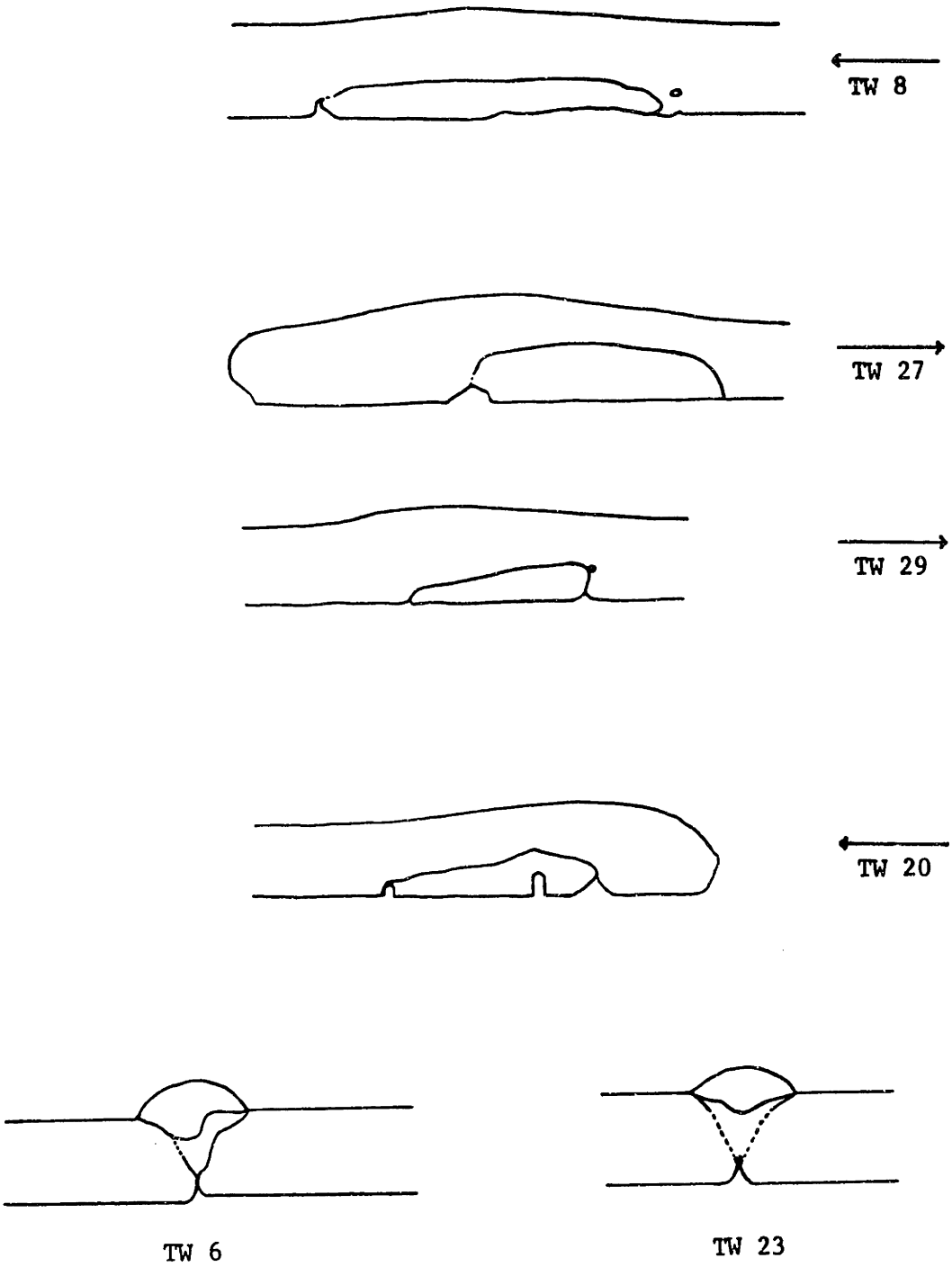

Figure 4.11 Selected sketches of tack weld cross sections. Arrows on longitudinal sections indicate direction of torch travel. Dotted lines indicate lack of fusion.

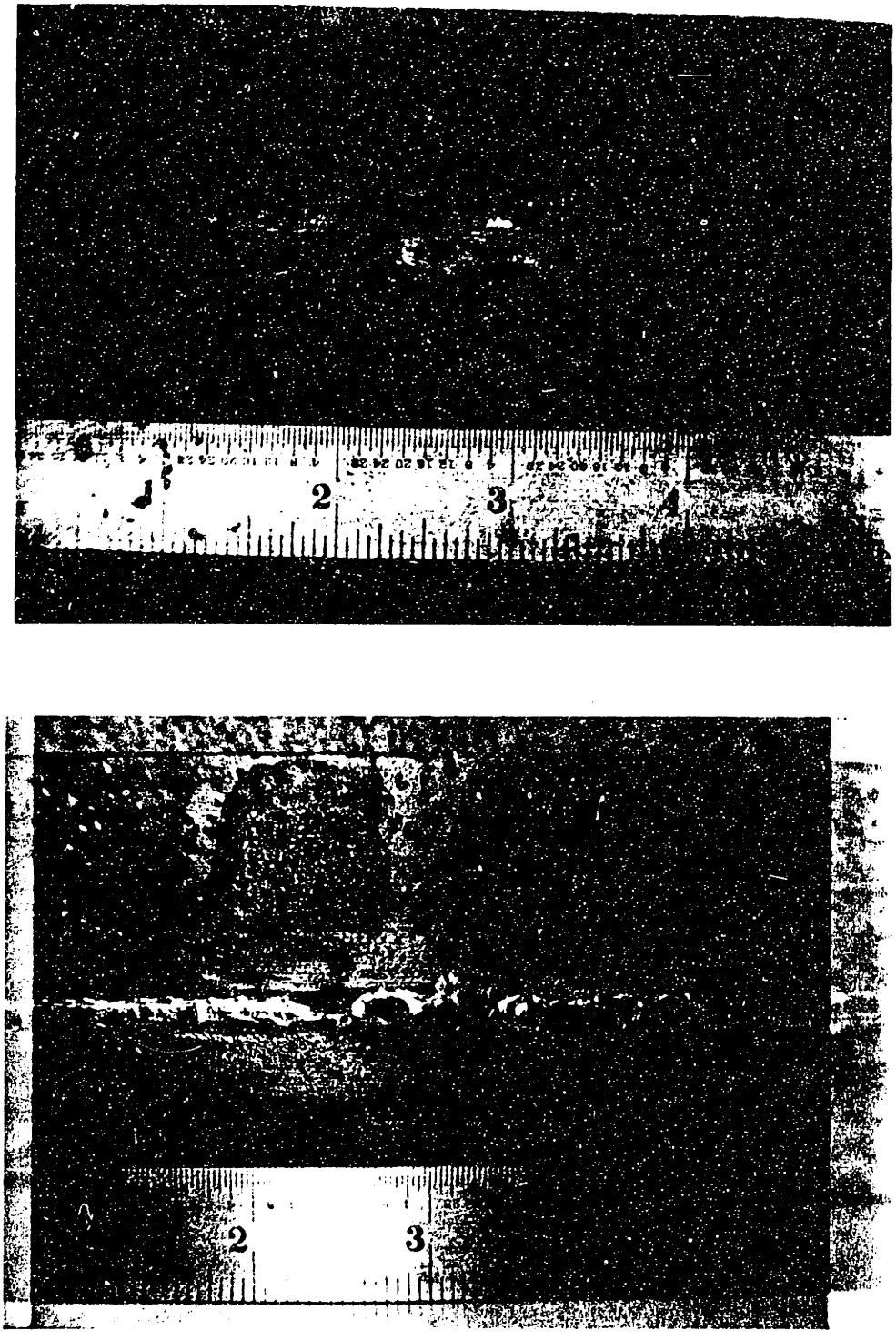

Figure 4.12 Photographs of backside of TW 21: (top) before, and (bottom) after final welding.

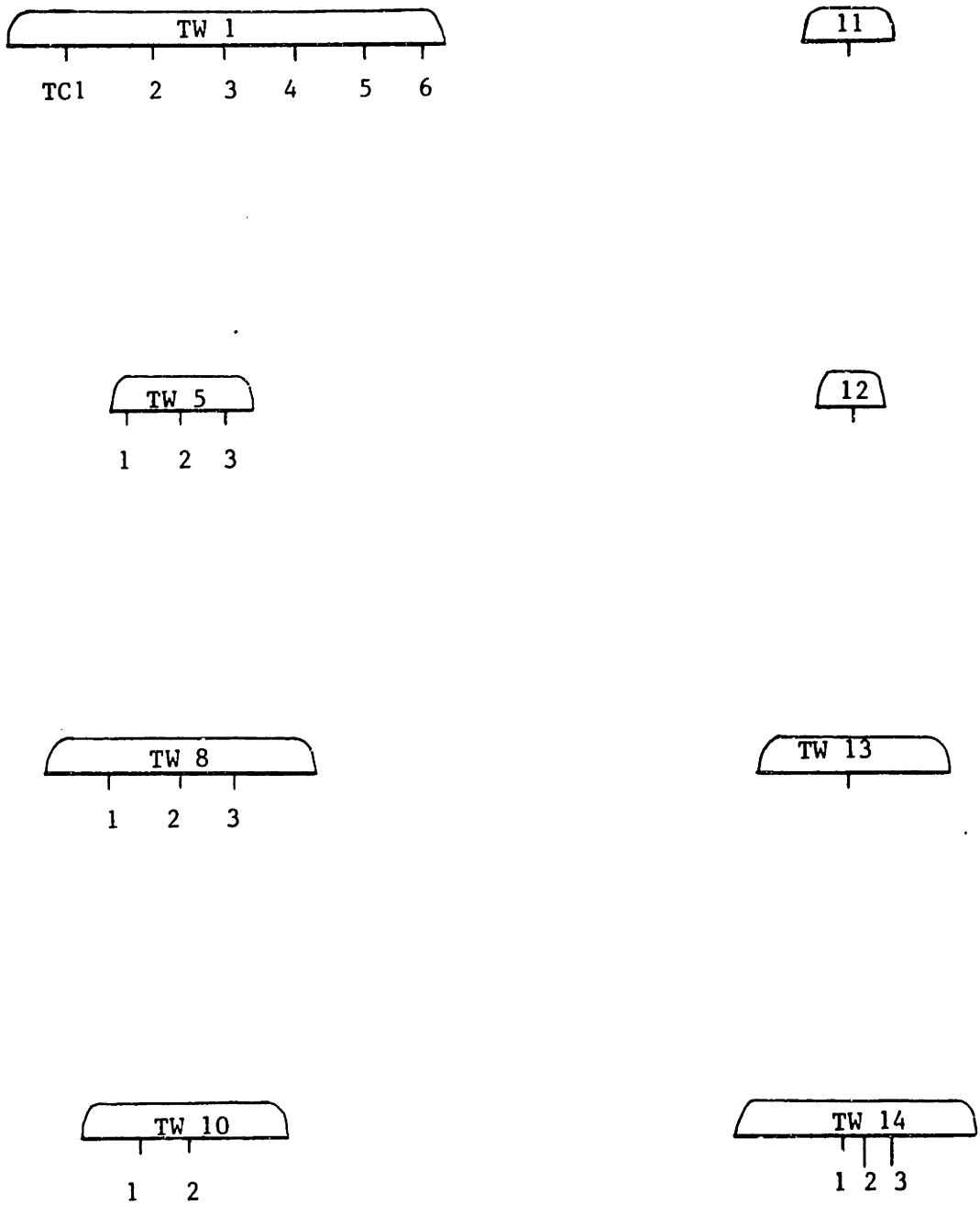

Figure 4.13 Thermocouple locations. Only the tack weld lengths and the longitudinal positions of the thermocouple markers are to scale.

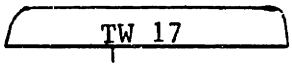
TW 17

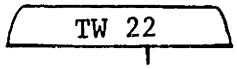
TW 22

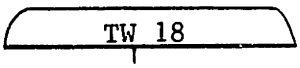
TW 18

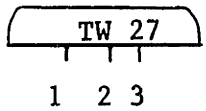
TW 27
1 2 3

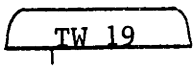
TW 19

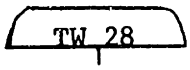
TW 28

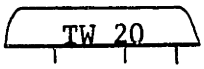
TW 20
1 2 3

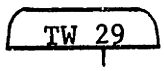
TW 29

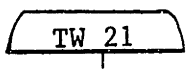
TW 21

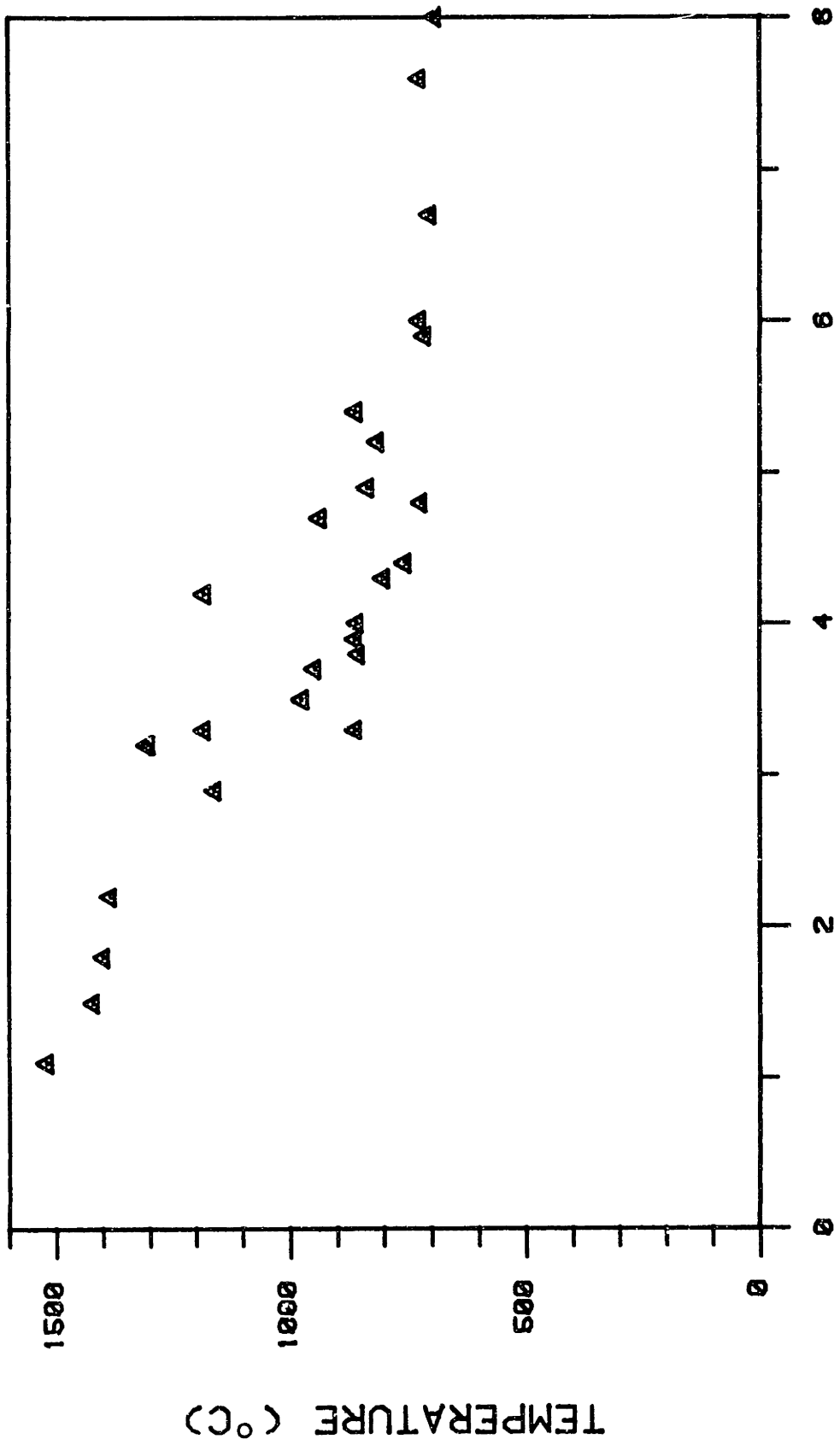

Figure 4.14 Maximum temperature versus thermocouple depth below surface.

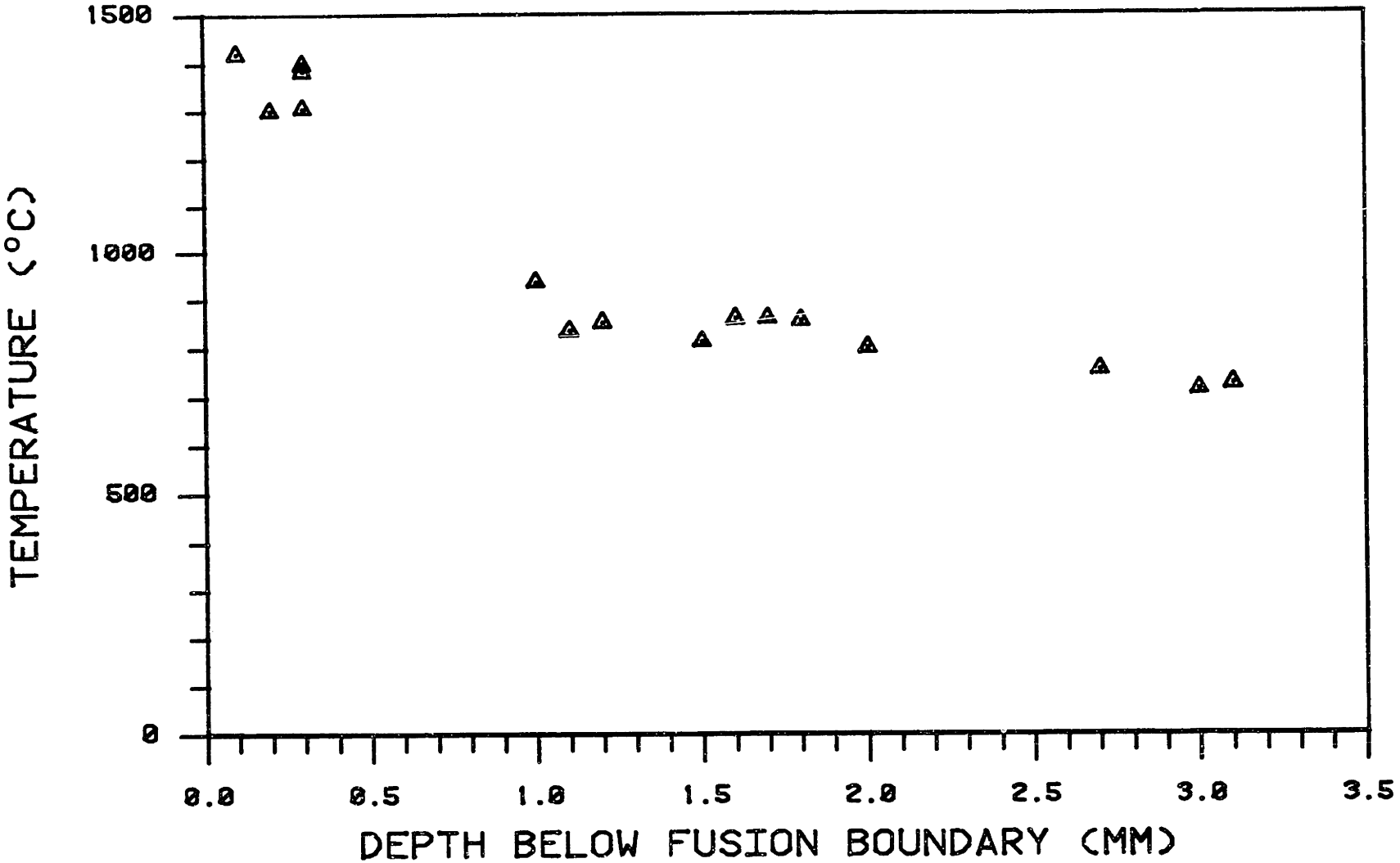

Figure 4.15 Maximum temperature versus thermocouple depth below fusion boundary.

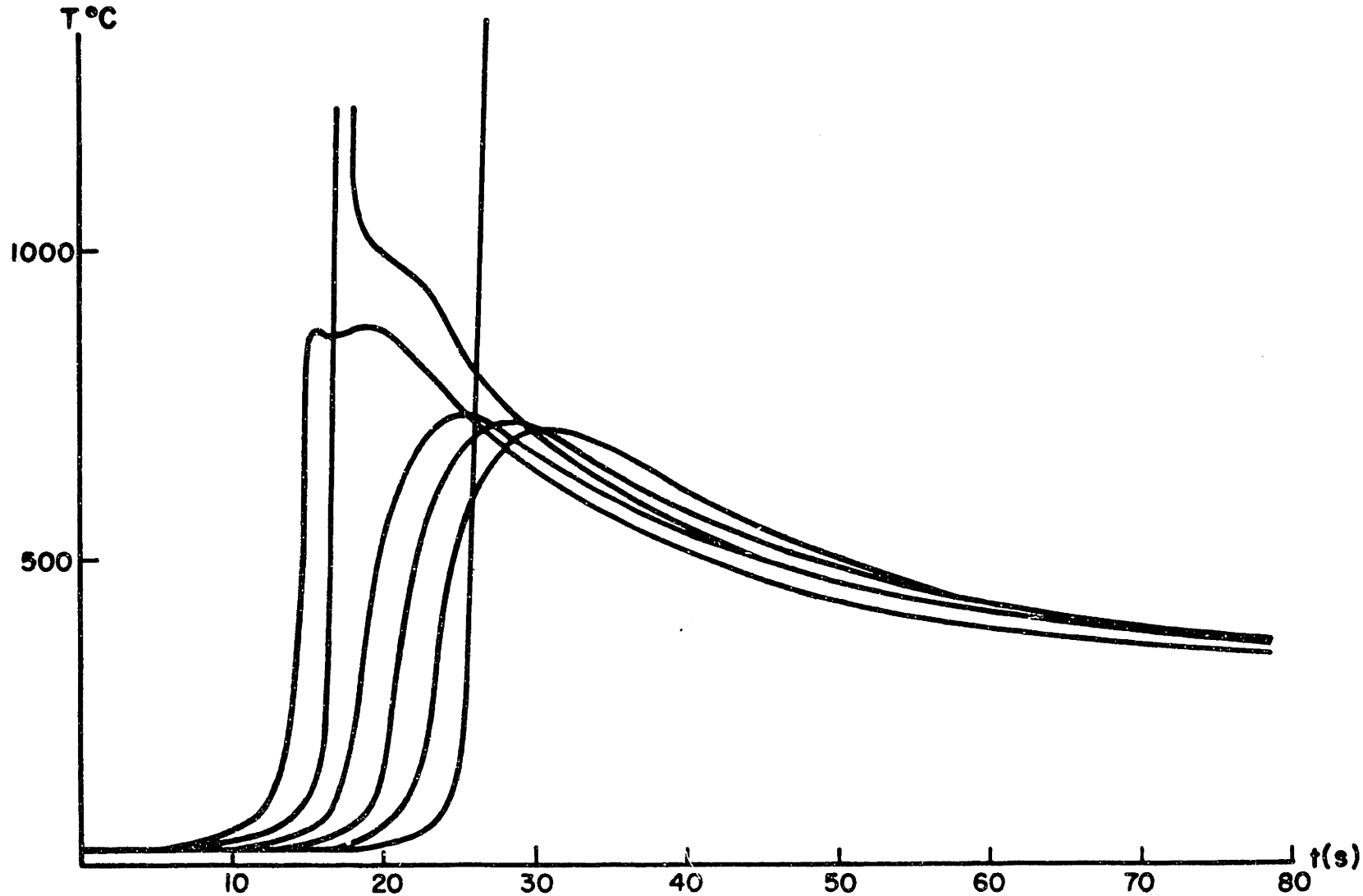

Figure 4.16 Thermocouple profiles: tack weld 1. From left to right: thermocouple 6, 5, 4, 3, 2, 1.

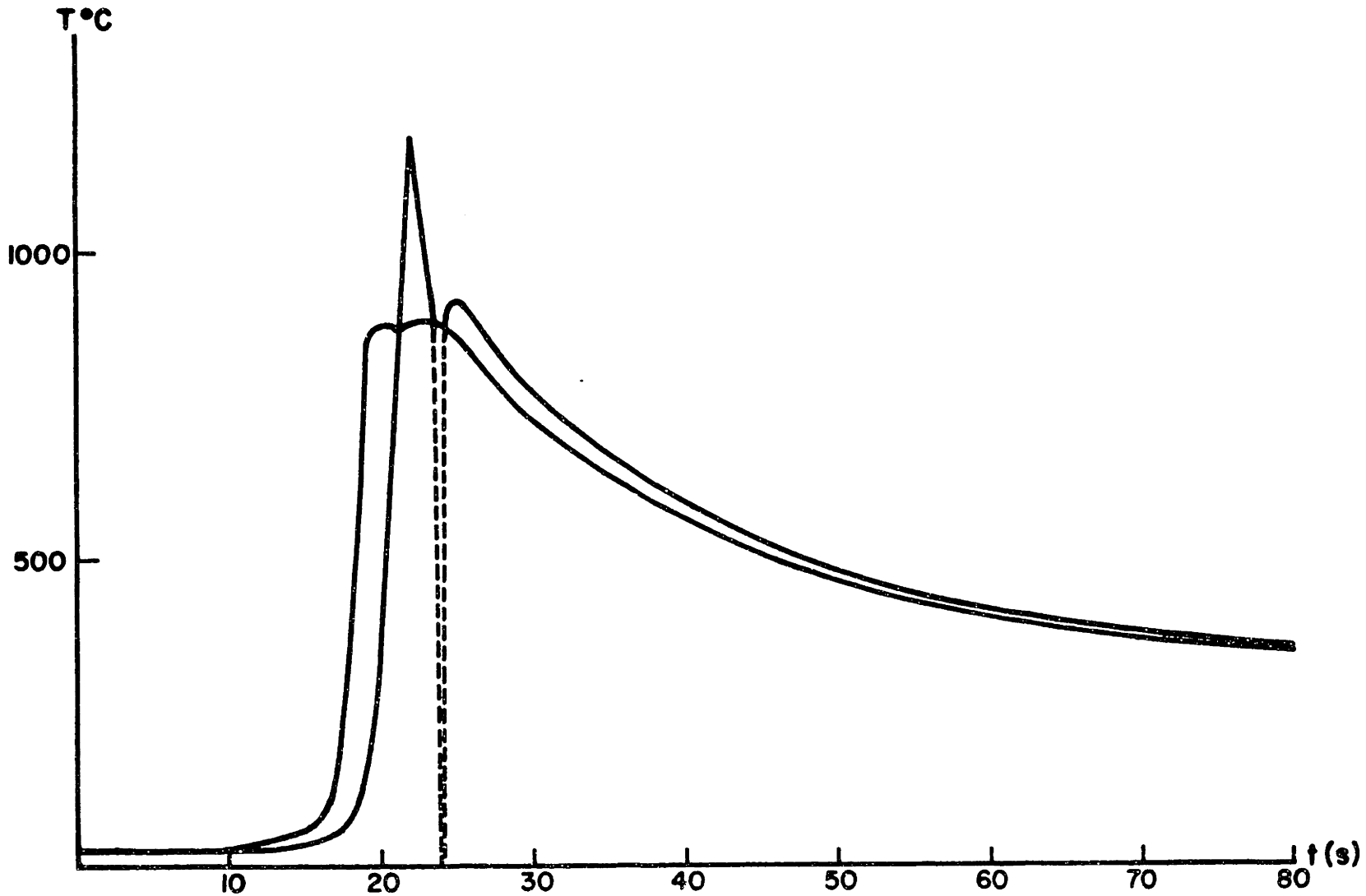

Figure 4.17 Thermocouple profiles: tack weld 5. From left to right: thermocouple 3, 1.

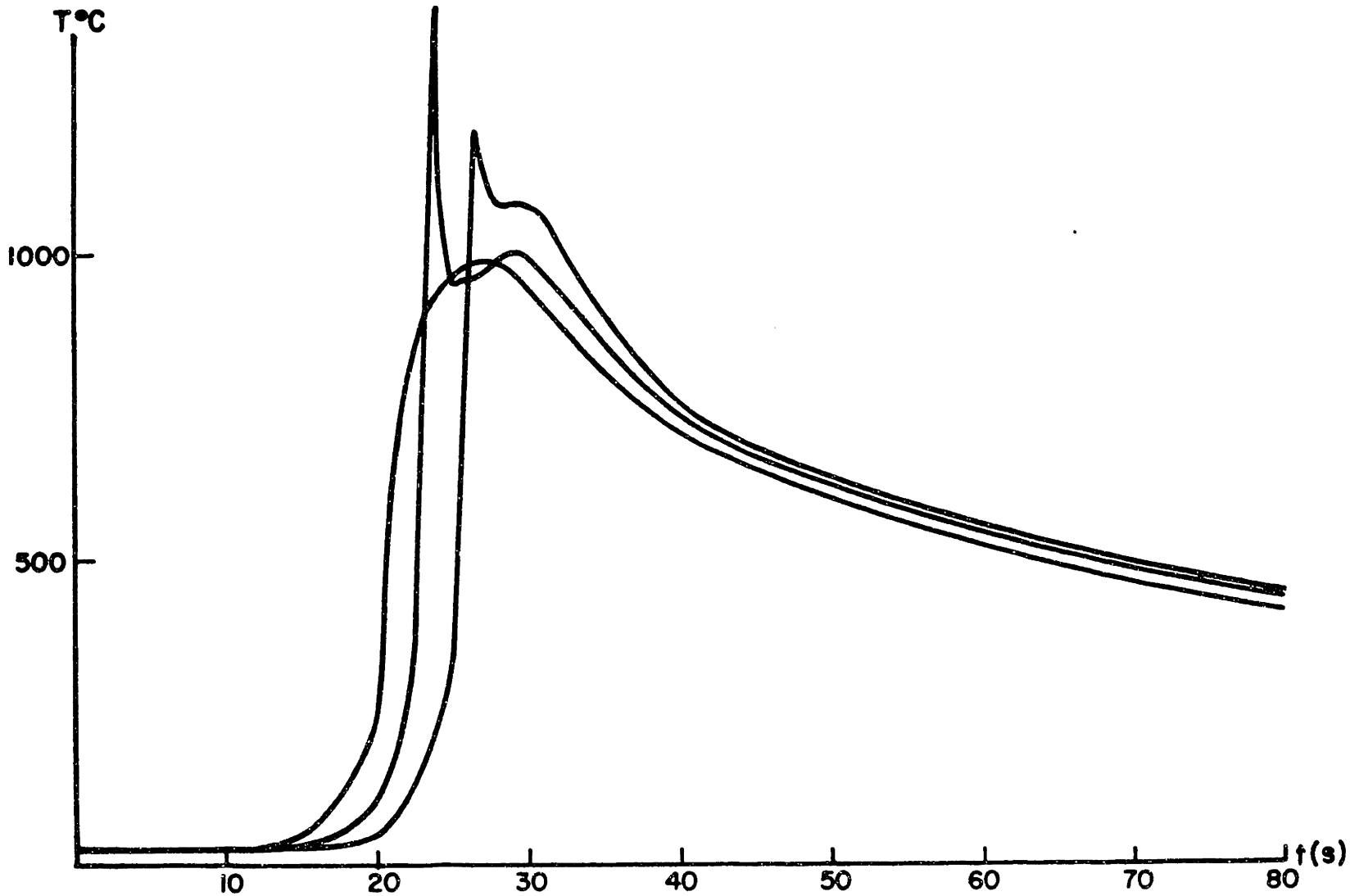

Figure 4.18 Thermocouple profiles: tack weld 8. From left to right: thermocouple 3, 2, 1.

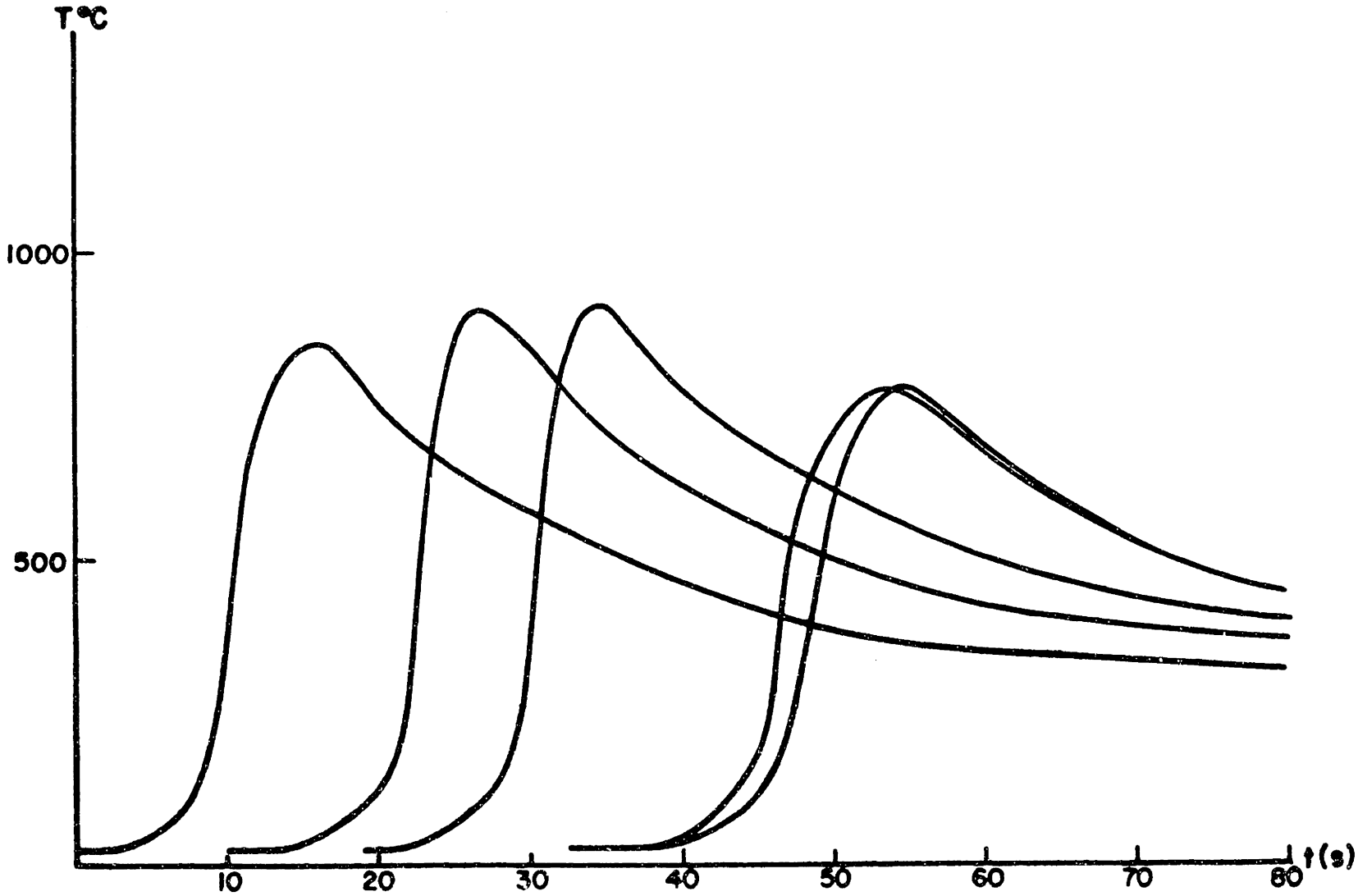

Figure 4.19 Thermocouple profiles. From left to right: tack weld 13, 12, 11, 10/2, 10/1.

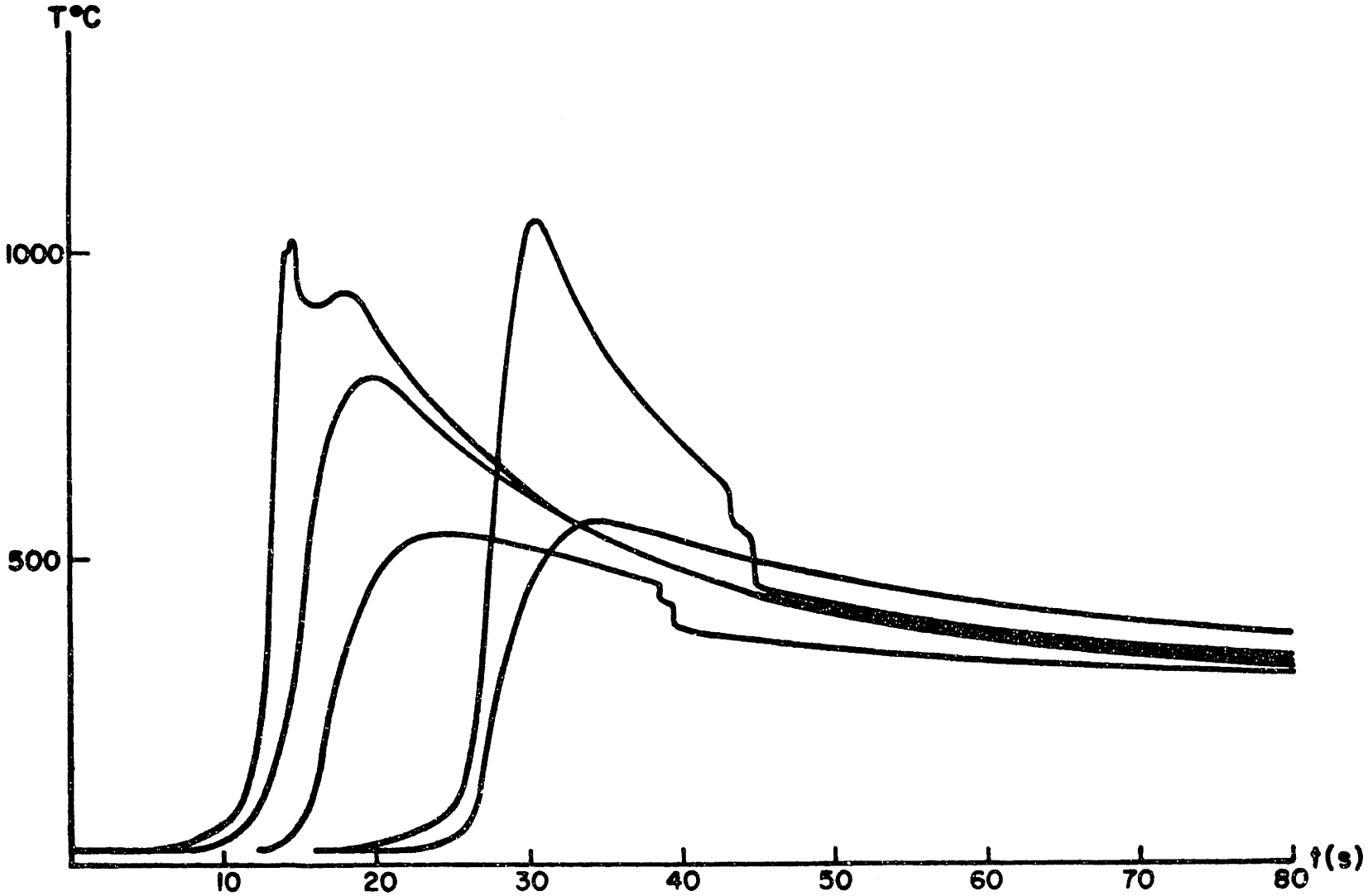

Figure 4.20 Thermocouple profiles: tack weld 14. From left to right: thermocouple 1, 2, 3, 4, 5.

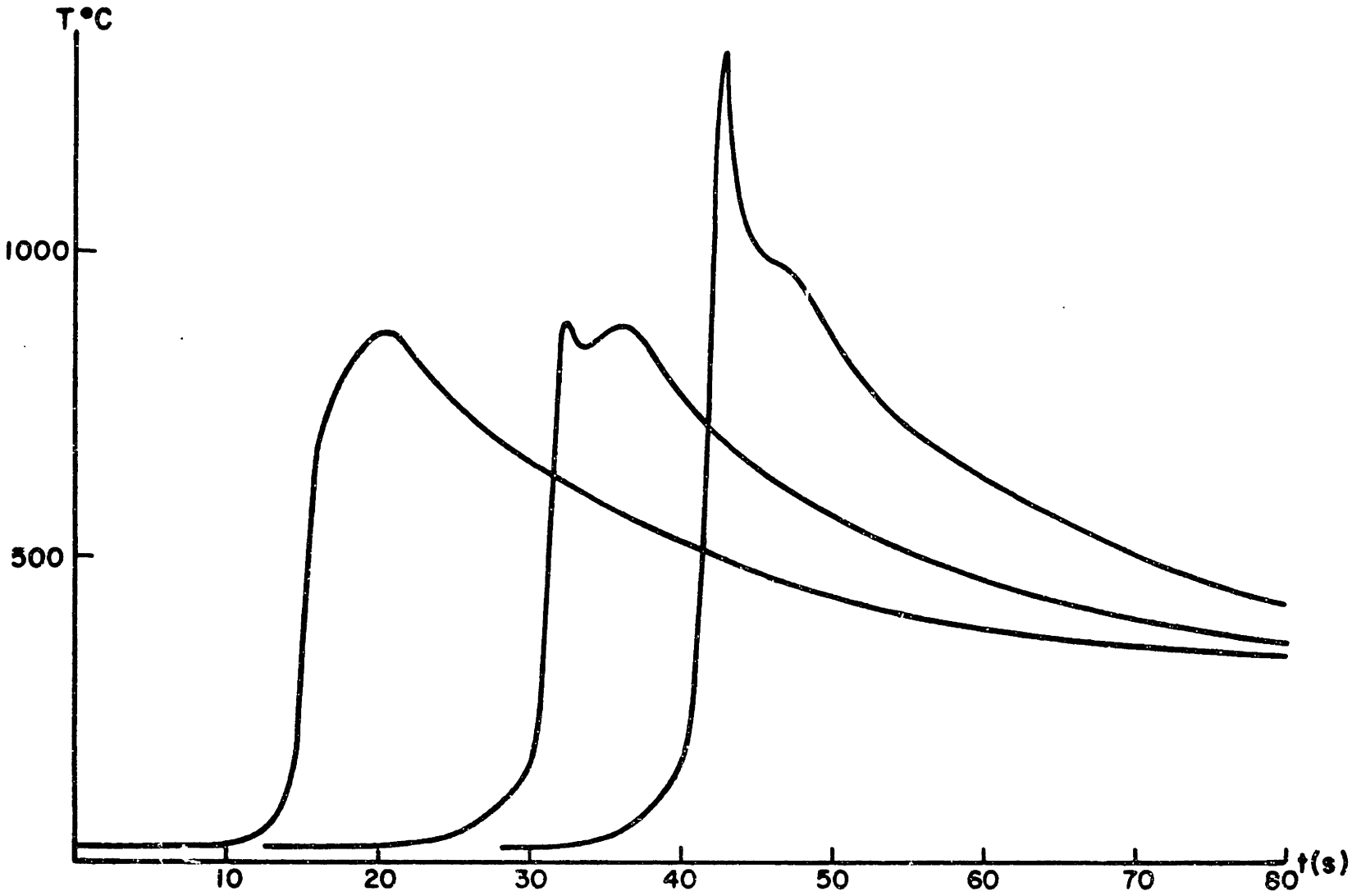

Figure 4.21 Thermocouple profiles. From left to right: tack weld 17, 18, 19.

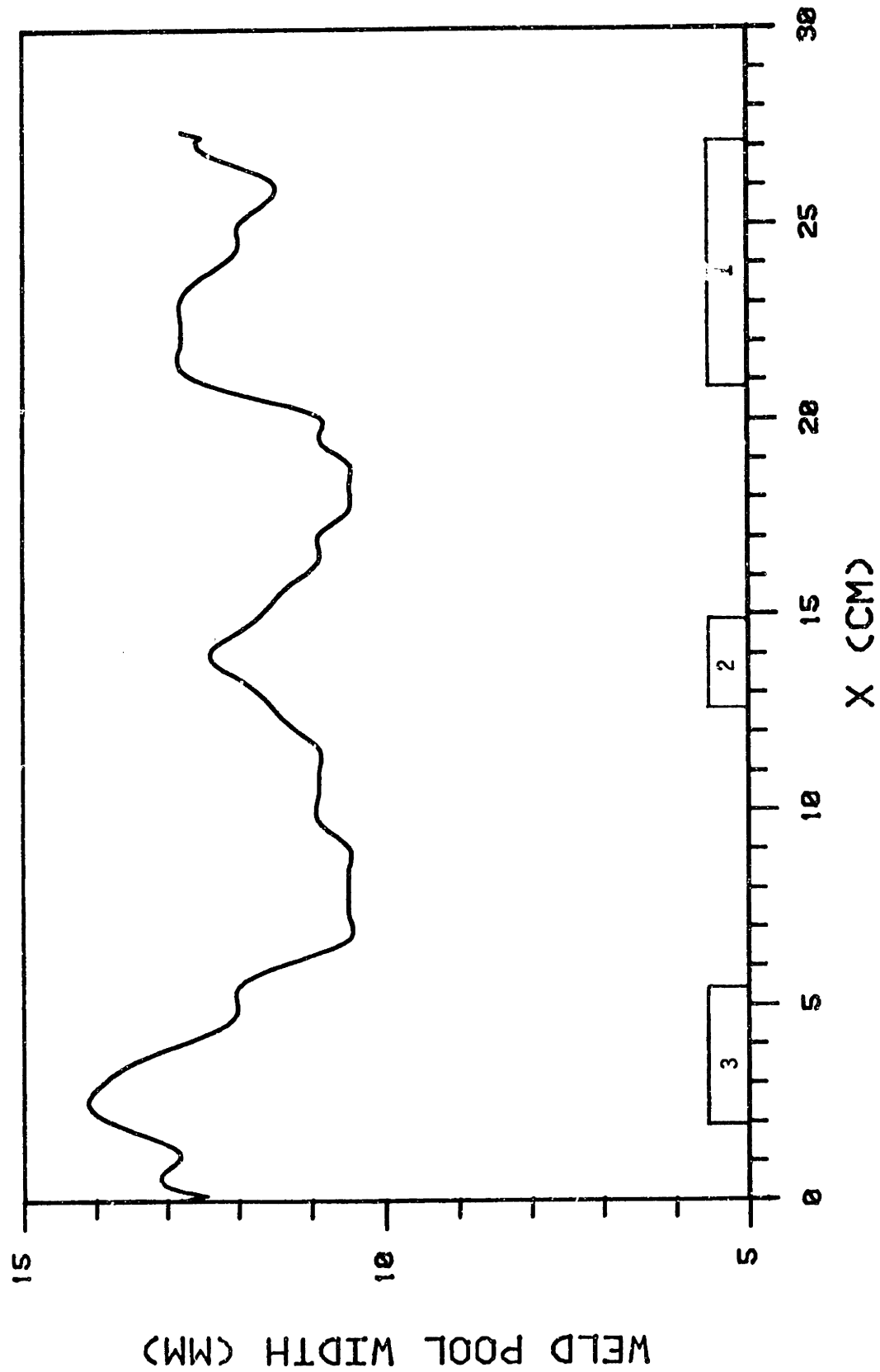

Figure 4.22 Videotaped weld pool width: plate 1.

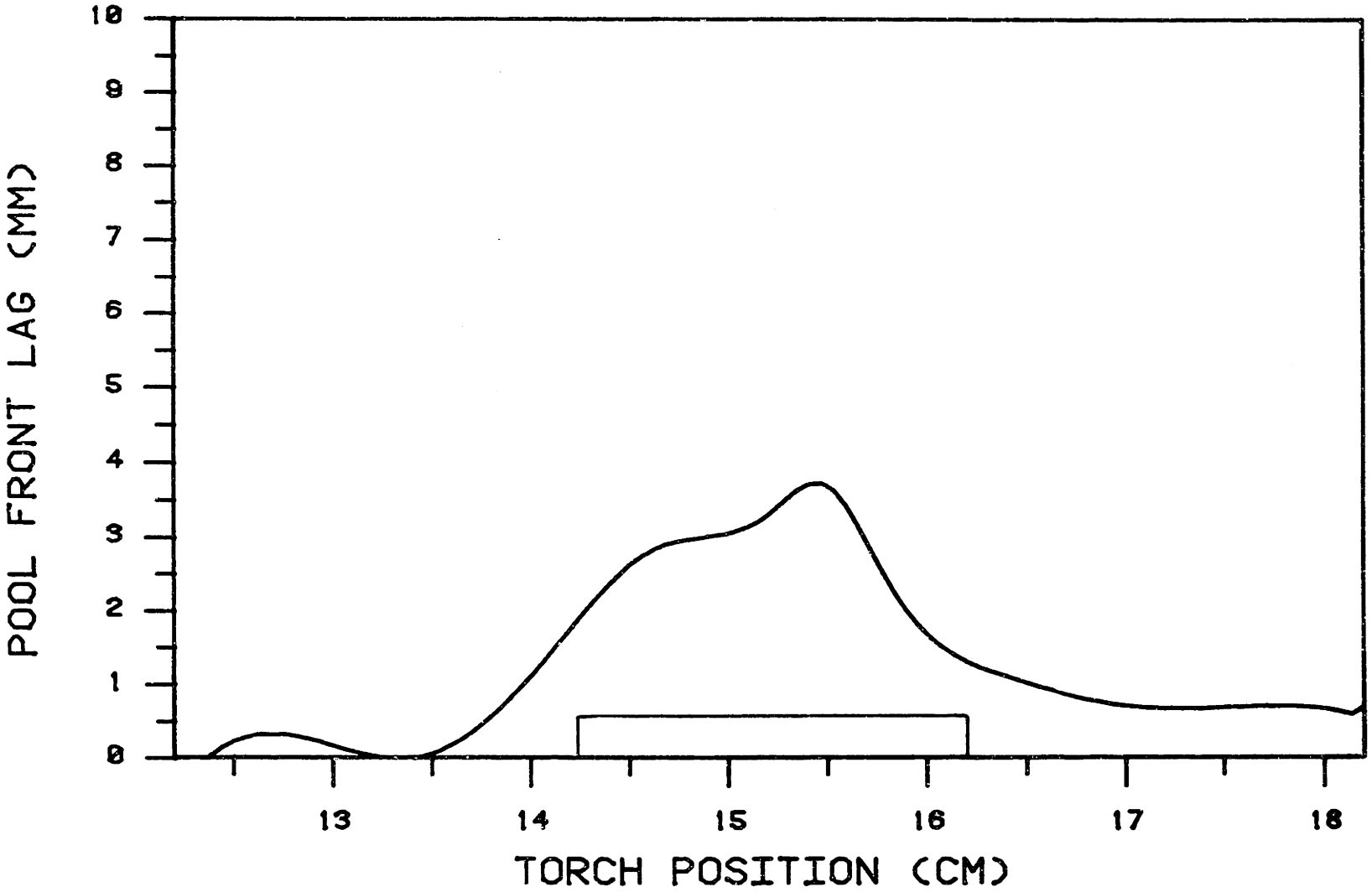

Figure 4.23 Videotaped weld pool advance: tack weld 5.

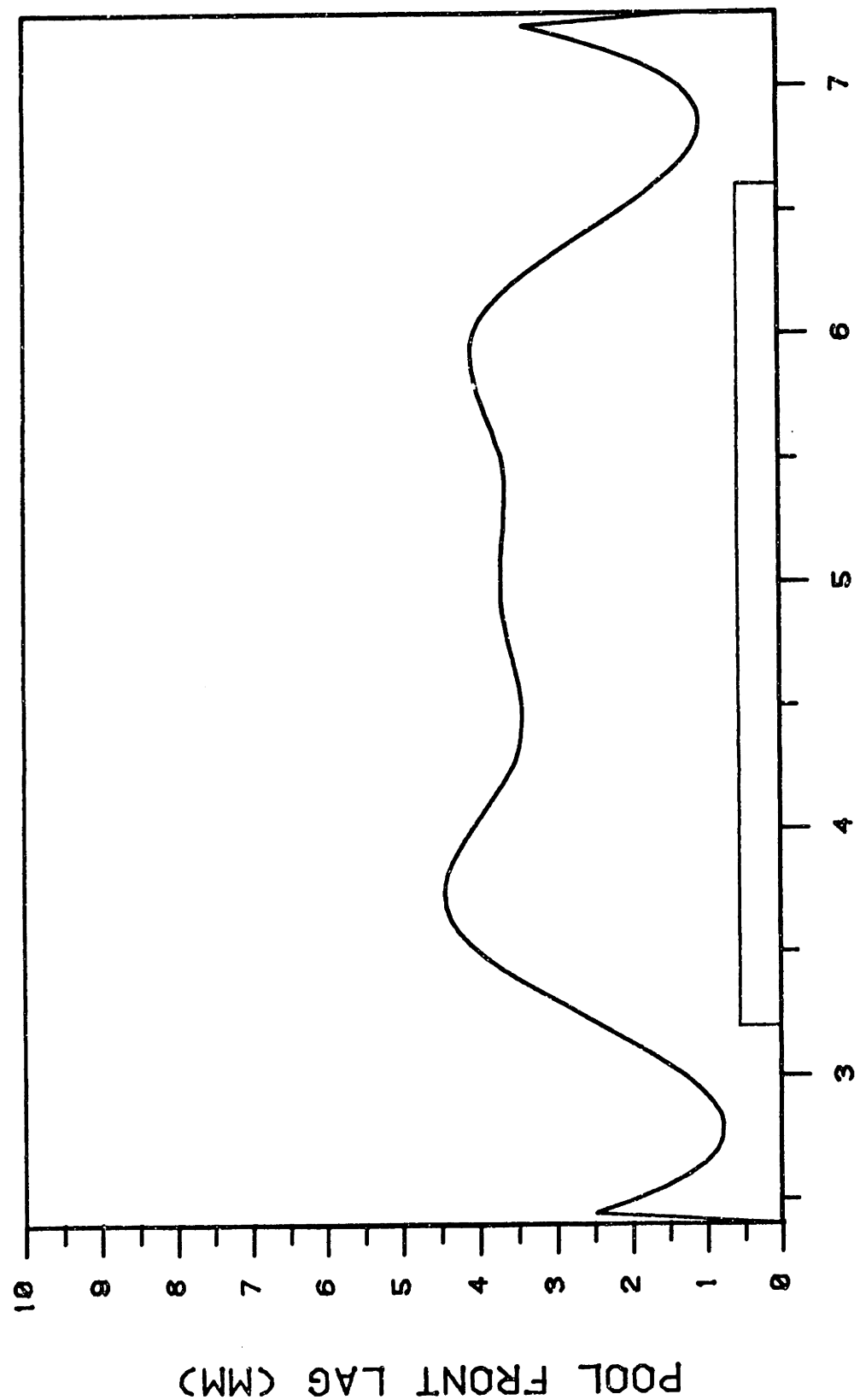

Figure 4.24 Videotaped weld pool advance: tack weld 6.

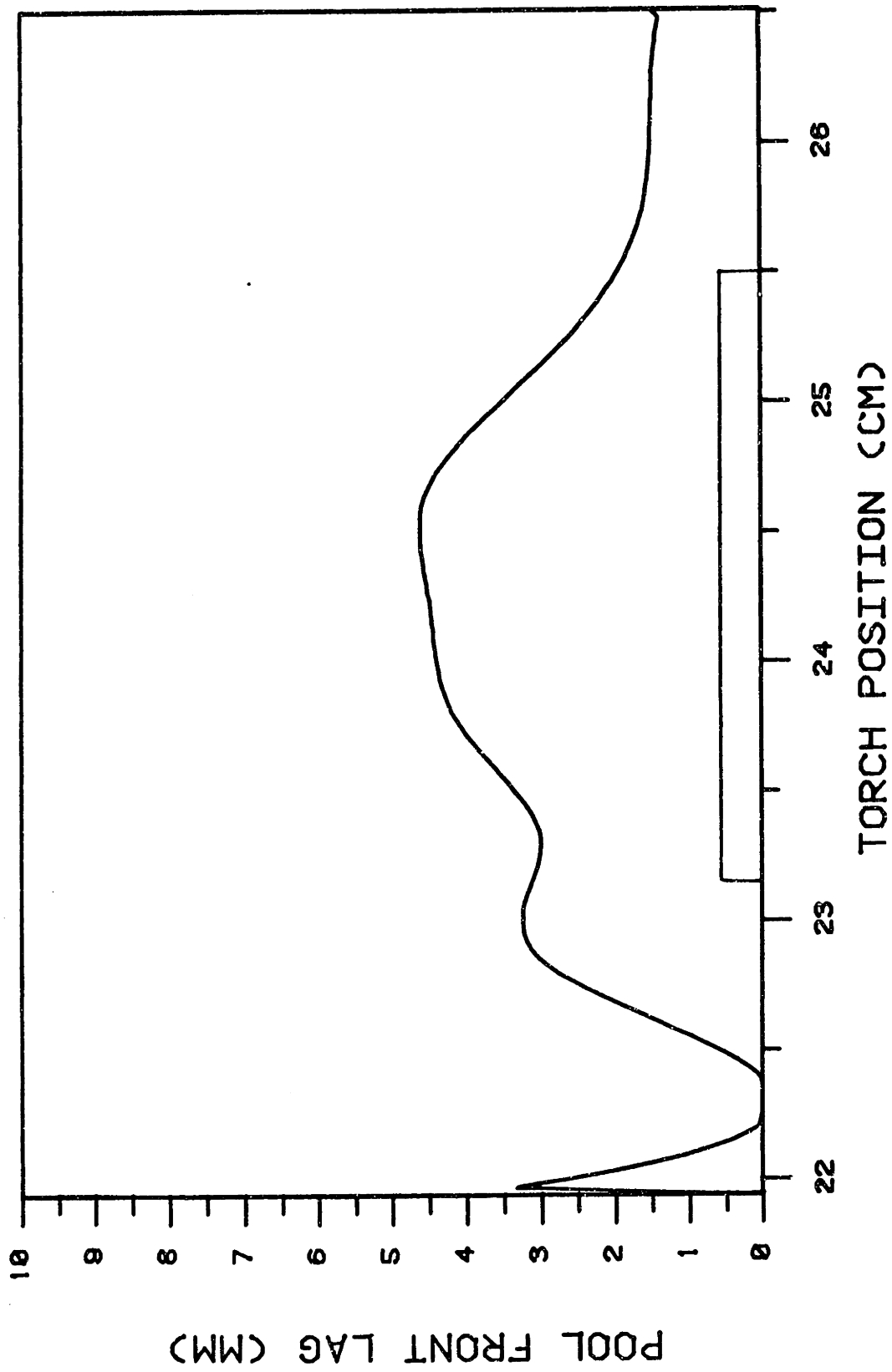

Figure 4.25 Videotaped weld pool advance: tack weld 7.

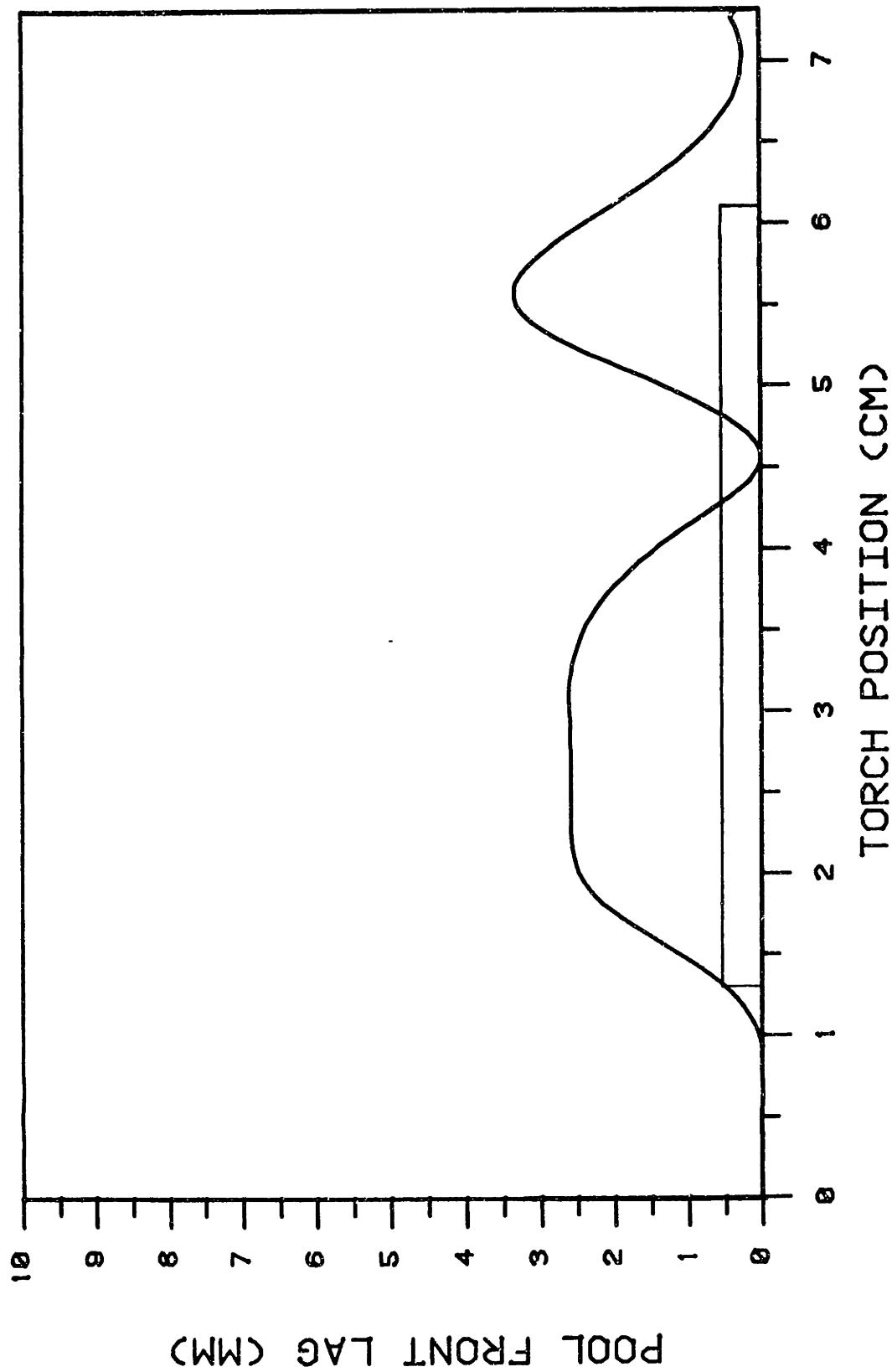

Figure 4.26 Videotaped weld pool advance: tack weld 9.

(a)

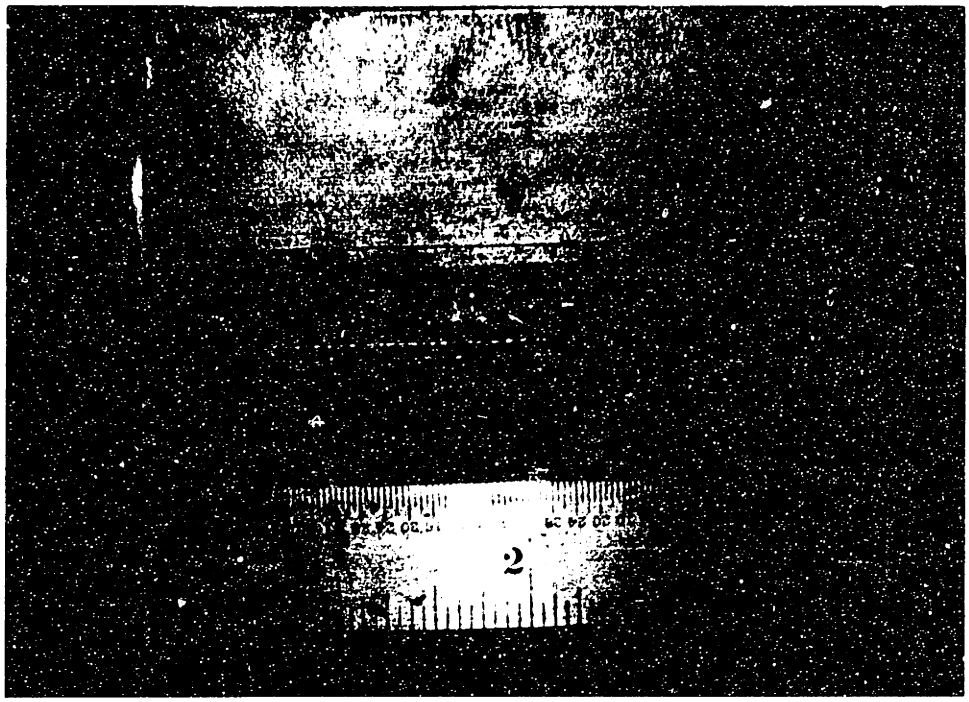

(b)

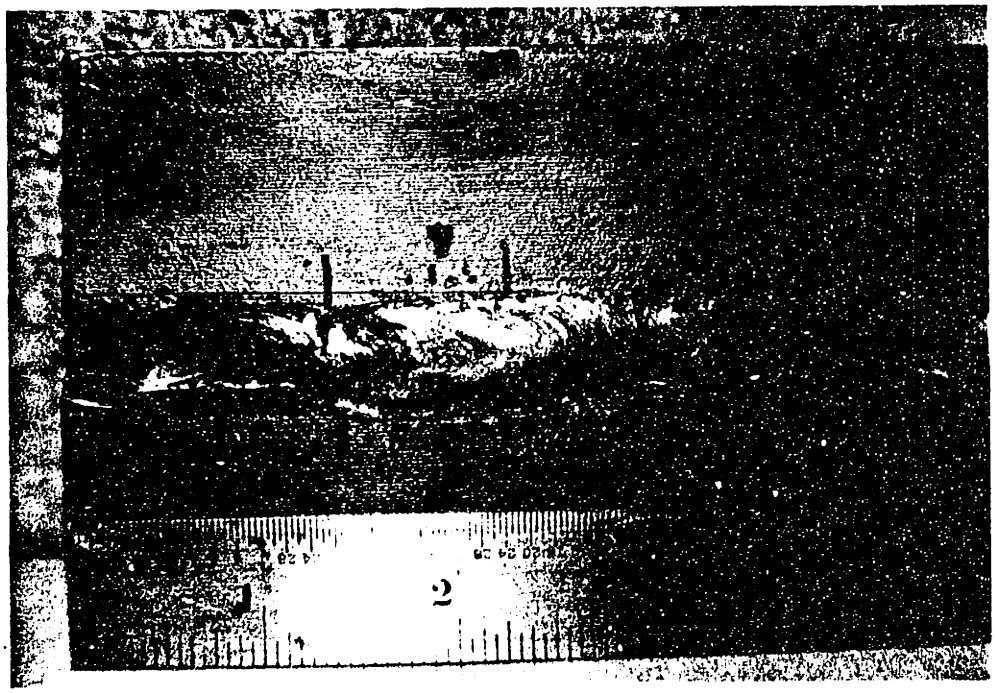

Figure 4.27 Tack weld surface contour photographs: (a) TW 7 before final welding, (b) TW 7 after final welding.

(c)

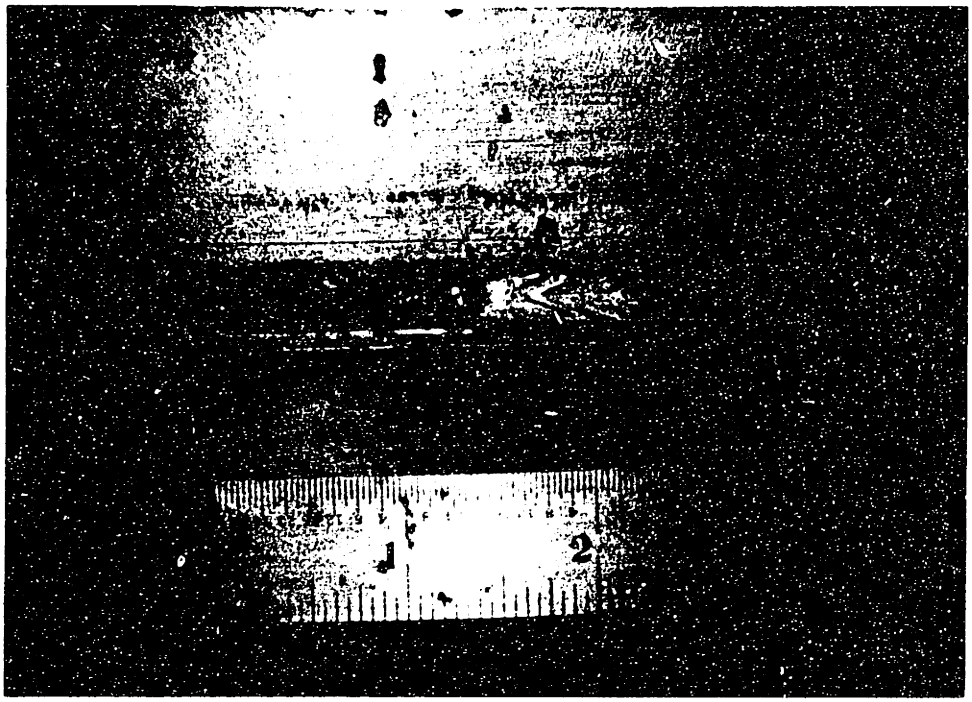

(d)

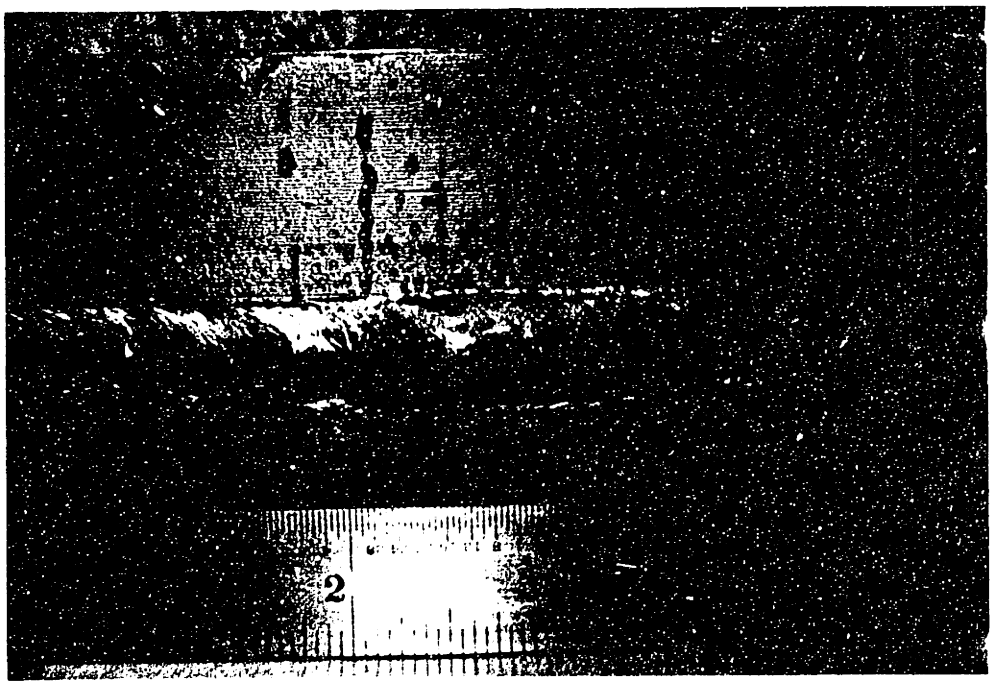

Figure 4.27 (c) TW 8 before final welding
(d) TW 8 after final welding

(e)

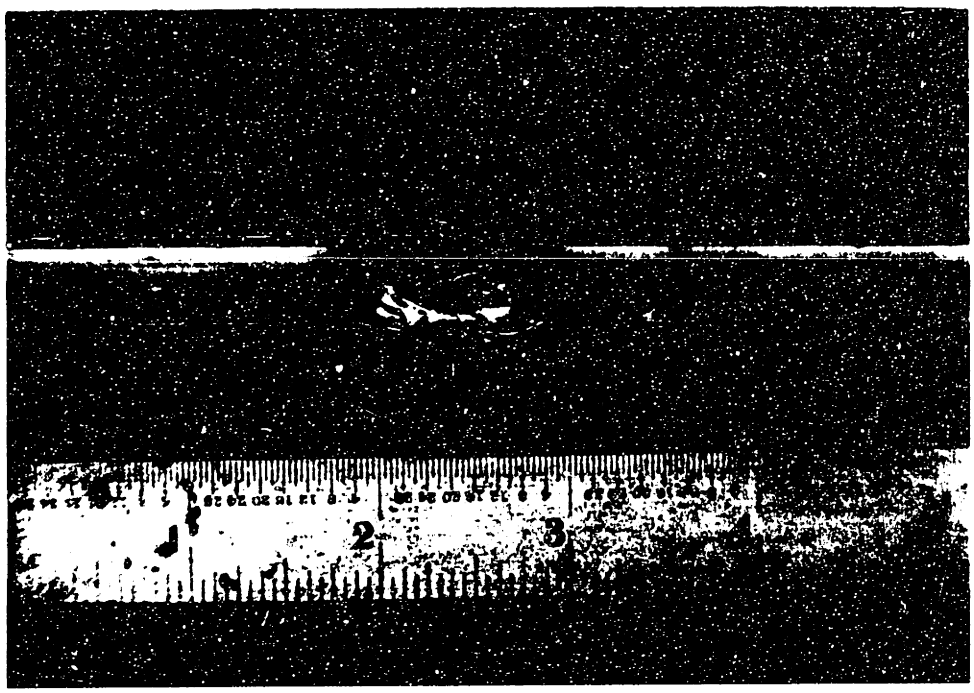

(f)

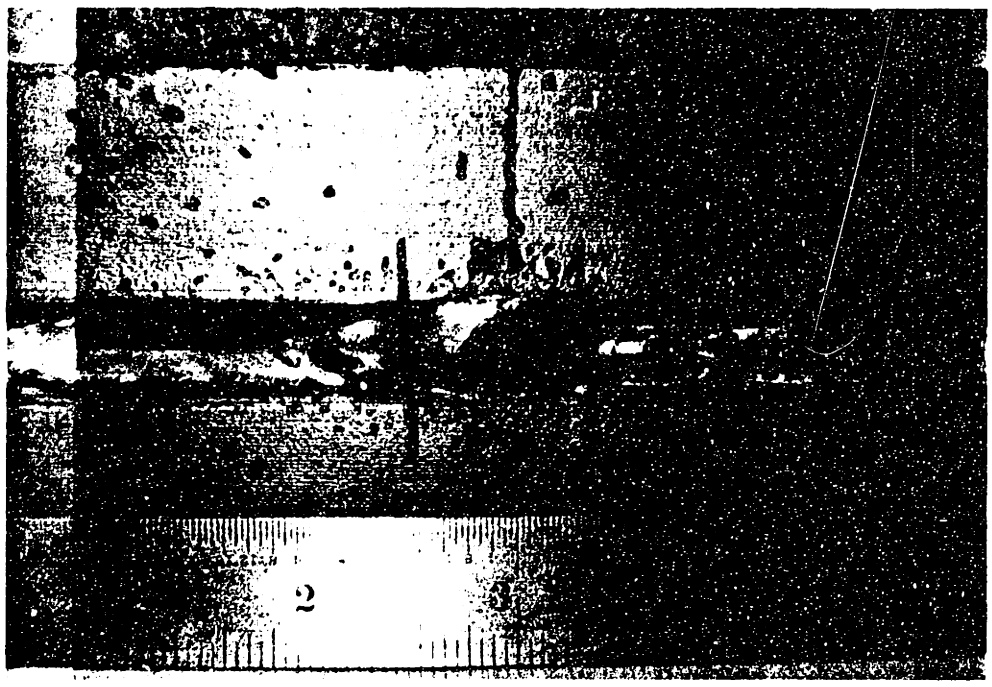

Figure 4.27 (e) TW 21 before final welding
(f) TW 21 after final welding

(g)

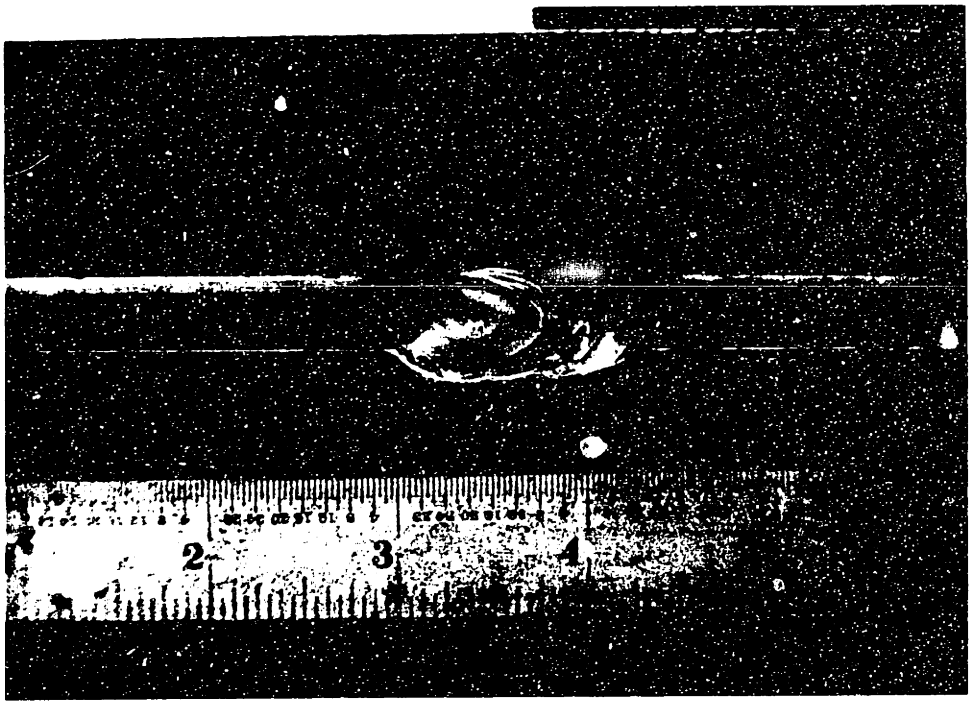

(h)

Figure 4.27 (g) TW 22 before final welding
(h) TW 22 after final welding

(i)

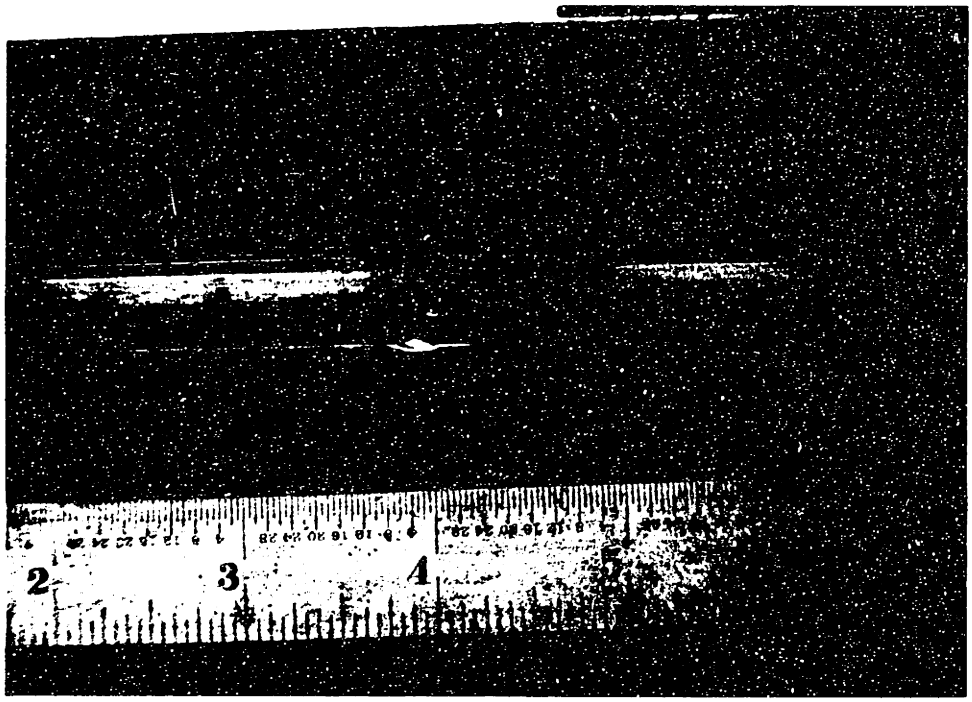

(j)

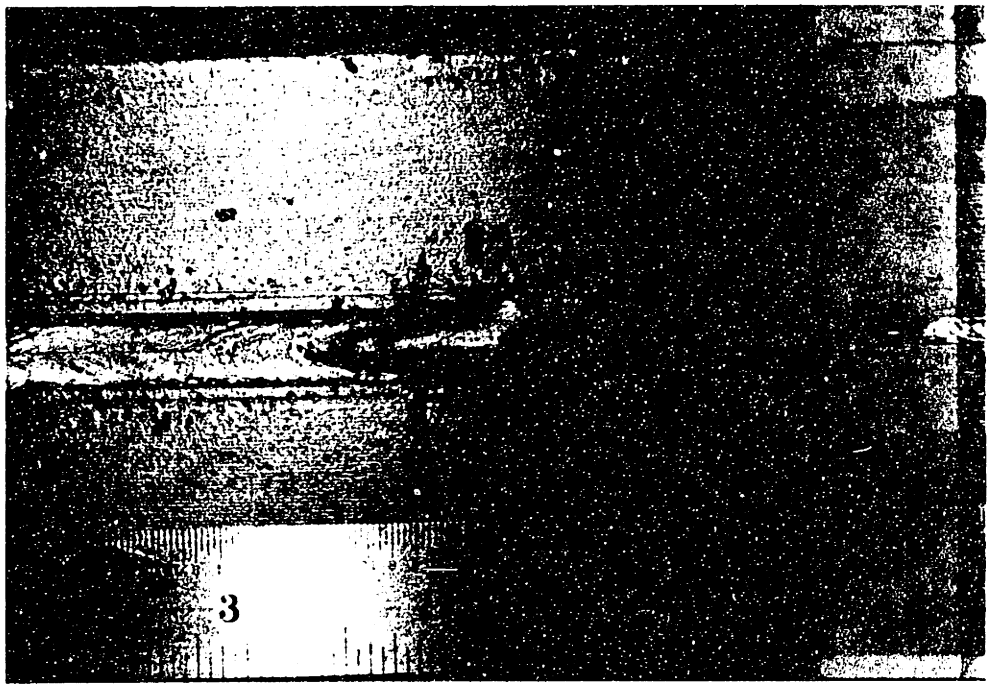

Figure 4.27 (i) TW 26 before final welding
(j) TW 26 after final welding

(k)

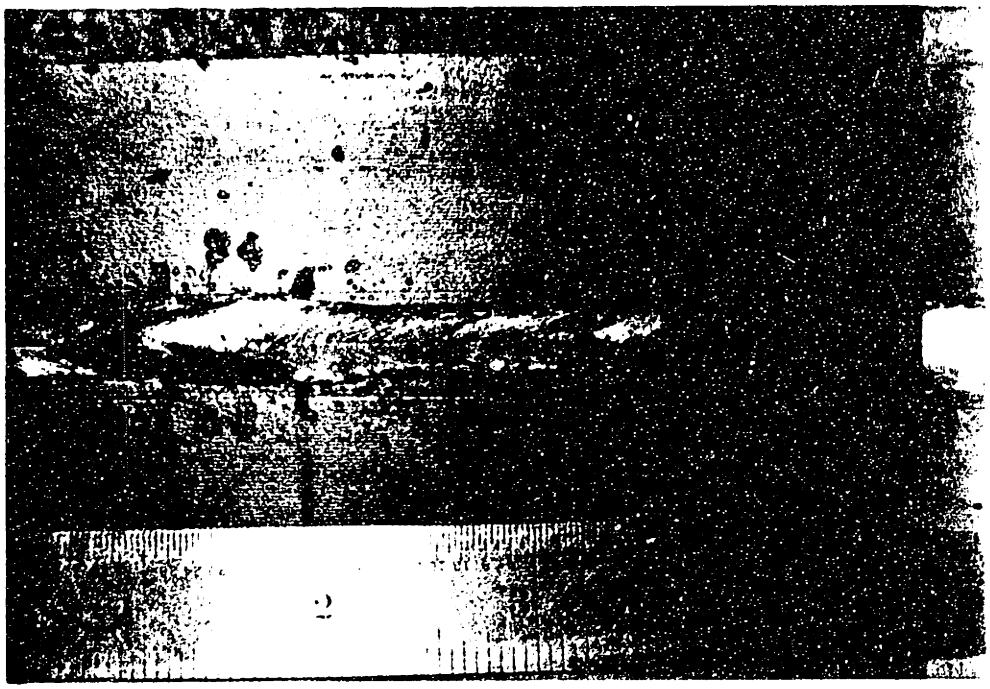

(l)

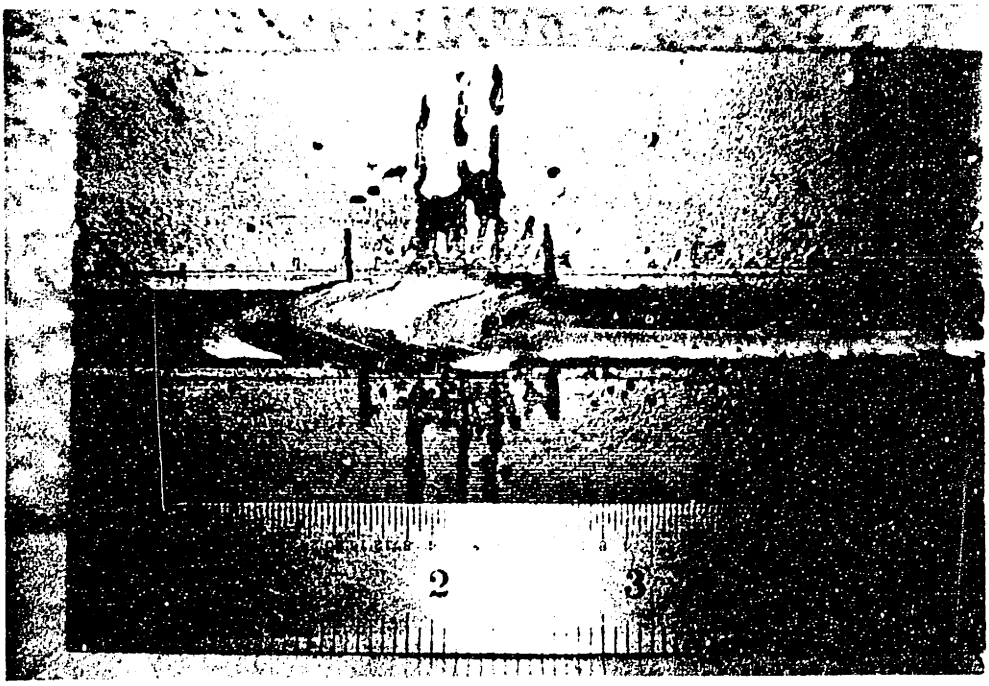

Figure 4.27 (k) TW 24, 25 after final welding
(l) TW 27 after final welding

(m)

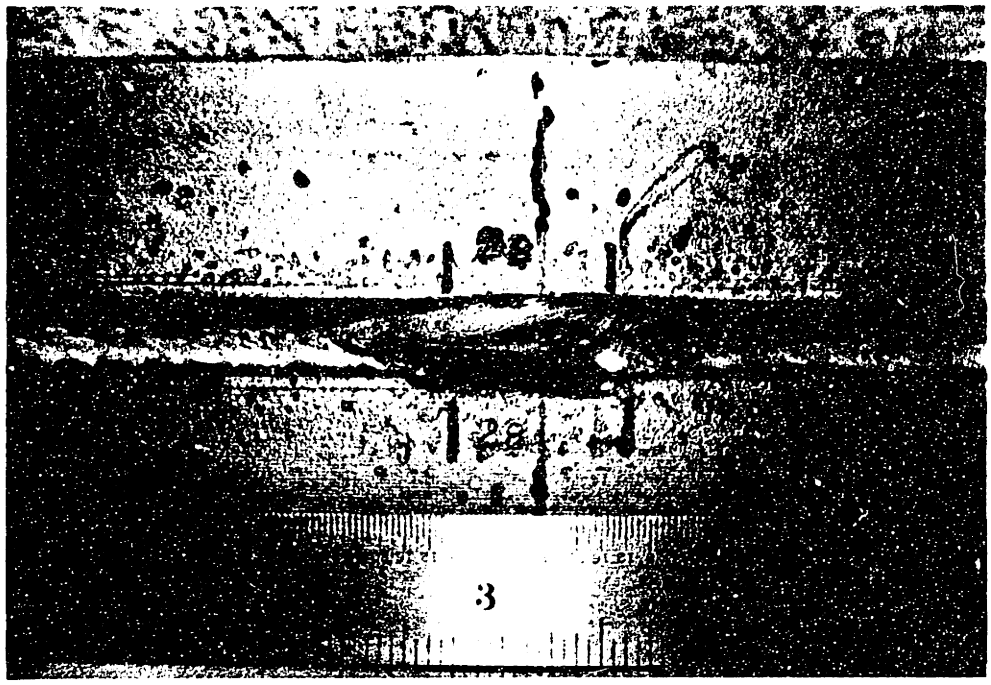

(n)

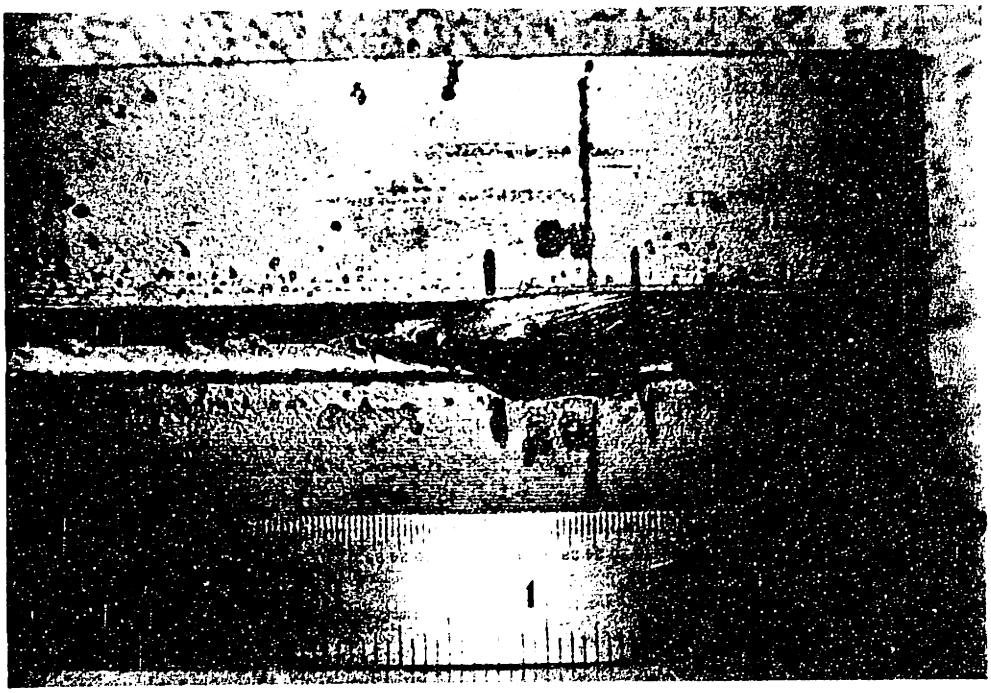

Figure 4.27 (m) TW 28 after final welding
(n) TW 29 after final welding

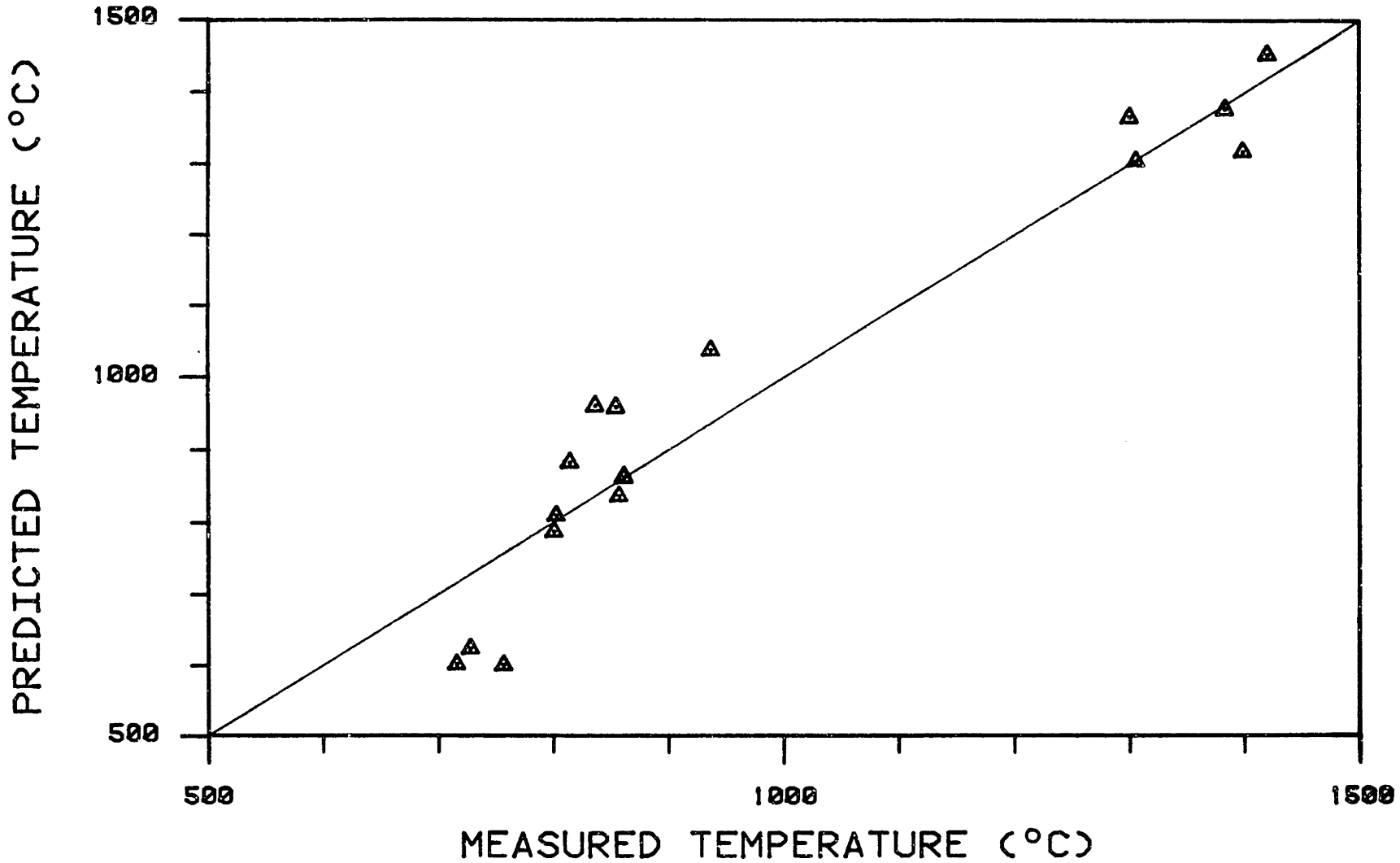

Figure 4.31 Measured versus predicted thermocouple temperatures.

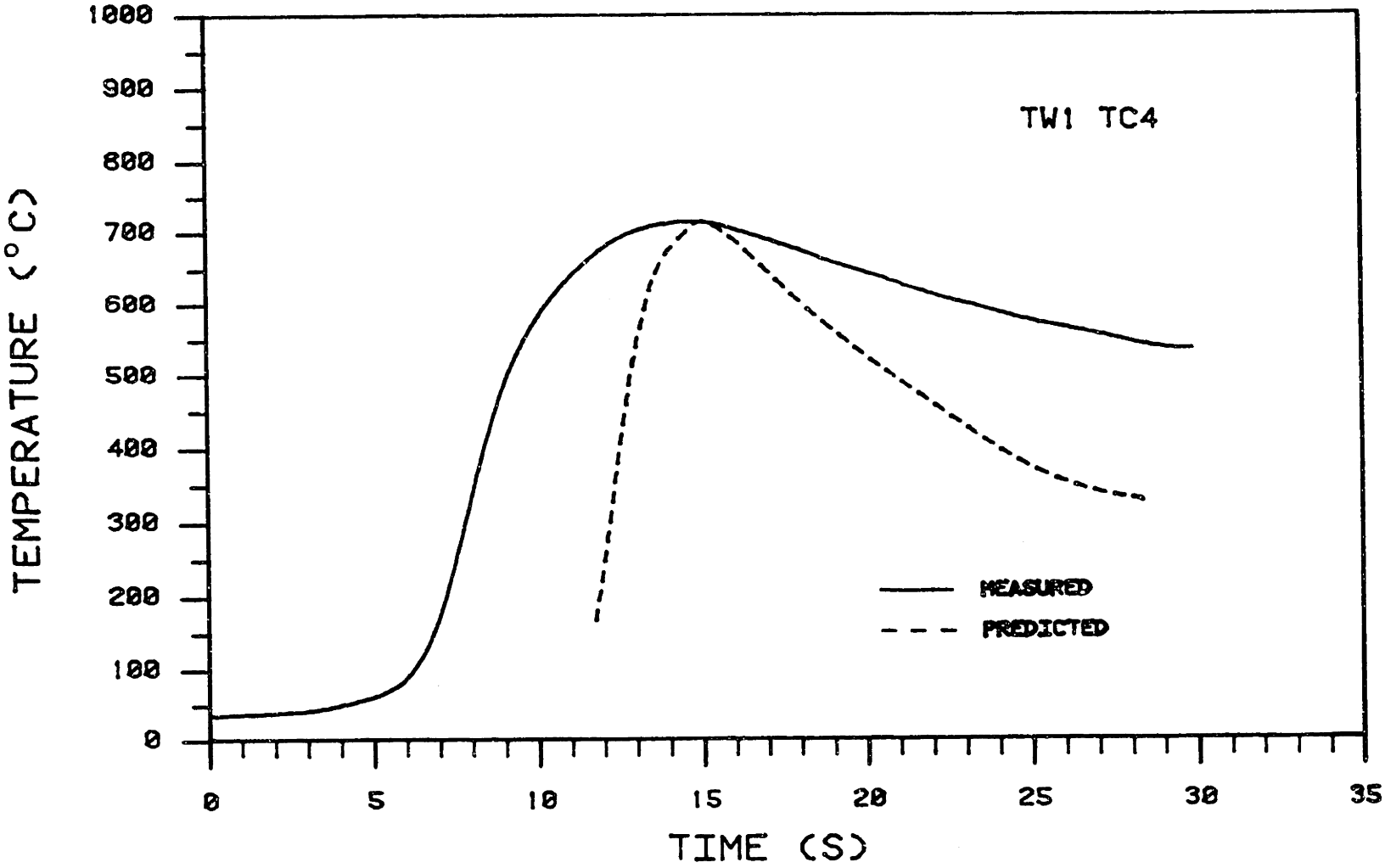

Figure 4.32 Temperature profile: tack weld 1, thermocouple 4.

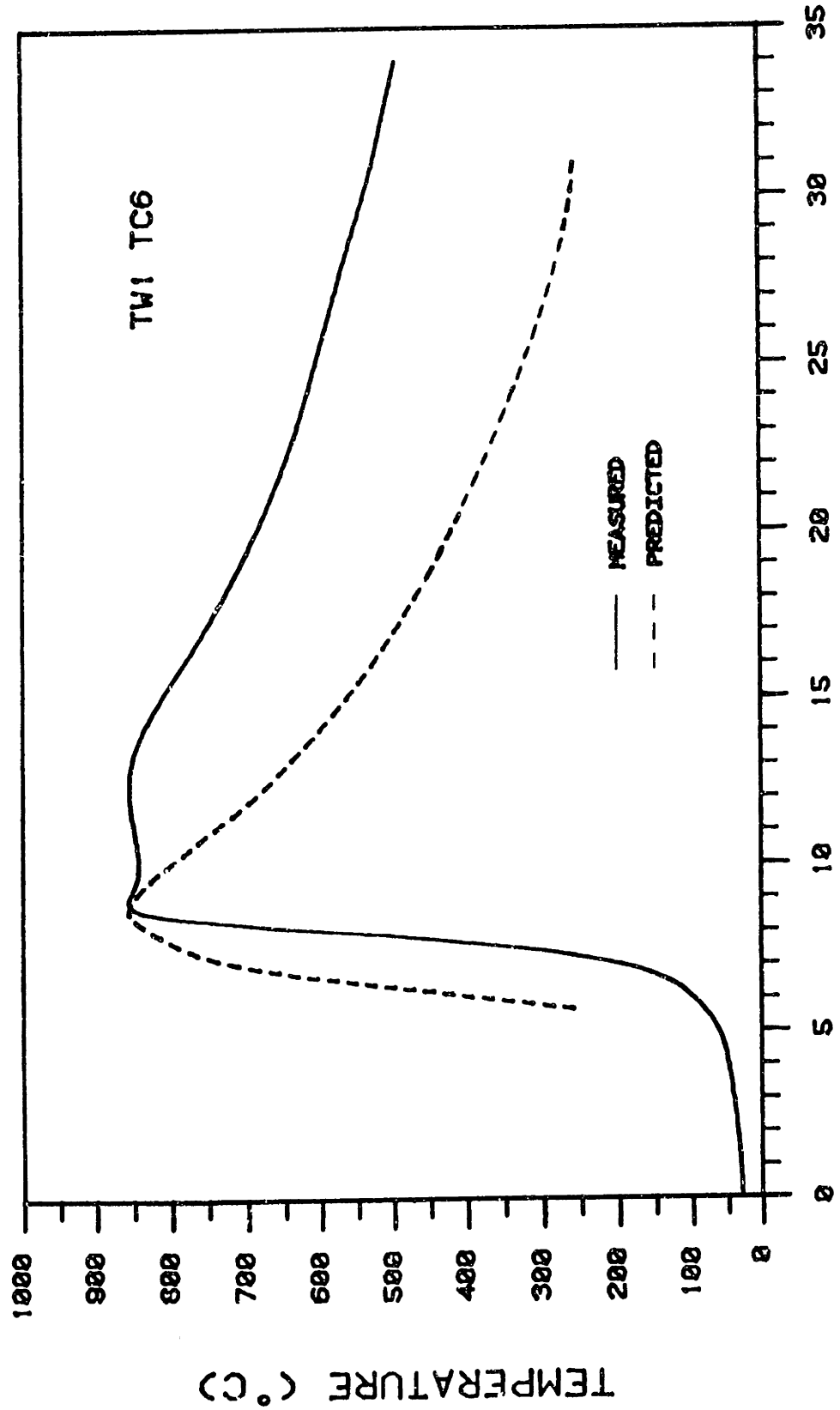

Figure 4.33 Temperature profile: tack weld 1, thermocouple 6.

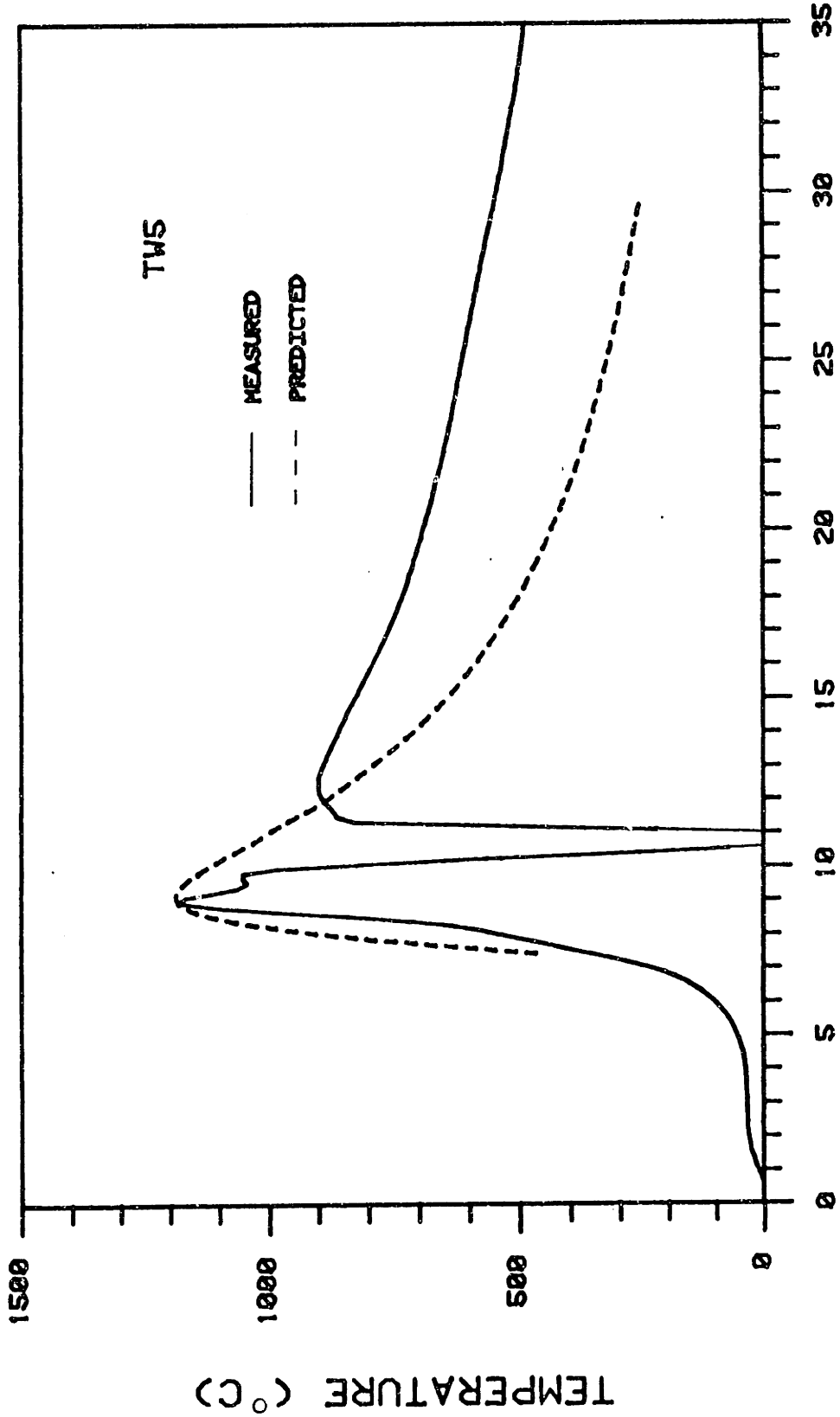

Figure 4.34 Temperature profile: tack weld 5.

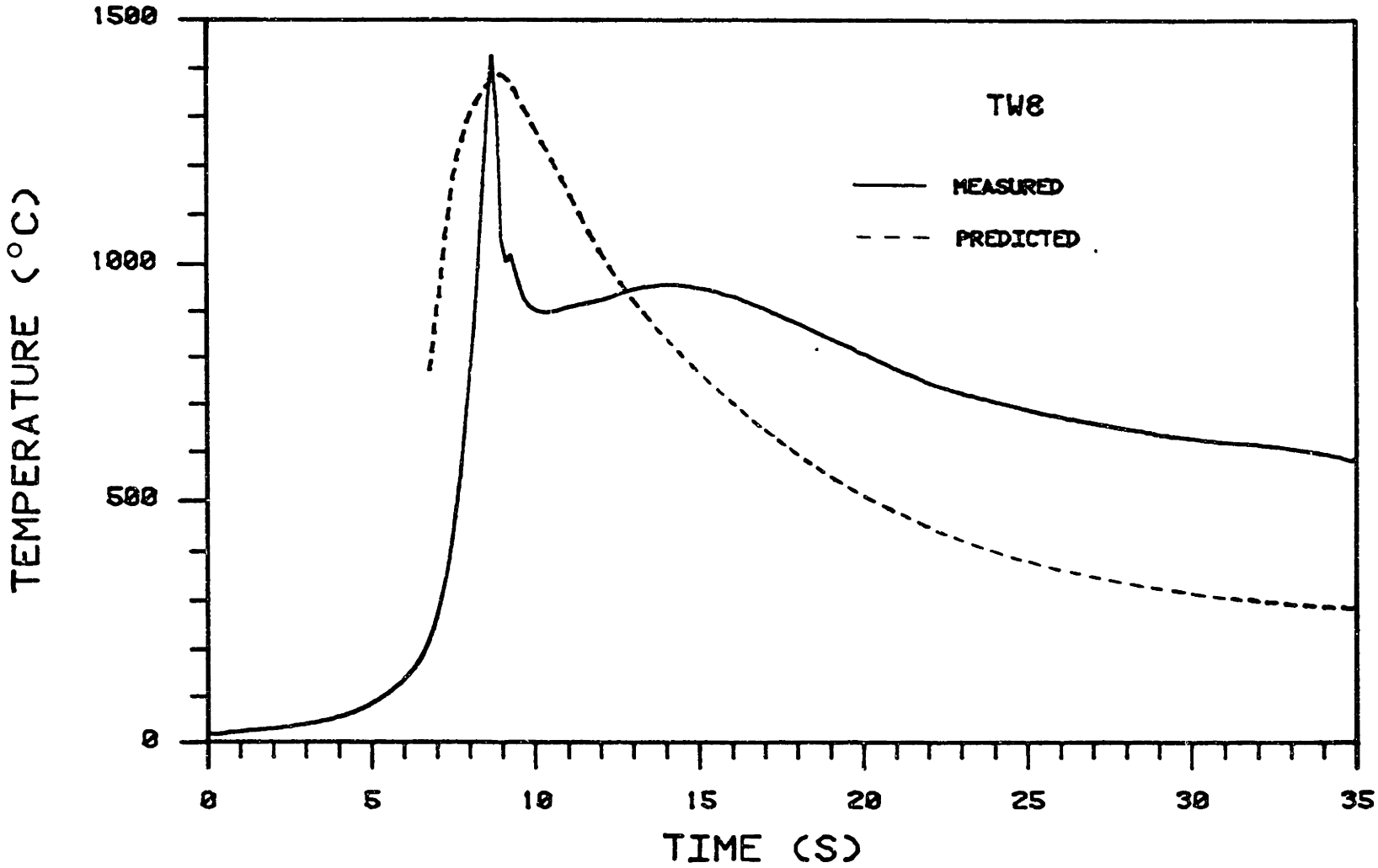

Figure 4.35 Temperature profile: tack weld 8.

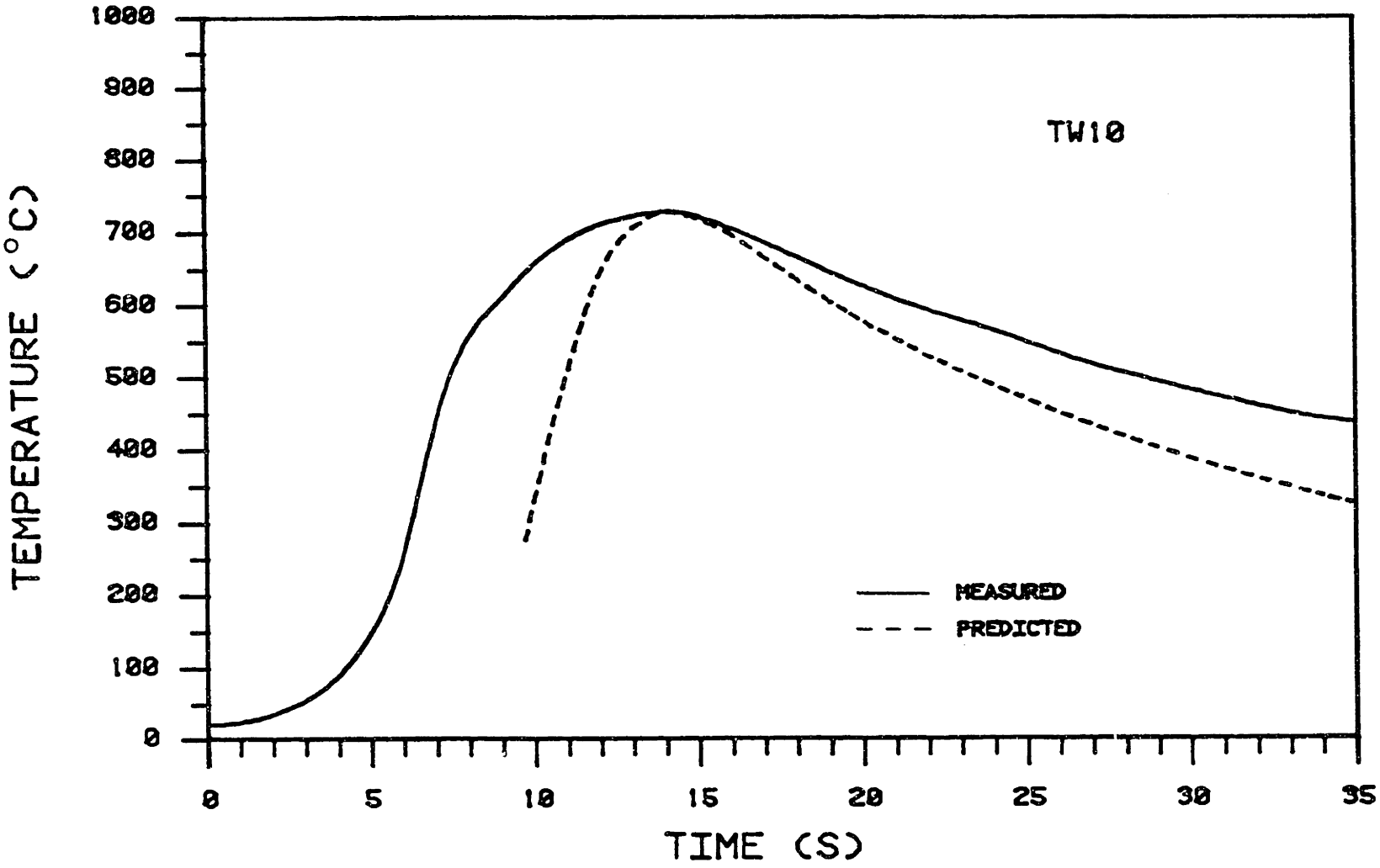

Figure 4.36 Temperature profile: tack weld 10.

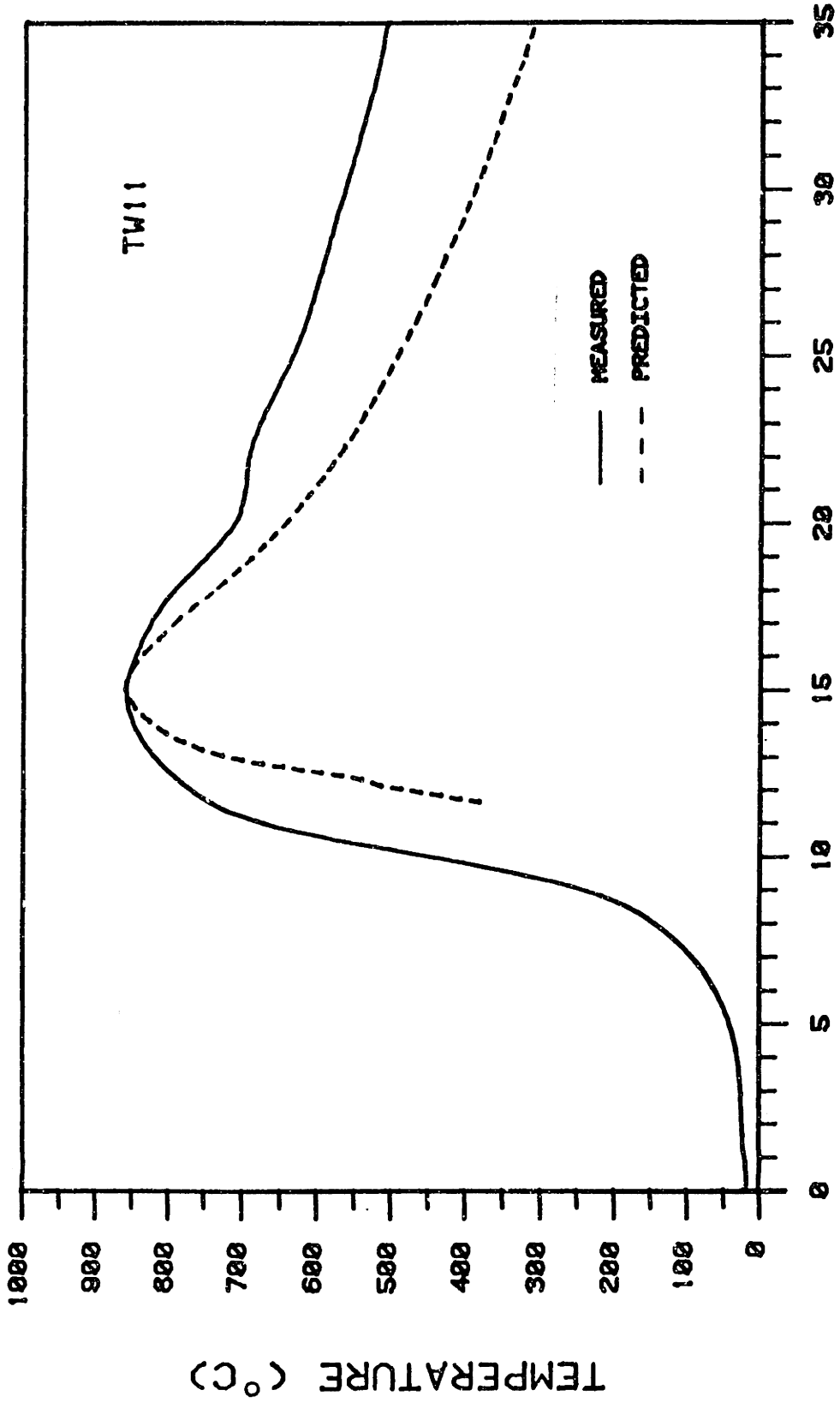

Figure 4.37 Temperature profile: tack weld 11.

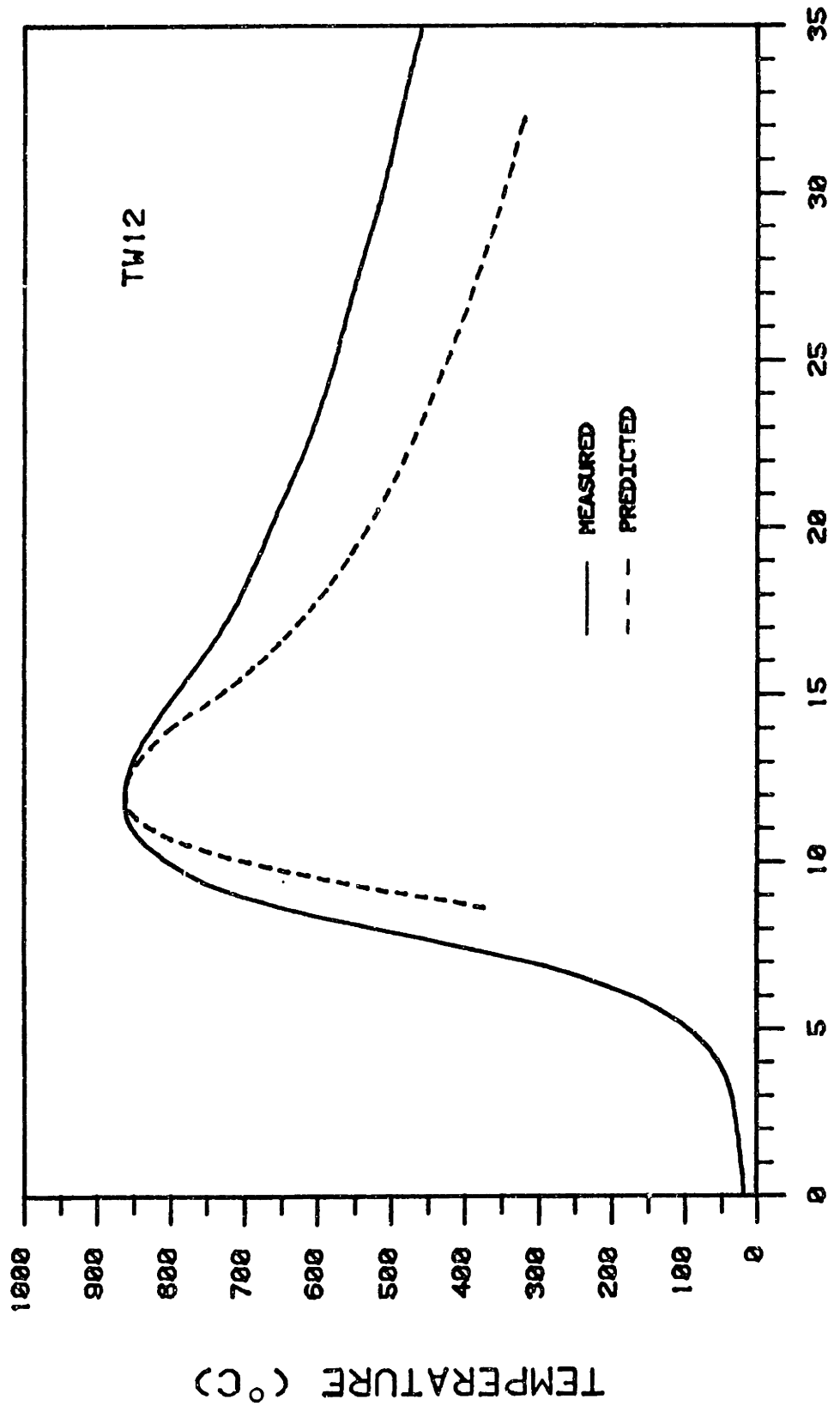

Figure 4.38 Temperature profile: tack weld 12.

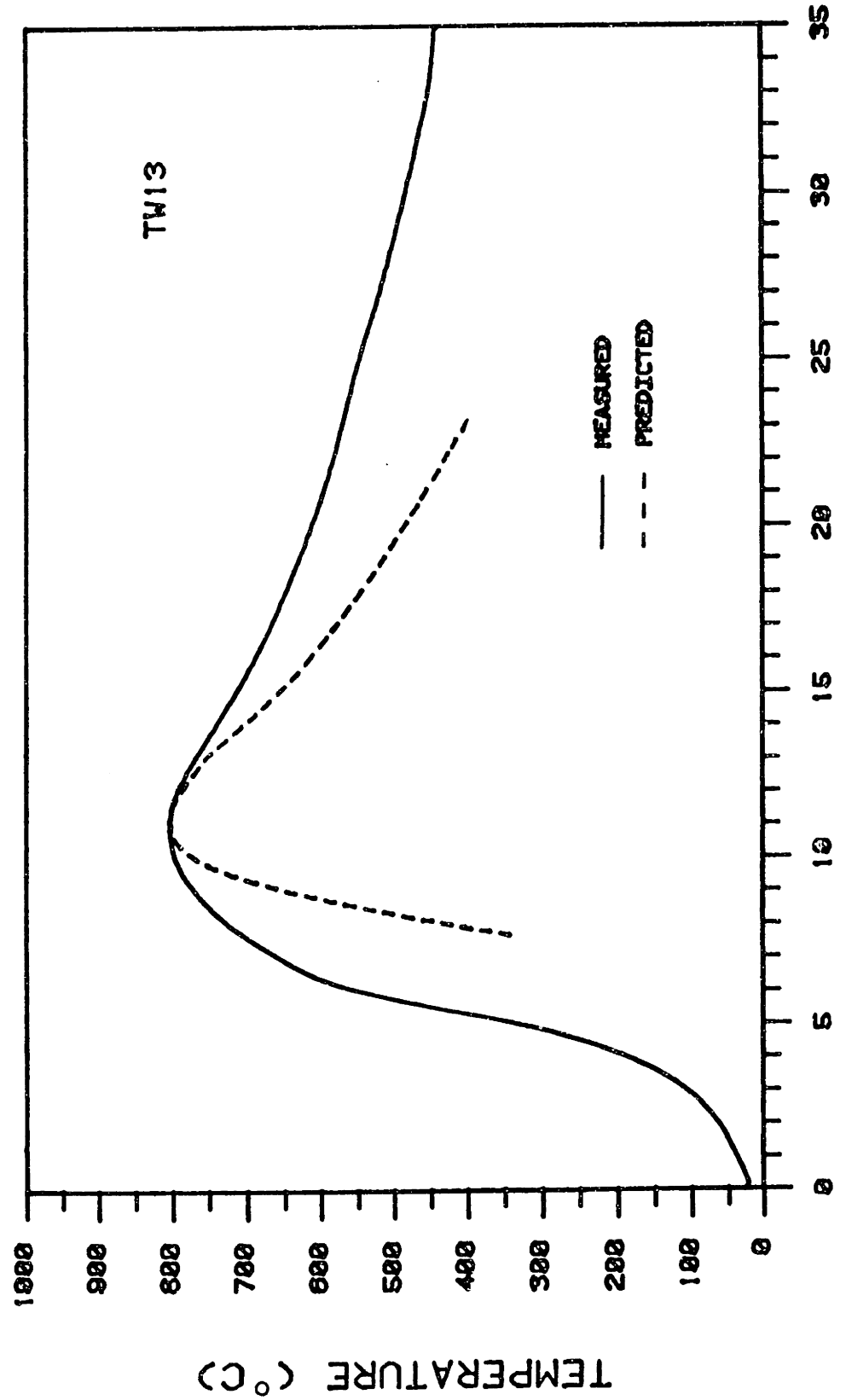

Figure 4.39 Temperature profile: tack weld 13.

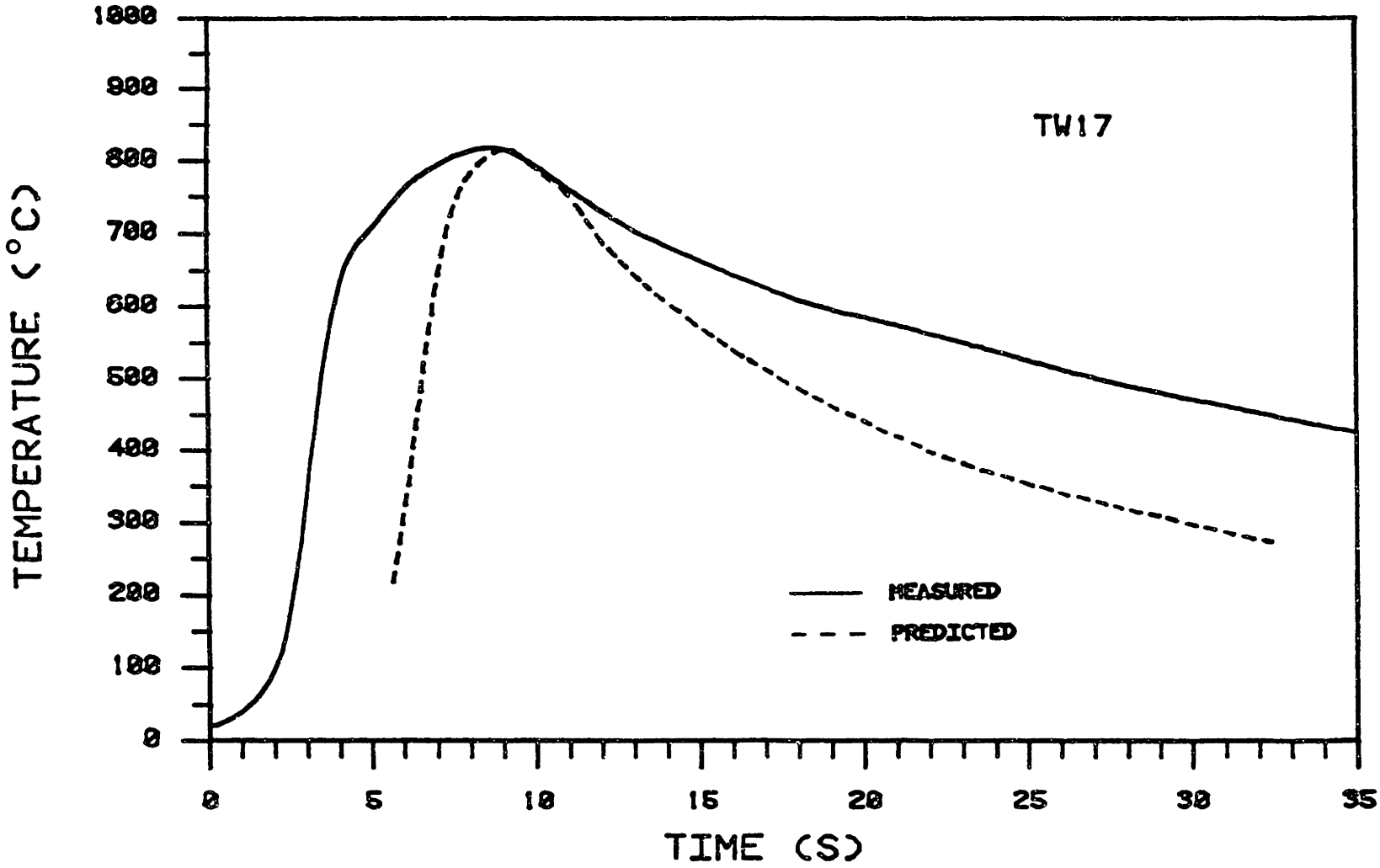

Figure 4.40 Temperature profile: tack weld 17.

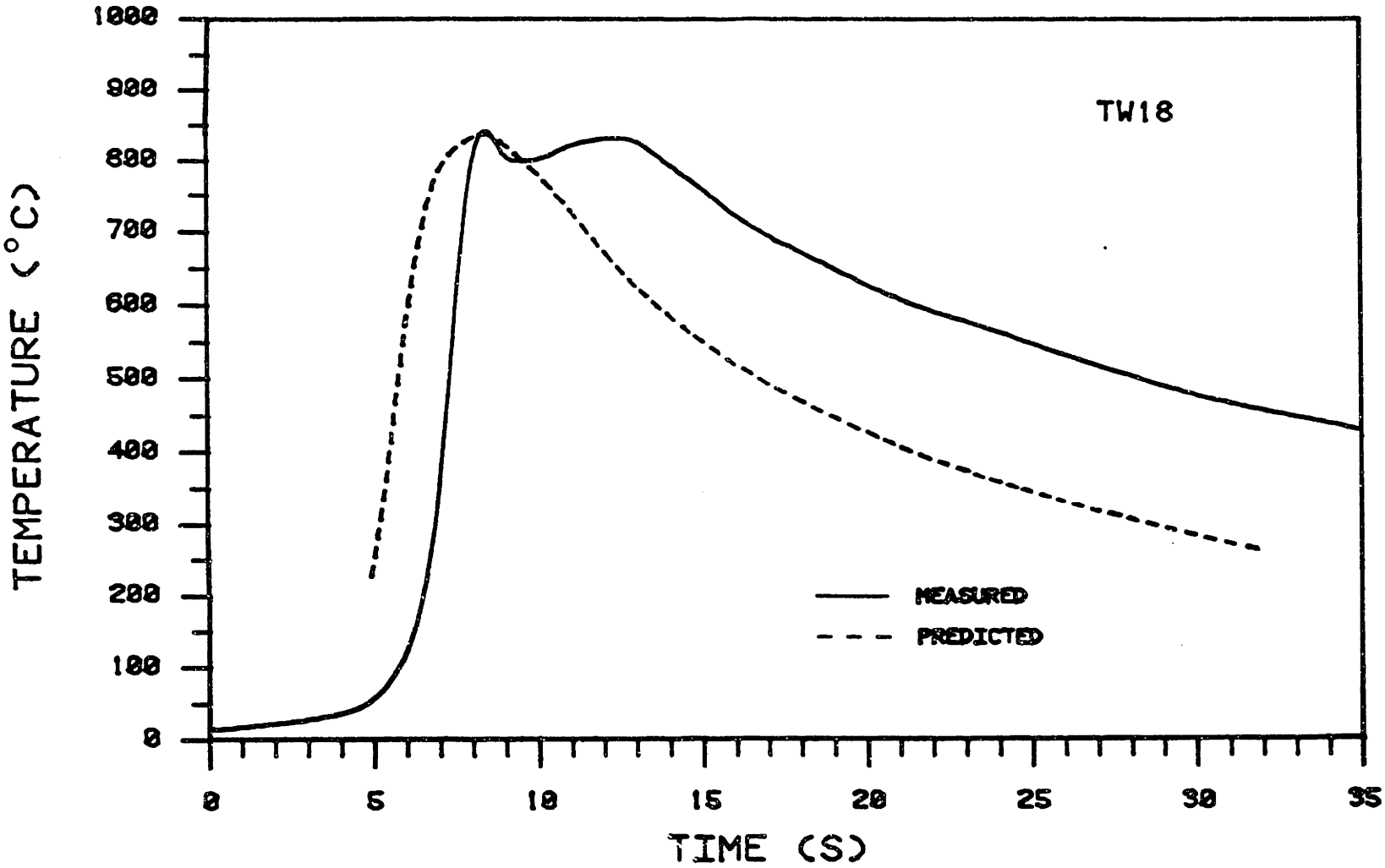

Figure 4.41 Temperature profile: tack weld 18.

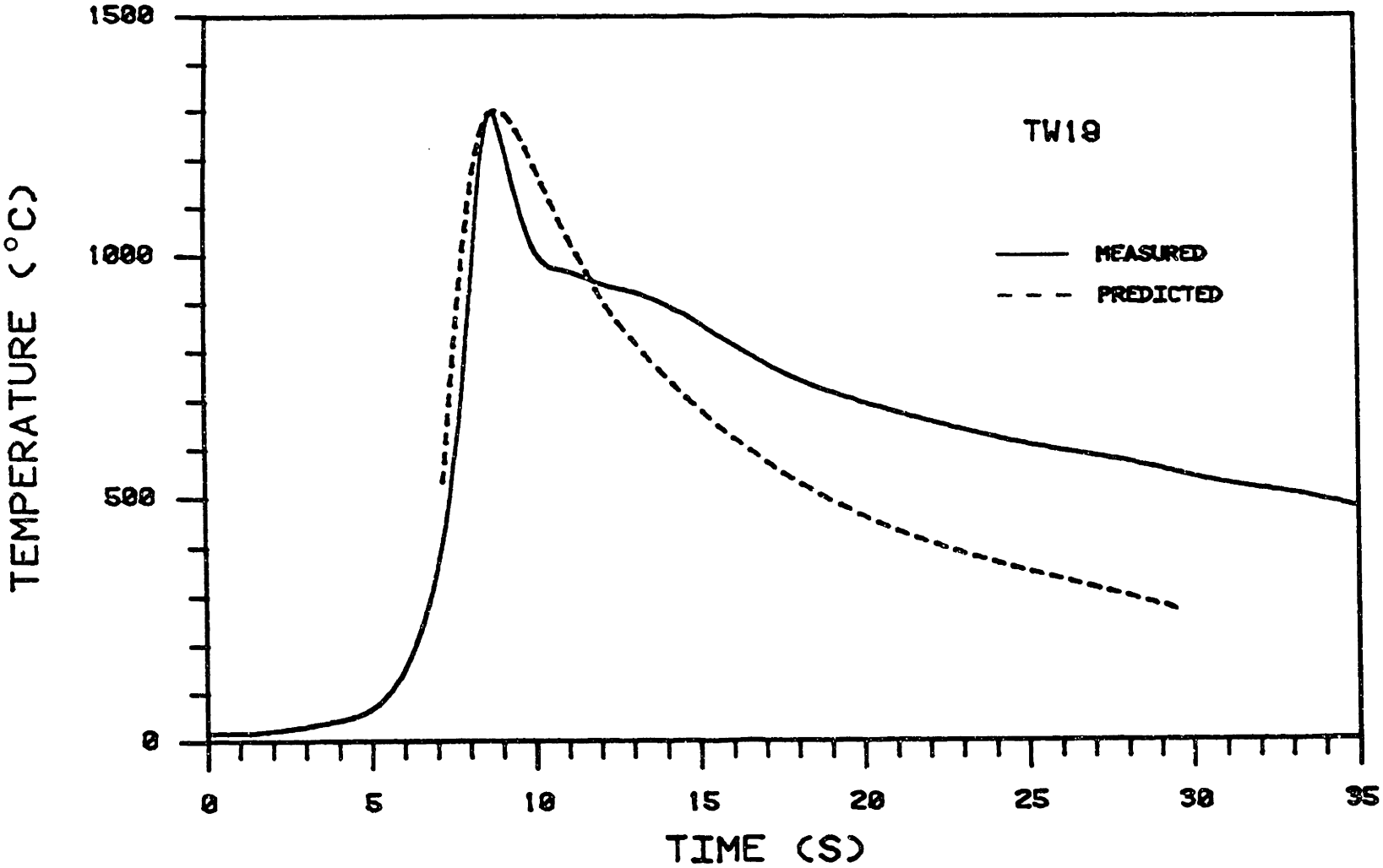

Figure 4.42 Temperature profile: tack weld 19.

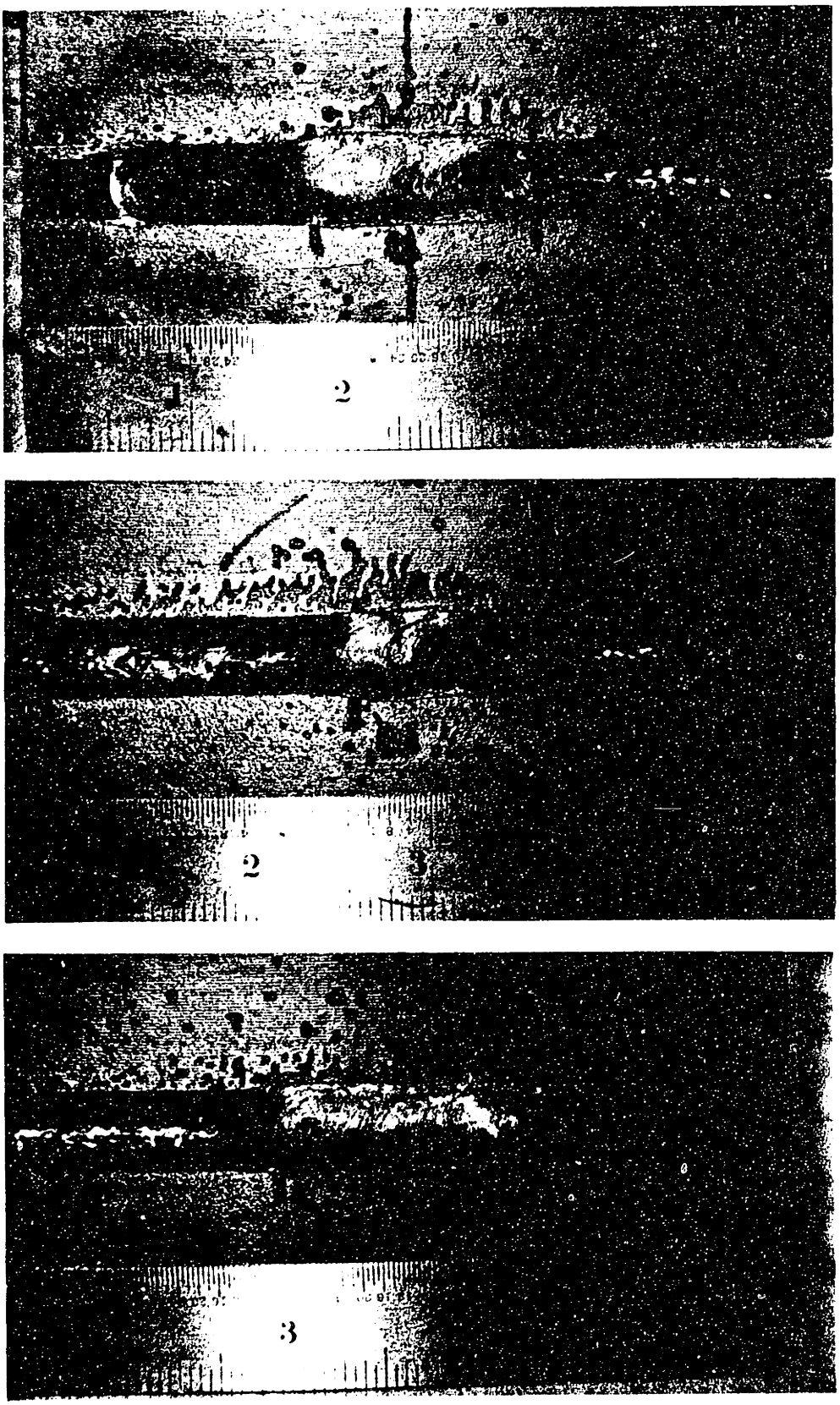

Figure 4.43 Photographs of TW 14, 15, and 16 after final welding.

CHAPTER 5

EXPERIMENTAL APPRATUS AND PROCEDURE

5.1 Equipment Description

5.1.1 Welding Equipment and Current Regulator

All pulsed GMA welds were made with a stationary torch and a moving workpiece. The workpiece was clamped onto a variable speed water-cooled copper plate. The wire feed mechanism was controlled by a logic circuit based on arc voltage feedback. Direct control of wire feed speed was not possible, so wire feed speed was measured with a tachometer in contact with the drive wheel. $Ar/2\%O_2$ was used as the shielding gas. Flow rate was 35 scfh unless otherwise specified. The end of the torch was equipped with a number 12 gas cup.

Power was supplied by two parallel Miller Gold Star 600SS power supplies through an Alexander Kusko 20kHz current regulator. The current regulator takes a voltage input from a function generator and produces an equivalent current output, magnified by a ratio of 100 A out for 1 V in. Details of the design of the current regulator are provided in references (87) and (131). Virtually all of the experiments were conducted with the rectangular waveform described in section 3.2.1. All parameters of the waveform were adjustable. The regulator output waveform was measured both with an oscilloscope hooked up to the regulator output reference signal and with a Honeywell 1858 Visicorder hooked up to a shunt resistor in the welding circuit. Figure 5.1 is a visicorder current trace, showing the high quality of the regulator output. Initially there was difficulty in low frequency pulsing. Between 12 Hz and 40 Hz, the current diminished substantially shortly after the beginning of the peak phase, then

recovered prior to the end of the peak phase. This phenomenon was caused by the dynamic interaction between the inductance of the power supply and the capacitance of the current regulator. It was eliminated by reducing the power supply inductance and increasing the current regulator capacitance, thereby allowing pulsing at all frequencies below 20 kHz.

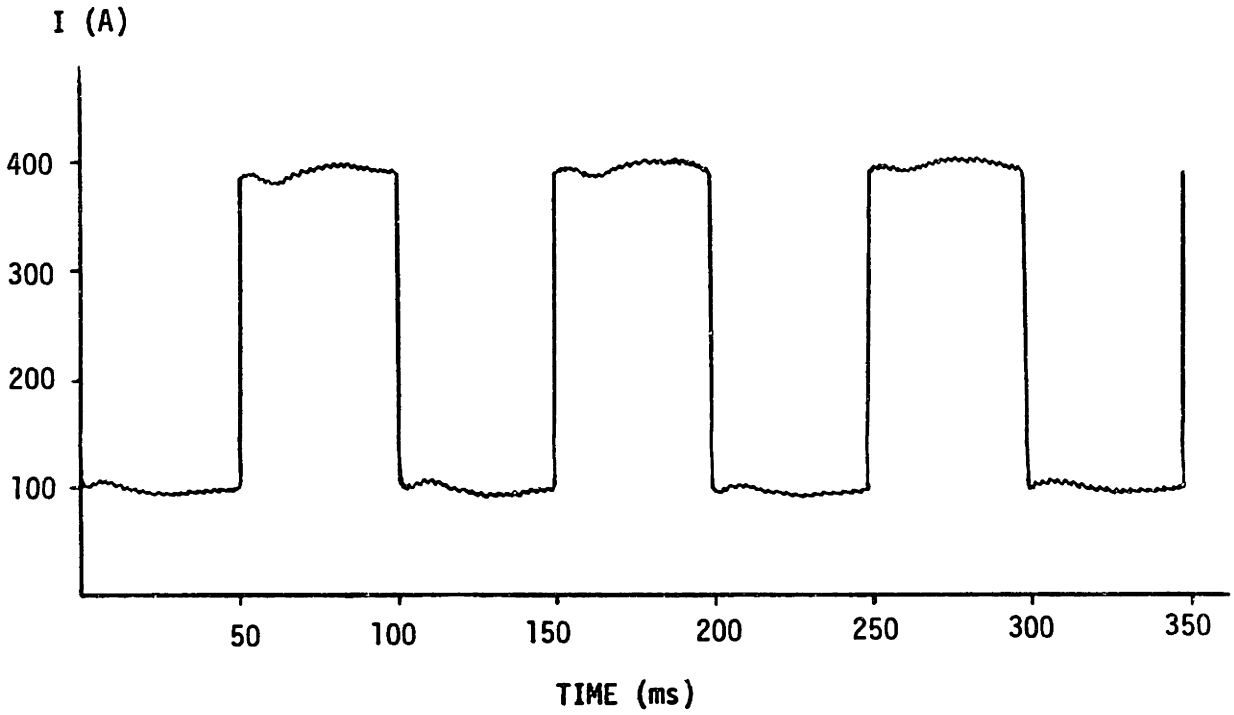

Figure 5.1 Current regulator output waveform.

5.1.2 Optical Train

An optical system enabled both videotapes and high speed films of the welding process to be taken. The electrode and arc received background illumination from a Melles Griot 5 mW He-Ne laser, from which the light was spread to a 20 mm beam. The laser light and arc light then went through a system of lenses including a neutral density filter and a variable aperature, allowing adjustment of the ratio of arc light to laser light. Video taping was done with an RCA NewVicon color video camera.

High speed films were made with a HYCAM II 16 mm high speed rotating prism camera, made by the Redlake Corporation of Morgan Hill, CA. Films were taken on 100 foot rolls at speeds ranging from 1000 to 5000 frames per second. A more thorough discussion of the optical system is provided in reference (132).

5.2 Experimental Procedures

5.2.1 Welding Procedures and Data Analysis

All pulsed welds were bead-on-plate. Except where otherwise indicated, C1016 cold rolled 12" x 6" x 1/2" mild steel plates were used. Weld lengths were approximately 9" long and were made at travel speeds ranging from 10 ipm to 20 ipm. Wire feed speeds were in the vicinity of 330 ipm. Six or seven welds were made on each plate, and each plate was cooled to ambient temperature prior to each weld. The plates were thoroughly cleaned with acetone prior to any welding.

The welded plates were cut at three locations, and three separate cross-sections were polished and etched with a 12% nital solution. The etched cross-sections were measured for penetration and bead width. The accuracy of the measurements is estimated to be approximately .25 mm. The measurements from the three cross-sections were averaged to arrive at the "measured value." The three separate measurements were always very close, and the differences are as likely to be due to measurement imprecision as to actual variation in the weld dimensions.

5.2.2 Pulsing Strategies

The intent of the current pulsing in these experiments was to increase penetration by exploiting one or more of the mechanisms of penetration described in chapter 3. Each of the mechanisms has its own characteristic

time, and the ability to adjust pulse parameters allows separate excitation of each penetration mechanism. Although the characteristic times are not precisely known for all the mechanisms, the data provided by these experiments should give additional insight into what those times are. Five pulsing strategies have been devised to increase penetration without increasing the metal deposition rate.

Low frequency pulsing is designed to utilize arc pressure to excite resonant modes of oscillation in the weld pool. These modes were described in section 3.3.2, and depending on weld pool size and shape, their natural frequencies can range from around 10 Hz to several hundred hertz. These experiments will concentrate on frequencies below 50 Hz, with a 100/400 A square wave. The peak period of a low frequency pulse should also be sufficient to excite the compound vortex and weld pool convection.

High frequency pulsing is designed to increase arc pressure by constricting the arc. This has already been shown to be effective in GTA welding, as discussed in section 3.3.2. Again a 100/400 A square wave will be used, with frequencies from 1 kHz to 8 kHz. High frequency pulsing is probably much too fast to allow formation of a compound vortex during the peak phase, and it is also too fast for weld pool convection to follow it. However, electromagnetically driven weld pool convection is proportional to current squared, so for pulsed welding it is likely to be proportional to the rms value of current. For a 100/400 A square wave, the rms value is 292 A, which is considerably larger than the 250 A mean current. Hence, for the same mean current, current pulsing should give greater electromagnetically induced weld pool convection.

The inertia of the penetration mechanisms can be exploited by high duty cycle pulsing. Once a weld pool convection pattern, a compound vortex, or surface depression is established, inertia will maintain it momentarily even after the arc is extinguished. The idea behind high duty cycle pulsing is to choose a peak current level that is comparable to the current in conventional welding, maintain the peak period long enough to establish the penetration mechanisms, and make the base periods so short that the mechanisms do not have time to die. In this way the mean current and deposition rate will decrease, while the penetration should remain relatively constant. The decreased heat input will reduce the penetration due to conduction, but the other mechanisms should be largely unaffected.

High peak pulsing utilizes a brute force approach to penetration. Above 500 A, the arc pressure exceeds the compound vortex as the primary cause of surface depression. As the current continues to increase above 500 A, the arc pressure and surface depression (and therefore penetration) will increase sharply. The intent of this strategy is to use short high peak currents to increase penetration by means of arc pressure.

Mid-peak drop transfer exploits the control that pulsing gives over metal transfer. Adjustment of the peak parameters can result in the drop transfer occurring during the peak period, thereby increasing drop velocity and penetration. An average current of 250 A was chosen for this set of experiments, and the frequency was determined based on the 50 Hz/100 A rule for 1.2 mm wire, giving a frequency of 125 Hz.

CHAPTER 6

EXPERIMENTAL RESULTS AND DISCUSSION

6.1 Introduction

Two sets of baseline experiments were run to get a general idea of the effects of pulsing and to further identify promising areas of investigation. The first set was a broad frequency sweep from 20 Hz to 1000 Hz using a 100/400 A square wave. The wire feed speed was measured to be 327 ipm, except that stubbing at 20 Hz reduced the speed to between 280 and 320 ipm. At 20 Hz, the background period is 25 ms, during which time almost no electrode melting occurs. At 327 ipm, the electrode advances 3.5 mm during 25 ms, and that is enough to cause a minor but persistent stubbing problem. The results of the broad frequency sweep are shown in figure 6.1. There is a peak at 25 Hz and there might be a slight increasing trend in the upper frequency range. Between 50 Hz and 200 Hz, it is difficult to say whether the points represent true minor peaks or just scatter. The baseline results give some promise to both low and high frequency pulsing.

The second set of experiments tested the effect of current excess. A 100 Hz square wave with a 225 A mean current was used for these experiments. The wire feed speed was measured to be 325 ipm, and the current excess was varied from 0 (constant current) to 350 A. The current parameters, penetration and penetration profile descriptions are listed in table 6.1. The constant current weld was made at 227 A rather than 225 A due to the limited precision of the current dial calibration. The effect on the weld bead geometry should be negligible. There appears to be no advantage in pulsing with only a slight current excess. With increasing

Table 6.1 Penetration (d) versus current excess (Ie).

I (A)	Ie (A)	d (mm)	penetration profile
227	0	2.33	severely offset finger
185/265	80	1.99	severely offset finger
150/300	150	2.33	significantly offset finger
100/350	250	2.75	slightly offset finger
50/400	350	3.39	barely offset finger

current excess, however, the penetration increases substantially and the penetration finger becomes more centrally located, both of which are desirable. This data indicates that the effect of the penetration mechanisms established during the peak phase both increase substantially with peak current and are not fully counterbalanced by the decrease in background current. Penetration is plotted as a function of current excess in figure 6.2.

6.2 Low Frequency Pulsing

Five sets of experiments were run to further define the low frequency peak identified in figure 6.1. The first set used 10 Hz intervals from 10 Hz to 50 Hz as well as a 100 Hz point with a 100/400 A square wave. Wire feed speed was measured to be 340 ipm and travel speed was set at 13 ipm. Table 6.2 lists the welding parameters and bead dimensions. These welds were made before the current regulator was modified as described in section 5.1.1. Consequently, the waveforms at 10, 20 and 30 Hz were distorted and the mean currents were lower. The penetration plotted in figure 6.3 nevertheless reveals a distinct peak at 20 Hz. This peak would conceivably be even higher if the current waveform had not been distorted and the mean current had been the intended 250 A. The decrease

in penetration when going from 40 Hz to 30 Hz could be due to the decrease in mean current or some sort of anti-resonance effects with the weld pool motion, or a combination of both.

Table 6.2 LF data set # 1. d = depth, w = width, h = height, σ_d = standard deviation of the three depth measurements.

f	<I>	V	d	w	h	σ_d
10 Hz	230 A	27.0 V	3.64 mm	12.78 mm	4.23 mm	.15 mm
20	230	24.6	4.53	10.84	4.15	.07
30	225	23.5	3.13	11.35	3.56	.15
40	253	27.3	4.06	12.28	3.43	0
50	252	27.8	3.98	12.28	3.39	.19
100	252	28.0	4.02	12.45	3.30	.07

The second set of data was taken at 2 Hz intervals from 10 Hz to 30 Hz with identical welding parameters. The data is listed in appendix D (table D.1), and penetration is plotted in figure 6.4. These welds also were made prior to the current regulator modifications, so there was waveform distortion above 12 Hz. Nevertheless, there is a slight peak at 20 Hz and a valley at 28 Hz. Penetration diminishes below 14 Hz despite the higher average current, indicating either that resonant modes are not being excited at these low frequencies or that penetration tends to die out during the long background phases.

The third set of data was taken with an older current regulator modified by the addition of an external capacitance bank. This allowed undistorted pulsing down to 20 Hz. A 50/400 A square wave was used at 15 ipm travel speed and 337 ipm wire feed speed. Shielding gas flow was set fairly high at 60 scfh, but later independent experiments showed that

this should not affect penetration. Penetration as a function of frequency is plotted in figure 6.5. Again there is a sharp increase at 20 Hz. The other peaks could either be real or scatter.

It was desired to pulse below 20 Hz in order to fully define the 20 Hz peak, so the newer current regulator and the power supply were modified as described in section 5.1.1. Using identical welding parameters, except a gas flow rate of 40 scfh, the frequency was varied in 2 Hz increments from 6 Hz to 50 Hz. Although the input square wave was adjusted to 50/400 A, the current meter indicated average currents of approximately 235 A. A 237 A constant current weld was made for comparison. The results, comprising the forth data set, are plotted in figure 6.6. Again there is a peak near 20 Hz (at 22 Hz), although it is not as high as in data set number 3. Below 22 Hz, the data is fairly unremarkable except for the isolated decrease at 18 Hz and the gradual decrease below 12 Hz. At all frequencies the pulsed welds penetrated deeper than the constant current welds. The increase in penetration at 22 Hz was 1.2 mm, or 48% of the constant current penetration. Above 22 Hz there are three peaks at almost exactly the same frequencies as in data set number 3: 30 Hz, 44 Hz, and 48 Hz. Although these peaks are small enough that they could be scatter rather than true peaks, the fact that both data sets had the peaks in the same locations would tend to indicate that they are real. On the other hand, if they are real, the applicable modal frequencies would have to be somewhat insensitive to pool diameter. In data set number 3, the bead diameters at the three peaks were 10.41, 11.01, and 10.75 mm, whereas they were 11.35, 11.57 and 11.35 mm in data set number 4.

The fifth and final data set was intended both to further define the 10 Hz to 20 Hz region and to determine the effect of travel speed and

therefore pool diameter on the peak structure. Welding parameters were identical to those in data set number 4, except that a 100/400 A square wave was used. Welds were made at 2 Hz intervals from 10 to 24 Hz at 10 ipm and 15 ipm travel speeds, and from 10 Hz to 30 Hz at 20 ipm. Results are shown in figure 6.7. Other than the slight peak at 14 Hz in the 10 ipm profile, the profiles are disappointingly flat. At 10 ipm, the weld pool is wider (14.0 - 14.5 mm), so it is expected that the peak would shift to a lower frequency. At 15 ipm, the profile is completely flat from 10 Hz to 24 Hz. Data set number five was taken with a 100/400 A square wave, whereas data sets number three and number four were taken with a 50/400 A square wave. It is possible that the change in background current extended the flat region slightly and that the penetration would have fallen off above 24 Hz and below 10 Hz. The penetration at 20 ipm shows some variation, but it is within the limits of what could be scatter. The weld pool widths at 20 ipm are between 9.6 mm and 10.8 mm, so resonant peaks would be expected at higher frequencies. 30 Hz might not have been a high enough frequency to capture the lowest frequency peak in the profile. Additionally, the scouring action is more significant at 20 ipm, and this changes the modal shape and frequency.

Section 3.3.2 contained modal shape and frequency estimates based on Tam's thin membrane model and Sorensen's distributed parameter model. The gross up and down membrane mode is not physically possible in a partial penetration weld, but the sloshing mode is, and the natural frequency for an elliptical membrane was given by equation 3.58 as 191/W Hz. Equation 3.52 gave the natural frequency for a cylindrical partial penetration weld. It can be approximated as $f = 400/W$ Hz, where W in both equations is the weld pool width in millimeters. Although Sorensen's model better

represents the physical reality of the weld pool, the motion described by equation 3.52 is axisymmetric with the inner part of the weld pool moving up and down in opposition to the outer part. As travel speed increases in an actual weld, this type of motion becomes less realistic. Either the same type of motion would persist without axisymmetry, or the motion would change to sloshing, which is a lower mode with a lower frequency. The weld pool widths in data sets three and four are approximately 10 mm, giving resonant frequencies of 19 Hz and 40 Hz for the elliptical membrane and distributed parameter models, respectively. If the 40 Hz frequency were adjusted downward to account for the lower frequency of the sloshing mode and to account for the elliptical rather than circular shape of the weld pool, then it would be much closer to 20 Hz. In the membrane analysis, going from a circle to an ellipse reduces the frequency approximately 25%, as does going from the third mode to the second mode. If comparable reductions occur in the distributed parameter model, the frequency would decrease from 40 Hz to 23 Hz. Thus, the major peak observed in data sets three and four correlates very well with the theoretical predictions for the sloshing mode of an elliptical weld pool. The smaller peaks could easily be due to higher theoretical modes, the irregular shape of the actual weld pool, and excitation of different modes by metal transfer.

These results contrast sharply with those of Richardson and Renwick (104), who measured frequencies of 130 to 393 Hz for pool widths of 7.21 to 3.73 mm in stationary welds. The difference could be attributable to metal transfer, argon versus helium shielding gas, travel speed, and a greater than expected frequency dependence on weld pool width.

The use of weld pool width as a feedback variable to control pulse

frequency depends on a well described correlation between pool width and resonant frequency. Figures 6.8 and 6.9 show pool width as a function of pulsing frequency for data sets three and four. Comparison of these with figures 6.5 and 6.6 reveals very little discernable correlation between peak location and pool width. The variations in pool width are so small, though, that their effect is obscured by modeling errors and by the effect of other variations, such as shape irregularities. Considerably more work would therefore need to be done before frequency adjustments could be made directly on the basis of measured weld pool width.

6.3 High Frequency Pulsing

Two sets of experiments were run at frequencies of 1000 Hz and above. The first set used a 100/400 A square wave with a wire feed speed of 342 ipm, a travel speed of 13 ipm, and a torch height of 3/4 inches. Frequencies ranged from 1000 Hz to 5000 Hz, and a weld was also made at 100 Hz for comparison. The results are shown in figure 6.10. The second set was run with a 100/380 A square wave, a wire feed speed of 337 ipm, a travel speed of 15 ipm, and a torch height of 1/2 inch. Frequencies ranged up to 8000 Hz, and the results are shown in figure 6.11.

Figure 6.10 shows a steady but remarkable increase in penetration from 1000 Hz to 5000 Hz. The total increase is only .15 mm, so it is less than the potential scatter, and it is not clear that there is any increase at all. All of the high frequency penetrations were approximately .5 mm less than at 100 Hz. Figure 6.11 similarly shows a slightly more significantly increasing trend, but it is not as consistent. The trend is interrupted by decreases in penetration at 4000 Hz and 8000 Hz. All of the penetrations in data set two are .75 to 1.0 mm less than in data set one, due to the faster travel speed and the lower peak current. The high

frequency data in general is inconclusive. Since both sets of experiments resulted in slight increases in penetration with frequency, the trend is probably real. However, the trend is so slight that even if it is real, it is too small to be useful for control purposes.

The significant increase in penetration found in high frequency GTAW does not seem to occur in high frequency GMAW. The metal transfer in GMAW could disrupt the arc constriction effect of high frequency GTAW in one of two ways. First, the metal droplets and the changes in tip geometry can disrupt the plasma jet. Second, metal vapors continue to boil off the electrode and linger in the arc during the background phase. As described in section 3.3.2, this allows re-establishment of the current channel more rapidly than in GTAW, and arc constriction will not be as significant. It is also possible that any effects of arc constriction are overshadowed by metal transfer characteristics. Metal transfer at high frequencies is not fully understood. Peak periods are much shorter than detachment times, so although it is reasonable to assume that a drop detaches every so many pulses, it is not clear what the arc conditions will be during detachment and transfer. High speed films were taken of 1000 Hz and 2000 Hz welds, but the stickout turned out to be longer than in the other filmed welds, and the electrode tip was below the field of view. Future research should include high speed films to study both metal transfer and arc characteristics.

6.4 High Duty Cycle Pulsing

One series of high duty cycle pulsed welds was compared with one series of equivalent mean current constant current welds, with the results shown in figure 6.12. The peak parameters were set at 260 A and 10 ms. The base current was set at 50 A, and the base period was varied from

.5 ms to 2.5 ms. The pulse parameters and resulting weld bead geometries are summarized in table 6.3. Travel speed was 13 ipm, torch height was 5/8 inches, and the wire feed speed was measured to be 341 ipm for all

Table 6.3 High duty cycle pulsing data.

T_b	<I>	I_m	V	d	w	h
.5 ms	241 A	248 A	30.9 V	3.85 mm	12.62 mm	3.29 mm
1.0	232	238	29.4	3.56	12.78	3.19
1.5	224	229	28.4	3.15	12.87	3.19
2.0	217	226	27.5	3.41	13.08	3.10
2.5	210	216	26.3	2.97	13.21	3.13

welds except the third, where it varied between 330 and 335 ipm. The measured currents on the regulator ammeter were slightly higher than the calculated mean currents. This is due to the limited accuracy with which the function generator output can be adjusted. The constant current welds were made with the same WFS, TS, and TH, and with currents ranging from 209 A to 242 A. Figure 6.12 clearly shows that for the same mean current, the pulsed welds had an additional .5 mm of penetration. 260 A is just high enough to form a compound vortex in GTAW, so all four mechanisms of penetration could have contributed to the penetration in the pulsed welds. The constant current welds could not have formed the vortex, so this could be the major source of the difference in penetration. Future experiments should be conducted in the same manner except with different peak currents. Peak currents that are too low to form a vortex would reveal the effects of the other mechanisms. Peak currents that are high enough to definitely form a vortex could then be used in comparison to isolate the effect of the vortex. The effects of the other mechanisms would need to be estimated at the higher peak current level, but since they increase

gradually (whereas the vortex forms suddenly), that is not difficult. The penetration in the constant current welds increased an average .022 mm per amp. According to the Rosenthal solution described in chapter four, penetration from conduction alone would increase .011 mm per amp over the current range from 210 to 230 A with a travel speed of 13 ipm and an arc voltage of 26V (from 3.97 mm to 4.19 mm). Increased conduction from the higher heat input can therefore account for half to the increase in penetration, and the other mechanisms must account for the other half. This current range is below the compound vortex threshold, and increased surface depression due to arc pressure was shown by Lin to be negligible in this region. There will be a slight increase in convection and a significant increase in surface depression due to droplet momentum. The largest single increase in surface depression due to droplet momentum occurs at the spray transition current, near 190 A, as verified by the calculations in table 3.2. The increase in final cavity depth from 170 A to 200 A is .025 mm/A. Drop frequency and radius for higher currents with a 1.2 mm wire are unavailable in the literature, and the high speed films taken at 250 A constant current revealed gross variations in drop size and velocity, making cavity depth calculations unrealistic. However, it is reasonable to assume that the cavity depth would continue to increase above 200 A, but at a slower rate. Drop frequency increases at a much slower rate after the transition region, so this along with the increase in drop velocity will account for a moderate increase in final cavity depth. If the rate were half of that between 170 A and 200 A, it would be .012 mm/A, and would explain very well the increase in penetration from 210 A to 230 A that was not due to conduction. More extensive experiments in this area will require a variable wire feed speed. Variations in the peak current of a high duty cycle waveform create significant variations in mean current, and the wire feed speed will need to be adjusted

accordingly.

6.5 High Peak Pulsing

The high peak pulsing experiments were designed to isolate the effect of arc pressure. Similarly to the high duty cycle experiments, the pulsed welds were compared to constant current welds of equivalent mean current to control for heat input and conduction. All welds were made with a wire feed speed of 340 ipm, a travel speed of 15 ipm, and an arc length of 1/2 inch. Each weld was videotaped, and the torch height was adjusted at the beginning of each weld to bring the electrode to a reference mark on the video screen which indicated a 1/2 inch arc length. The pulsed welds were all 100 Hz with a 7 ms background period and a 3 ms peak period. The background current was 100 A, and the peak current varied from 400 A to 750 A. The shielding gas flow rate was 40 scfh for all welds, and when the torch height was very large, the welds were duplicated at 60 scfh both to ensure adequate shielding of the weld pool and to test the effect of changes in gas flow rate. All welds were made on 3/8" ASTM A36 hot rolled mild steel plates. The welding parameters and bead dimensions are listed in table 6.4. Measured currents were not exactly equal to the theoretical mean currents, but, other than the 100/400 A pulsed weld, they were so close that resultant differences in bead geometry are negligible. For the 100/400 A pulsed weld, the measured mean current is 12 A below the theoretical mean current. At a slope of .02 mm/A, that is a penetration difference of .24 mm, which is significant. The results are plotted in figures 6.13 and 6.14. Figure 6.13 shows penetration as a function of peak current for the pulsed welds. There is a significant increase as the peak current is increased from 500 A to 650 A. This correlates very well with the region in which arc pressure overtakes the compound vortex as the dominant factor in surface depression. Above 500 A the rapidly increasing

Table 6.4 High peak pulsing data.

<I>	I	I_m	gas flow	TH	d	w
190 A	100/400 A	178 A	40 scfh	34.0 mm	2.16 mm	9.14 mm
	190	190	60	43.7	2.11	10.32
205	100/450	205	40	29.5	2.56	10.41
	100/450	205	60	29.5	2.39	9.91
	205	207	60	40.4	2.54	10.58
220	100/500	216	40	25.4	2.52	10.24
	100/500	219	60	25.4	2.71	10.12
	220	221	60	35.1	2.69	11.26
235	100/550	234	40	23.1	3.05	10.16
	100/550	232	60	23.1	2.94	10.14
	235	236	60	30.2	2.69	11.60
250	100/600	246	40	19.8	3.87	9.80
	250	247	40	29.5	2.96	12.23
265	100/650	267	40	17.5	4.13	8.81
	265	264	40	25.4	3.09	12.66
280	100/700	275	40	16.0	4.15	9.44
	280	278	40	22.6	3.03	12.98
295	100/750	290	40	13.5	4.23	10.50
	295	293	40	20.6	3.15	13.21

arc pressure causes the rapid increase in penetration. Above 650 A there is almost no increase in penetration, in spite of the continuing increase in arc pressure. This is due to the fact that the arc cannot effectively deliver heat to the bottom of a deep cavity, as discussed in section 3.3.1. The cavity is very deep and narrow at high peak currents, and the arc impinges on the cavity sidewalls. Delivery of heat by convection to the cavity bottom will increase as plasma velocity increases, but much of

the convection heat will go to the cavity sides, and virtually all of the electrical heat will go to the sides. Even the metal droplets are likely to hit the sidewalls, since they would have to travel exactly down the cavity axis to make it to the bottom. There is almost always some radial deflection of the drop or some asymmetry of the cavity, and this will prevent the drop from delivering its heat to the very bottom of the cavity. Consequently, penetration is self-limiting, and there would not appear to be any advantage in pulsing above 650 A. The additional arc pressure might eventually (at even higher peak currents) increase penetration due to convection heating, but the resulting weld pool turbulence will limit the practical use of such a technique. Even at pulse heights of 700 A there were significant defects, particularly deep undercutting. Additional high peak pulsing experiments were run, but with the intention of studying metal transfer characteristics. These will be discussed in the next section.

6.6 Mid-Peak Drop Transfer

Drop detachment in pulsed welding is controlled by the detachment parameter in equation 3.8. For GMA welding in Ar/CO_2 shielding gas mixtures, the detachment parameter for one drop per pulse welding is approximately 500. Appropriate values for Ar/O_2 mixtures are not available in the literature, but these experiments will give an indication of the appropriate value. Four sets of experiments were run. Each was filmed with the high speed camera. All welds were made on 3/8" ASTM A36 hot rolled mild steel plates with a mean current of 250 A, a travel speed of 15 ipm, a wire feed speed of 335 ipm, and a shielding gas flow rate of 40 scfh. The plates were abrasive blasted and cleaned with acetone prior to welding. The experiments were designed to follow one drop per pulse conditions as much as possible, so a frequency of 125 Hz was used for all

welds, based on the 50 Hz/100 A rule. The basic purpose of these experiments was to describe drop detachment and metal transfer characteristics under varying pulse conditions and to determine their effect on penetration. This information can then be used to control penetration through the variation in pulse parameters. These experiments used higher peak currents and larger detachment parameters than are elsewhere found in the literature.

The data from the drop transfer experiments is listed in appendix D in table D.2. The primary items of interest are the drop detachment times, the drop velocities, and the resulting penetration. Drop diameter is of interest too, but most of the drops were irregularly shaped, and any estimate of drop mass based on a linear dimension measured from the film would be guesswork. Since the wire feed speed is the same for all the welds, the metal transfer mass is the same for all the welds. Differences in metal transfer momentum can therefore be uniquely described by drop velocity. A qualitative description of the metal transfer for each weld is also of interest, and a summary is included in table D.3.

Drop detachment time is defined here as the time from the initiation of the pulse to the detachment of the drop. It is the time that it takes for the tip of the electrode to melt and for the resulting drop to be pinched off by the electromagnetic force. Reference (122) derives the theoretical drop radius at the time of detachment to be:

$$R_d = \frac{\pi\ (R_d + R_e)}{1.25n\ \ [1 + \frac{\mu_o I^2}{\pi^2 (R_e + R_d)\gamma}]^{1/2}} \qquad (6.1)$$

R_d = drop radius
R_e = electrode radius
n = ratio of drop length to drop diameter
γ = surface tension

Equation 6.1 is based on the onset of pinch instability, and it shows that drop radius decreases as current increases, and that the dependence is on the square of the current. Detachment time will therefore depend on the current and the time it takes to form the drop of the appropriate radius. In constant current welding, the time to form the drop is also a function of current, so detachment time is uniquely determined by current (for a given electrode radius, shielding gas, etc.). In pulsed current welding, both the peak and background currents play a role. The overall dependence is rather complicated, since drop formation due to ohmic heating is proportional to I^2, drop formation due to arc heating is proportional to I, and the radius at detachment has a complicated inverse dependence on I^2. Background current will have an effect in that it preheats the wire and it will be the current at the time of detachment if detachment has not occurred by the end of the pulse. The literature commonly assumes detachment time to be inversely proportional to I^2 and the time of detachment in pulsed welding to be uniquely determined by the detachment parameter, $I_p^2T_p$. This is an approximation, but is qualitatively correct, as shown in figure 6.15. We could account for the influence of the background current by defining a total detachment parameter that is the sum of $I_p^2T_p$ and $I_b^2T_b$. Detachment time as a function of this parameter is plotted in figure 6.16. Both figure 6.15 and 6.16 neglect the uncertainty that arises regarding whether the drop detaches during the pulse. Another source of error is the ambiguity of the term "drop detachment". In only a few of the welds did the drops detach cleanly with

a discernable time of detachment. Generally the drop forms and is propelled downward, but a stream of liquid metal maintains contact between it and the electrode. Eventually the stream breaks, but the drop has already begun its transit. If the time of detachment were defined to be the time at which the drop lost physical contact with the electrode, that would be misleading. Since we are really interested in the time at which the drop begins its downward transit, that is how it has been defined for this data. That is a difficult item to determine from films, though, and it certainly led to some errors in the data.

Another way of analyzing detachment time is to plot it as a function of peak period for each peak current, as is done in figure 6.17. When detachment time is larger than the peak period, the detachment time decreases gradually as the peak period increases. The longer peak period produces greater electrode melting and allows detachment to occur sooner in the ensuing background phase. As the peak period lengthens to equal the detachment time, there is a sudden drop in detachment time. Detachment now occurs during the peak phase, and the drop pinches off much faster at the higher current. As the peak period continues to increase, the detachment time remains relatively constant. The additional peak time occurs after detachment and contributes to trailing drop detachment but not to initial drop detachment.

To summarize drop detachment, it is strongly a function of peak current and peak period, although the relationship is more complex than a straight dependence on the detachment parameter. The relationship between detachment time and peak period at a given peak current is intuitively correct and is experimentally verified at moderate peak currents. More data is required to verify it at higher peak currents.

The basic concept of the mid-peak drop transfer strategy is to increase drop velocity by appropriate choice of pulse parameters, thereby increasing penetration. These experiments found that drop velocity increases with increasing detachment parameter, but the correlation suffers from wide ranges of velocities that occur at the same detachment parameter. Figure 6.18 is a plot of drop velocity versus peak period for various peak currents. Here the correlation is extremely good. At each current, drop velocity increases steadily with peak period, and the slope of the increase is steeper at higher currents. The high speed films showed that the drop acceleration occurs entirely in the first few millimeters of travel. It is due to the electromagnetic pinch and the drag from the plasma jet, both of which increase strongly with current. It is significant to note in figure 6.18 that there is not a steep increase in velocity for detachments that occurred during the peak. The closer that detachment occurs to the peak phase, the higher the velocity, but it is a gradual phenomenon. As the 400 A peak period extended to 3.5 ms, thereby incorporating detachment, the velocity showed only a slight increase. The same is true of the 500 A curve at 2.88 ms. The only anomaly in figure 6.18 is the near intersection of the 500 A and 600 A lines. This is probably due to data imprecision, as the 600 A line is based on only two data points. Although each point is the average of numerous drop velocity measurements, an error on the order of .2 m/s is very possible. Increasing the lower velocity of the 600 A line from 2.18 m/s to 2.38 m/s would substantially reduce the proximity of the lines. It would appear, then, that drop velocity can be pre-determined fairly accurately from a knowledge of the pulse parameters. Drop velocity for a 250 A constant current weld was found from high speed films to be 1.48 m/s, which is substantially less than the velocities in the majority of

pulsed welds.

The final item to consider is penetration. Penetration as a function of peak period at various peak currents is shown in figure 6.19. The graph is very similar in nature to figure 6.18, except that there are a few more data point anomalies. It is not clear why penetration is deeper at 2.88 ms than at 3 ms in the 600 A curve. Both welds had similar metal transfer characteristics, with the 3 ms peak period giving a slightly higher drop velocity. The velocity of trailing drops were almost identical in both welds. Weld bead dimension data tends to be characterized by considerable scatter, and these curves are evidently no exception. The other anomaly that merits discussion is the slope of the 800 A line. It is smaller than the slope of the 700 A line and would intersect it at 2 ms. The reason for this could be that the drops in the 800 A 1.72 ms weld were frequently off center. This could account for the diminished penetration at that point.

Essers and Walter (118) claim that the product of drop momentum and frequency is the most significant factor in GMAW penetration. Since all of these welds were made with the same wire feed speed and frequency, drop velocity should have a unique correlation to drop momentum times frequency. Penetration as a function of drop velocity is plotted in figure 6.20. Although a strong trend is evident, there is not the high degree of correlation found by Essers and Walter. There are three reasons for this. First, figure 6.20 does not account for the different velocities of trailing drops. This reduces the equivalency of drop velocity and the product of drop momentum and frequency. Second, figure 6.20 does not account for off-center drop impact, which could reduce penetration even though the velocity is high. Third, it is quite possible that drop

velocity and penetration are correlated but not causally related. While drop velocity is partially responsible for penetration, the same factors that create a high drop velocity (such as large plasma jet velocity) also create a deep penetration. This is supported by the fact that the 250 A constant current weld had an average drop velocity of 1.48 m/s but a penetration of 3.07 mm. This penetration is about .7 mm deeper than the drop velocity would indicate, and it is believed to be due to a shorter arc length. Pulsing gives a shorter electrode extension for the same wire feed speed and average current. The shorter arc with the constant current weld does not increase drop momentum or frequency, but it does increase arc pressure, which therefore has an effect on penetration independently of metal transfer characteristics.

In addition to droplet velocities and droplet masses, the arc characteristics of the welds were examined on the high speed films. Specifically, the arc diameter at 1.5 mm below the electrode tip was measured, with the thought that the expansion in arc diameter (and hence the downward Lorentz force) should coorelate with droplet velocity. No analysis was done, but the data is included in figures 6.21 through 6.33 for completeness.

PENETRATION vs. FREQUENCY

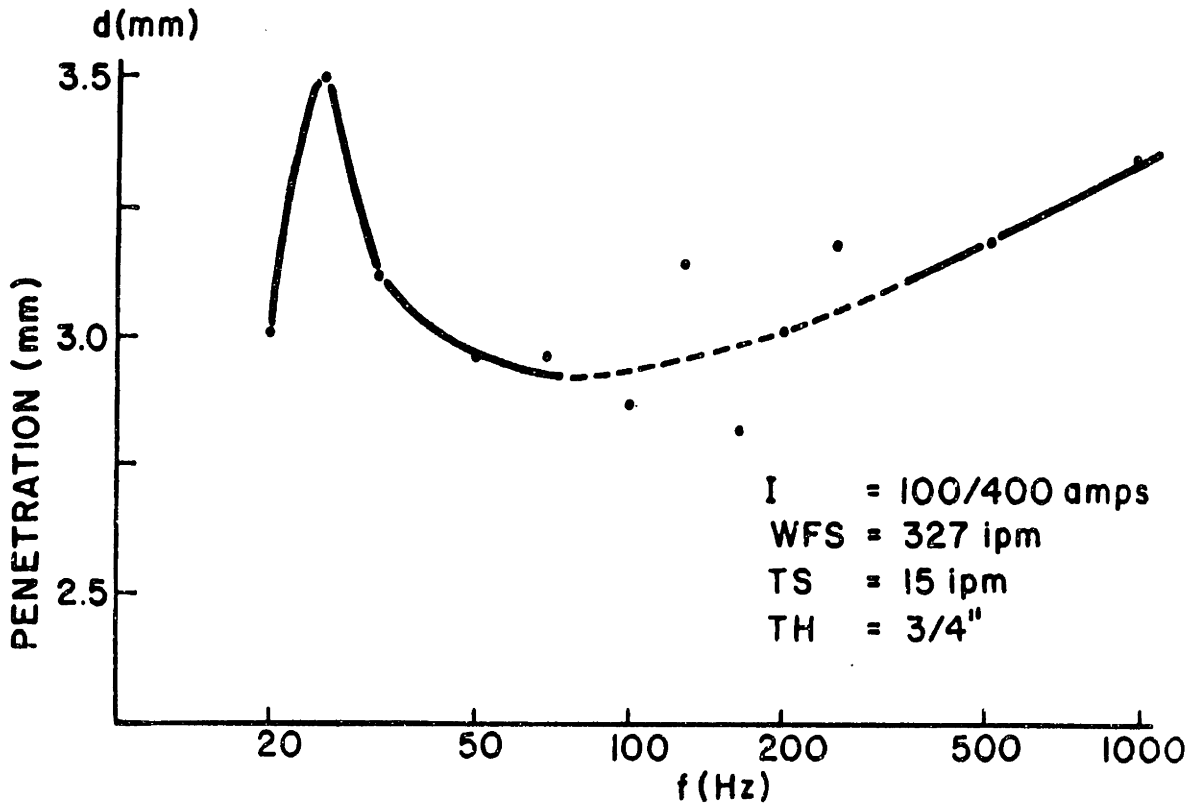

Figure 6.1 Penetration versus frequency.

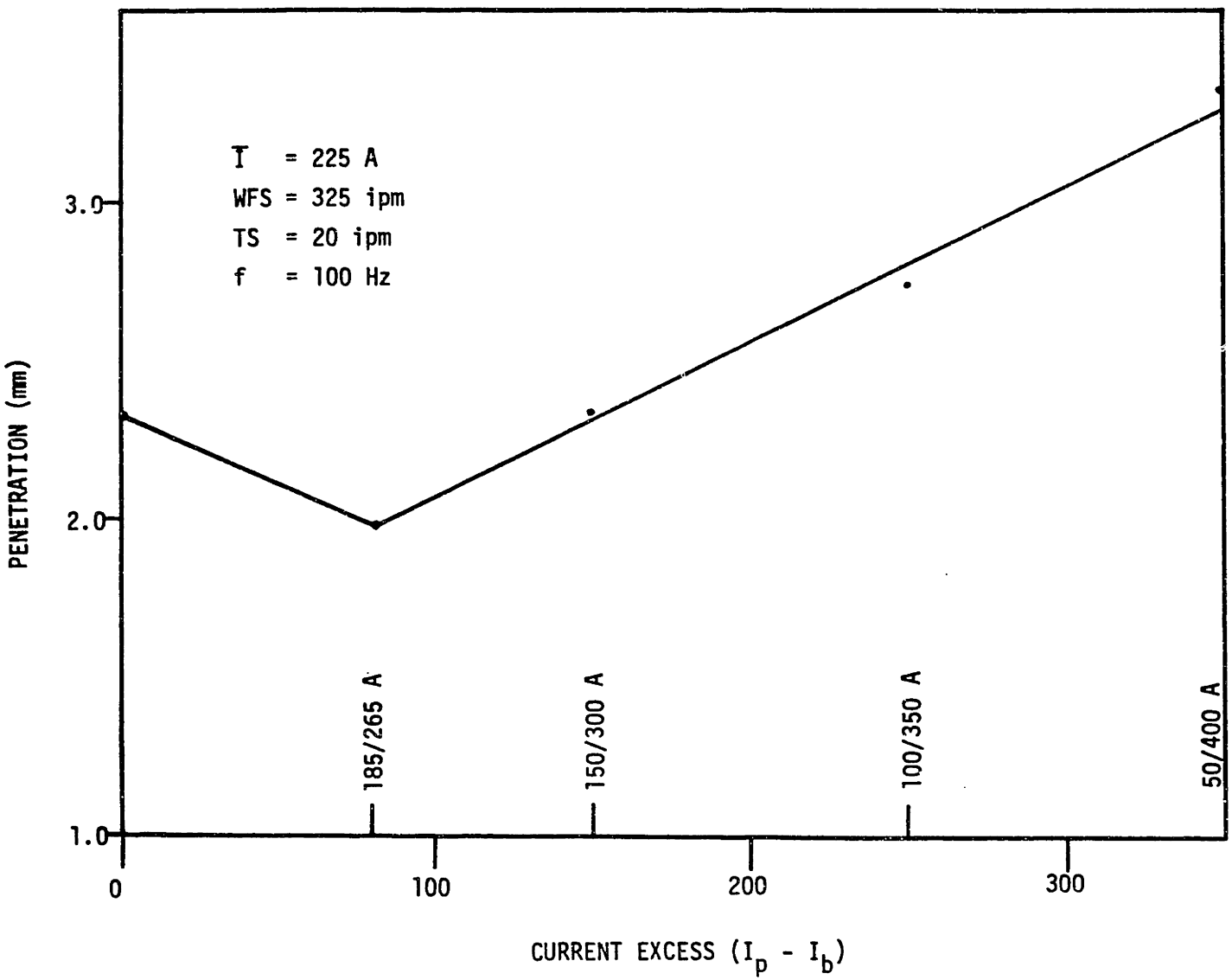

Figure 6.2 Penetration versus current excess.

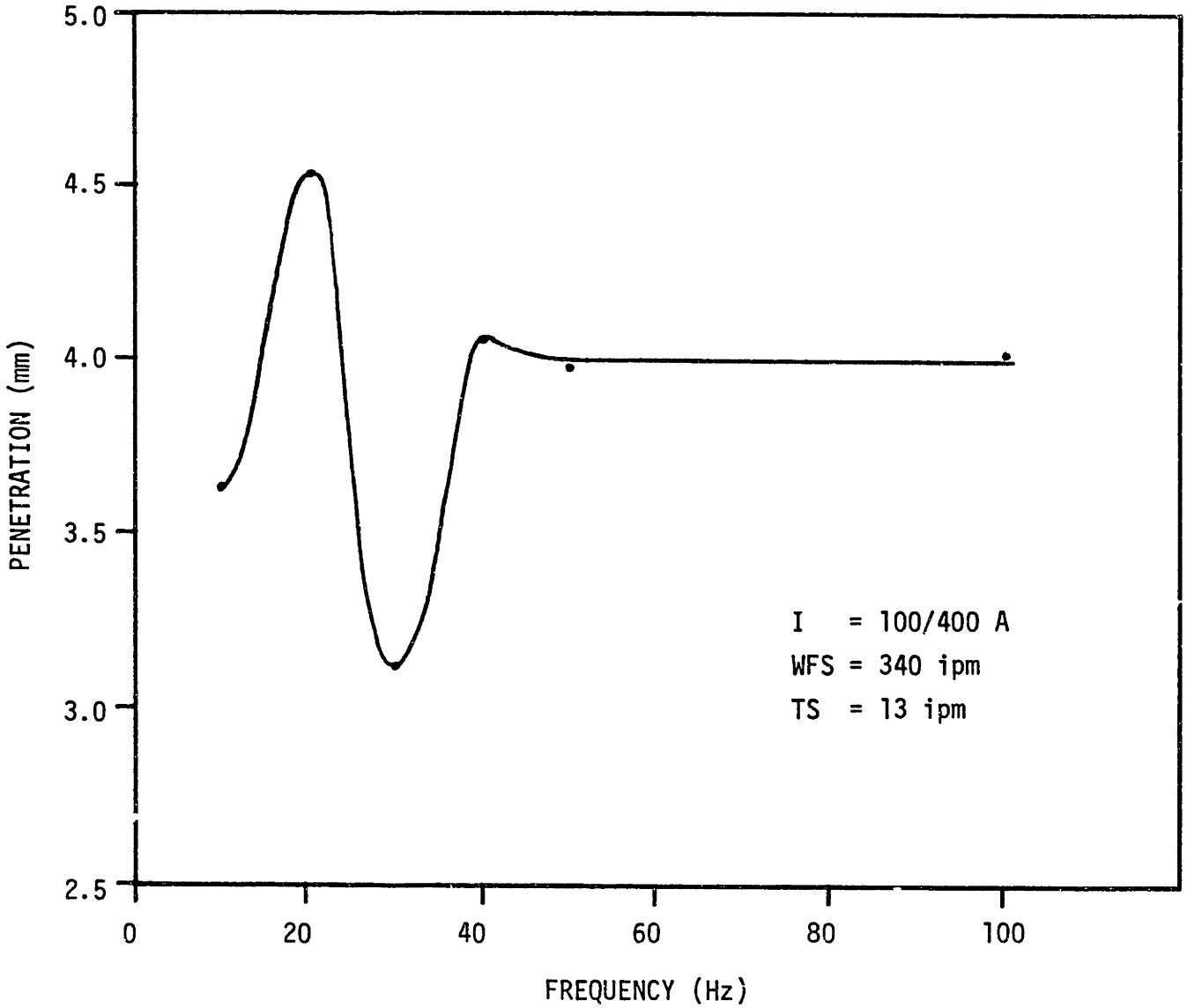

Figure 6.3 Penetration at low frequencies, data set #1.

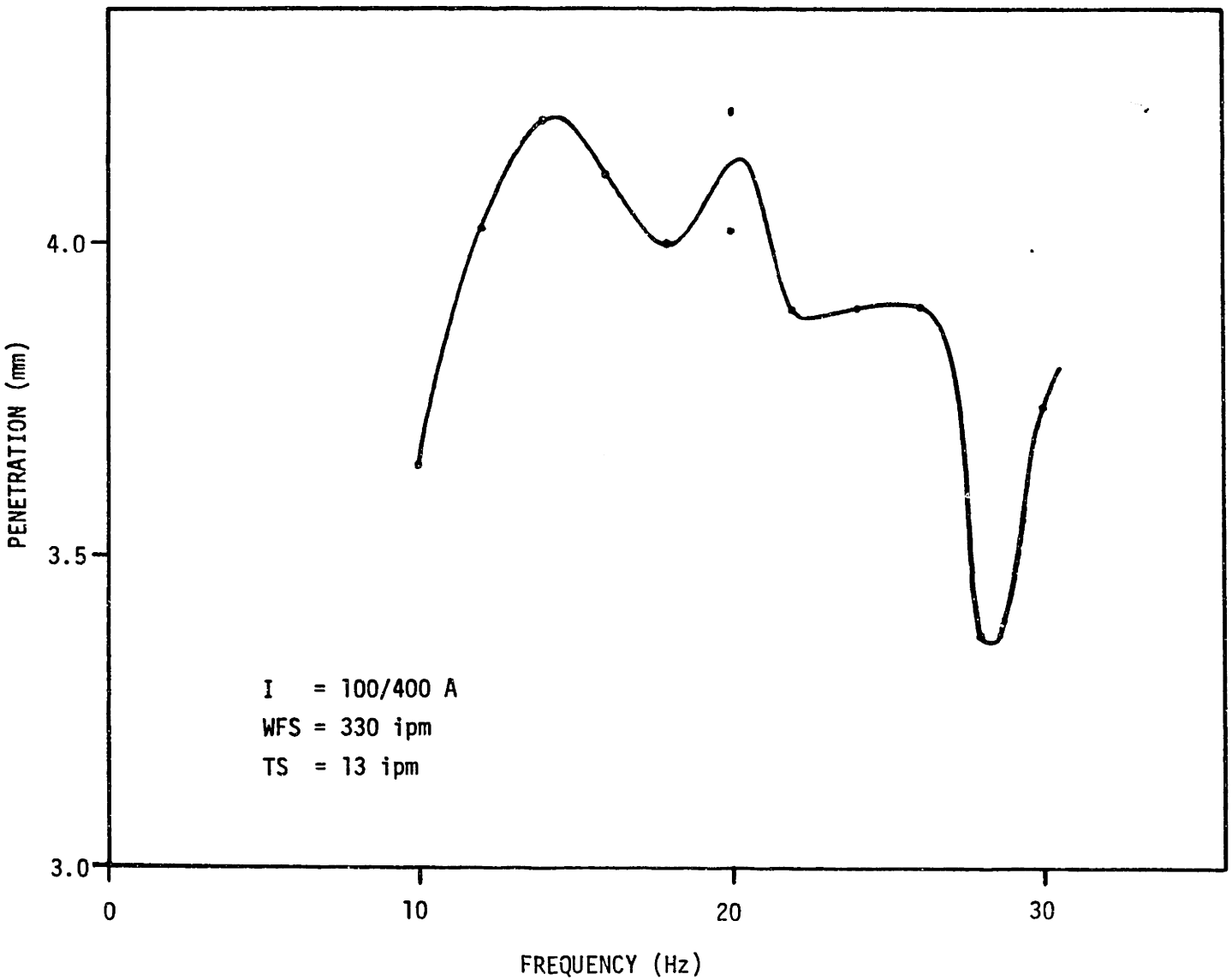

Figure 6.4 Penetration at low frequencies, data set #2.

PENETRATION AT LOW FREQUENCIES

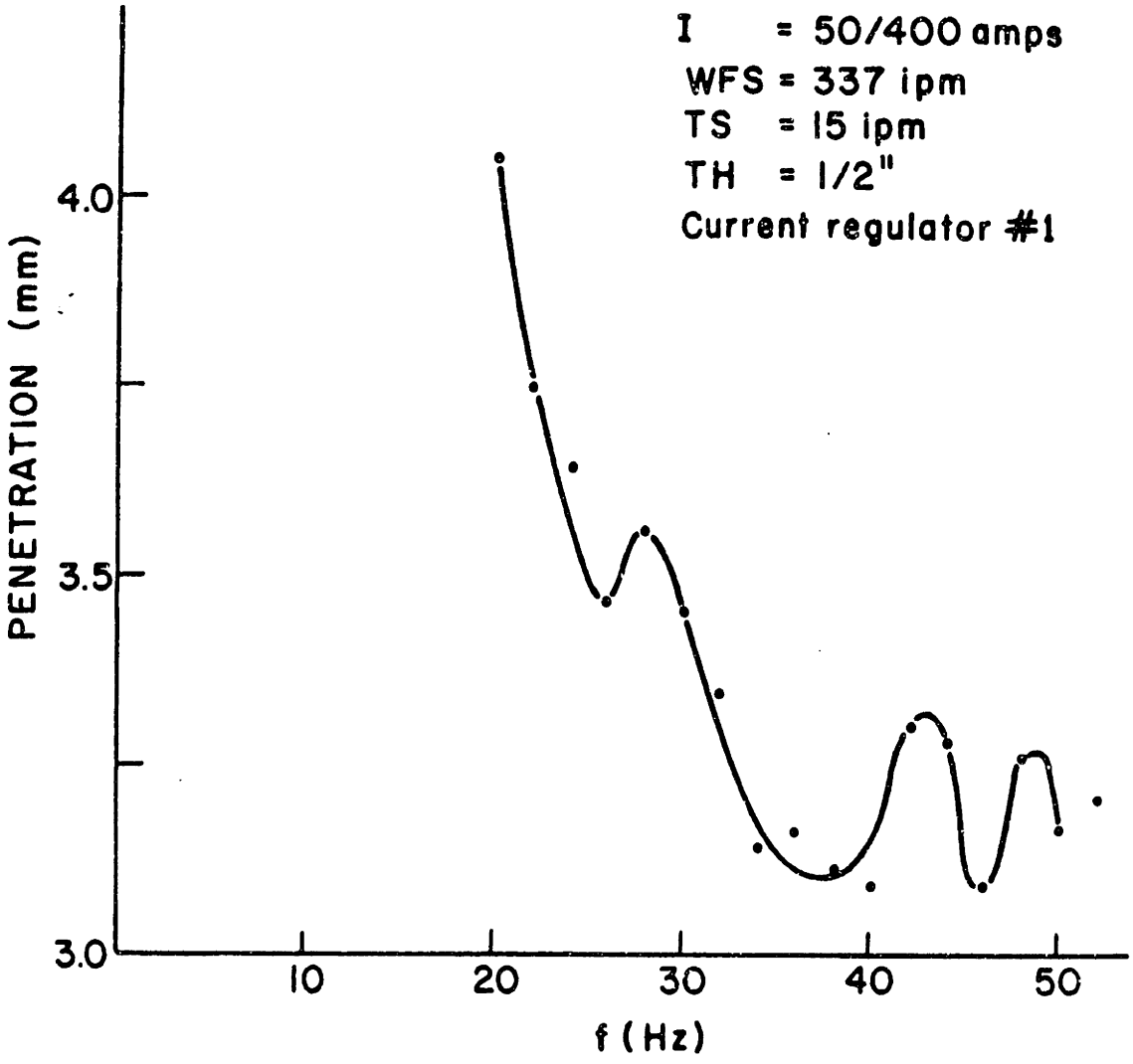

Figure 6.5 Penetration at low frequencies, data set #3.

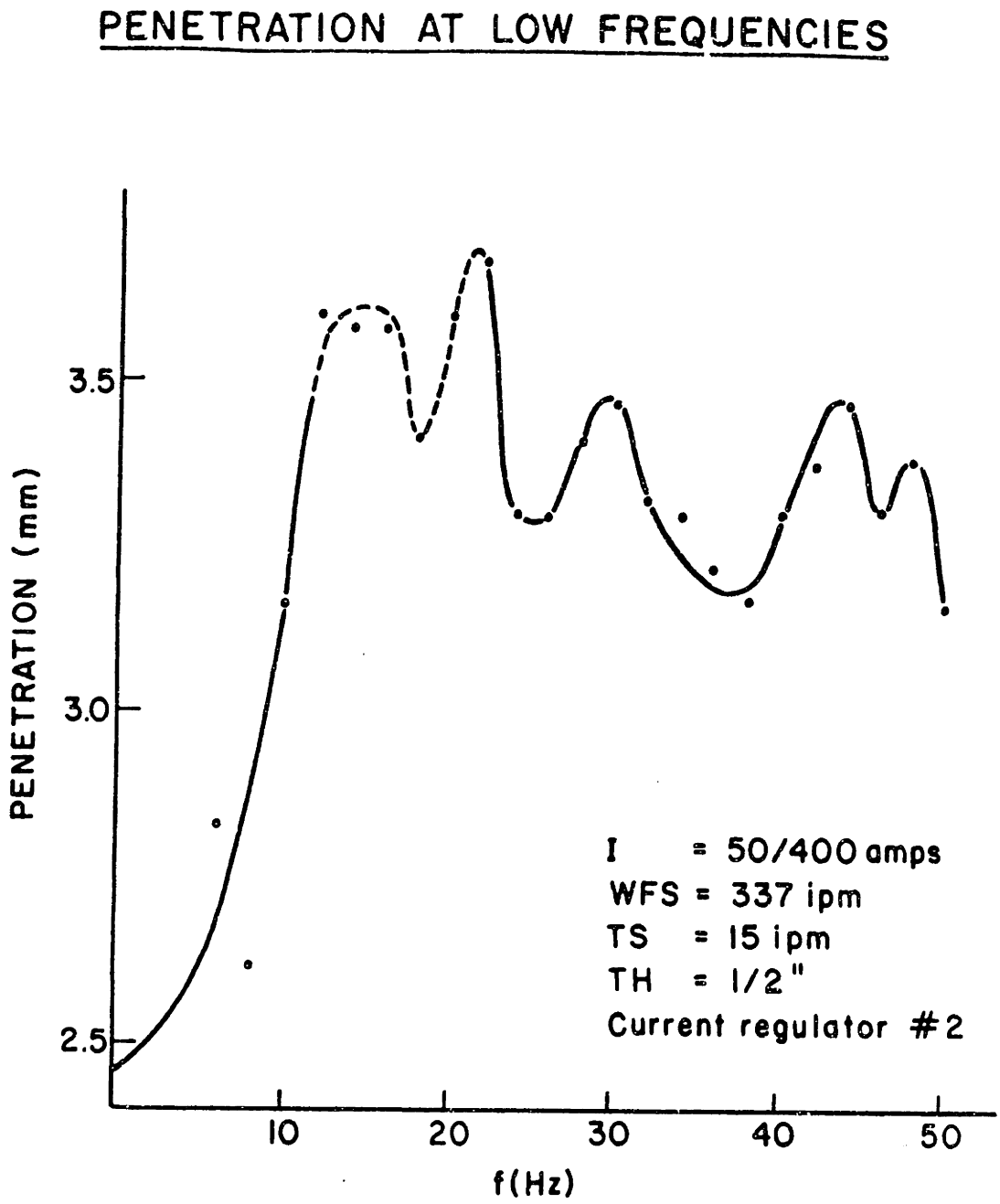

Figure 6.6 Penetration at low frequencies, data set #4.

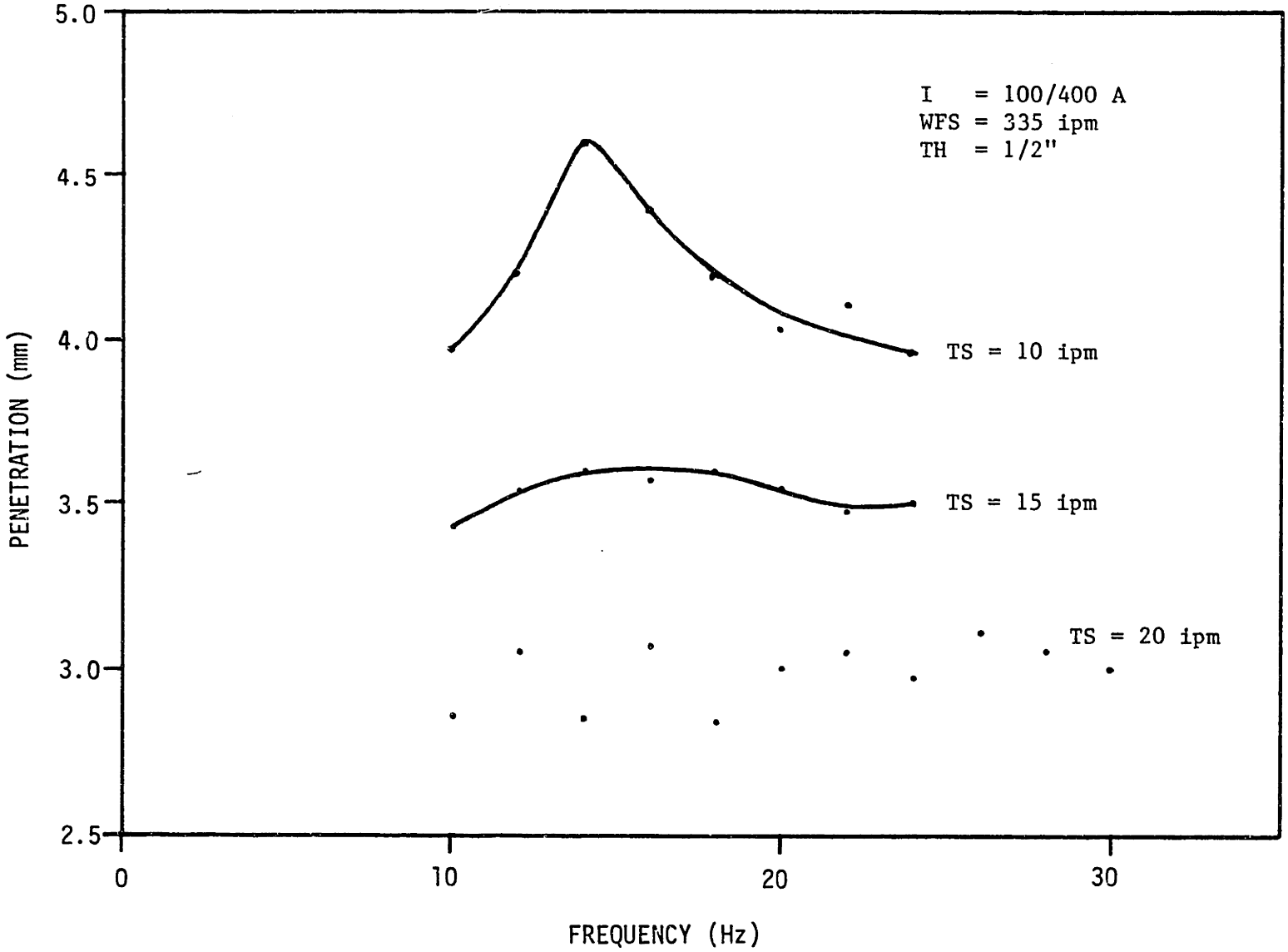

Figure 6.7 Penetration at low frequencies, data set #5.

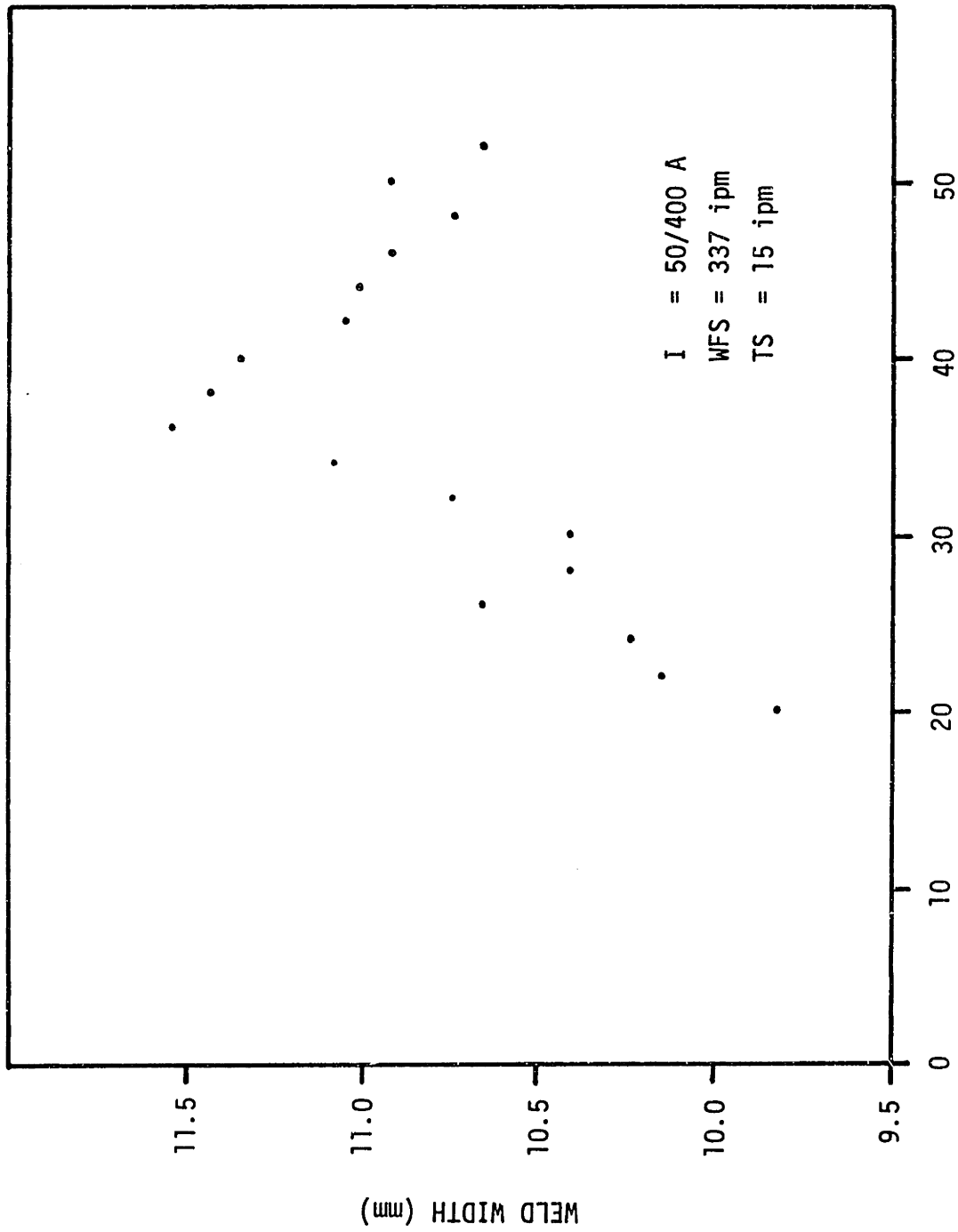

Figure 6.8 Weld pool width at low frequencies, data set #3.

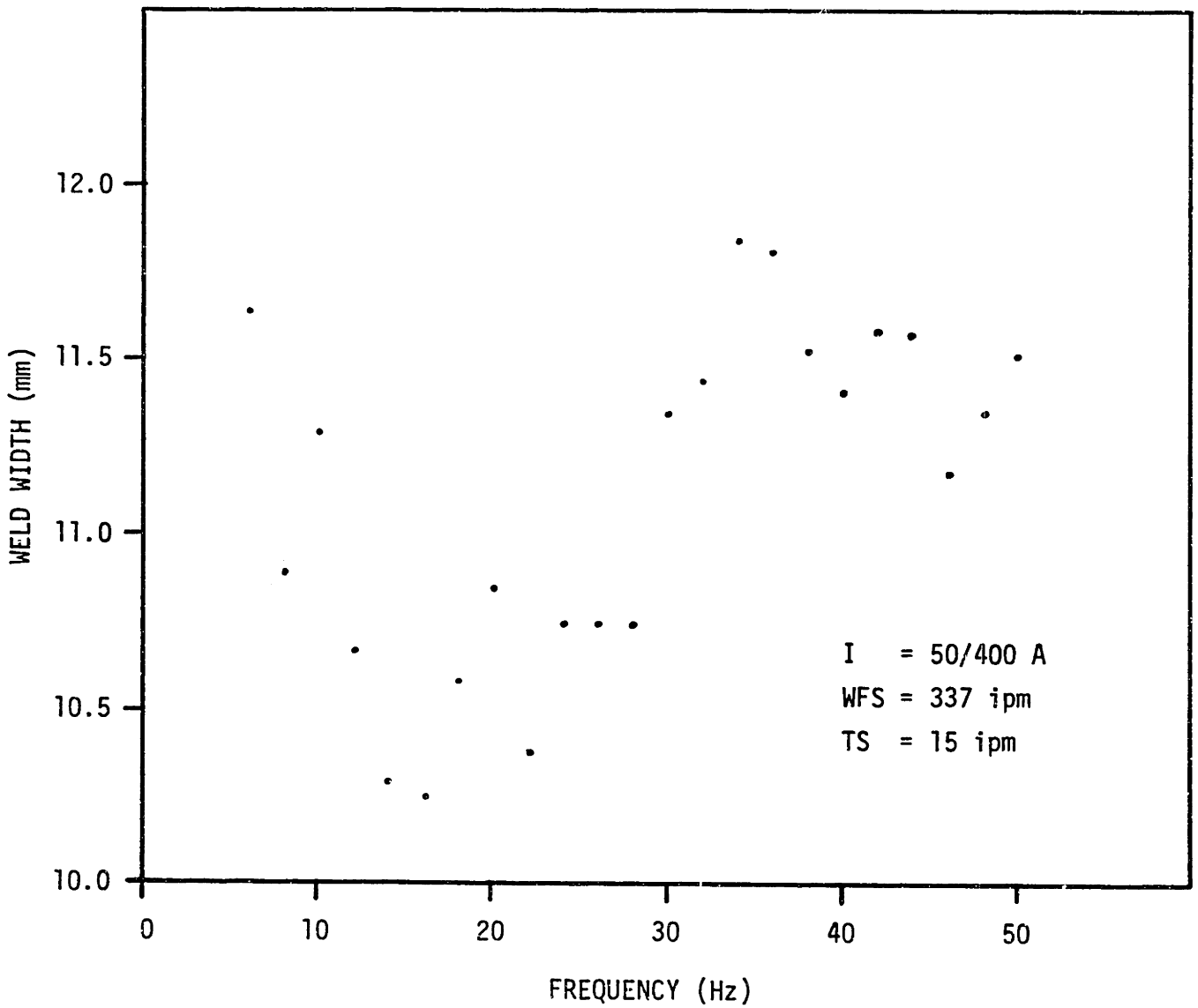

Figure 6.9 Weld pool width at low frequencies, data set #4.

PENETRATION AT HIGH FREQUENCIES

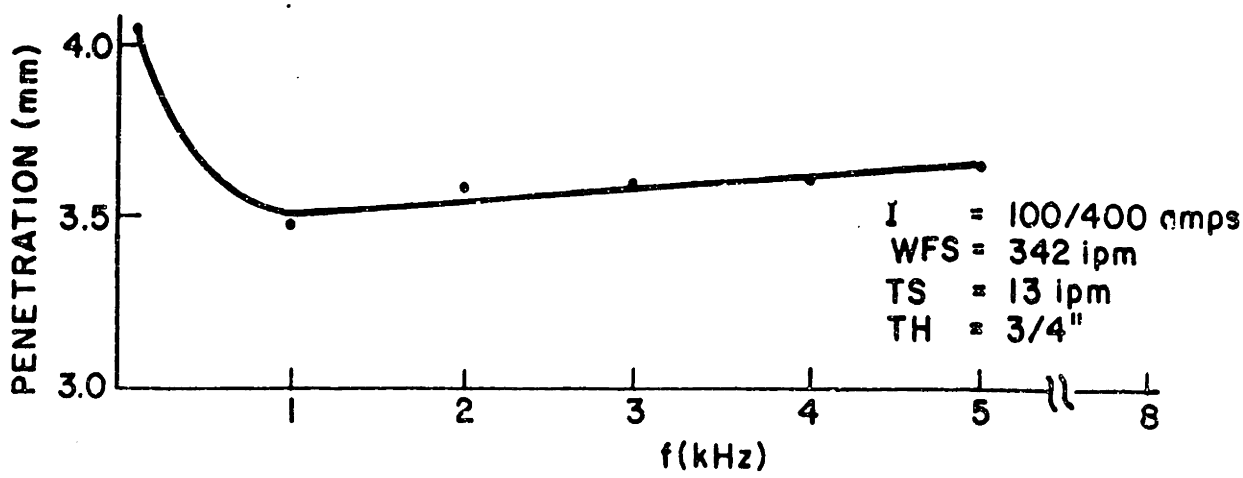

Figure 6.10 Penetration at high frequencies, data set #1.

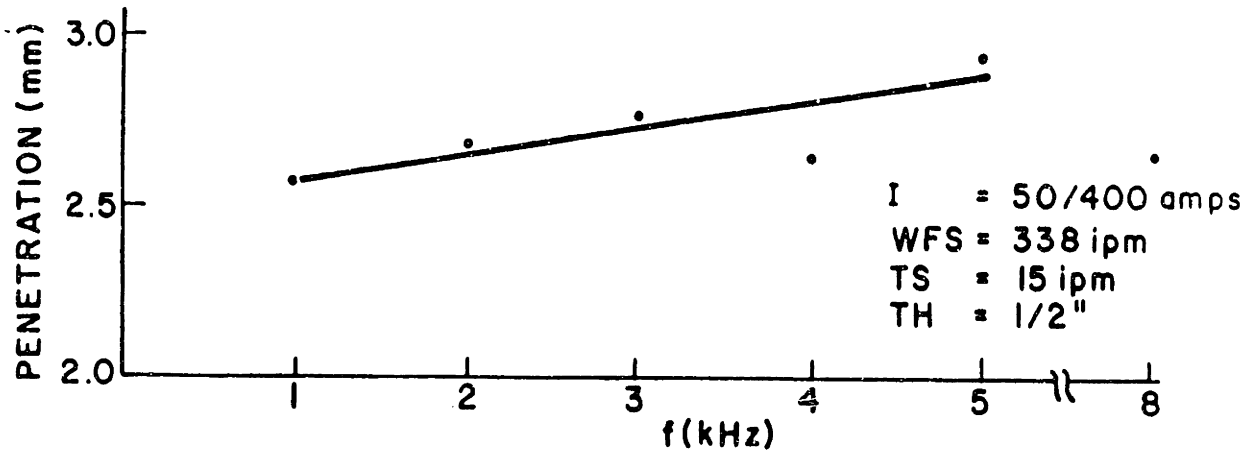

Figure 6.11 Penetration at high frequencies, data set #2.

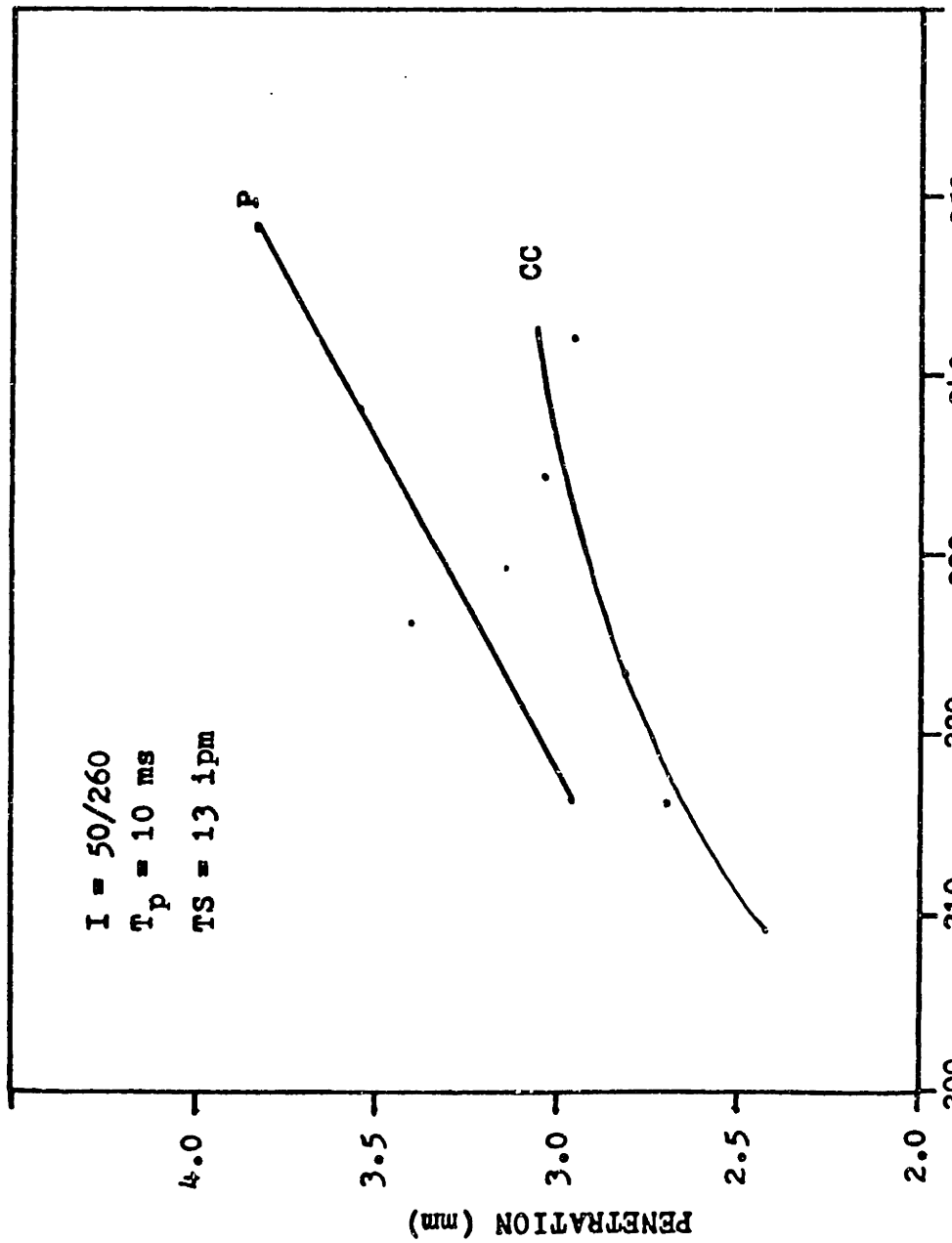

Figure 6.12 Penetration in high duty cycle pulsed welds.

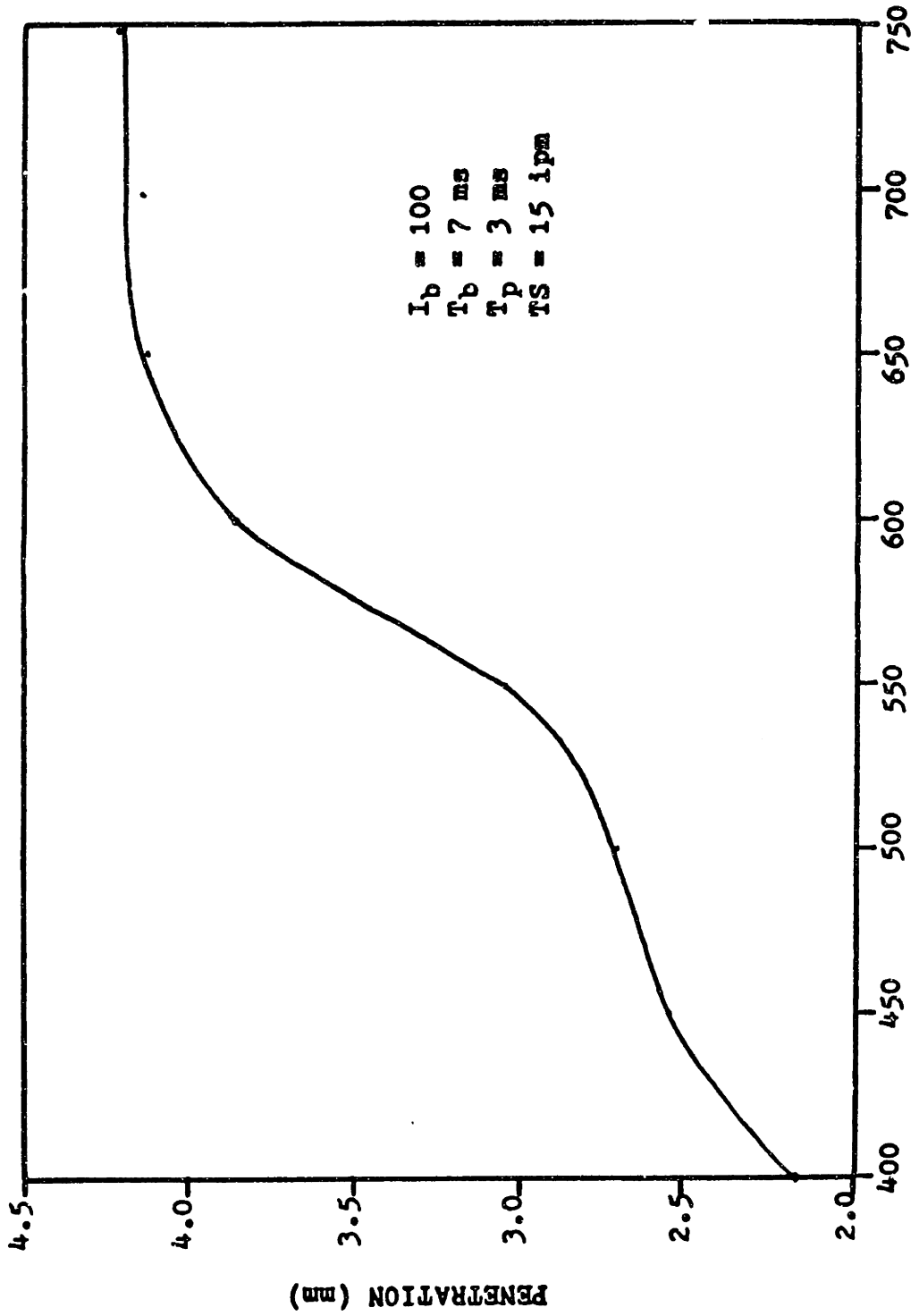

Figure 6.13 Penetration versus peak current.

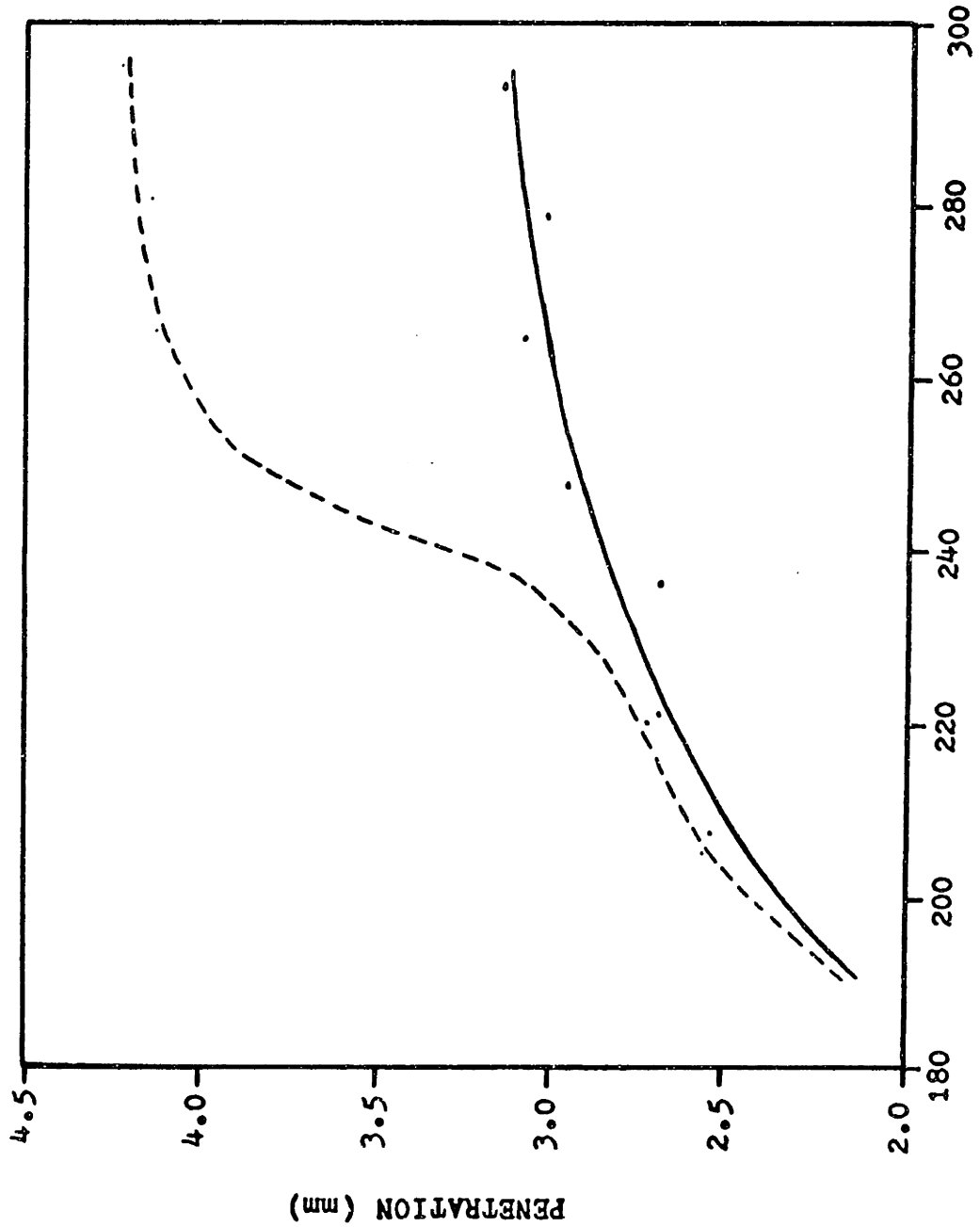

Figure 6.14 Penetration versus mean current.

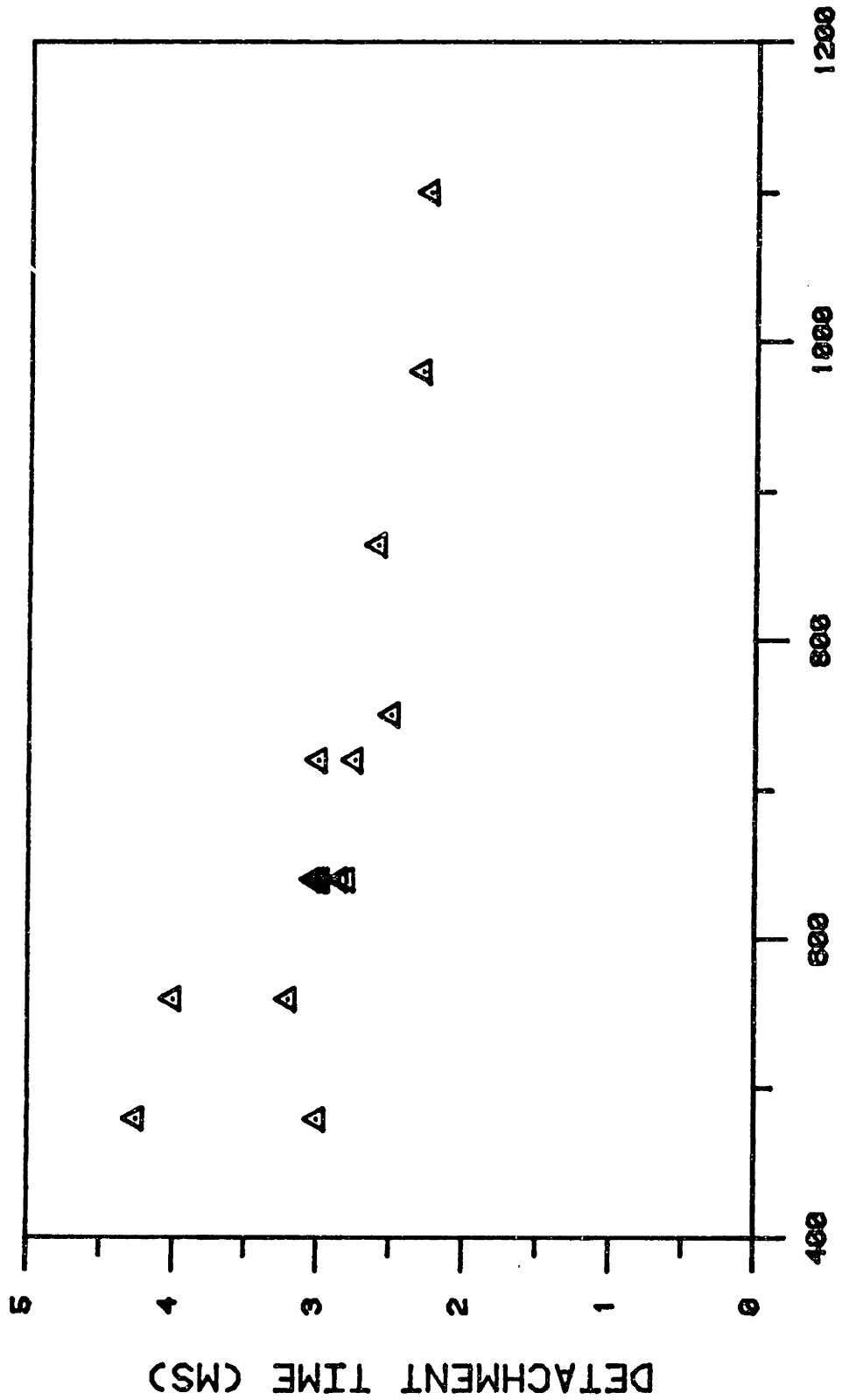

Figure 6.15 Detachment time versus detachment parameter.

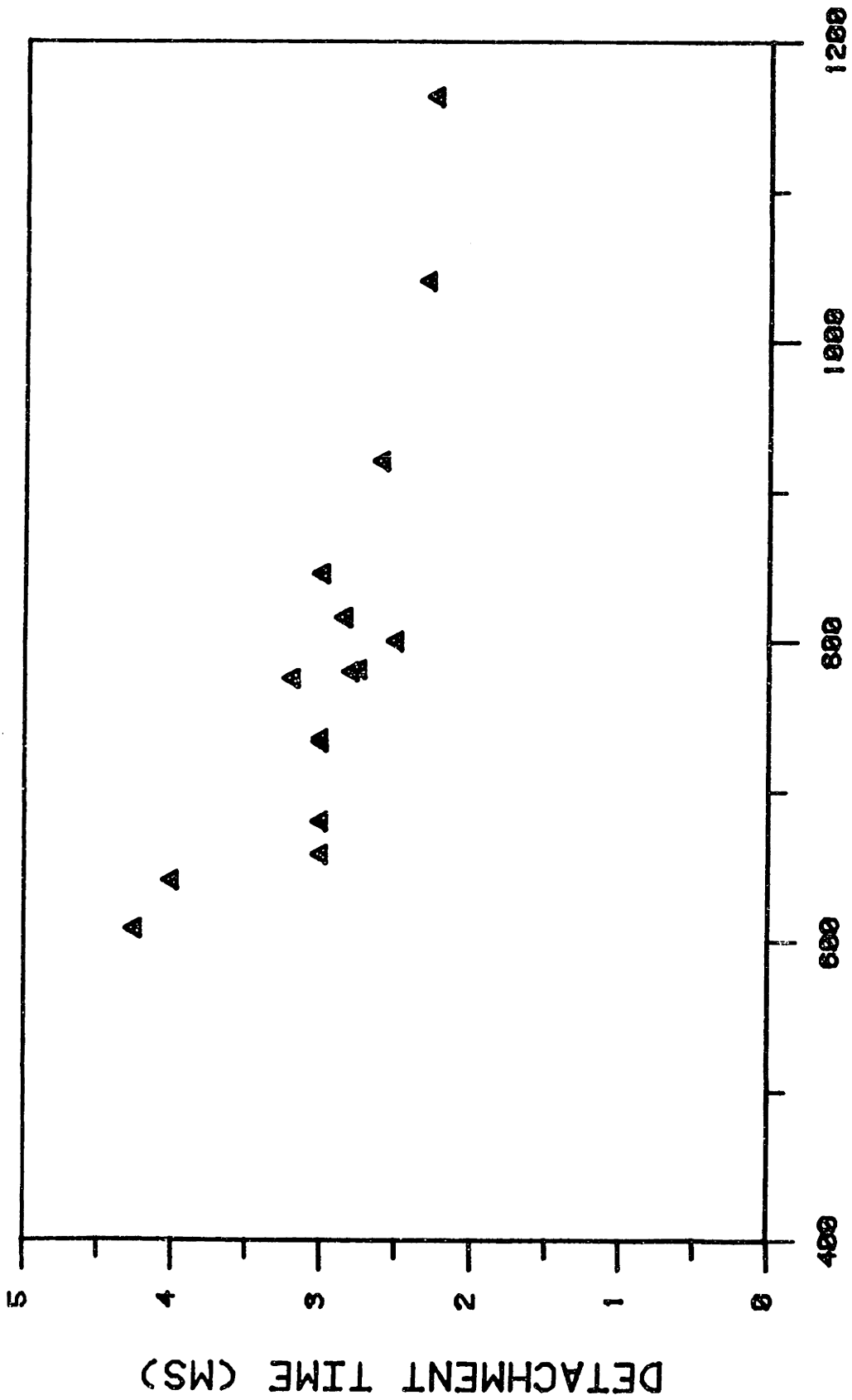

Figure 6.16 Detachment time versus total detachment parameter.

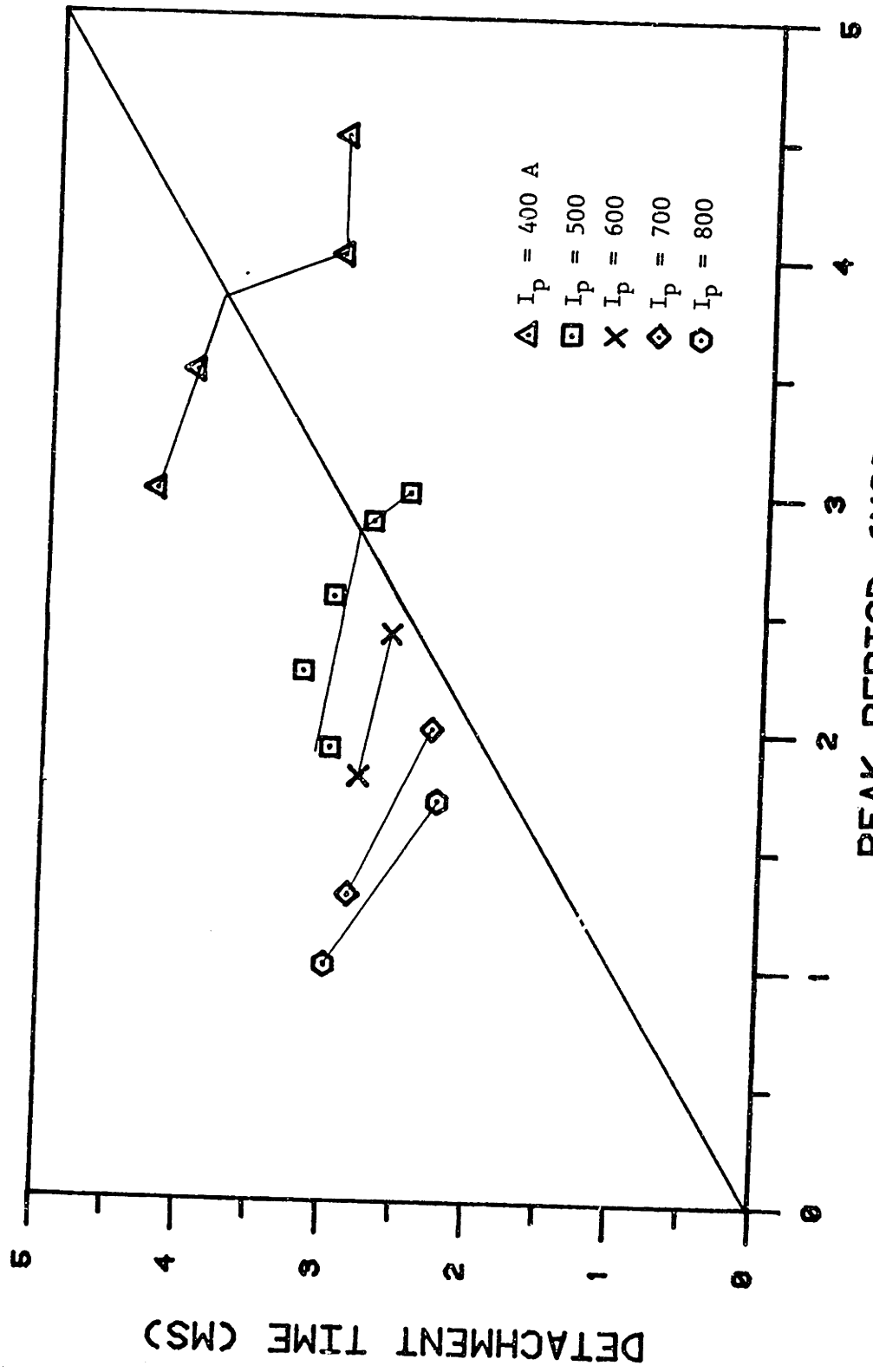

Figure 6.17 Detachment time versus peak period.

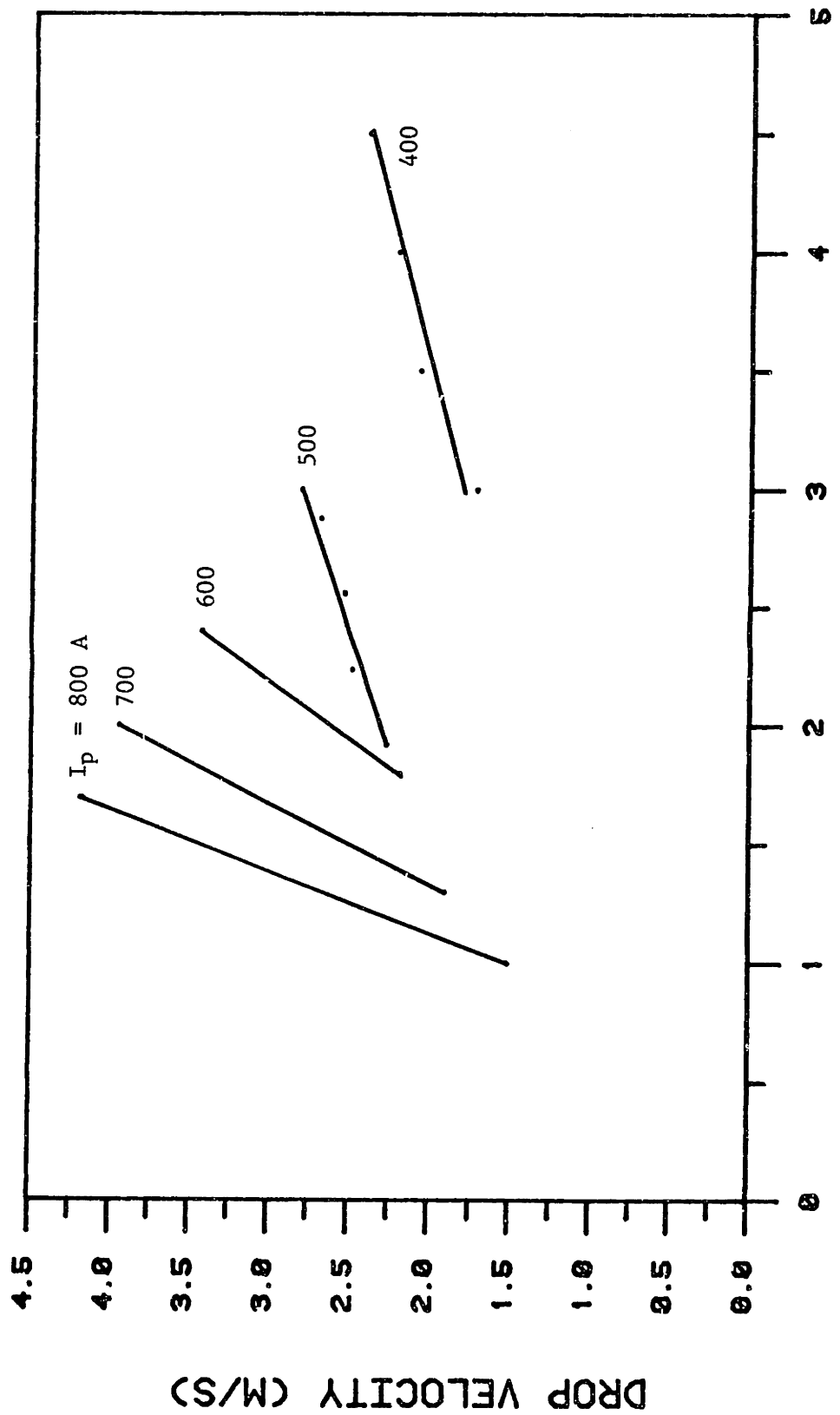

Figure 6.18 Drop velocity versus peak period.

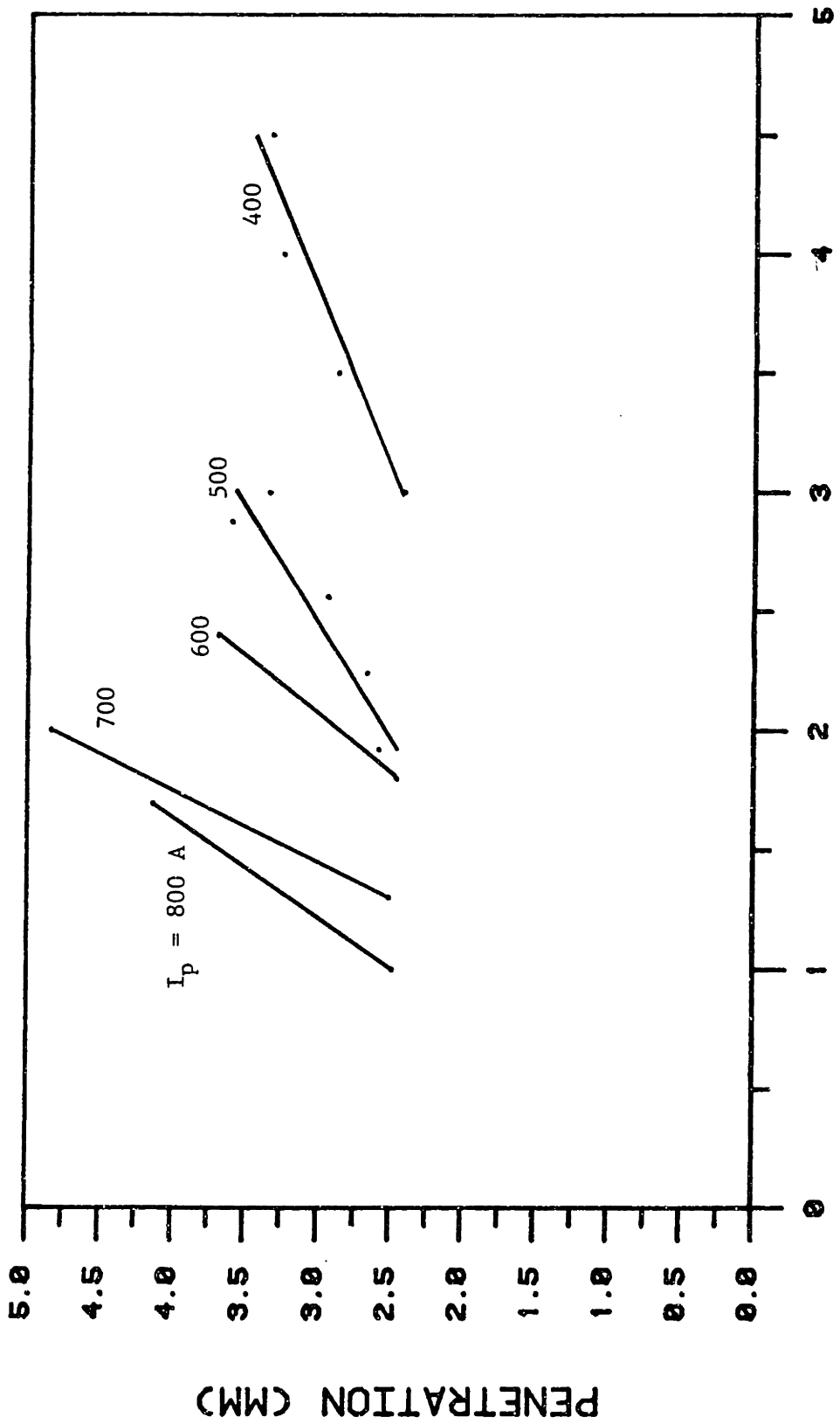

Figure 6.19 Penetration versus peak period.

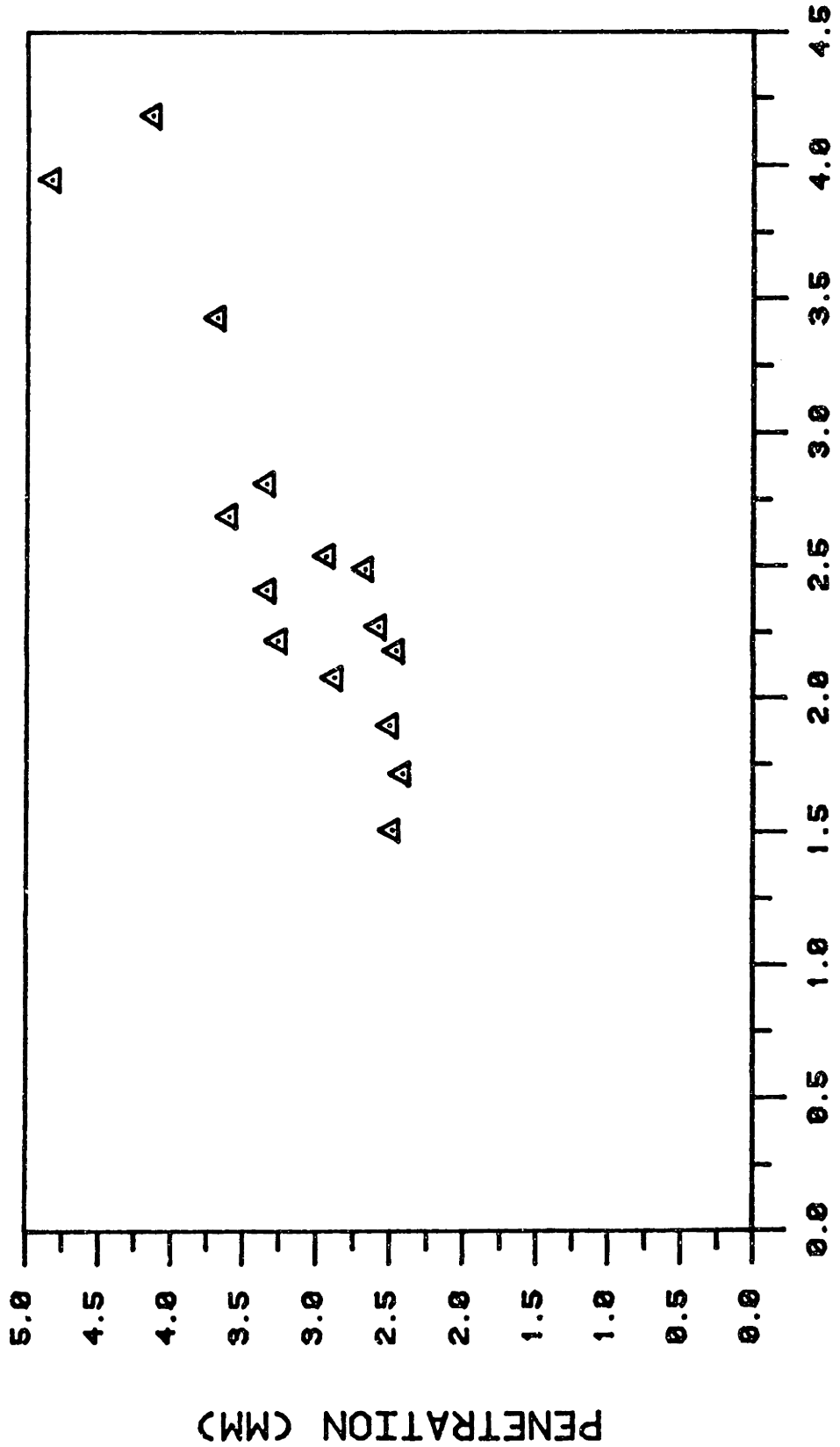

Figure 6.20 Penetration versus drop velocity.

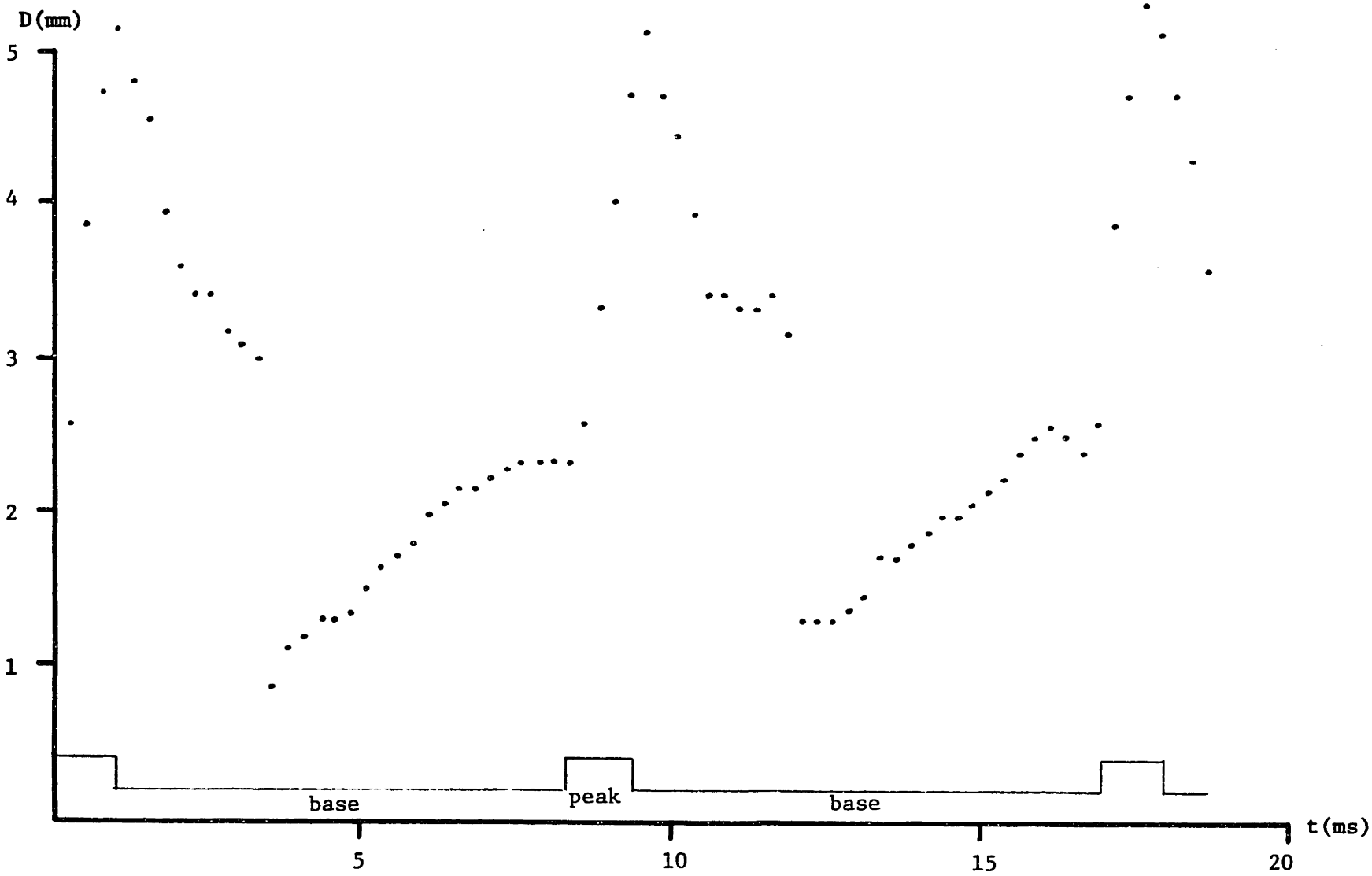

Figure 6.21 Arc diameter 1.5 mm below the electrode tip for HSF weld #1. I = 171/800 amps. T_b = 7 ms, T_p = 1 ms. The current line shows only period and is based on visual observation of the film.

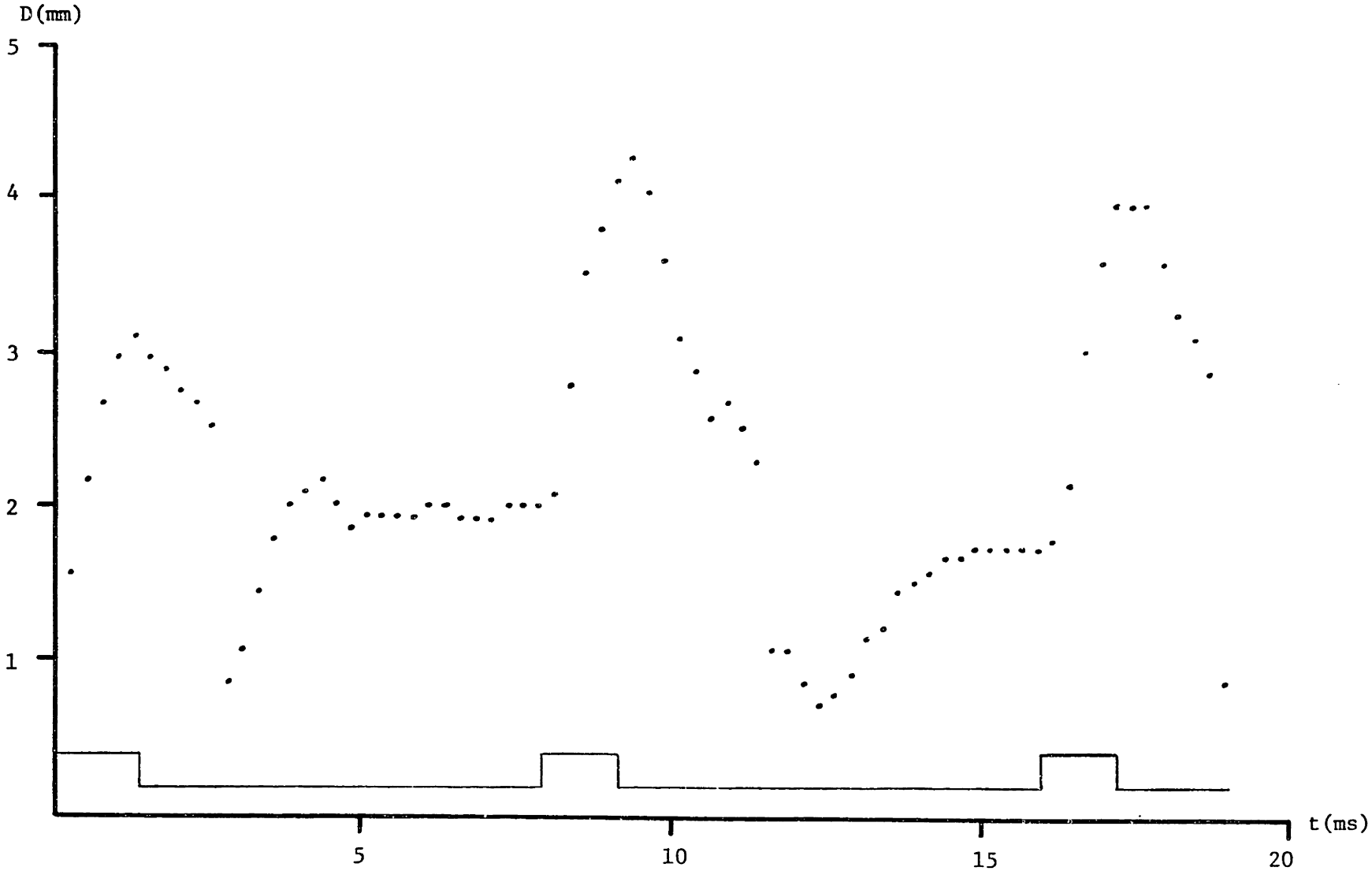

Figure 6.22 Arc diameter 1.5 mm below the electrode tip for HSF weld #2. I = 162/700 amps. T_b = 6.69 ms, T_p = 1.31 ms.

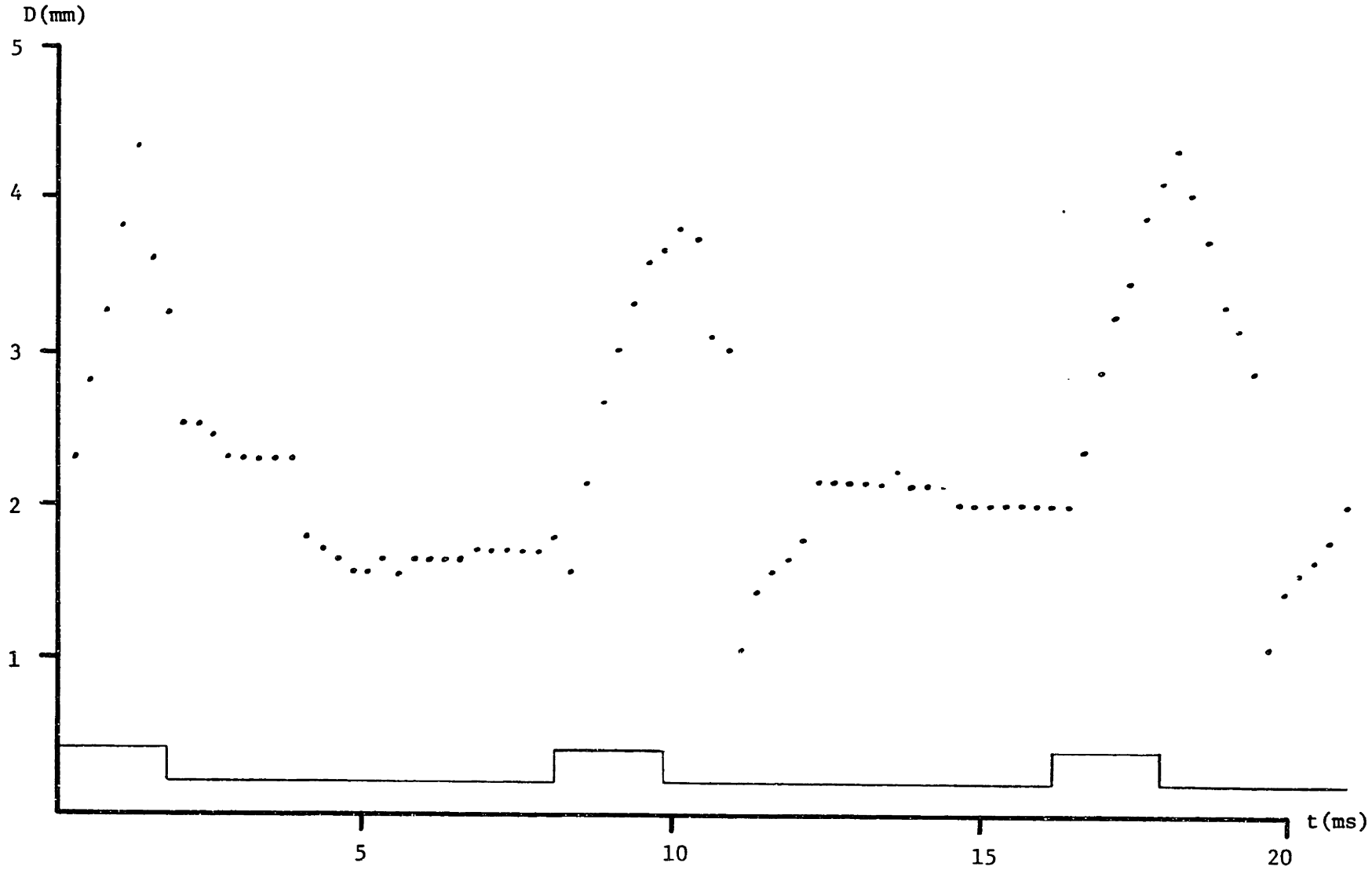

Figure 6.23 Arc diameter 1.5 mm below the electrode tip for HSF weld #3. I = 150/600 amps. T_b = 6.22 ms, T_p = 1.78 ms.

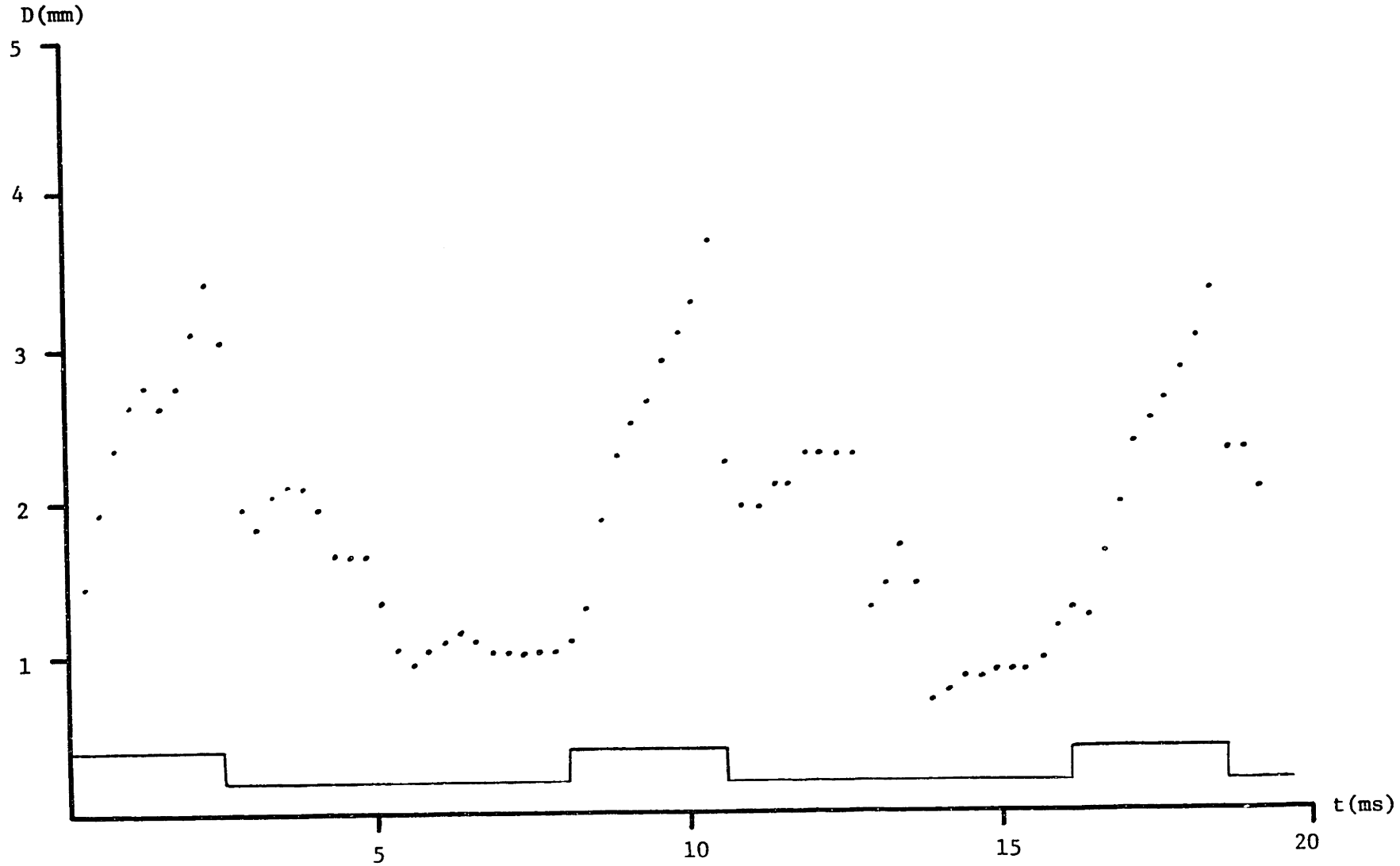

Figure 6.24 Arc diameter 1.5 mm below the electrode tip for HSF weld #4.
I = 132/500 amps. T_b = 5.44 ms, T_p = 2.56 ms.

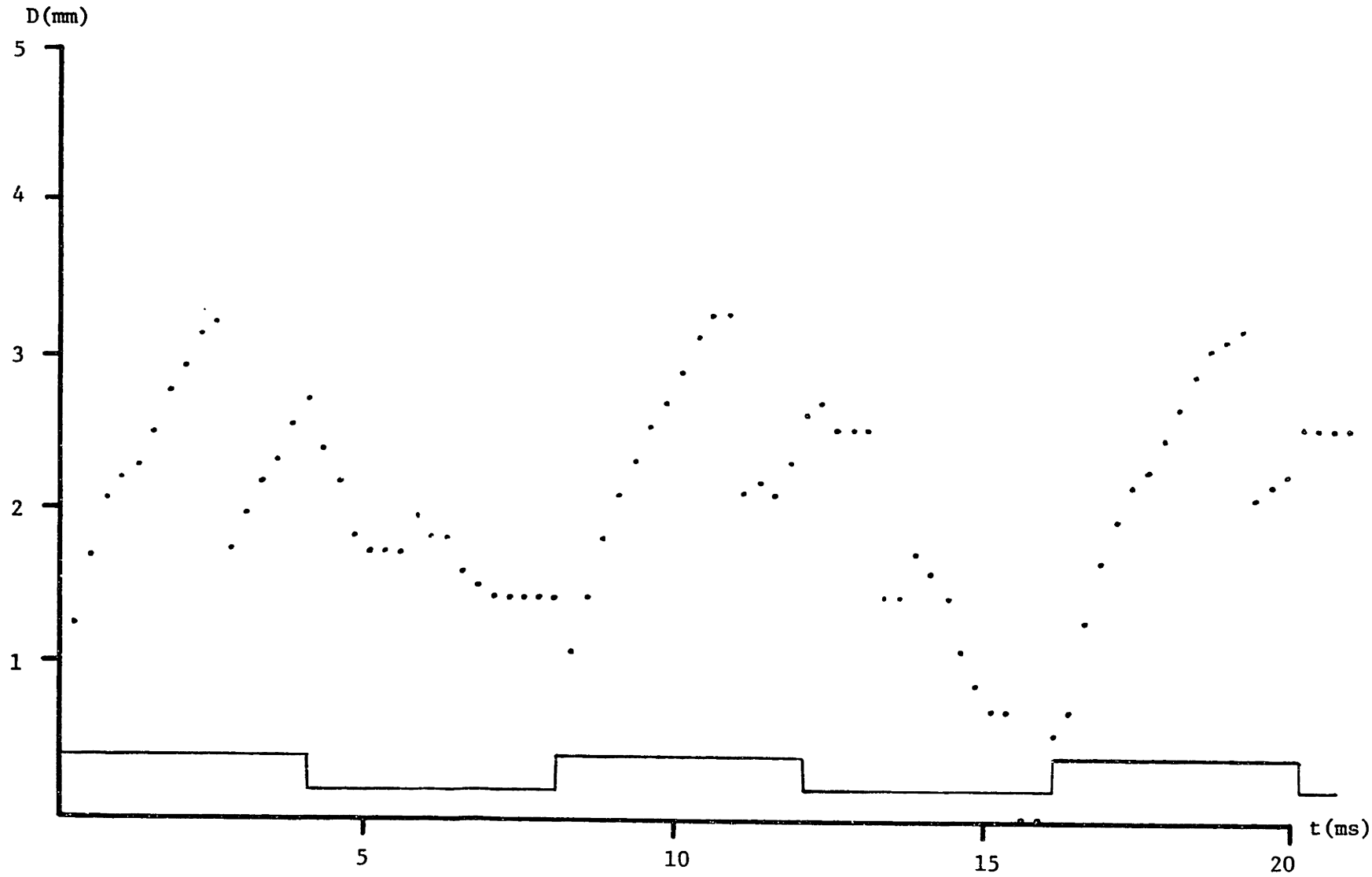

Figure 6.25 Arc diameter 1.5 mm below the electrode tip for HSF weld #5. I = 100/400 amps. T_b = 4 ms, T_p = 4 ms.

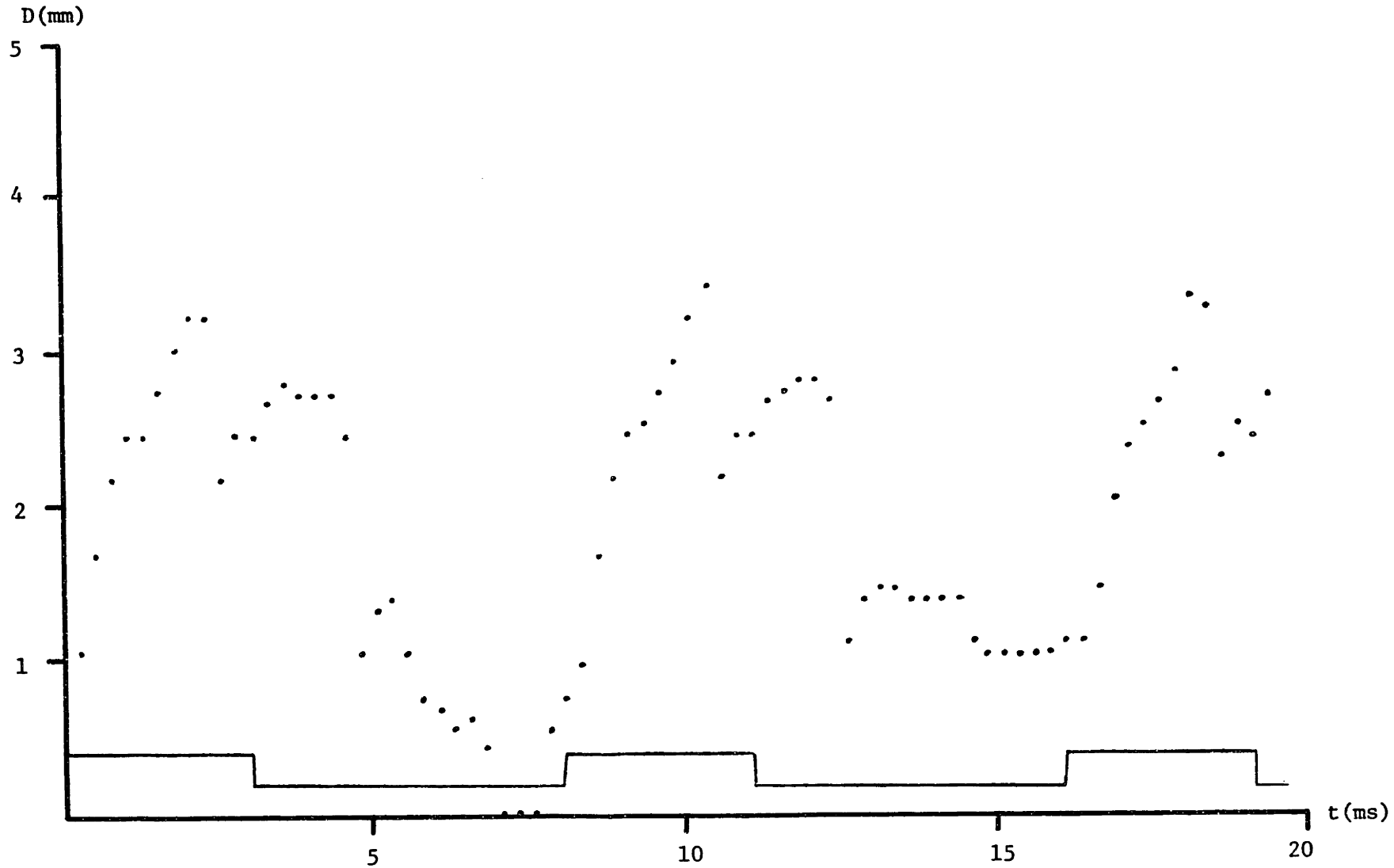

Figure 6.26 Arc diameter 1.5 mm below the electrode tip for HSF weld #6. I = 100/500 amps. T_b = 5 ms, T_p = 3 ms.

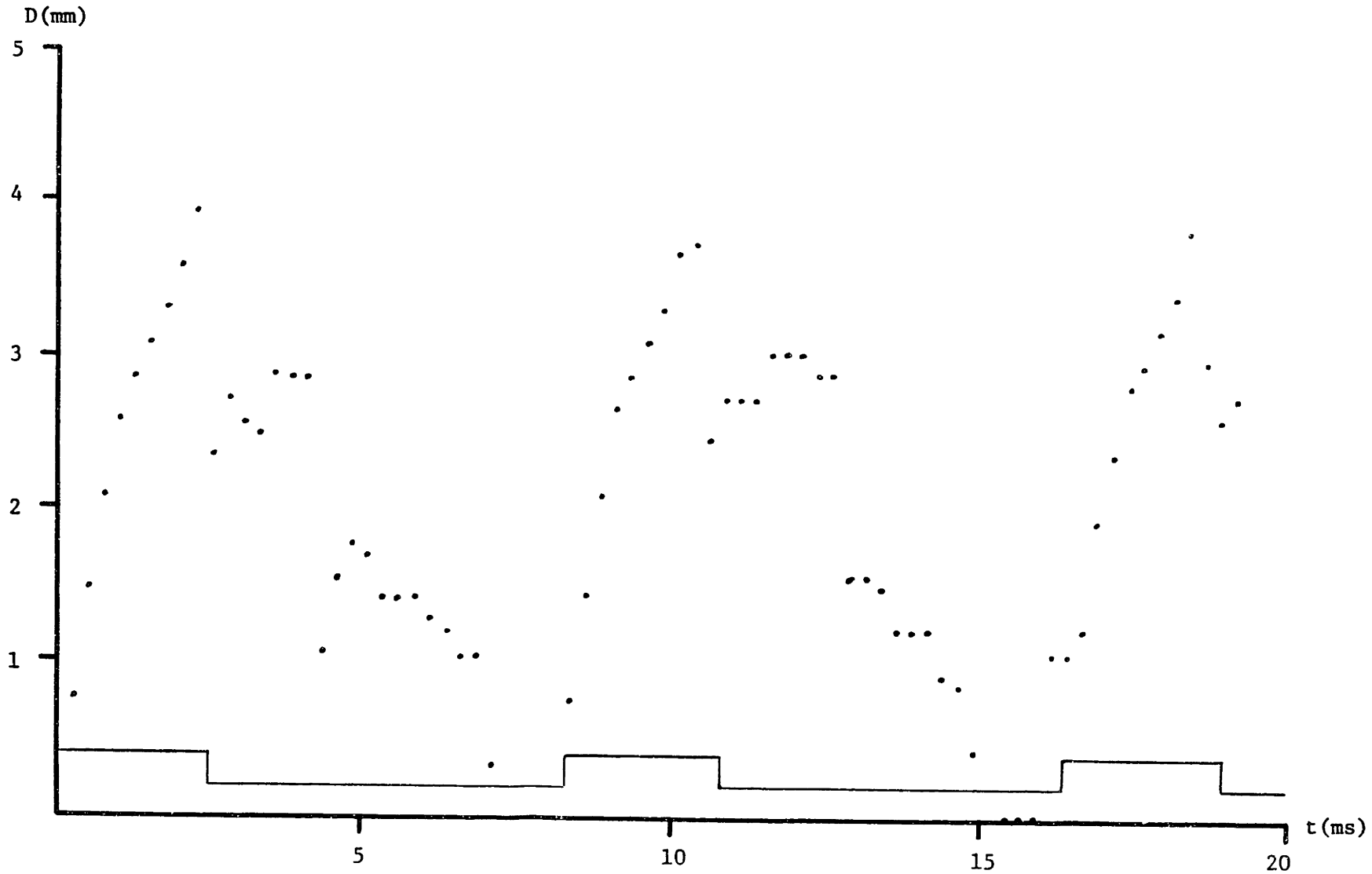

Figure 6.27 Arc diameter 1.5 mm below the electrode tip for HSF weld #7. I = 100/600 amps. T_b = 5.6 ms, T_p = 2.4 ms.

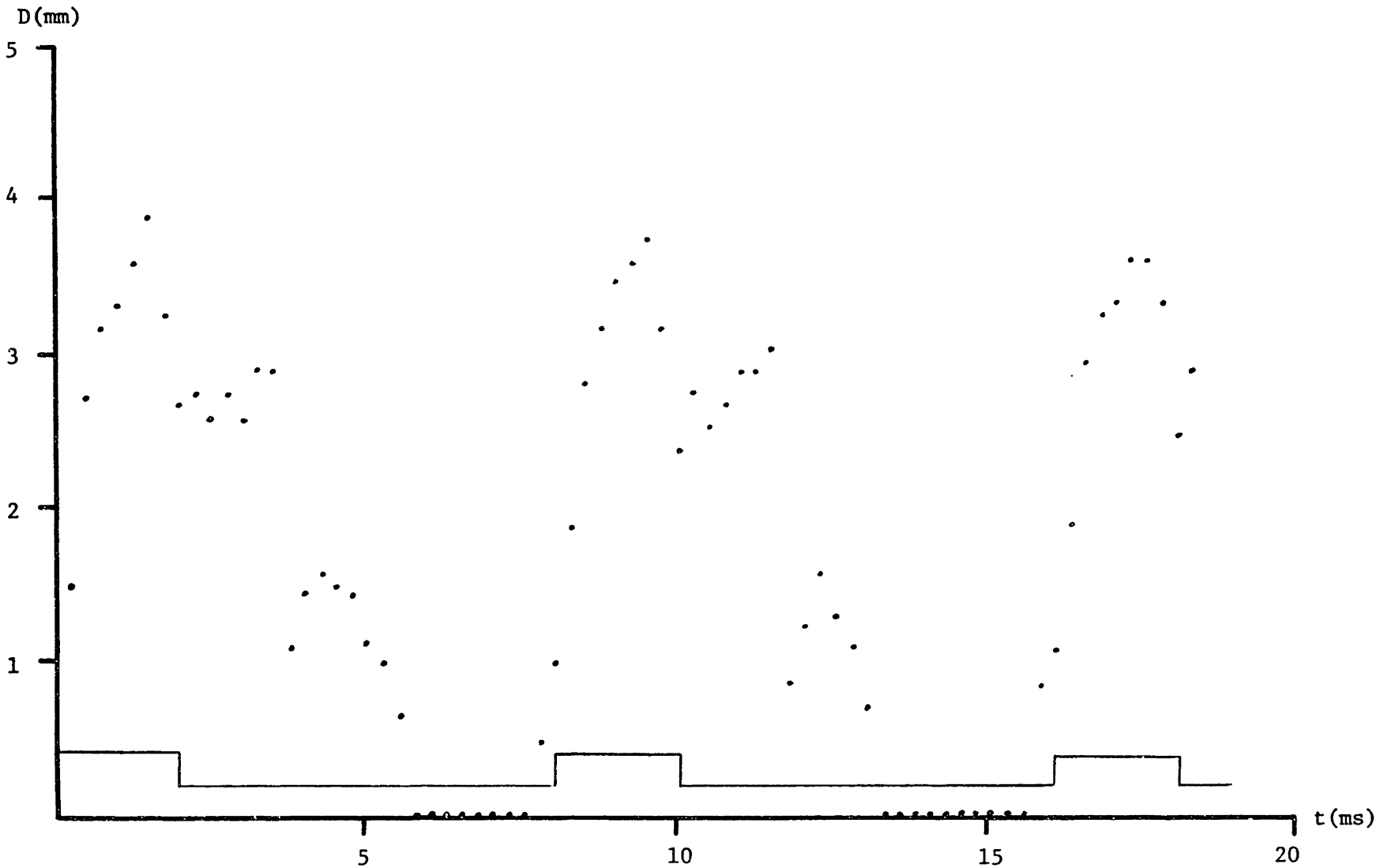

Figure 6.28 Arc diameter 1.5 mm below the electrode tip for HSF weld #8. I = 100/700 amps. T_b = 6 ms, T_p = 2 ms.

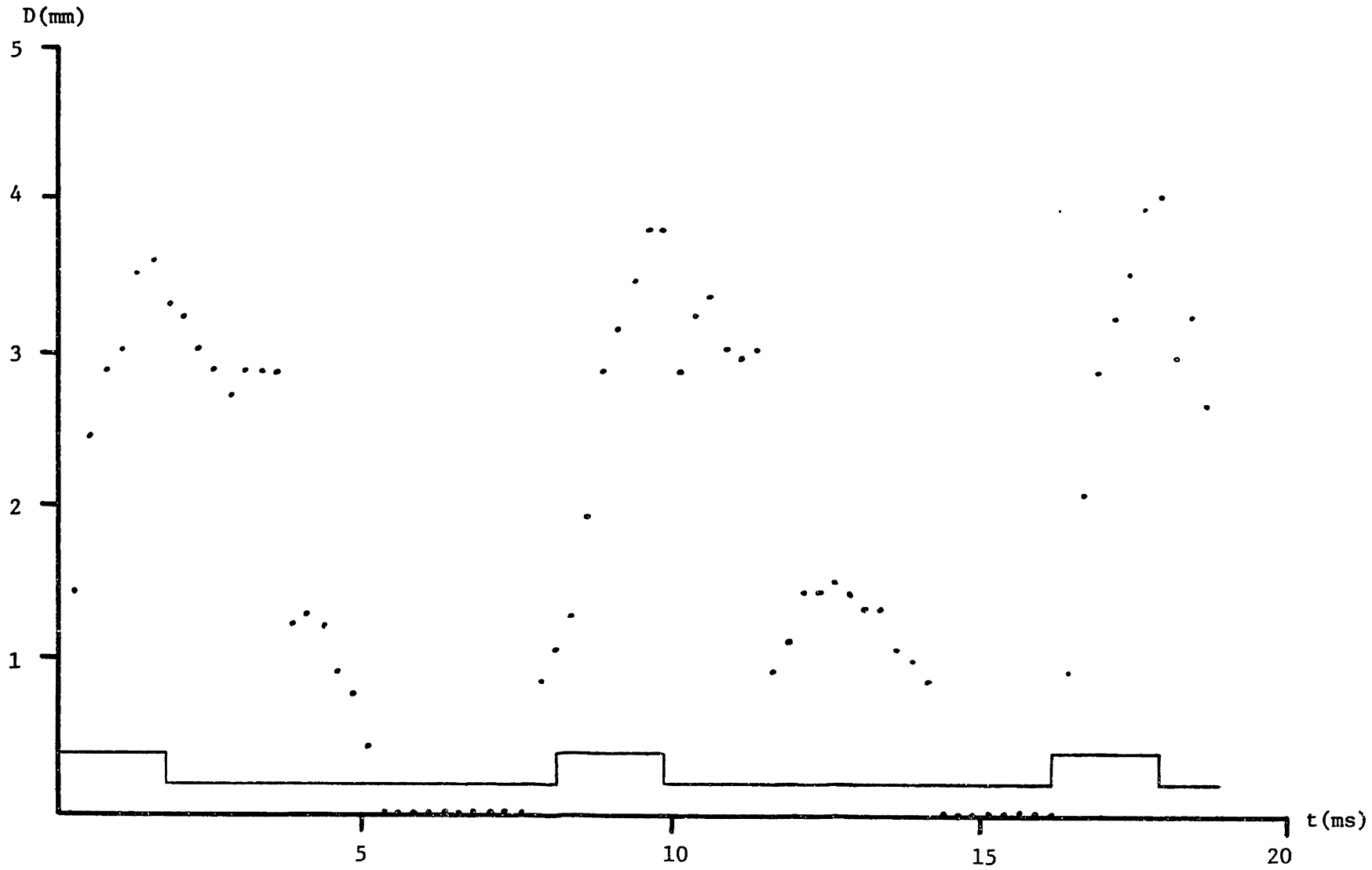

Figure 6.29 Arc diameter 1.5 mm below the electrode tip for HSF weld #9. I = 100/800 amps. T_b = 6.28 ms, T_p = 1.72 ms.

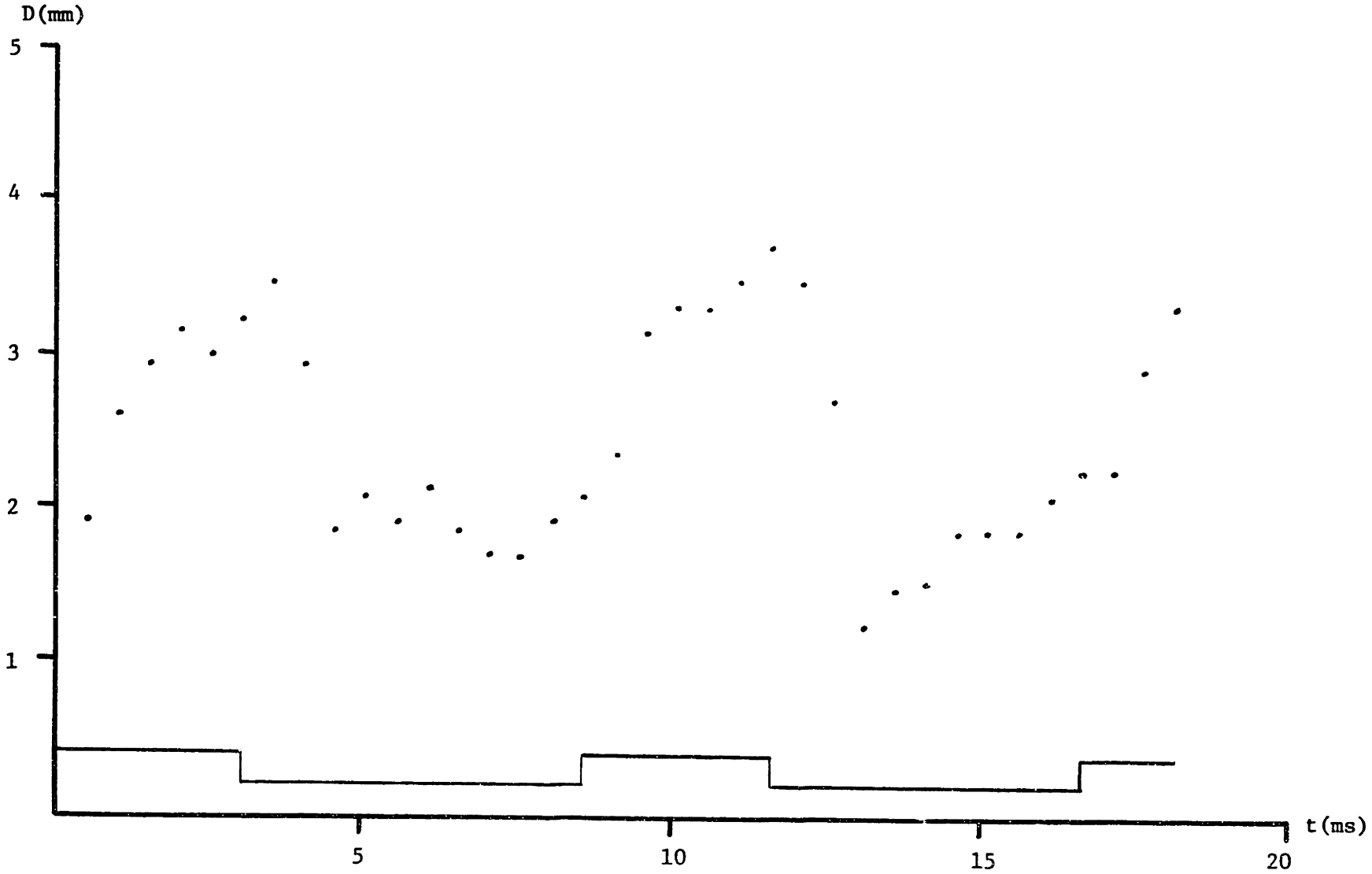

Figure 6.30 Arc diameter 1.5 mm below the electrode tip for HSF weld #10. I = 160/400 amps. T_b = 5 ms, T_p = 3 ms.

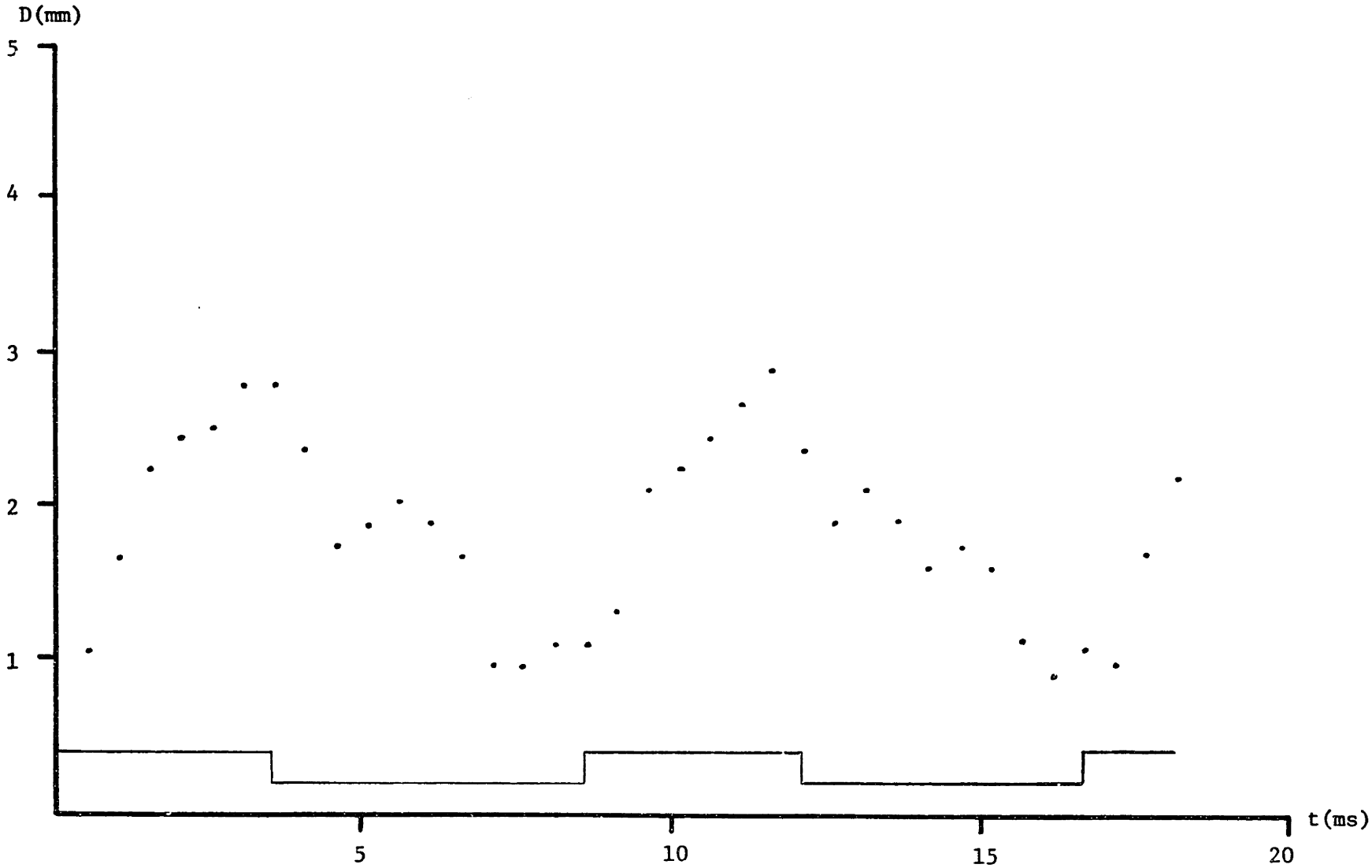

Figure 6.31 Arc diameter 1.5 mm below the electrode tip for HSF weld #11. I = 133/400 amps. T_b = 4.5 ms, T_p = 3.5 ms.

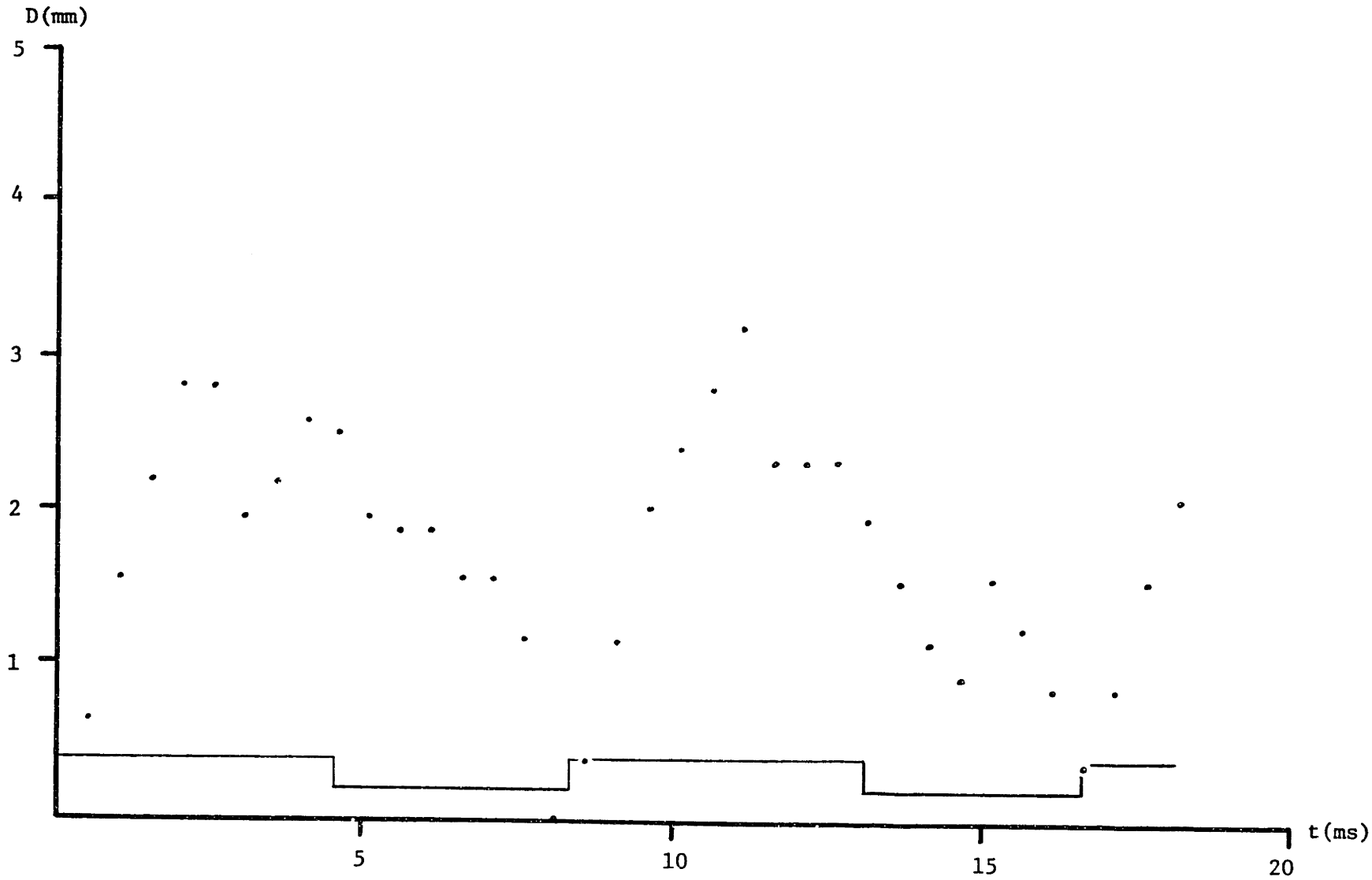

Figure 6.32 Arc diameter 1.5 mm below the electrode tip for HSF weld #12. I = 62/400 amps. T_b = 3.5 ms, T_p = 4.5 ms.

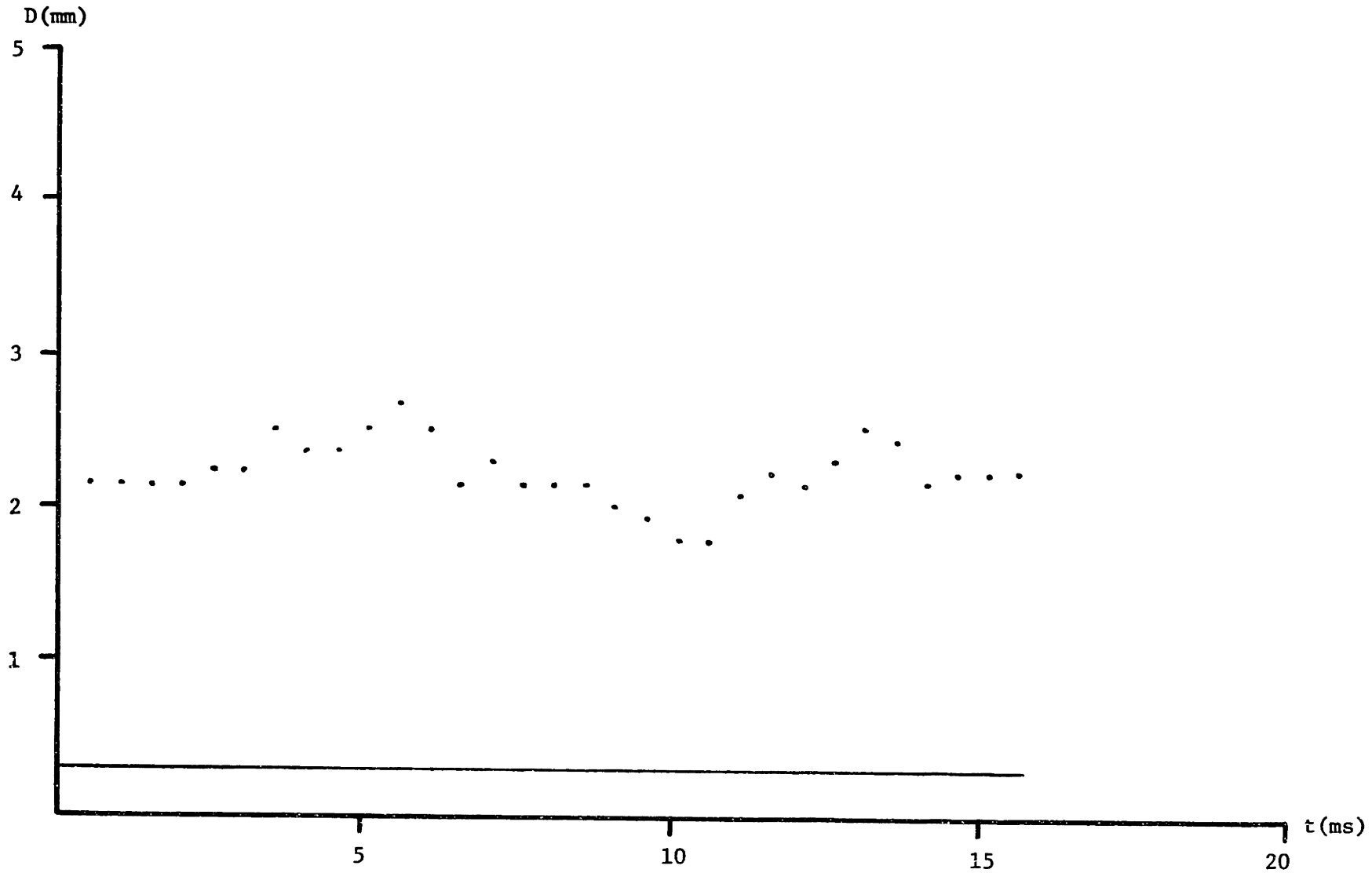

Figure 6.33 Arc diameter 1.5 mm below the electrode tip for HSF weld #13.
I = 250 amps constant current.

CHAPTER 7

APPLICATION

7.1 Control Strategy

The experimental results of the previous chapter clearly show that pulsing can be used to substantially increase penetration in GMAW. It is not clear that the increase is sufficient to fully penetrate tack welds; in fact, it probably is not, and pulsing will need to be used in conjunction with other techniques. Such other techniques are described in section 7.2. This section will discuss implementation issues for current pulsing alone.

Current pulsing could be used in a feed-forward adaptive control system, as described in section 2.4.2, and shown in figure 2.16. A vision system would detect groove geometry, including the presence and dimensions of tack welds, and an open loop control algorithm would adjust the parameters accordingly. Considerable progress has been made in vision system technology in recent years, and existing systems are capable of providing the information necessary for feed-forward adaptive control. Vision technology is discussed more fully in references (133-137). Figure 7.1 shows the structured lighting profiles of a bare V-groove and a prewelded V-groove. The cross-section of the prewelded V-groove is equivalent to that of a tack welded V-groove, and the tack weld dimensions can be determined from a series of cross-sectional images. The key to the system, then, is the control algorithm, which takes the tack weld geometry, the surrounding groove geometry, and the desired bead geometry, and formulates the pulse parameters, torch position, and wire feed speed.

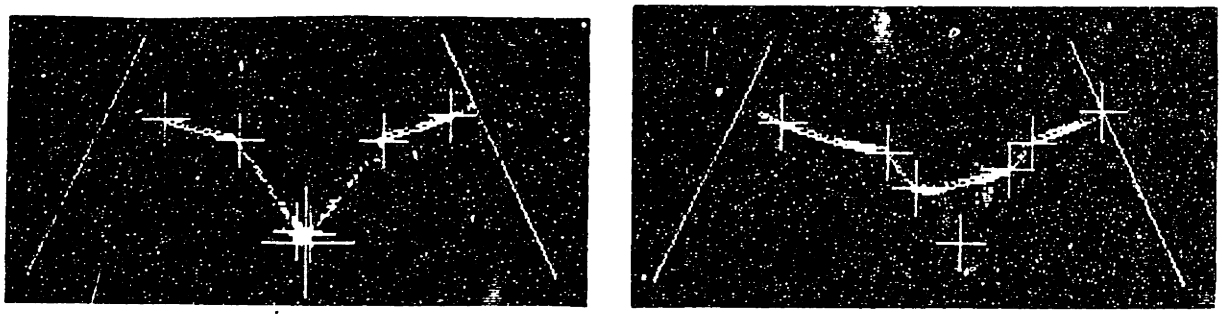

Figure 7.1 Structured lighting profiles of (a) bare V-groove (b) prewelded V-groove. (135)

This thesis has shown that several strategies can be effective in increasing penetration and has provided some quantitative data on them, but significantly more data is needed for control algorithm design. A wider range of parameters must be studied, and the strategies must be tested on actual tack welds of various sizes and shapes. The effort is necessarily both empirical and analytical. One issue that will require particular attention is the transition from bare groove parameters to the tack weld parameters and vice-versa. Should the transition be instantaneous or gradual? Since the change in groove geometry is instantaneous, an instantaneous change in weld parameters would seem appropriate. However, the transient dynamics of such a change must be studied. Furthermore, the tack weld end points will be the most important locations at which to eliminate defects. A comprehensive tack weld strategy will necessarily require the improvement of tack weld quality, but end point defects will remain a problem regardless of the quality of the tack welds themselves, and here the transient dynamics will be of particular importance.

Further research can therefore be divided into two areas: more

extensive investigation into the quantitative characterization of each control strategy, and the application of each control strategy to actual tack welds.

7.2 Alternatives to Pulsing

This section will discuss techniques other than current pulsing that can be used to increase penetration and or decouple penetration and heat input from metal deposition rate. These techniques could be used either in place of or in addition to current pulsing.

In conventional GMAW, there are two techniques that can partially decouple penetration from deposition rate. The first is torch height control. In a constant voltage weld, lowering the torch height will decrease the electrode stickout, thereby increasing the current and the penetration without increasing metal transfer. Experiments run with a Millermatic constant potential power supply showed that current increased approximately 6A for each millimeter decrease in torch height, as shown in figure 7.2. Lowering the torch height should be used in conjunction with current pulsing, since the two techniques are complementary rather than mutually exclusive. The graph also shows that current increases approximately 7A for each volt increase in arc voltage, again due to the decrease in electrode stickout. However, the effect of the higher current on penetration is mitigated by the longer arc length. Cross-sections of the welds showed that, for any given torch height, the penetration increased as voltage increased up to about 28V, then penetration decreased as the longer arc length took effect. Arc voltage is therefore of limited use in controlling penetration. In constant current welding, lowering the torch height does not increase the current, but it does decrease the arc

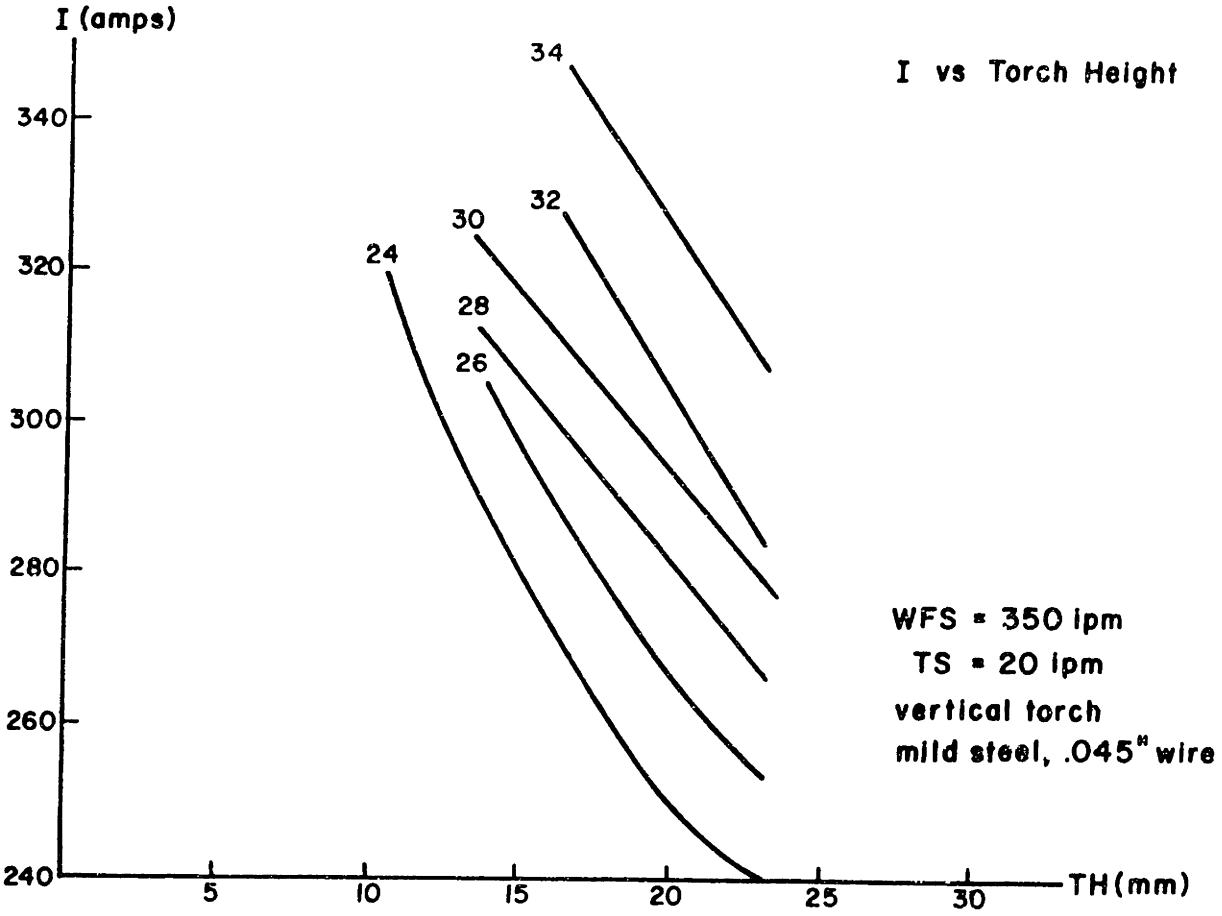

Figure 7.2 Current versus torch height in constant potential welding.

length, thereby increasing penetration. The second technique that can be used in conventional welding is to increase both the wire feed speed and the travel speed in equal proportions or with a larger increase in travel speed. The increase in wire feed speed gives a larger current and deeper penetration, while the increase in travel speed maintains a moderate linear metal deposition rate. The faster travel speed reduces the penetrating effect of the higher current, but only partially. Faster travel speeds give greater scouring action, and this prevents penetration from decreasing proportionately to the increase in travel speed. However,

this technique is limited by the undercutting which occurs at high currents with fast travel speeds.

A technique that could be used with only minor equipment modifications is to change the shielding gas to helium while going over tack welds. Helium's higher ionization potential results in a higher voltage than in an argon arc, resulting in a greater heat input and more base plate melting. Helium does not give spray transfer nor finger penetration, but the greater heat input compensates for this and produces a fuller penetration cross section. This is particularly suitable for remelting the tack to correct lack of fusion defects. The only equipment modification necessary to implement this technique is a solenoid valve which controls gas flow from either the normal cylinder or the helium cylinder. The valve operation must be timed so that the helium arrives at the beginning of the tack weld, and this would be simple to implement on welding apparatus that includes a vision system. Multiple shielding gas sources might become commonplace on flexible automation systems (for greater flexibility) irrespective of tack welds (138), so eventually this technique might be possible without any equipment modifications.

Complete decoupling of heat input and metal transfer is provided by GTAW with a filler wire. While going over a tack weld, the wire feed speed could be reduced as much as necessary or even stopped, and the current and wire feed speed could be adjusted to provide complete remelting of the tack. While this technique is ideal from the standpoint of allowing independent control of heat and mass, the metal transfer that does occur is globular. It is therefore limited to downhand welding, and even then the globular transfer is undesirable. Thus, although this technique provides the flexibility to remelt tack welds, it is severely

constrained by the globular metal transfer. Moderate equipment modifications would be involved.

With slightly more extensive equipment modifications, a TIG-MIG welding system could be installed which would provide the flexibility of the TIG with filler wire but without the shortcomings. Hitachi invented the system for welding copper, in which the high thermal conductivity requires a higher heat input to metal transfer ratio than is possible with standard GMAW. The system, described in more detail in reference (139), has two electrodes in close proximity: one consumable and one non-consumable. Welding is done with an AC rectangular wave. The reverse polarity section of the wave comes through the consumable electrode, while the straight polarity section comes through the non-consumable electrode. The duty cycle of the waveform can be varied to adjust the ratio of heat input to metal transfer. Such a system could be very effective in handling tack welds.

CHAPTER 8

SUMMARY AND CONCLUSIONS

8.1 The Effect of Tack Welds on Shipbuilding

U.S. shipbuilding has undergone a revolution in the past fifteen years. The development of modern shipbuilding techniques, most notably zone construction and outfitting, has significantly increased productivity and reduced cost. It has brought the industry to the point where automation can begin to play a substantial role. Welding is the major process to be automated, and small scale subassembly manufacture and panel assembly lanes are the most promising tasks in which to apply automated welding. The major technical barrier to widespread welding automation is adaptability. Sensing technology has improved substantially in recent years, particularly with the development of vision systems, but the utilization of the sensing information is still an area in need of progress. Our understanding of the welding process has progressed to the point where the welding parameters can be accurately established for a familiar set of welding conditions. Successful adaptation to gradual variations in the welding conditions (i.e., groove geometry) is also possible to a limited degree. However, adaptation to sudden variations in the welding conditions, such as is the case with a tack weld, has not been previously studied and is not yet possible. Consequently, tack welds pose a major obstacle to the implementation of automated welding.

A large naval or merchant ship has on the order of 50,000 to 100,000 feet of welded seams, with tack welds spaced every one to four feet. Additionally, there is considerable welding in the production of small independent assemblies such as foundations. SRI developed two conceptual

robotic welding stations, both with very favorable returns on investment, and both of which performed their welds on workpieces which had been tack welded together. In order to obtain the benefits of these or other automation concepts, the problem of tack welds must be solved.

In the current shipyard environment of manual and mechanized welding, tack welds create four problems. First, they are a source of defects. Second, welders tend to make the entire weld oversized in order to obtain to smooth contour over the tack weld. This pays a penalty in terms of weight, time, material, and distortion. Third, one-sided welding is not possible due to the back-side defects at the tack weld sites. Two-sided welding is more time consuming and results in higher total heat input and distortion. Fourth, extensive fixturing can be used to avoid tack welds, but this is a very expensive alternative. The study presented in reference (58) showed improved fixturing to be ten times as expensive as adding adaptability to an automated welding system. This study dealt with the utilization of a vision system in the manufacture of automobile assemblies. Although the specific numbers will be different in other industries, the same conclusion will apply: adaptability is less expensive than improved fixturing. With regard to tack welds, adaptability will require a vision system, a pulsed power supply, and possibly other items discussed in section 7.2. All of these are technically feasible, and their costs will continue to decline as the technology improves. Furthermore, many of them will become common features irrespective of tack welds, so tack weld adaptability will be made possible by equipment changes implemented for flexibility in other areas. The only barrier at that point will be lack of an effective control strategy.

8.2 Local Transient Analysis of Tack Welds

Although tack welds have long been suspected of being sources of defects, this work is the first known study of the significance and type of defects. Lack of fusion and lack of penetration were found to be prevalent in the tack welds, and simply welding over them with no change in welding parameters failed to correct these defects in the final welds. Backside discontinuities at the beginnings and ends of tack welds occurred in the majority of cases. These are serious defects, and they will continue to be a problem no matter how much effort is put into improving the quality of the tack welds themselves. Finally, there seemed to be a slightly higher incidence of porosity around the tack welds, possibly due to increased weld pool turbulence.

The tack weld thermocouple profiles correlated fairly well with the predicted profiles, except that the cooling rates were slower due to the finite thickness of the plates. Additionally, several of the profiles exhibited a small second peak believed to be due to transient heat flow characteristics. The measured peak temperatures were very close to the predicted peak temperatures based on the measured depth of the thermocouples below the fusion boundary.

The videotapes taken of the weld pool reveal that the pool widens while going over the tack weld, and the pool front slows down momentarily when it encounters the tack weld, then rushes forward at the end of the tack weld. These results are fully expected. The weld pool shape is quite irregular while transiting the tack weld. Considerably more research will be required before weld pool dimensions could be used as feedback variables for controlling welding parameters at tack weld locations.

The most important conclusion to be drawn from this study is that tack welds are a significant source of defects, and not all of the defects can be eliminated by improving the quality of the tack welds. Even if the tack welds did not contain any lack of fusion or lack of penetration defects, the final weld would still be degraded by the discontinuities at the beginnings and ends of the tack welds. The total approach to handling tack welds must therefore include both improvement of tack weld quality and a means of eliminating the end-point defects. Increased penetration was chosen for further study because it is the best way to reach backside defects, including the end-point discontinuities.

8.3 Pulsing as a Means of Increasing Penetration

The flexibility offered by the additional parameters in pulsed welding allows greater control over weld bead geometry. In conventional welding, all the mechanisms of penetration are tied to current, which in turn determines heat input and deposition rate. It is therefore difficult to increase penetration without increasing heat input and metal transfer. Arc length and electrode extension are the two parameters that allow limited decoupling of penetration from heat input and metal transfer, but they alone are insufficient. Pulsing allows more decoupling and therefore greater control opportunities.

Conduction is the primary mechanism of penetration, but it does not offer independent control opportunities since it is strongly dependent on heat input. Arc pressure, formation of a compound vortex, convection, and droplet momentum are the additional mechanisms of penetration, and all can be exploited independently of heat input by pulsed GMAW. The five strategies developed to do this were low frequency pulsing, high frequency pulsing, high duty cycle pulsing, high peak pulsing, and mid peak drop

transfer. Low frequency pulsing was successful in using arc pressure to excite resonant frequencies in weld pool oscillations, thereby increasing the effective surface depression and penetration. This was most prominent at 20 Hz, where penetration was 50% deeper than in a constant current weld of equivalent mean current (figure 6.6). This frequency is somewhat lower than that predicted by analytical models (102) and found by other investigators (104) for axisymmetric weld pools, but this was shown to be due to the elliptical shape and lower resonant mode (sloshing) of a moving weld pool.

Although other investigators have found that high frequency pulsing increases GTAW penetration by increasing the arc pressure due to arc constriction, the effect in GMAW was found in this study to be negligible. The probable reasons for this are that unfavorable metal transfer characteristics of high frequencies mitigate against increased penetration and that the presence of metal vapors speeds up the establishment of the arc channel, thereby precluding arc constriction.

High duty cycle pulsing increased penetration by approximately .5 mm over constant current welds with equivalent mean currents. The peak current used in these welds was 260A, just high enough to form a compound vortex, so the increased penetration could have come from any of the mechanisms of penetration. The most important conclusion to be made from the high duty cycle pulsing experiments is that the deeper penetration of a higher current can be sustained through short base periods. Conduction decreases due to the lower mean current, but the other mechanisms have time constants of formation and decay that allow them to form during the long peak period and to maintain at least part of their effect on penetration despite the short base periods. More extensive experiments

with a wider range of base and peak periods would help to further define the time constants. Utilizing a variety of peak currents would isolate the effect of the compound vortex and give additional insight into its existence/significance in GMAW.

High peak pulsing was extremely effective at increasing penetration for peak currents above 500 A. When compared to constant current welds of equivalent mean current, the pulsed welds had about .25 mm deeper penetration until the peak current was set above 500 A. The extra penetration then quickly increased to over 1 mm. 500 A is the approximate current at which arc pressure exceeds the compound vortex as the dominant mechanism of surface depression. Arc pressure is therefore believed to be the mechanism responsible for this increase. Penetration does not increase from 650 A to 750 A, due to the inability of the arc to deliver heat to the bottom of a very deep cavity. The peak period in these experiments was 3 ms, but a different value could result in a different upper bound peak current. For peak currents of 700 A and greater, significant weld defects occur due to excessive weld pool turbulence. This would appear to be a limiting factor in the practical application of very high peak pulsing.

The mid-peak drop transfer experiments showed that pulse parameters could be controlled in a way that increases penetration by increasing drop velocity. At a given peak current, drop velocity increases with peak period, and the slope of the increase is steeper at higher currents. Similarly, penetration increases with peak period at a given peak current. However, there is not the unique correlation between drop velocity and penetration that Essers and Walter (118) found. While droplet momentum therefore plays a role in penetration, it is not the

sole determinant.

It is clear that current pulsing gives extensive flexibility to the welding process, and this flexibility can be used to increase penetration in a number of ways. All four mechanisms of penetration would appear to play some role in determining weld bead geometry, and the relative significance of each mechanism changes as the welding parameters are varied. Arc pressure becomes dominant during high peak pulsing. Weld pool oscillations from arc pressure become dominant at low frequency pulsing. The compound vortex might be dominant for high duty cycle pulsing at peak currents just above the vortex formation threshold. Droplet momentum is always a factor, and it might have been dominant over the parameter ranges examined by Essers and Walter. Based on the experiments in this thesis, pulsing control strategies could be implemented to increase penetration and more effectively deal with tack welds. High peak pulsing would be the most direct method to implement, since it is very effective and the choice of pulse parameters is not dependent on the weld pool dimensions. Further research over a wider range of parameters in all the strategies will help with the design of specific control algorithms and with gaining a better understanding of the nature of penetration in GMAW.

APPENDIX A

REVIEW OF THE WELDING PROCESS

A.1 Background

Since 1885, when Nikolas de Bernardos and Stanislav Olszewki were awarded the first patent for a welding process (140), arc welding technology has advanced by a series of leaps and bounds. The first major advance came in 1889, when N.G. Slavianoff of Russia and Charles Coffin of the U.S. were independently granted patents for welding processes utilizing consumable metal electrodes. The original process had employed carbon electrodes and had the disadvantage of making the welded joint brittle due to carbon inclusion. The second major advance came in 1910, when Oscar Kjellborg of Sweden developed covered electrodes, thereby protecting the joint from atmospheric contamination.

The first major industrial impetus came several years later when the Rock Island Line Railroad bought 33 arc welding units for use in the repair and maintenance of locomotive engines. The $40,000 initial investment plus $34,000 per year operating costs saved the company $200,000 per year in reduced down time. A later increase in arc welding capacity obviated the need to purchase 23 new locomotives, thereby saving $1 million. The vast increase in demand for fabricated metal products accompanying WWI provided the next major impetus for welding, as well as the next major demonstration of its utility. Beginning in 1917, the U.S. Navy used arc welding to repair over 100 captive ships scuttled by the Germans. The repairs were extremely successful, and the durability of the repaired components removed some of the controversy from arc welding. Arc welding also came to be used extensively in shipbuilding, and in 1920,

England built the first all welded ship, the Fulgar.

The next major technical leap came in 1927 with the development of an extrusion process that substantially lowered the cost of covered electrodes. Granular flux was then developed in 1932, enabling the introduction of submerged arc welding in 1935. Arc welding did not come into full prominence, however, until the industrial demands of WWII placed it there. This was perhaps most vividly demonstrated in the shipbuilding industry. Between 1939 and 1945, the US built over 5700 merchant ships and nearly 1400 naval combatants (7). Several factors entered into the success of this aggressive shipbuilding program, including design simplification and standardization, prefabrication, a sense of urgency, and technological innovation. By far the most significant technological innovation was arc welding. Whereas it had been used on a limited basis in WWI, it was pressed into full service in WWII. It was faster than riveting, it enabled the use of mechanized welding in panel assembly lines, and welded joints were lighter than riveted joints. The Exchequer, the first all-welded dry cargo ship built in the U.S., was 600 tons lighter than its riveted predecessors. Unfortunately, design mistakes and a general lack of quality control led to major structural failures in 25 merchant ships, eight of which were lost at sea. Subsequent design changes and quality control procedures brought the problem under control in 1944.

The experiences of WWII firmly established welding as the metal joining process of choice for most ferrous applications. Welding technology continued to develop after the war, both through a refinement of existing procedures based on a better understanding of the physics, chemistry, and metallurgy involved, and through the development of new

welding processes. The metal inert gas (MIG) process became vital to the development of semi-automated welding. Tungsten inert gas (TIG) welding carved a niche in thin plate and high quality applications. More recent developments were flux cored arc welding (FCAW) and electron beam welding (EBW) in the 1950's and laser welding in the 1960's. By 1982 welding had become a $2 billion industry, with $9 billion in other industry salaries related to welding. Over 25% of U.S. industries use welding extensively (3).

A.2 GMA Welding

When MIG welding was first developed, many thought that it would become the predominant welding process for most arc welding applications. It offered the advantages of high deposition rate, no slag, good toughness, and a continuous wire feed which makes it amenable to automation. However, MIG welding suffers from the disadvantages of poor fusion characteristics and is of limited use in out of position welding. Additionally, it requires an expensive DC power source and more extensive operator training than manual shielded metal arc welding (141). As a result, MIG has not replaced manual metal arc to the extent originally predicted. In heavy fabrication such as pressure vessels, MIG accounts for only 5 to 10% of the welding, with SMA still around 80% (83).

A diagram of the MIG process is shown in figure A.1. A continuous wire is fed through the torch, consumed by the arc, and deposited on the workpiece. The weld pool and the molten drops transiting the arc are protected from atmospheric contamination by shielding gas flowing through the torch. The term "MIG" originally was derived from the use of inert gases (Ar or He) for shielding. Small amounts of oxygen or larger amounts of carbon dioxide are now added to the shielding gas in order to improve

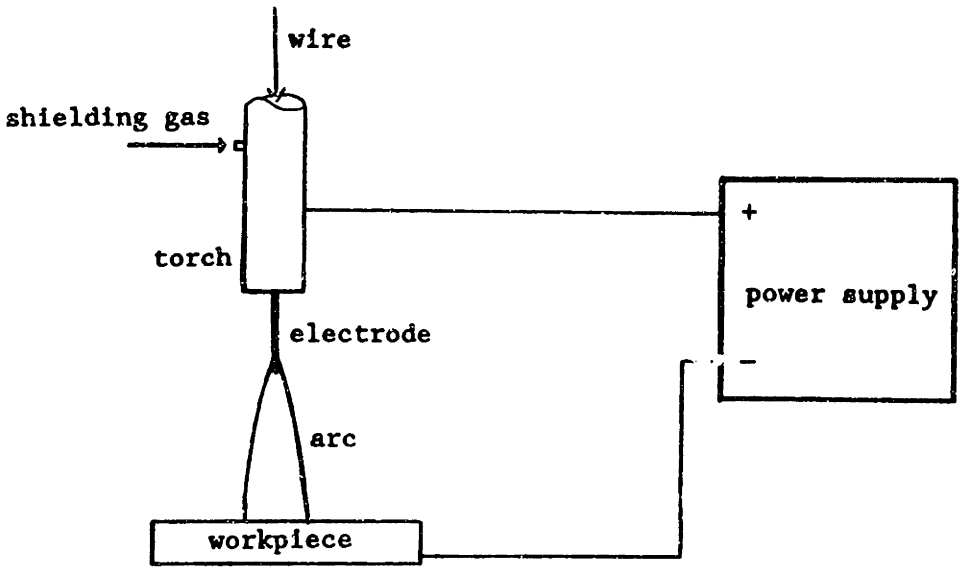

Figure A.1 The MIG welding process, shown with reverse polarity.

arc characteristics and/or reduce cost, and the term "MAG" (Metal Active Gas) is sometimes used to describe this process. "GMAW" (Gas Metal Arc Welding) includes both MIG and MAG.

A.3 Arc Characteristics

The gas metal arc has a relatively high current, typically 100 to 400 A, with electrons flowing from the negative cathode to the positive anode. The arc contains three regions: the anode region, the arc column, and the cathode region. The voltage profile of the arc across these three regions is shown in figure A.2. The anode and cathode regions are characterized by steep voltage drops across extremely short distances. The anode receives electron flow, and yet because of its high temperature (above the metal's boiling point), it thermionically emits electrons (69). These electrons have insufficient energy to escape the anode's electric field, so they form an electron cloud around the anode. It is this negative

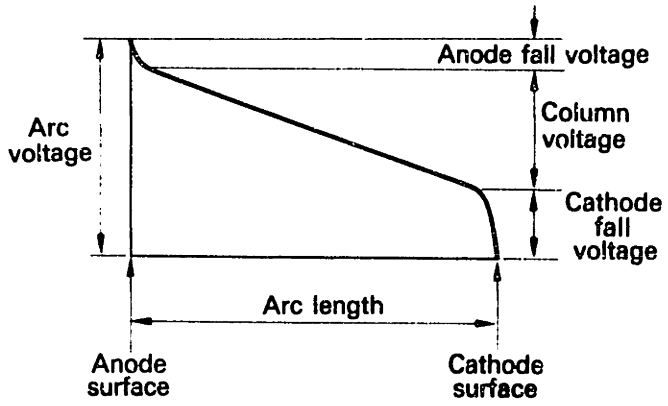

Figure A.2 Arc voltage profile. (122)

space charge which causes the anode voltage drop of approximately 2V over a distance of roughly 10^{-4} m. This traditional anode theory, however, has recently come under doubt. Sanders and Pfender (142) experimentally found negative anode falls (for water-cooled copper anodes) ranging from -2.1 to -1.4 V for currents ranging from 100 to 250A, which is in general agreement with the theoretical work of Dinulescu and Pfender (143). The anode region might therefore be more complicated than originally thought, and the anode region in an actual weld still requires much further study.

The cathode is surrounded by a positive space charge, creating a cathode voltage drop of 5 to 8 V over a distance on the order of 10^{-6} m. The cathode's primary function is to emit electrons, thereby allowing the current to flow. Electron emission can occur either by thermionic or field emission. The cathode temperature in GMAW is too low to support thermionic emission, so it is generally believed that the cathode functions by field emission. The electron current density for field emission is given by (122):

$$J_e = \frac{6 \times 10^{-6} \, (\mu/\phi)^{1/2}}{\mu + \phi} E^2 \exp\left(- \frac{6.8 \times 10^9 \, \phi^{3/2}}{E}\right) \quad (A/m^2) \quad (A.1)$$

μ = cathode material fermi energy level
ϕ = cathode material work function
E = electric field strength

It is clear that an extremely large electric field is required to produce significant field emission. The secondary effects of the electrons transiting the space charge have not been included in equation A.1. When they are, it has been shown that field emission is possible under the field conditions associated with a current density of 10^7 A/cm^2. Although this is much higher than the average GMAW current density, cathode electron emission does not occur uniformly over the entire region of arc impingement. Rather, it occurs in very contracted "spots". During field emission, these cathode spots are mobile and appear to be dependent on surface contamination, such as an oxide layer. Surface contamination lowers the work function of the surface and facilitates emission according to equation A.1. It is believed that the cathode spot removes the surface oxide, then randomly moves to another area. Arcs tend to become unstable when there is insufficient surface contamination, so a small percentage (1-5%) of oxygen is generally added to the argon shielding gas for steel.

The arc column has a relatively shallow voltage drop. The "plasma" in the arc column is an electrically neutral, ionized, conductive gas consisting of electrons, positive ions, and neutral gas atoms. It is formed by the heat of the arc and the stream of electrons ionizing the shielding gas. It also contains metal vapor from the melting electrode and the molten weld pool. The current consists of electrons drifting toward the anode and positive ions drifting toward the cathode. For the same kinetic energy, the electrons have a much higher velocity than the positive ions, due to their much smaller mass. Therefore, the electrons carry over 99% of the current. This imbalance is exaggerated by the fact

that there is not complete thermal equilibrium. Despite the continual energy exchange taking place during frequent collisions, the electrons are accelerated more by the electric field in between collisions, giving them a higher average kinetic energy and a higher temperature.

The current density through the arc was shown in section 3.3.1 to follow the simple ohmic relationship:

$$J = \sigma E \qquad (A.2)$$

where σ is the plasma electrical conductivity. The constituency of the plasma has a strong impact on the arc characteristics. The electrical conductivity depends on the degree of ionization, which in turn depends on the gas properties and temperature. Electrical conductivities of argon, helium, and air as functions of temperature are shown in figure 3.22. Below 6000 K, argon is virtually non-ionized, and its conductivity is very small. Above 20,000 K, argon is 50% ionized, and conductivity is very large (144).

Electric field strength is given by:

$$E = \frac{V}{L} \qquad (A.3)$$

where V is the voltage drop across length L. The column voltage increases as the gas ionization potential increases. The ionization potentials of argon and helium are 14.6 V and 24.1 V, respectively. Hence, helium shielded arcs have higher voltages and electric fields than argon shielded arcs. Electric field strengths are approximately 8 V/cm for argon and 15 V/cm for helium.

The radial distribution of the current density is strongly influenced by the thermal conductivity of the gas. The thermal conductivities of argon, helium, and air as functions of temperature are shown in figure A.3. The arc radius is the radius at which the gas electrical conductivity becomes negligible. That occurs in argon at approximately 11,000 K. However, since helium has a much higher thermal conductivity, its temperature distribution is broader than that of argon, and both gases yield comparable arc radii. The temperature and current distributions for 100 A argon and helium gas tungstsen arcs are shown in figure A.4.

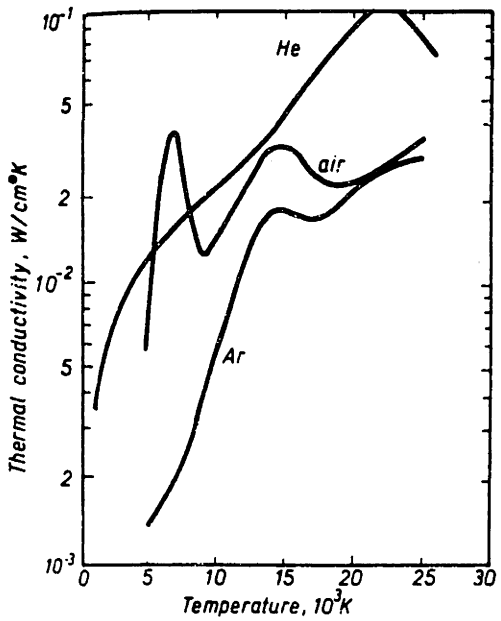

Figure A.3 Thermal conductivities of Ar, He, and air. (96)

Of critical concern in welding is the relationship between arc voltage and arc current. Since the anode and the cathode falls remain relatively constant, the arc voltage is a function of the column voltage. At very low currents, the column voltage decreases with increasing current, due to the increased ionization of the gas at higher currents. The additional

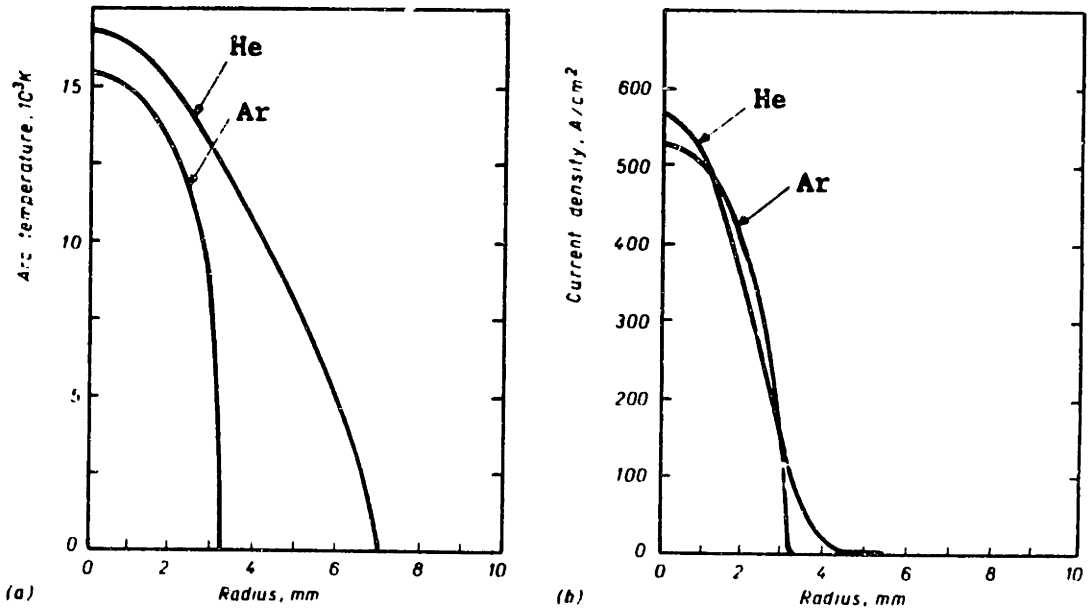

Figure A.4 (a) Temperature and (b) current density distributions for 100 A Ar and He gas tungsten arcs. (96)

ionization increases the electrical conductivity of the plasma and allows the arc to be maintained at a lower voltage. At higher currents, the conductivity no longer increases, and a higher voltage increases the particle drift velocity, thereby increasing the current. A distinction should be made here between true arc voltage and the voltage commonly referred to in the literature. True arc voltage is the voltage across the arc and is the sum of the anode drop, the column voltage, and the cathode drop. The voltage commonly referred to in the literature is the voltage measured at the power supply output or at some other location in the welding circuit, and it includes the voltage drop across the electrode and cables. True arc voltage for a 1.2 mm steel wire in Ar/2%O_2 shielding gas is at a minimum when the current is approximately 200 A, as shown in figure A.5. When cable electrode voltage is included, the voltage is at a minimum between 5 and 10 A, and steadily rises at higher currents. At any current, arc voltage increases with arc length.

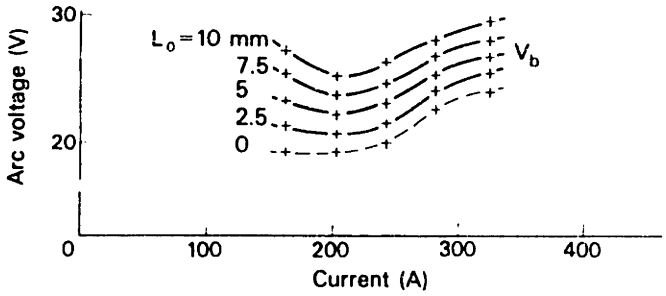

Figure A.5 Arc voltage as a function of current. (122)

A.4 Process Characteristics

The electrical characteristics of the welding process are determined by the interaction of the power supply characteristics and the arc characteristics. Power supplies are generally classified as either constant current or constant potential, as shown in figure A.6. The current output of a constant current power supply is relatively independent of voltage, and the voltage output of a constant potential power supply is relatively independent of current. The term "drooping" is applied to power supplies with moderate degrees of slope in the

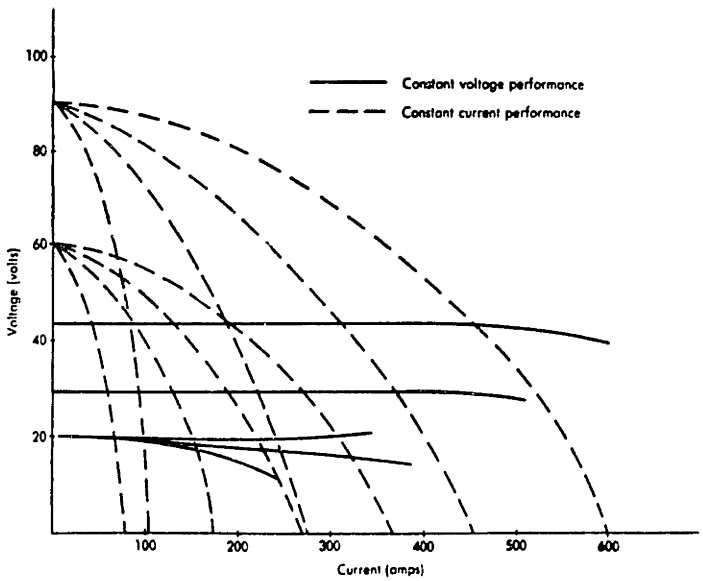

Figure A.6 Power supply characteristics.

voltage-current curve. The voltage of a drooping power supply decreases with increasing current, as would the voltage across a variable load in series with a voltage source and a resistor.

For the GTA process, this interaction is relatively straightforward, since arc length can be directly controlled by the operator. The current and voltage are given by the intersection of the power supply curve with the arc curve for that pre-determined arc length. GMAW is complicated by the dynamic nature of arc length in a consumable electrode process. Arc length is determined by the contact tip to workpiece distance and the electrode extension, the latter of which is determined by equilibrium between wire feed speed and burnoff rate. Constant voltage power supplies simplify this to a large extent by making the arc length self regulating. Arc length can then be pre-determined by the power supply voltage setting, and the current will adjust itself accordingly to match the burnoff rate to the wire feed speed. If wire feed speed momentarily exceeds the burnoff rate, the arc length shortens, causing a decreased voltage and an increased current. This increases the burnoff rate and brings the arc length back to the desired value. A drooping power supply gives similar self-regulation, but is somewhat slower in its response due to the smaller change in current with a given change in voltage. Constant current power supplies do not self-regulate in this manner, and wire feed speed and current must be carefully selected. Some degree of latitude is provided by electrode extension, since this will automatically adjust itself to balance wire feed speed and burnoff. A lower current will result in a longer stickout, thereby increasing the ohmic heating of the electrode and maintaining burnoff at equilibrium with feed rate, as will be discussed further in the next section.

A.5 Heat Transfer

The arc delivers heat to the anode, the cathode, and to the surrounding atmosphere. The total heat produced by the arc is the arc power:

$$Q_{total} = V_t I \qquad (A.4)$$

where V_t is the true arc voltage. The percentage of the total heat that is delivered to the workpiece is the arc efficiency, and it varies from approximately 40% in DC TIG welding of mild steel to 65-85% in DC MIG welding of mild steel to as high as 99% in SAW (128). The fundamental heat transfer mechanisms that deliver heat to both the electrode and the workpiece are the electric current, conduction/convection, and radiation. In GMAW, molten metal transfer is an additional mechanism that delivers heat from the electrode to the workpiece. Various estimates have been made regarding the percentage that each mechanism contributes to the total heat transfer, but it is generally agreed that the electric current is the most significant mechanism, especially for heat transfer to the anode.

Radiation is a function of arc temperature and configuration, and although radiation losses to the atmosphere are significant for arc temperatures exceeding 10,000 K, the radiation heating of the anode and cathode is very small. Conduction and convection are quite difficult to distinguish, and their contribution depends on the plasma temperature, flow pattern and velocity. Sanders and Pfender (142) distinguish the anode jet dominated (AJD) mode from the cathode jet dominated (CJD) mode in straight polarity TIG welding, in which the workpiece is a water-cooled copper anode. The CJD mode is created by a bell shaped arc, and the

dominant plasma jet flows from the cathode to the anode. In this case, conduction/convection accounts for 44% of the heat delivered to the workpiece. Radiation accounts for 5%, and electric current for 51%. The AJD mode occurs when the arc constricts at the anode, creating a plasma jet from the anode to the cathode. In this case, conduction/convection accounts for only 12% of the anode heating, with radiation remaining at 5% and electric current increasing to 83%. Unfortunately, a water cooled copper anode is not truly representative of an actual weld, since the copper has a much lower temperature and slightly higher work function than an actual weld pool.

Electric current heating is the result of a combination of electron kinetic, potential and thermal energies. The heat delivered to the anode by one electron flowing into it is:

$$q_a = eV_a + \phi + \frac{3}{2}kT_e \qquad (A.5)$$

V_a = anode fall voltage
ϕ = work function (eV)
k = Boltzman constant
T_e = electron temperature in the hot plasma

The first term is the kinetic energy the electron gains while transitting the anode fall voltage and then releases to the anode in the form of heat. The second term is the metal's work function. It is the energy required to remove an electron from the metal lattice structure, or, conversely, the energy released to the metal when an electron re-enters its lattice structure. Since electrons are entering the anode, the work function energy is released to the metal. The electron enters the anode carrying heat as well as current, and the third term is the thermal energy

transferred to the anode when the electrons comes into thermal equilibrium with it. For a current I, the flux of electrons is I/e, so the heat delivered to the anode by current I is:

$$q_a = I\ (V_a + \phi + \frac{kT_e}{e}) \qquad (A.6)$$

where ϕ is now in volts rather than electron volts. Typical values for the 3 terms are:

$$V_a \approx 2\ V$$

$$\phi \approx 4.2\ V$$

$$\frac{3}{2}\ k\ \frac{T_e}{e} < 1\ V$$

Heat transfer to the cathode is more complex and is not will understood. The metal lattice must provide the work function energy to each electron leaving the cathode, and this cools the cathode. Each electron also takes its thermal energy with it, so this term represents a heat loss. The only heat addition comes from the cathode drop term. We can therefore write the cathode heat flow equation as:

$$q_c = I(V_c - \phi - \frac{3}{2}\ \frac{kT}{e}\ ) \qquad (A.7)$$

where V_c is the cathode voltage drop and T is the cathode temperature. This equation is only approximate, since it is based on macroscopic analysis of microscopic phenomenon. Cathode electron emission occurs in very contracted spots, and the local conditions at those spots can differ significantly from the overall cathode conditions. Nevertheless, comparison of equations 3.6 and 3.7 properly reveals that the work function and thermal terms are removing energy form the cathode and

delivering energy to the anode. Consequently, significantly more heat evolves at the anode. Masubuchi (145) reports that in a 1/4 inch 200 A arc between a tungsten cathode and a copper anode, 80% of the heat goes to the anode, with only 5% to the cathode and the other 15% lost to the atmosphere. Since a cooled copper anode absorbs heat more readily than a molten steel weld pool, the heat transfer in an actual weld is less one-sided. Eagar (146) estimates that two-thirds of the heat in an actual weld is evolved at the anode. GTAW uses the workpiece as the anode, both to increase the workpiece melting rate and to prolong the usable life of the tungsten electrode by keeping it cooler.

In GMAW, however, deposition rate in increased by making the anode the electrode. This arrangement (reverse polarity) has the added benefit of spray transfer, which is not possible in straight polarity. The disadvantage is an increased incidence of lack of fusion defects due to the inherently lower dilution factor of GMAW. Dilution factor is defined as the ratio of the cross-sectional area of the melted base plate to the total cross-sectional area of the weld bead. It is 100% for GTAW with no filler wire, and it varies from 15 to 20% in GMAW.

Metal transfer must be accounted for when analyzing GMAW heat transfer. Essers and Walter (118) report the following breakdown for heat delivered to the cathode workpiece in GMAW using a 1.2 mm mild steel wire in Ar/7%CO_2:

34% Radiation, convection, conduction

41% Electric current

25% Metal drops

75% of the heat came from the arc, with 25% from the metal transfer.

A.6 Melting Rate

One of the keys to a stable GMAW process is that the wire feed rate must equal the burnoff rate. The burnoff rate will be examined in detail in this section. The discussion will apply to reverse polarity (electrode positive).

The heat that melts the wire comes for two sources: (1) ohmic heating that results from the current flowing through the section of wire below the contact tube, and (2) arc heat from the electric, radiation, and conduction/convection phenomena described in the previous section. The total heat to the wire can thus be described as:

$$Q_t = Q_r + Q_a \tag{A.8}$$

Q_t = total heat to the wire (anode) (J)
Q_r = resistance (ohmic) heating (J)
Q_a = arc heat (J)

The resistance heating follows the traditional relationship:

$$Q_r = I^2R = \frac{LI^2}{A\sigma_w} \tag{A.9}$$

I = current (A)
R = total resistance of wire extension (Ω)
L = length of wire extension (m)
A = wire cross-sectional area (m^2)
σ_w = wire electrical conductivity ($m^{-1}\ \Omega^{-1}$)

This is complicated by the fact that σ_w (and therefore its inverse,

resistivity) is a function of temperature, as shown in figure A.7.

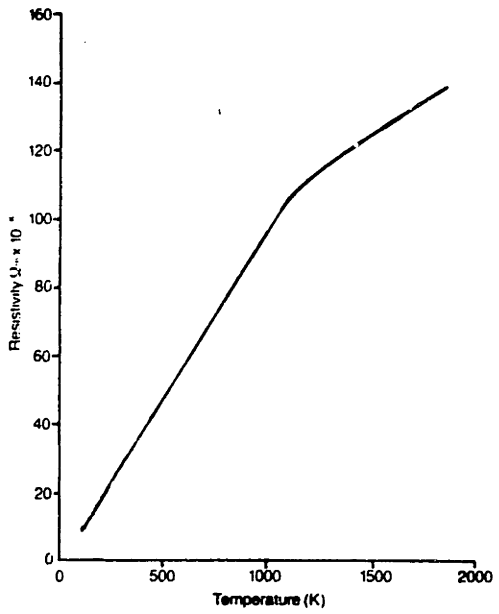

Figure A.7 Mild steel electrical resistivity as a function of temperature. (148)

In order to correctly calculate the total resistance R, $\sigma_w(T)$ must be determined by solving the partial differential equation describing the energy balance in the wire:

$$\frac{\partial}{\partial z}\left[\lambda(T)\,\frac{\partial T}{\partial z}\right] + C_p(T)\rho v\,\frac{\partial T}{\partial z} + \frac{I^2}{A^2\sigma_w(T)} = 0 \qquad \text{(A.10)}$$

T = wire temperature

z = coordinate along wire axis

C_p = specific heat

ρ = density

λ = thermal conductivity

v = wire feed speed

This equation (from reference 147) assumes no radial dependence of

temperature. The first term represents heat entering a control volume due to conduction. The second term represents heat leaving the control volume as it is carried away by the moving wire. The third term represents the heat generated within the control volume by resistance heating. In reference (147) it is shown that conduction can be neglected without significantly affecting the total resistance calculation. Total resistance is then given by:

$$R = \frac{\alpha L}{A} - \frac{\beta \rho A v}{I^2} \qquad (A.11)$$

where, for mild steel, $\alpha = 1.35 \times 10^{-6}$ Ωm

$\beta = .54 \times 10^{6}$ J/kg

For normal welding currents, the first term is much larger than the second term, which agrees with experimental results that R is nearly independent of I. The resistance heating, given by equation 3.9, is therefore proportional to current squared.

Generally the resistance heating is insufficient to melt the wire, so it is the arc heating that brings the wire to the melting point, melts it, and superheats it to some degree. If we let T_R designate the temperature to which resistance heating raises the wire and T_m the melting temperature, then the heat the arc must provide to just melt the wire is:

$$Q_m = \rho v A \, [H(T_m) - H(T_R) + \Delta H_m] \qquad (A.12)$$

where $H(T) = \int_{T_o}^{T} c_p(T')dT'$

T_o = ambient temperature

ΔH_m = latent heat of fusion

Since the arc actually delivers more heat than that,

$$Q_a > Q_m$$

and superheating results. The degree of superheating seems to be an area of some disagreement. References (148) and (118) report drop temperatures well above T_m, perhaps even above the boiling point, while reference (149) reports that convection within the detaching drop and conduction to the wire keep the average temperature of the drop just slightly above T_m. However, most experimental evidence suggests strong superheating, as was discussed in section 3.6.2.

Regardless of the amount of superheating, the dominant mechanism of electrode arc heating is electrical, and its magnitude is proportional to current, as shown by equation 3.4. Hence, the total electrode heating is given by:

$$Q_t = Q_{res} + Q_{arc}$$

$$= c_1 \frac{L}{A} I^2 + c_2 I \qquad \text{(A.13)}$$

After transforming this from heating rate to melting rate, reference (147) gives the analytical values for the constants for mild steel in a reverse polarity arc as follows:

$$\dot{m} = (5.1 \times 10^{-13}) \frac{I^2 L}{A} + (2.2 \times 10^{-6}) I \qquad \text{(A.14)}$$

with $\dot{m}$ being the melting rate in kg/s and all other terms in mks units. Lesnewich (69) examined the melting rate empirically, with a plot of

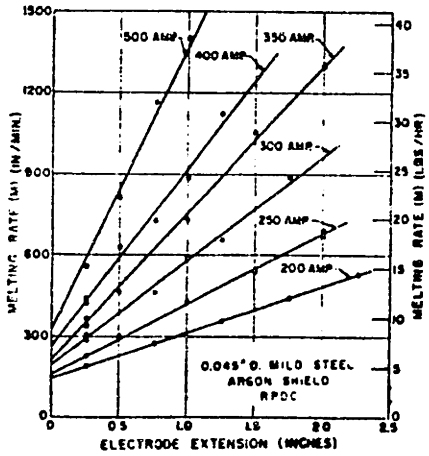

Figure A.8 Electrode melting rate versus stickout and current. (69)

melting rate versus stickout and current for a .045" mild steel wire shown in figure A.8. The empirical relation describing the melting rate of mild steel wires of various diameters is given in mks units by:

$$\dot{m} = \frac{(1.74 \times 10^{-14})L}{A^{1.26}} I^2 + (2.1 \times 10^{-6} + .073A)I \qquad (A.15)$$

A.7 Metal Transfer

In addition to the rate at which the tip of the wire melts, the mode by which the molten metal detaches and transfers to the weld pool has a significant effect on the final weld. The three most common modes of metal transfer are short circuiting, globular, and spray. Short circuit ("dip") transfer occurs when the wire physically touches the weld pool, resulting in a current surge that melts the end of the wire by resistance heating. The average voltage and current are very low, and there is no steady arc between the electrode and the workpiece. Metal transfer takes place only when the electrode physically dips into the weld pool. This

mode is used for sheetmetal and out-of-position welding, since the low heat input reduces risk of burn-through and results in a small weld pool which doesn't run when welding vertically or overhead (150). It gives shallow penetration and excessive spatter, and is considered a low quality process.

Globular transfer occurs when resistance heating and arc heating combine to gradually melt the wire tip, thereby forming a large ball of molten metal at the wire tip which eventually detaches and falls into the weld pool. A drop hanging on the tip of the wire is subject to the following forces:

$$F = F_{em} + F_d + F_g - F_s \qquad (A.16)$$

where F_{em} = electromagnetic (Lorentz) forces

F_d = drag from surrounding plasma jet

F_g = gravity

F_s = surface tension forces

The first three tend to detach the drop and propel it down towards the weld pool, while the fourth tends to make the drop hang on to the wire end. Detachment in globular transfer occurs when the drop grows so large that the sum of electromagnetic, drag and gravity forces exceeds the surface tension force.

As current increases, detachment occurs at smaller drop diameters. Eventually a point is reached where drop diameter decreases very rapidly with increasing current, and this is the region of transition to spray transfer. The actual transition current is generally defined as that

current at which the drop diameter equals the wire diameter. As current continues to increase, very small drops are propelled at high frequency and high velocity toward the workpiece. Drop volume and frequency are plotted versus current for a 1/16" mild steel wire in Ar/1%O_2 in figure A.9. The precise phenomena responsible for the transition to spray transfer is an area of ongoing research, but it is believed to be due to

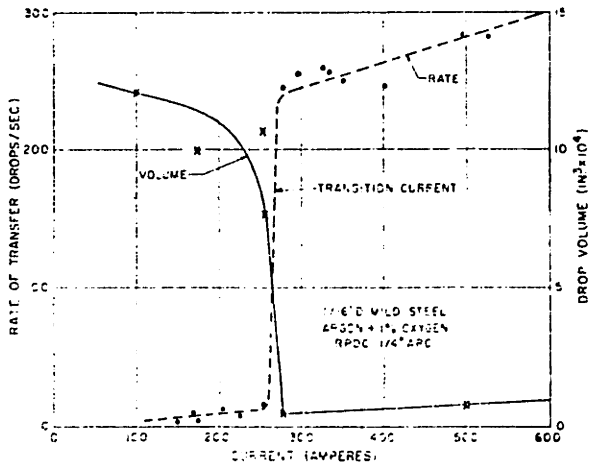

Figure A.9 Drop volume and frequency versus current. (151)

the arc climbing up the electrode. This changes the wire tip configuration from that shown in figure A.10(a) to that shown in figure A.10(b) and allows smaller drops to be rapidly pinched off the end of

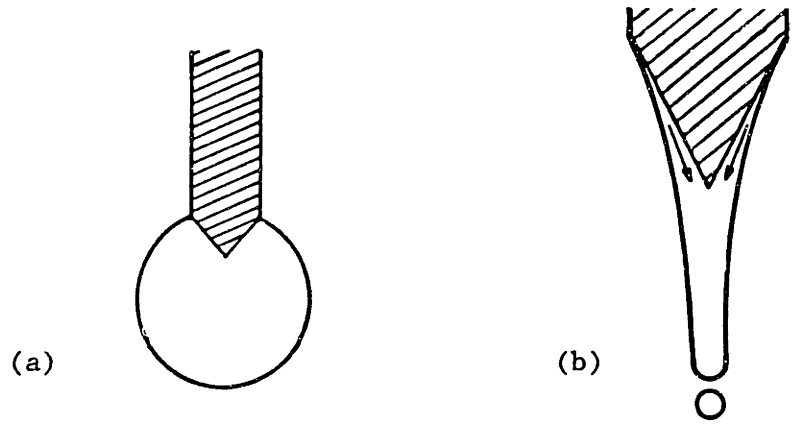

Figure A.10 Wire tip configuration: (a) globular transfer, (b) spray transfer. (147)

the wire by the Lorentz force (150). The formation of a plasma jet (85) and the presence of a critical concentration of metal vapor in the arc (151) have also been identified as contributing to the formation of spray transfer.

The current at which transition to spray transfer occurs depends on the electrode composition, diameter, extension, and shielding gas composition. Spray transfer is only possible in argon based gas mixtures. The dissociation of non-monatomic gases such as CO_2 consumes too much of the arc energy and deters the arc from climbing up the electrode to form the configuration shown in figure A.10(b). While spray transfer is normally possible only in reverse polarity, the addition of sufficient alkali, alkali-earth, or rare-earth metals to the electrode surface allows the transfer with straight polarity. Higher concentrations of these activating elements result in lower transition currents.

For a bare mild steel electrode in $Ar/1\%O_2$, reference (150) empirically found the transition current to be given by:

$$I_s = 60 + 3400D - 30L \qquad (A.17)$$

I_s = transition current to spray transfer (A)
D = electrode diameter (in)
L = electrode extension (in)

Thus, for a .045" wire with a 3/4" stickout, spray transfer would be expected above 190 amps.

At even higher currents, the metal transfer eventually turns from axial spray (as described above) to rotating spray, in which the end of the wire softens and whips around, sending the drops all over the place. For the same conditions as equation A.17, reference (151), gives the transition to rotating spray as:

$$I_R = 25 + 1350D + (14.5 \times 10^4) \frac{D^2}{L} \qquad (A.18)$$

Axial spray is the metal transfer mode of choice for most GMAW applications. The plasma jet and steady stream of drops give the arc directional stiffness and result in much deeper penetration than is possible with globular or short-circuit transfer. The useful current range of GMAW is therefore bounded on the lower end by the axial spray transition and at the upper end by the rotating spray transition. Although spray transfer is generally preferred, the large current necessary to achieve it results in a very high heat input and a large weld pool, making spray transfer unsuitable for sheet metal and out-of-position welding.

APPENDIX B

TEMPERATURE PLOTS OF α AND $(H_c - H_o)$

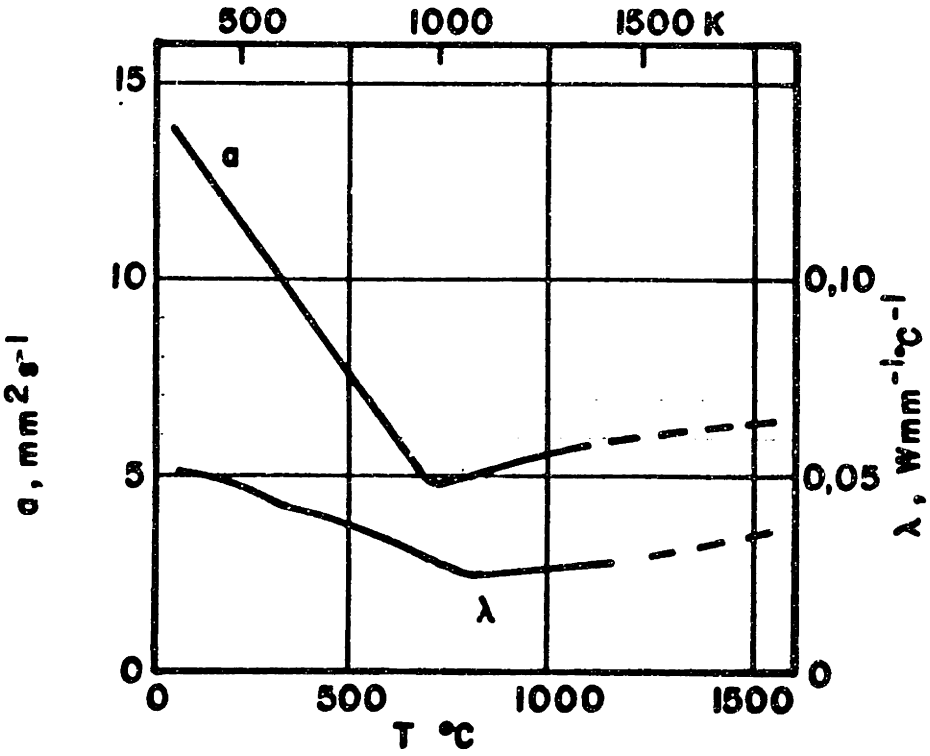

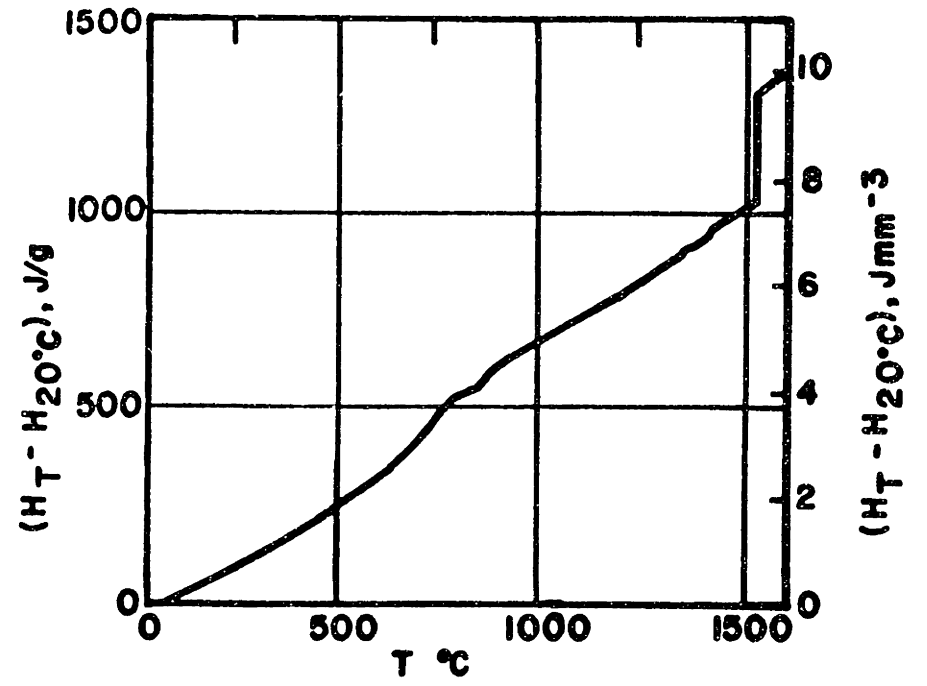

APPENDIX C

CHRISTENSEN'S TIME-TEMPERATURE PROFILES

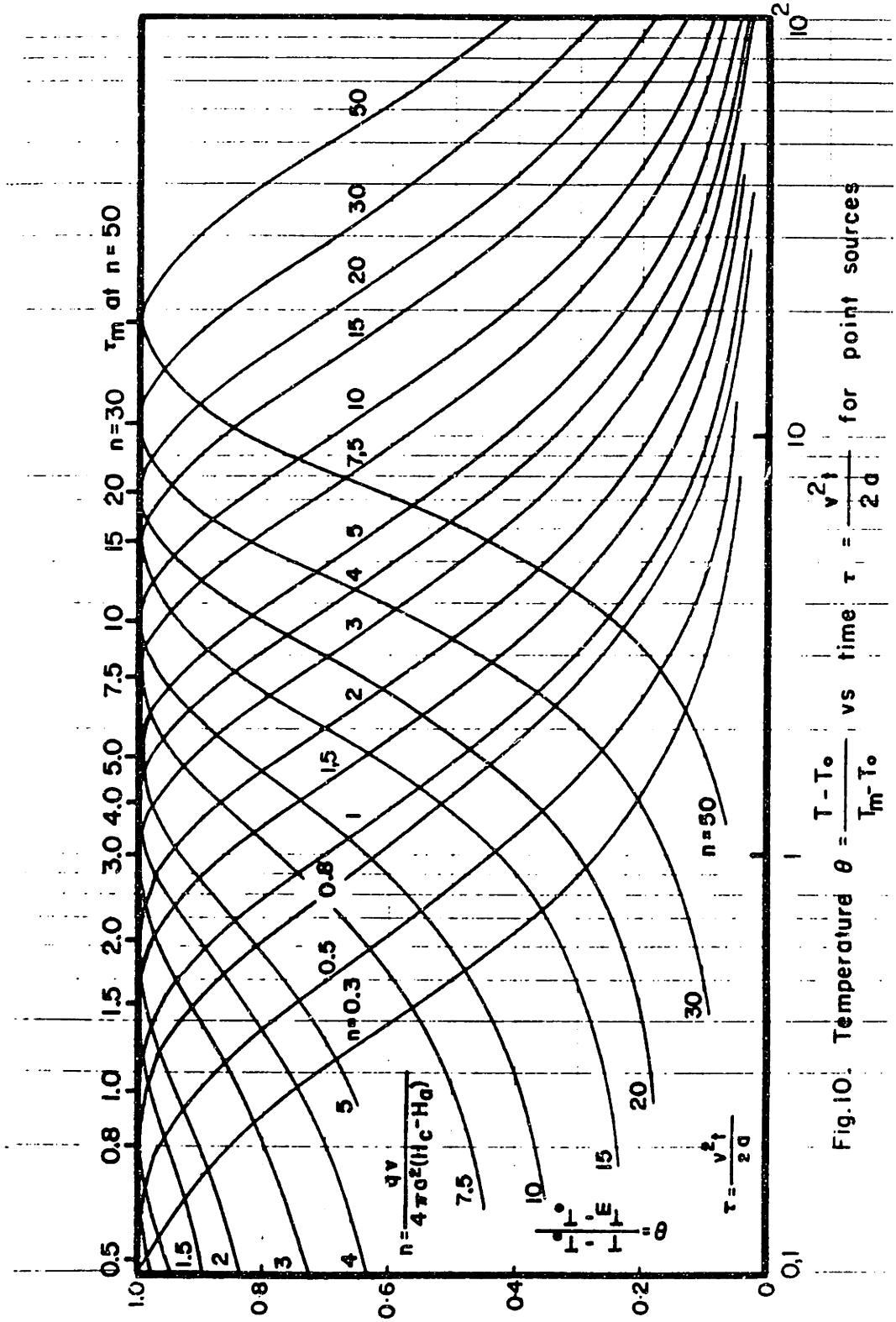

APPENDIX D

Table D.1 LF data set #2. Current set at 100/400 A square wave. <I> is the measured average current. V is the measured average voltage. d, w, and h are the measured weld bead dimensions. σ_d is the standard deviation of the three depth measurements. TS = 13 ipm, TH = 1/2". WFS was measured to be 339 ipm except at 16 Hz, where it was measured to be 325 ipm. These welds were made with the new Kusko current regulator before it was modified by increasing the capacitance.

f	<I>	V	d	w	h	σ_d
10 Hz	250 A	28 V	3.64 mm	12.78 mm	4.61 mm	.07 mm
12	250	28	4.02	12.02	4.66	.19
14	240	27	4.19	11.05	4.40	.13
16	240	25.7	4.11	11.26	4.36	.07
18	238	25.6	4.00	12.19	4.23	.06
20	238	26	4.02	12.15	4.15	.19
20	240	25	4.21	11.68	4.21	.20
22	230	24	3.89	11.43	4.09	.29
24	226	23.4	3.89	11.43	3.64	.15
26	226	23.4	3.89	11.43	3.73	.41
28	225	23.2	3.37	12.19	3.66	.11
30	229	23.6	3.73	12.70	3.47	.15

Table D.2 Drop transfer data

$I_{b/p}$(A)	$T_{b/p}$ (ms)	$I^2_pT_p$(A^2s)	d(mm)	W(mm)	DT(ms)	V(m/s)
100/400	4.00/4.00	640	3.26	11.85	3.00	2.22
132/500	5.44/2.56	640	2.94	10.86	3.00	2.54
150/600	6.22/1.78	640	2.46	12.04	2.80	2.18
162/700	6.69/1.31	640	2.50	12.07	2.85	1.90
171/800	7.00/1.00	640	2.48	12.83	3.00	1.51
100/400	4.00/4.00	640	3.26	11.85	3.00	2.22
100/500	5.00/3.00	750	3.34	11.54	2.50	2.81
100/600	5.60/2.40	864	3.68	10.24	2.60	3.43
100/700	6.00/2.00	980	4.83	7.96	2.30	3.95
100/800	6.28/1.72	1100	4.13	9.91	2.25	4.19
162/400	3.5/4.5	720	3.34	12.13	3.00	2.41
100/400	4.0/4.0	640	3.26	11.85	3.00	2.22
133/400	4.5/3.5	560	2.88	11.85	4.00	2.08
160/400	5.0/3.0	480	2.41	11.39	4.25	1.72
100/500	5.00/3.00	750	3.34	11.54	2.50	2.81
109/500	5.12/2.88	720	3.60	11.15	2.75	2.69
132/500	5.44/2.56	640	2.94	10.86	3.00	2.54
153/500	5.76/2.24	560	2.67	11.49	3.20	2.49
171/500	6.08/1.92	480	2.58	12.45	3.00	2.27

Table D.3 Metal transfer description.

$I_{b/p}$ (A)	$T_{b/p}$ (ms)	$I_p^2T_p$	Description
100/400	4.00/4.00	640	One large drop followed by either one medium drop or two small drops that later combine into a medium drop. The large drop elongates excessively and frequently splits into two drops . The second drop velocity is typically 1.91 m/s versus 2.22 m/s for the first drop.
132/500	5.44/2.56	640	One large drop detaches at the trailing edge of the pulse. It is followed by several small drops.
150/600	6.22/1.78	640	Very clean ODPP transfer, although there is usually a tiny trailing drop.
162/700	6.69/1.31	640	ODPP, but the pulse ends far enough prior to detachment that the drop hangs on the end momentarily.
171/800	7.00/1.00	640	ODPP with no trailing drops.
100/500	5.00/3.00	750	One large drop, one medium drop, and one small drop that usually catches up to and joins the medium drop. Velocity of second drop is 2.17 m/s versus 2.81 m/s for the first.
100/600	5.60/2.40	864	One large drop followed by a stream that breaks up into two or three very small drops.
100/700	6.00/2.00	980	One large drop followed by a stream that breaks up into two small drops.
100/800	6.28/1.72	1100	Stream breaks up into one large drop and one or two small drops. Drops are frequently off center. Second drop velocity is typically 3.10 m/s versus 4.19 for the first.

62/400	3.5/4.5	720	One large drop detaches cleanly and is followed by a stream that breaks up into a large drop and a small drop. Picture is obscured by smoke. Second drop velocity is 2.33 m/s versus 2.41 m/s for the first.
133/400	4.5/3.5	560	One large drop with two to four very small trailing drops with each pulse.
160/400	5.0/3.0	480	One large drop with one or two very small trailing drops on about two thirds of the pulses.
109/500	5.12/2.88	720	One large drop detaches cleanly and is followed by a stream that quickly breaks up into a medium and a small drop. Second drop velocity is typically 2.15 m/s versus 2.69 m/s for the first drop.
153/500	5.76/2.24	560	One large drop followed by one or two small drops. Large drops deflect about half a wire diameter to one side, and the small drops defleet about a full wire diameter to the other side. The second drop velocity is typically 1.91 m/s versus 2.49 m/s for the first drop. Some small drops tend to linger between pulses with velocities of around 1.1 m/s.
171/500	6.08/1.92	480	One large drop followed by a stream that whips around and throws small drops off center. Large drops are nearly a full wire diameter to one side; small drops are even more to the other side. Metal transfer is irregular. Small drop velocity is typically 1.86 m/s versus 2.27 m/s for the first drop. Some small drops tend to linger between pulses with velocities of around 1.2 m/s.

REFERENCES

(1) Butman, Boris S., "Soviet Shipbuilding: Productivity Improvement Efforts", Journal of Ship Production Vol. 2, No. 4, November 1986, pp.225-237

(2) Munson, George E., "Robotics in Perspective", Robotics Today, Vol. 8, No. 2, April 1986, p.29

(3) Schreiber, Rita R., "Robots 10 in Retrospect", Robotics Today, Vol. 8, No. 4, August 1986, p.31

(4) Bortz, Alfred B., "Joseph Engelberger: The Father of Industrial Robots Reflects on his Progeny", Robotics Age, April 1985, pp.15-22

(5) Lane, Frederick C., Ships for Victory, A History of Shipbuilding Under the U.S. Maritime Commission in World War II, Johns Hopkins Press, 1951

(6) Toward More Productive Naval Shipbuilding, Committee on U.S. Shipbuilding Technology, Marine Board, National Research Council, National Academy Press, Washington, D.C., 1984

(7) Kolodziejczak, Gregory C., Group Technology Applications in Shipboard Piping System Manufacture, Ocean Engineer's thesis, MIT, May 1985

(8) Koreisha, Nicholas A., The Application of Robotic Arc Welding to Shipbuilding, Ocean Engineer's thesis, MIT, June 1984

(9) Chirillo, L.D. and Chirillo, R.D., "The History of Modern Shipbuilding Methods", testimony submitted to the U.S. House of Representatives, Committee on Merchant Marine and Fisheries, June 20, 1984, p.3

(10) Report of the Commission on American Shipbuilding, Volume II, Washington, D.C., October 1973, p.86

(11) Weiers, Bruce J., The Productivity Problem in United States Shipbuilding, U.S. Department of Transportation, Transportation Systems Center, Cambridge, MA, 1984

(12) Brasher, J.W., "Benefits of the National Shipbuilding Research Program to the Navy and the Industrial Base: Part 2 - Industry Perspective", Journal of Ship Production, Vol. 2, No. 4, November 1986, pp.203-208

(13) Nierenberg, A., "Pre-Contract Effort and Key Plans", Design for Zone Outfitting, Seminar at Avondale Shipyards, Inc., July 21, 1982, p.2

(14) Dufrene, A., "Coding Systems", Process Lanes and Design Engineering for Zone Outfitting, Seminar at Avondale Shipyards, Inc., June 7, 1984, graph PL-16

(15) Agapakis, John E., et al, Basic Research on the Introduction of Welding Robots to Commercial Shipbuilding, Report No. MA-RD-760-85020, MIT, February 1985

(16) Grimsley, G., "Zone Outfitting Concepts", Process Lanes and Design Engineering for Zone Outfitting, Seminar at Avondale Shipyards, Inc., June 8, 1984, graph PL-49

(17) Storch, Richard L. and Gribskov, Jon R., "Accuracy Control for U.S. Shipyards," Journal of Ship Production, Vol. 1, No. 1, February 1985, p. 74

(18) Christensen, W.L., "Benefits of the National Shipbuilding Research Program to the Navy and the Industrial Base: Part 3 - Navy Perspective," Journal of Ship Production, Vol. 2, No. 4, November 1986, pp. 209-216

(19) Taylor, J. and Weidman, W., "Accuracy Control, Process Lanes and Design Engineering for Zone Outfitting," Seminar at Avondale Shipyards, Inc., June 8, 1984, p. 74

(20) Fetchko, Joseph A., "Methods of Estimating Investment Costs of Ships," lecture notes for Intensive Course in Economics in Ship Design and Operation, University of Michigan Engineering Summer Conferences, June 1968, p. 21

(21) Hill, John W., et al, Advanced Automation for Shipbuilding, SRI International, Project 1221, November 1980

(22) Wright, R.R., "Welding Automation in Action", International Conference on Developments in Mechanized, Automated, and Robotic Welding, London, 18-20 November 1980, paper 13

(23) Eichhorn, F., "Aspects of the Mechanization, Automation, and Utilization of Robots in Welding", Welding and Joining Techniques, July/August 1985

(24) Malin, V., "Designer's Guide to Effective Welding Automation -Part II: Flexibility and Economics", Welding Journal, June 1986, pp. 43-52

(25) Implementation Plan for Flexible Automation in U.S. Shipyards The Charles Stark Draper Laboratory, Inc., CSDL-R-1908, October 1986

(26) Anon, "Automated Welding Machines - An AWS Primer About Robots", Welding Journal, November 1985, p.69

(27) Stauffer, Robert N., "Justification of Robotic Systems", Robotics Today, Vol. 8, No. 3, June 1986, pp. 35-43

(28) Rogers, Peter R., "The Economics of Robotic Arc Welding Workcells", Robotics Today, Vol. 6, No. 3, June 1984, pp.46-48

(29) Shunk, Dan L., "Group Technology Characterization Code and Support Software," USAF ICAM Technology Transfer Seminar notes, Arizona State University, February 12-13, 1985

(30) Lardner, James F., "Executive View of Group Technology Applications for Successful CIM Implementation," technical paper presented at SME's 1982 International Tool and Manufacturing Engineering Conference, May 17-20, 1982, p.3

(31) Houtzeel, Alexander, "Classification and Coding: A Tool to Organize Information," Attachment 4 to lecture 2 in Ship Production Technology Course at University of Washington, p.462

(32) Wilson, R.C. and Henry, R.A., Introduction to Group Technology in Manufacturing and Engineering, University of Michigan, 1977, p.25

(33) Gallagher, C.C., Banerjee, S.K., and Southern, G., "Group Technology in the Shipbuilding Industry," International Journal of Production Research, Vol. 12, No. 1, 1974, p.45

(34) Bobrowicz, Vincent F., "CODE: Group Technology Classification System," Coding and Classification Workshop, Arlington, Texas, June 23, 1975, p.95

(35) Ham, Inyong, "Introduction to Group Technology and its Application to Shipbuilding Industry," Pennsylvania State University, June 1977, p.1

(36) Hyer, Nancy L. and Wemmerlov, Urban, "Group Technology and Productivity," Harvard Business Review, July-August 1984, p.144

(37) Hendrixson, Dale, "Trends and Transitions in the Robotics Industry," Robotics Age, November 1985, p.23

(38) Starkenburg, C., "Production Planning Interface," Design Engineering for Zone Outfitting, Seminar at Avondale Shipyards, Inc., July 22, 1982, p.5

(39) Naval Sea Systems Command Integrated Robotics Program, NAVSEA Technical Report No. 450-90G-TR-0002, Office of Robotics and Autonomous Systems, Annual Report, Fiscal Year 1984, December 1984

(40) "All Electric Doodle Bug Automatic Dual Head Stiffener Welder," product brochure, M.K. products, Inc., Irvine, CA.

(41) Malin, V., "Designer's Guide to Effective Welding Automation -Part I: Analysis of Welding Operations as Objects for Automation", Welding Journal, November 1985, p.17

(42) Linden, G., Lindskog, G. and Nilsson, L., "A Control System Using Optical Sensing for MIG Arc Welding", International Conference, London, November 1980, p.17-1

(43) Weymueller, C.R., "Robotic Welding Draws Hundreds to Cleveland", Welding Design and Fabrication, August 1981, p. 80-81

(44) Ostrowski, M.A. and Green, M.F., "It's Here - the First Robot Arc Welding Line", Welding Design and Fabrication, April 1981, p.94

(45) Weymueller, C.R., "Cabinets by the Gross - Tight Fits Easy for Robot", Welding Design and Fabrication, August 1982, p. 59

(46) Wolke, R.C., "Integration of a Robotic Welding System with Existing Manufacturing Processes", Welding Journal, September 1982, p.24

(47) Brosilow, R., "Robot Welder Boosts Circuit Breaker Production", Welding Design and Fabrication, August 1982, p.58

(48) Sigman, R.D., "Robotic Welding: Productive, Versatile", Welding Design and Fabrication, November 1982, p.63

(49) Grannan, D., "The New Weld Joint Tackers - Their History and Technology", Welding Journal, March 1986, p.49

(50) Reeve, R.C., "Self-Programming Robotic Weld System", International Conference, London, November 1980 p.4-1

(51) Verdon, D.C., Langley, D. and Moscardi, M.H., "Adaptive Welding Control Using Video Signal Processing", International Conference, London, November 1980, p.29-1

(52) Kuk, K.A., "Determining Acceptable Joint Mislocation in Systems Without Adaptive Control", Welding Journal, November 1985, p.65

(53) Everett, H.R., "Robotics in the Navy", Robotics Age, November 1985, p.7

(54) Anon, "LNG Storage Tanks Welded Automatically", Welding and Metal Fabrication, January/February 1982, pp.27-29

(55) Dornfeld, D.A. and Tomizuka, M., "Development of a Comprehensive Control Strategy for Gas Metal Arc Welding", Proc. 10th Conference on Production Research and Technology, Detroit, March 1983, p.272

(56) Masaki, I. et al, "Welding Robot with Visual Seam Tracking: Unika-80A", International Conference, London, November 1980, p. 12-2

(57) Masaki, I. et al, "Arc Welding Robot Visually Tracks it Way Along Seam", Welding and Metal Fabrication, January/February 1982, p.19

(58) Clocksin et al, "Visually Guided Robot Arc Welding of Thin Sheet Steel Pressings", Twelfth International Symposium on Industrial Robots, 1982, p.225-229

(59) Chang, In Hwa, "Real-Time Control of a Root Gap During Butt Welding", PhD thesis (in progress), MIT Department of Ocean Engineering

(60) Miyachi, Hiroshi, "Distortion Control of Fillet Joints During the Welding Process", PhD thesis (in progress), MIT Department of Ocean Engineering

(61) Scott, J.J. and Brandt, H., "Adaptive Feed-Forward Digital Control of GTA Welding", Welding Journal, March 1982, p.36

(62) Holmes, J.G. and Resnick, B.J., "Human combines with Robot to Increase Welding Versatility", Welding and Metal Fabrication, January/February 1980, p.17

(63) Vroman, A.R. and Brandt, H., "Feedback Control of GTA Welding Using Puddle Width Measurement", Welding Journal, September 1976, p.742-749

(64) Garlow, D., "Closed Loop Control of Full Penetration Welds Using Optical Sensing of Back Bead Width", S.M. Thesis, Dept. of M.E., MIT, June 1982

(65) Hardt, D.E. and Katz, J.M., "Ultrasonic Measurement of Weld Penetration", Welding Journal, September 1984, p.273s

(66) Hardt, D.E. and Doumandis, C., "A Model for Real-Time Control of Weld Material Properties", Modeling, Sensing, and Control of Manufacturing Processes, The Winter Annual Meeting of ASME, Anaheim, CA, December 1986, pp. 143-163

(67) Smith, D.R., Weld Reduction Pilot Program, Final Report, Bath Iron Works, September 10, 1986.

(68) Forrest, Dave, Senior Welding Engineer at Bath Iron Works, private communications on April 4, 1986, and January 19, 1987

(69) Lesnewich, A., "Control of Melting Rate and Metal Transfer in Gas-Shielded Metal-Arc Welding: Part I - Control of Electrode Melting Rate," Welding Journal, August 1958, pp. 343s-353s

(70) Rosenthal, D., "The Theory of Moving Sources of Heat and Its Applications to Metal Treatment", Transactions of ASME, 68 (11), 1946, pp.849-866

(71) Rykalin, N.N., "Calculation of Heat Processes in Welding", Moscow, 1960

(72) Rykalin, N.N., and Nikolaev, A.V., "Welding Arc Heat Flow", Welding in the World, 9 (3/4), 1971

(73) Rykalin, N.N., "Energy Sources Used for Welding", 1974 Houdremont Lecture, Welding in the World, Vol. 9/10, 1974

(74) Matsuda, Fukuhisa et al, "Metal Transfer Characteristics in Pulsed GMA Welding", Transactions of JWRI, Vol. 12, No. 1, 1983

(75) Bartholomew, S.J., "Pulsed MIG for Improved Weld Quality", The Welding Institute Research Bulletin, Vol. 25, No. 10, October 1984, pp.332-335

(76) Troyer, W., Tomsic, M., and Barhorst, R., "Investigation of Pulsed Wave Shapes", Welding Journal, January 1977, pp.26-32

(77) Lucas, W. and Naseer-Ahmed, "Control of Weld Penetration in TIG Welding: A Review of Factors Affecting Weld Pool Behavior and of Techniques to Improve Process Control", Welding Institute Research Report, No. 260/1985, February 1985

(78) Allum, C.J., "MIG Welding - Time for a Reassesment", Metal Construction, June 1983

(79) Allum, C.J., "Welding Technology Data: Pulsed MIG Welding", Welding and Metal Fabrication, January/February 1985, pp.24-30

(80) Matsuda, Fukuhisa et al, "Pulsed GMAW: One-Drop-Transfer and Process Parameter", Transactions of JWRI, Vol. 13, No. 2, 1984

(81) Buchinskii, V.N. and Potap'evskii, A.G., "Selecting the Parameters of the Welding Conditions for Pulsed-Arc Welding with a Consumable Steel Electrode", Automatic Welding, 32 (6), June 1979, pp.53-57

(82) Quintino, L. and Allum, C.J., "Pulsed GMAW: Interactions Between Process Parameters - Part 2", Welding and Metal Fabrication, April 1984, pp.126-129

(83) Anon, "Synergic MIG Welding and Its Application", Welding and Metal Fabrication, August/September 1985, pp.267-268

(84) Amin, M., "Synergic Pulse MIG Welding", Metal Construction, Vol. 13, No. 6, June 1981

(85) Chang, C.W., Eagar, T.W. and Szekely, J., "The Modelling of Gas Velocity Fields in Welding Arcs", Arc Physics and Weld Pool Behavior, The Welding Institute International Conference, London, May 1979, paper 13

(86) Burleigh, T.D., "Measurement of the Arc Force in GTA Welding", M.S. thesis, Department of Material Science and Engineering, MIT 1980

(87) Converti, Jose, "Plasma Jets in Arc Welding", PhD thesis, Department of Mechanical Engineering, MIT, July 1981

(88) Masubuchi, Koichi, Analysis of Welded Structures, Pergamon Press, 1980, p.305

(89) Lin, Min Long, Transport Processes Affecting the Shape of Arc Welds, PhD thesis, Department of Material Science and Engineering, MIT, 1985

(90) Mills, G.S., "Fundamental Mechanisms of Penetration in GTA Welding", Welding Journal, January 1979, pp.21s-24s

(91) Hamloy, "The Pressure of the Arc Acting on the Weld Pool", Arc Physics and Weld Pool Behavior, The Welding Institute International Conference, London, May 1979, paper 28

(92) Selyanenkow et al, "The Dependance of the Pressure of the Welding Arc on the Parameters of Tungsten Electrodes", Welding Production, 27 (5), 1980, pp. 6-8

(93) Yamauchi, N. and Taka, T., "TIG Arc Welding with Hollow Tungsten Electrodes", IIW Document 212-452-79

(94) Ushio, Masao and Matsuda, Fukuhisa, "Mathematical Modelling of Heat Transfer of Welding Arc (Part 1)", Transactions of JWRI, 11 (1), 1982

(95) Ishizaki, K., "A New Approach to the Mechanism of Penetration", Weld Pool Chemistry and Metallurgy, The Welding Institute International Conference, London, April 15-17, 1980, paper 24

(96) Glickstein, S.S., "Arc Modelling for Welding Analysis", Arc Physics and Weld Pool Behavior, The Welding Institute International Conference, London, May 1979, paper 5

(97) Saedi, Hamid R., "Transient Response of Plasma Arc and Weld Pool Geometry for GTAW Process", Doctor of Science thesis, Department of Mechanical Engineering, MIT, May 1986

(98) Yamaoto, T. et al, "Characteristics of High Frequency Pulsed D.C. TIG Welding Process", Welding Research Abroad, Vol. 25, No. 10, December 1979, pp.16-29

(99) Bachelis, I.A., "Calculation of Deflection of Welding Arc in a Constant Transverse Magnetic Field", Welding Production, 10 (7), 1963, pp.15-18

(100) Kang, Chung Sun, "Control Parameters for the Arc-Weld Pool Geometry", M.S. thesis, Department of Mechanical Engineering, MIT, 1983

(101) Schellhase, M. and Weinschenk, H.E., "Dynamic Behavior of Consumable Metal Arcs", Arc Physics and Weld Pool Behavior, The Welding Institute International Conference, London, May 1979, paper 32

(102) Sorensen, Carl D., "Digital Signal Processing as a Diagnostic Tool for Gas Tungsten Arc Welding", PhD thesis, Department of Material Science and Engineering, MIT, 1985

(103) Tam, Albert S., "Measurement of Weld Pool Geometry by Frequency Analysis of Pool Impedance", Master of Science thesis in Mechanical Engineering, MIT, October 1986

(104) Renwick, R.J. and Richardson, R.W., "Experimental Investigation of GTA Weld Pool Oscillations', Welding Journal, February 1983, pp. 29s-35s

(105) Chihoski, R.A., "The Rationing of Power Between the Gas Tungsten Arc and Electrode", Welding Journal, 49 (2), February 1970, pp.69s-82s

(106) Lin, M.L. and Eagar, T.W., "Influence of Arc Pressure on Weld Pool Geometry", Welding Journal, June 1985, pp. 163s-169s

(107) Craine, R.E. and Weatherill, N.P., "Asymmetric Fluid Flow in a Hemispherical Container Induced by Electromagnetic Forces", Journal of Applied Mathematics and Physics, (ZAMP), Vol. 31, 1980, pp.514-522

(108) Atthey, D.R., "A Mathematical Model for Fluid Flow in a Weld Pool at High Currents", Journal of Fluid Mechanics, 98 (4), 1980 pp. 787-801

(109) Millere, R.P., Sharamkin, V.I. and Shcherbinin, E.V., "Effect of a Longitudinal Magnetic Field on Electrically Driven Rotational Flow in a Cylindrical Vessel", Magnetohydrodynamics, 16 (1), 1980, pp. 66-69

(110) Heiple, C.R. et al, "Surface Active Element Effects on the Shape of GTA, Laser, and Electron Beam Welds", Welding Journal, March 1983, pp. 72s-77s

(111) Sundell, Robert E. et al, "Minor Element Effects on Gas Tungsten Arc Weld Penetration",Proceedings of the Tenth Conference on Production Research and Technology, Detroit, February 28 - March 2, 1983, P - 128

(112) Glickstein, S.S. and Yeniscavich, W., "A Review of Minor Element Effects on the Welding Arc and Weld Penetration", WRC Bulletin, May 1977

(113) Bad'yanov, B.N., et al, "The Selection of the Composition of the Gas Mixture for Increasing the Penetration Capability of the Arc", Welding Production, April 1977, pp.28-30

(114) Woods, R.A. and Milner, D.R., "Motion in the Weld Pool in Arc Welding", Welding Journal, April 1971, pp.153s-172s

(115) Oreper, B.M., Eagar, T.W. and Szekely, J., "Convection in Arc Weld Pools", Welding Journal, November 1983, pp.307s-312s

(116) Wang, Y.H. and Kou, Sindo, "Driving Forces for Convection in Weld Pools", Advances in Welding Science and Technology, Proceedings of an International Conference on Trends in Welding Research, Gatlinburg, Tennessee, May 1986, pp.65-69

(117) Szekely, Julian, "The Mathematical Modeling of Arc Welding Operations", Advances in Welding Science and Technology, May 1986, pp.3-14

(118) Essers, W.G. and Walter, R., "Heat Transfer and Penetration Mechanisms with GMA and Plasma-GMA Welding", Welding Journal, February 1981, pp.37s-42s

(119) Essers, W.G. and Walter, R., "Some Aspects of the Penetration Mechanisms in Metal-Inert-Gas (MIG) Welding", Arc Physics and Weld Pool Behavior, The Welding Institute International Conference, London, May 8-10, 1979, paper 11

(120) Ando, K. and Nishiguchi, K., "Mechanism of Formation of Pencilpoint-Like Wire Tip in MIG Welding", IIW Document 212-156-68

(121) Jelmorini, G., Tichelaar, G.W. and van den Heuvel, G.J.P.M., "Droplet Temperature Measurements in Arc Welding", IIW Document 212-411-77

(122) The Physics of Welding, International Institute of Welding, edited by J.F. Lancaster, Pergamon Press, 1984

(123) Lancaster, J.F., "Metal Transfer and Mass Flow in the Weld Pool", The Physics of Welding, 1984, pp.238-241

(124) Pintard, J., "Characteristiques de la Fusion et du Transfert dans la Procede MIG de Soudage de L'Acier sous Argon", IIW Document 212-111-67

(125) Jonsson, M., Karlsson, L. and Lindgren, L.E., "Simulation of Tack Welding Procedures in Butt Joint Welding of Plates", Welding Journal, October 1985, pp.296s-301s

(126) Andersson, B.A.B., "Thermal Stresses in a Submerged-Arc Welded Joint Considering Phase Transformations", Journal of Engineering Materials and Technology, Transactions of the ASME, Vol. 100, October 1978, pp.356-362

(127) Andersson, Borje and Karlsson, Lennart, "Thermal Stresses in Large Butt-Welded Plates", Journal of Thermal Stresses, 4 (3-4), July/October 1981, pp. 491-500

(128) Christensen, Nils, et al. "Temperature Distribution in Welding", British Welding Journal, February 1965, pp.54-75

(129) Christensen, Nils, Welding Metallurgy, unpublished notes, 1981

(130) Fundamentals of Welding, Welding Handbook, Vol. 1, American Welding Society, edited by Charlotte Weisman, 1976

(131) Ries, Daniel E., Gas Metal Arc Welding of Titanium, Ocean Engineering thesis, Department of Ocean Engineering, MIT, 1983

(132) Allemand, C.D. et al, "A Method of Filming Metal Transfer in Welding Arcs", Welding Journal, January 1985, pp.45-47

(133) Agapakis, J.E., Vision-Aided Remote Robotic Welding, PhD thesis, Department of Ocean Engineering, MIT, 1985

(134) Agapakis, J.E., Wittles, N. and Masubuchi, K. "Automated Visual Weld Inspection for Robotic Welding Fabrication", Automation and Robotisation in Welding and Allied Processes, IIW International Conference, Strasburg, France, September 1985, pp.151-160

(135) Agapakis, J.E. et al, "Joint Tracking and Adaptive Robotic Welding Using Vision Sensing of the Weld Joint Geometry", Welding Journal, November 1986, pp.33-40

(136) Bamba, Takao et al, "A Visual Sensor for Arc-Welding Robots", Eleventh International Symposium on Industrial Robots, Tokyo, October 1981, pp.151-158

(137) Kremers, Jan et al, "Development of a Machine-Vision-Based Robotic Arc-Welding System", Thirteenth International Symposium on Industrial Robots and Robots 7, Conference Proceedings, April 1983

(138) Soroka, D.P. and Sigman, R.D., "Robotic Arc Welding: What Makes a System?", Welding Journal, September 1982, pp.15-21

(139) Kokura, Satashi, "Arc Phenomena and Effects in Switching TIG-MIG Welding Method", Transactions of the Japanese Welding Society, 15 (1), April 1984, pp.3-7

(140) Miskoe, W.I., "The Centenary of Modern Welding, 1885-1985, A Commemoration," Welding Journal, 65 (4), April 1986, pp.19-24

(141) Nakanishi, Mutso et al., "Development of AC MIG Arc Welding," Welding Research Abroad, 31 (8/9), Aug/Sept. 1985, pp.2-14

(142) Sanders, N.A. and Pfender, E., "Measurement of Anode Falls and Anode Heat Transfer in Atmospheric Pressure High Intensity Areas," Journal of Applied Physics, 55(3), February 1, 1984, pp.714-722

(143) Dinulescu, H.A. and Pfender, E., "Analysis of the Anode Boundary Layer of High Intensity Arcs," Journal of Applied Physics, 51 (6), June 1980, pp.3149-3157

(144) Quigley, M.B.C., "Physics of the Welding Arc", Welding and Metal Fabrication, December 1977, pp.619-626

(145) Masubuchi, Koichi, course notes for course 13.17, chapter 2, MIT

(146) Eagar, Tom, lecture notes for course 3.37, MIT

(147) Waszink, J.H. and van den Heuvel, G.J.P.M., "Heat Generation and Heat Flow in the Filler Metal in GMA Welding", Welding Journal, August 1982, pp.269s-282s

(148) Willgoss, R.A., "Mathematical Model Predicts Equilibrium", Welding and Metal Fabrication, November/December 1984, pp.340-351

(149) Halmoy, E., "Wire Melting Rate, Droplet Temperature, and Effective Anode Melting Potential", Arc Physics and Weld Pool Behavior, Welding Institute International Conference, London, May 1979, paper 29

(150) Anon, "Metal Inert Gas (MIG) Arc Welding - Part 4", Welding and Metal Fabrication, May 1982, pp.165-172

(151) Lesnewich, A., "Control of Melting Rate and Metal Transfer in Gas-Shielded Metal-Arc Welding: Part II - Control of Metal Transfer," Welding Journal, September 1958, pp.418s-425s

(152) Welding Processes, Welding Handbook, Vol. 2, American Welding Society, edited by Arthur L. Phillips, 1969